

UC San Diego

UC San Diego Electronic Theses and Dissertations

Title

First principles modeling of planar and point defects in materials

Permalink

<https://escholarship.org/uc/item/3tp7x6wh>

Author

Tran, Richard

Publication Date

2020

Peer reviewed|Thesis/dissertation

UNIVERSITY OF CALIFORNIA SAN DIEGO

First principles modeling of planar and point defects in materials

A dissertation submitted in partial satisfaction of the
requirements for the degree
Doctor of Philosophy

in

NanoEngineering

by

Richard Tran

Committee in charge:

Professor Shyue Ping Ong, Chair
Professor Olivia A. Graeve
Professor Jian Luo
Professor Francesco Paesani
Professor Andrea Tao

2020

Copyright
Richard Tran, 2020
All rights reserved.

The dissertation of Richard Tran is approved, and it is acceptable in quality and form for publication on microfilm and electronically:

Chair

University of California San Diego

2020

DEDICATION

To my loving parents and siblings.

TABLE OF CONTENTS

Signature Page	iii
Dedication	iv
Table of Contents	v
List of Figures	ix
List of Tables	xv
Acknowledgements	xvii
Vita	xx
Abstract of the Dissertation	xxi
Chapter 1 Introduction	1
1.1 Background	2
1.2 Database of surface properties and Wulff shapes	3
1.2.1 Surface properties of materials	3
1.2.2 Efficient and accurate predictions of surface properties . . .	4
1.2.3 Challenges and overview	5
1.3 Interfacial dopant segregation to improve the ductility of refractory materials	6
1.3.1 Refractory materials	6
1.3.2 Nanoparticle morphology control with surface dopant segregation	7
1.3.3 Grain boundary dopant segregation	8
1.3.4 Objectives and overview	8
1.4 Defect assisted metal insulator transition for neuromorphic computing	9
1.4.1 Neuromorphic computing	9
1.4.2 Mott insulators	10
1.4.3 Use of defects	11
1.4.4 Use of DFT	11
1.4.5 Objectives and project summary	12
Chapter 2 Surface energies of elemental crystals	13
2.1 Introduction	14
2.2 Methods	16
2.2.1 Slab model generation	16
2.2.2 Computational methodology	17
2.2.3 Wulff shape	18

2.2.4	Anisotropy measures	19
2.2.5	Data scope	20
2.2.6	Surface calculation workflow	21
2.2.7	Code availability	24
2.3	Data records	24
2.3.1	File format	25
2.3.2	Properties	26
2.4	Technical validation	26
2.4.1	Comparison to experimental measurements	26
2.4.2	Comparison with previous computational studies	31
2.5	Conclusion	34
Chapter 3	Anisotropic work function of elemental crystals	37
3.1	Introduction	38
3.2	Methods	41
3.2.1	Definitions	41
3.2.2	Modeling non-uniform work functions	42
3.2.3	Computational details and workflow	43
3.2.4	Data availability	44
3.3	Results	44
3.3.1	Experimental and computational validation	46
3.3.2	Work function of missing-row reconstructions	49
3.4	Discussion	50
3.4.1	Periodic trends in the work function	50
3.4.2	Discrepancies in the comparisons	51
3.4.3	Effect of reconstruction on work function	53
3.4.4	Models for the work function	54
3.5	Conclusions	57
Chapter 4	Morphology control of tantalum carbide nanoparticles through dopant additions and surface segregation	59
4.1	Introduction	60
4.2	Methods	61
4.2.1	Synthesis and characterization of TaC powders	61
4.2.2	Computational methods	63
4.3	Results	65
4.3.1	Undoped TaC nanoparticles	65
4.3.2	Doping efficacy on morphology control	67
4.3.3	Surface segregation of dopants	71
4.3.4	Dopant shape preference and bonding	74
4.4	Discussion and conclusion	78

Chapter 5	Computational study of metallic dopant segregation and embrittlement at Mo grain boundaries	80
	5.1 Introduction	81
	5.2 Methods	82
	5.2.1 Grain boundary structural models	82
	5.2.2 DFT calculations	84
	5.2.3 Key parameters for segregation studies	85
	5.2.4 Empirical continuum models	86
	5.3 Results	87
	5.3.1 Site preference for dopants in Mo twist and tilt GBs	87
	5.3.2 Dopant segregation energy	90
	5.3.3 Strengthening energy	94
	5.4 Discussion	97
	5.4.1 Conclusions	100
Chapter 6	Metal insulator transition under intrinsic defects in V ₂ O ₃	103
	6.1 Introduction	104
	6.2 Methods	106
	6.2.1 DFT calculations	106
	6.2.2 Initial structures and magnetic configurations	107
	6.2.3 Intrinsic defects	107
	6.2.4 Thermodynamic analysis	108
	6.3 Results	110
	6.3.1 Functional assessment of bulk properties	110
	6.3.2 Charged defects in LT AFI V ₂ O ₃	112
	6.3.3 Effect of defects on MIT	117
	6.4 Discussion	119
	6.5 Conclusion	120
Chapter 7	Imaging of proton distributions in nickelate-based neuromorphic Devices	122
	7.1 Introduction	123
	7.2 Experimental details	126
	7.3 Computational Details	126
	7.4 Results	127
	7.5 Discussion	133
	7.6 Conclusion	134
Chapter 8	Summary and outlook	137
Appendix A	Supporting information: Anisotropic work function of elemental crystals .	141

Appendix B	Supporting information: Morphology control of tantalum carbide nanoparticles through dopant additions and surface segregation	163
	B.1 Surface energy	164
	B.2 Compositions and X-ray diffraction patterns	168
Appendix C	Supporting information: Computational study of metallic dopant segregation and embrittlement at molybdenum grain boundaries	174
	C.1 Convergence tests	175
	C.2 Comparison of E_{seg}^X for Mo and W grain boundaries	176
	C.3 Solubility of dopants in Molybdenum	177
	C.4 Corresponding figures for $\Sigma 5$ (100) twist GB	178
Appendix D	Supporting Information: Metal insulator transition under intrinsic defects in V_2O_3	183
	D.1 Derivation of thermodynamic quantities for the calculation of the defect formation energy	185
	D.1.1 Chemical potential	185
	D.1.2 Freysoldt correction	186
Appendix E	Supporting Information: Proton distribution visualization in nickelate neuromorphic devices	190
	E.1 Spatially resolved diffraction studies	191
	E.2 Simulation of RNO crystal lattice	195
	E.2.1 Rotation operator $\hat{R}(\alpha, \beta, \gamma)$	198
	E.2.2 Simulation of diffraction	201
	E.3 Theoretical results	203
	E.3.1 Structural and magnetic considerations	203
	E.3.2 H-doping concentration from XAS shift	204
	E.3.3 Integrated charge density analysis	204
Bibliography	207

LIST OF FIGURES

<p>Figure 1.1: Left: 2D projection of the Wulff construction for an orthorhombic crystal with the $x - y$ plane parallel to the (001) plane. Center: Projection of the resulting equilibrium shape on the (001) plane. Right: Examples of Wulff shapes for a cubic crystal with varying γ.⁵</p> <p>Figure 1.2: Types of phase transitions available to Mott insulators. The inner circle shows the underlying mechanism behind transition. The mid-ring represents various stimuli to trigger transition and the outer ring illustrates the physical properties that can be changed. Note that some property changes are coupled</p> <p>Figure 2.1: Construction of Y (10̄12) slab from the conventional unit cell. Note that the \mathbf{c} lattice vector does not necessarily need to be perpendicular.</p> <p>Figure 2.2: The Wulff shape of α-Fe generated with surface energies for facets up to a max Miller index of (a) 3 and (b) 1.</p> <p>Figure 2.3: A schematic of the high throughput-infrastructure for the calculation the surface energies of elemental crystalline solids. Dashed blocks represent workflow steps performed in parallel.</p> <p>Figure 2.4: Screenshot of the Crystalium web application at Crystalium</p> <p>Figure 2.5: Plot of experimental versus calculated weighted surface energies for ground-state elemental crystal. Structures known to reconstruct have blue data points while square data points correspond to non-metals. Points that are within the standard error of the estimate ($\pm 0.27 \text{ J m}^{-2}$) lie in the white region.</p> <p>Figure 2.6: (a) Plot of the difference in surface energy ($\Delta\gamma_{110} = \gamma_{110}^{\text{reconstruct}} - \gamma_{110}^{\text{relaxed}}$) between the reconstructed and unreconstructed (110) surface of fcc metals. Negative values indicate a tendency to reconstruct. (b) Unreconstructed and (c) reconstructed models for a (110) fcc slab are shown.</p> <p>Figure 3.1: Plot of the electrostatic potential along the hcp Rb (0001) slab model. The Fermi energy (E_f), electrostatic potential of the vacuum region (V_{vac}), average electrostatic potential of the slab region ($V_{\text{slab}}^{\text{interior}}$) and work function ($\Phi$) are indicated.</p> <p>Figure 3.2: Marker shape and color scheme for plots.</p> <p>Figure 3.3: Plot of (a) experimentally measured $\Phi_{\text{poly}}^{\text{expt}}$ vs the computed $\bar{\Phi}$ and (b) $\Phi_{\text{poly}}^{\text{expt}}$ vs the computed $\Phi_{\text{hkl}}^{\text{lowest}}$. The single-factor linear regression line $y = x + c$ for both plots are indicated as dashed blue lines along with the R^2 value and standard error of the estimate (SEE). Values within the light blue (light</p> <p>Figure 3.4: Plot of computed facet-dependent $\Phi_{\text{hkl}}^{\text{HT}}$ in this work vs (a) experimental values^{171,183,196} (b) literature PBE values^{8,20,176,177}, (c) literature LDA values^{8,20,177} and (d) RPBE values (this work).</p>	<p>4</p> <p>10</p> <p>17</p> <p>19</p> <p>22</p> <p>25</p> <p>29</p> <p>30</p> <p>41</p> <p>45</p> <p>46</p> <p>47</p>
---	--

Figure 3.5:	Plot of the (110) work function for an unreconstructed ($\Phi_{110}^{\text{unrecon}}$) and 1×2 missing-row reconstructed ($\Phi_{110}^{\text{recon}}$) surface for fcc materials. Data points corresponding to materials where reconstruction is thermodynamically favorable ($-2 \text{ meV\AA}^{-2} < \gamma_{110}^{\text{recon}} - \gamma_{110}^{\text{unrecon}}$) are labelled in blue.	49
Figure 3.6:	Plot of $\bar{\Phi}$ versus (a) group number and (b) $\bar{\gamma}$ for transition metals, and (c) $\bar{\Phi}$ versus group number for lanthanides. The left and right dashed lines in (a) corresponds to the parabolic peak when plotting group number against $\bar{\gamma}$ and $\bar{\Phi}$ respectively.	50
Figure 3.7:	Plot of the normalized broken bonds vs $\Phi_{\text{hkl}}/\bar{\Phi}$ normalized by average work function for (a) fcc, (b) bcc and (c) hcp structures for elemental crystalline solids commonly observed in literature. A legend indicating the element of each corresponding marker is shown at the bottom right.	54
Figure 3.8:	Plot for the calculated $\bar{\Phi}$ against (a) Pauling electronegativity χ and metallic radius R , and (b) predictions from improved model for $\bar{\Phi} = 1.55 + 3.76 \frac{\chi}{r_{\text{atom}}}$, where $r_{\text{atom}} = \sqrt[3]{V_{\text{atom}}}$ and V_{atom} is the unit cell volume per atom.	56
Figure 4.1:	Characterization of undoped TaC powders, particle shapes and surface energies. (a) Scanning electron micrograph and (b) X-ray diffraction pattern of undoped TaC powders. (c) Varying morphologies corresponding to the surface energy ratio ($R = \gamma_{111}/\gamma_{100}$) and (D) surface energies for the TaC	67
Figure 4.2:	Electron microscopy of powders. Scanning electron micrographs for (a) Fe-doped, (b) Ni-Ti co-doped, and (c) Nb-doped TaC powders.	69
Figure 4.3:	Statistical abundance of particle shapes. For the undoped, Co-, Ni-, Fe- and Ni/Ti- doped TaC powders, the resulting morphologies are (a) non-faceted, (b) faceted polyhedrons, and (c) cubic.	71
Figure 4.4:	Dopant concentrations, surface energies and slab models. (a) Plot of the concentration of dopants detected by X-ray photoelectron spectroscopy with respect to the concentration detected by energy dispersive spectroscopy. The samples chosen for comparison have the highest abundance of modified	73
Figure 4.5:	Calculated enthalpy maps of R as a function of $\Delta\mu_X$ with respect to $\Delta\mu_C$. (a) Ni in TaC, (b) Co in TaC, (c) Fe in TaC, (d) Ti in TiTa_3C_4 with $\Delta\mu_{Ti} = -0.4$ eV, and (e) Ni in TiTa_3C_4 with $\Delta\mu_{Ti} = -2$ eV at the surface. The dashed line indicates $R = 1.15$ (formation of cuboctahedrons) and partitions the enthalpy -ICOHP bond contributions of dopant bonds at the surface. (a) Table of the percentage of covalency for the dopant bonds at the surface and the corresponding metal atom that was substituted in the undoped surface. The remainder percentage represents metallicity. Ni* indicates Ni substituting Ti	76
Figure 4.6:	Structure model for (a) the Mo $\Sigma 5(310)$ tilt GB and (b) the Mo (310) surface slab. Symmetrically distinct sites in the tilt GB are numbered with increasing integers representing increasing distance from the mirror plane.	83
Figure 5.1:	Structure model for Mo $\Sigma 5(100)$ twist GB. Coincident sites are labeled with the number 0, while non-coincident sites are labeled as 1.	84

Figure 5.3:	Plot of energy difference between GBs doped at different sites $E_{GB+X}^{SiteM} - E_{GB+X}^{SiteN}$ against relative radius R_X/R_{Mo} . (a) $E_{GB+X}^{Site1} - E_{GB+X}^{Site0}$ of the $\Sigma 5$ (310) tilt GB; (b) $E_{GB+X}^{Site1} - E_{GB+X}^{Site2}$ of the $\Sigma 5$ (310) tilt GB; (c) $E_{GB+X}^{Site1} - E_{GB+X}^{Site0}$ of the twist $\Sigma 5$ (100) GB.	89
Figure 5.4:	Comparison between the lowest E_{seg}^X of the tilt and twist GBs of Mo.	92
Figure 5.5:	Comparison of the E_{seg}^X calculated using (a) the McLean model and (b) the Miedema model with the lowest DFT predicted values for the $\Sigma 5$ (310) tilt GB. For the Miedema model, E_{seg}^X is given as a range, and E_{seg}^X for Bi, Mg and Sn have no minimum value stated in the literature ⁵⁵	93
Figure 5.6:	Plot of the lowest tilt segregation energy E_{seg}^X against (a) the relative metallic radius difference $\frac{R_X-R_{Mo}}{R_{Mo}}$ for each dopant X, and (b) the square of the relative Pauling electronegativity $(\chi_X - \chi_{Mo})^2$ for each dopant X.	94
Figure 5.7:	Plots of the strengthening energy E_{SE}^X versus segregation energy E_{seg}^X for the 27 dopants in the $\Sigma 5$ (310) tilt GB. (a) based on lowest energy dopant site in GB and free surface (l-to-l approach); (b) based on Site 0 (m-to-s approach). Dopants in the white region (positive E_{seg}^X) prefer to stay in the	96
Figure 5.8:	Plot of the observed strengthening energy E_{SE}^X for the site with the lowest E_{seg}^{GB} versus the two factor linear model for $E_{SE}^{X, \text{model}}(E_{coh}^X, \frac{R_X-R_{Mo}}{R_{Mo}})$ for the 27 dopants in the $\Sigma 5$ (310) tilt GB. (a) Fitting performed	97
Figure 6.1:	Conventional unit cells of (a) the LT monoclinic (large red/blue spheres correspond to opposite spins) (b) and HT corundum phases of V_2O_3 . The Wyckoff symbols and spin directions of each symmetrically distinct site is given on the right of each structure.	107
Figure 6.2:	Plots of the (a) band gap of the LT AFI phase of V_2O_3 and (b) energy difference per formula unit relative to the HT FM phase for the PBE, PBE+ U , SCAN, SCAN+ U and HSE functionals. The U parameters of 2.68 eV and 1.35 eV for PBE+ U and SCAN+ U , respectively, were calibrated to reproduce 112	
Figure 6.3:	Stability map for charged and neutral defects in LT V_2O_3 as a function of ϵ_F and $\Delta\mu_O$. The legend at the top indicates the colors representing defect types. The lighter red region indicates where the formation of vanadium-deficient V_2O_3 is favorable relative to stoichiometric V_2O_3 , i.e., $E_{form} < 0$ eV, while 114	
Figure 6.4:	Total (green), O-2p (blue), and V-3d (red) orbital DoS for a $2 \times 2 \times 2$ supercell of (a) LT stoichiometric V_2O_3 and non-stoichiometric V_2O_3 containing a (b) v_V , (c) v_V' ; (d) v_O' or (e) v_O defect. The VBM and CBM of the non-stoichiometric V_2O_3 (black	116
Figure 6.5:	The $2 \times 2 \times 2$ supercell of V_2O_3 containing v_V (a) and v_O (b). All sites with Bader charges that differ from bulk-like charges are labelled while all other sites have bulk-like charges. Bulk-like charges are labelled on the top left sites for oxygen (-1.24) and vanadium (+1.87).	117

Figure 6.6:	The neutral defect formation energy (E_{form}) for O_i , V_i , v_V and v_O in LT AFI (solid) and HT FM (dashed) V_2O_3 as a function of the oxygen chemical potential ($\Delta\mu_O$, top x axis). The temperature scales based on $p_0 = 0.1$ ($p_0 = 10^{-13}$ MPa in parenthesis) is provided on the bottom x axis.	118
Figure 7.1:	(a) Orthorhombic crystal structure of SNO. The breathing mode is shown by color: expanded NiO_6 octahedra are yellow and contracted are orange. (b) Rotation of the NiO_6 octahedra described by three angles α , β , and γ (c) breathing mode with magnitude B , (d) displacement $\mathbf{d} = (d_x, d_y, d_z)$ of the .	125
Figure 7.2:	(a) Spatially-resolved map of the fluorescence signal at $E=8345$ eV. The white dashed lines outline the Pd and Au electrodes. Bright areas next to the Pd electrode correspond to the reduced valence of nickel ions due to the presence of H^+ . (b) Experimentally measured normalized XAS spectra at .	129
Figure 7.3:	(a) Normalized intensity map of the $\{101\}$ reflection. The white dashed lines outline Pd and Au electrodes. The dark region between the electrodes corresponds to the area where H^+ doping results in structural changes in the film. (b) Spatially-resolved map of the Q -position (\AA^{-1}) of the $\{202\}$. . .	133
Figure A.1:	Plot of computed facet-dependent Φ_{hkl} using LDA from the literature ^{8,20,177} vs experimental values ^{171,183,196}	158
Figure A.2:	Plot of the cohesive energy (E_{coh}) versus the group number for lanthanides.	159
Figure B.1:	X-ray diffraction patterns of Ni-doped TaC powders.	169
Figure B.2:	X-ray diffraction patterns of Co-doped TaC powders.	170
Figure B.3:	X-ray diffraction patterns of Fe-doped TaC powders.	171
Figure B.4:	X-ray diffraction patterns of Nb-doped TaC powders.	172
Figure B.5:	X-ray diffraction patterns of Ni/Ti-doped TaC powders.	173
Figure C.1:	Convergence tests for validating GB size and k -points. $E_{GB+Nb} - E_{GB}$ is converged with respect to the lattice size along the $[001]$ and $[1\bar{3}0]$ direction for the twist GB C.1a and tilt GB C.1b. The GB energy (γ_{GB}) is converged with respect to k_1 ($k_1 = k_2$) for the twist GB C.1c and the tilt GB C.1d. . . .	175
Figure C.2:	Comparison of E_{seg}^X for selected dopants in Mo tilt and twist and W GB. The values for the W system are obtained from a study by Li et al. ⁵⁰	176
Figure C.3:	The dependence of the segregation energy E_{seg}^X on the solubility of the dopants (K_X) in bulk Mo. Values for K_X were extrapolated at 800 K from experimentally derived phase diagrams ^{322–325}	177
Figure C.4:	Plot of the strengthening energy E_{SE}^X versus segregation energy E_{seg}^X for the 29 dopants in the $\Sigma 5$ (100) twist GB. (a) based on the site with the lowest E_{seg}^X ; (b) based on Site 0. Dopants in the white region (positive E_{seg}^X) prefer to stay in the bulk. For dopants that segregate, those with negative E_{SE}^X (blue	178

Figure C.5:	Plot of the observed strengthening energy E_{SE}^X for the site with the lowest E_{seg}^{GB} versus the two factor linear model for $E_{SE}^{X, \text{model}}(E_{coh}^X, \frac{R_X - R_{Mo}}{R_{Mo}})$ for the 29 dopants in the $\Sigma 5$ (100) twist GB. (a) Fitting performed based on the site with the lowest E_{seg}^{GB} . $k_{coh} = 0.259 \pm 0.029$, $k_R = 5.898 \pm 0.730$.	179
Figure C.6:	Plot of the relative difference in atomic size versus the difference in the cohesive energy between the dopant X and host Mo.	180
Figure D.1:	Plots of the (a) band gap of the LT AFI phase of V_2O_3 and (b) energy difference per formula unit relative to the HT FM phase for the PBE+U (red) and SCAN+U (blue) functionals as a function of the effective Hubbard U (U_{eff}) correction value (x-axis). Dashed lines depict a linear fitting for . . .	184
Figure D.2:	Neutral defect formation energy (E_{form}) for O_i , V_i , v_V and v_O in LT AFI (solid) and HT NM (dotted) V_2O_3 as a function of the oxygen chemical potential ($\Delta\mu_O$, top x axis). The temperature scales based on $p_0 = 0.1$ ($p_0 = 10^{-13}$ MPa in parenthesis) is provided on the bottom x axis.	188
Figure D.3:	Total density of states for corundum phase V_2O_3 containing v_V (red), v_O (blue) and no defects (green) under a (a) FM and (b) and NM configuration.	189
Figure E.1:	Averaged diffraction pattern for the {101} reflection (a) and the {202} reflection (b). Projection of the averaged diffraction pattern along the vertical direction is shown in (c,d). The signal from the {101} reflection can be fitted by a single Gaussian function (c), while the signal from the {202} reflection . . .	192
Figure E.2:	(a-c) Intensity (a), Q -position (b), and the width (c) of the {202} reflection from the SNO film. (d-f) Intensity (d), Q -position (e), and the width (f) of the LAO {111} substrate reflection. The electrodes are outlined with dashed lines.	193
Figure E.3:	(a-b) Fluorescence signal from Au (a) and Pd (b) indicates position of electrodes. (c) Non-resonant fluorescent signal from Ni shows the uniform SNO film across the device.	194
Figure E.4:	(a) Orthorhombic unit cell of $SmNiO_3$ taken from the literature ¹⁵ . For better visualization, NiO_6 octahedra are shown around each Ni atom. The contracted octahedra are orange, and expanded are yellow (the breathing mode). (b) An identical unit cell of $SmNiO_3$ consisting of 36 atoms (see . . .	199
Figure E.5:	Intensity of the {101} reflection I_{101} (a-c) and {202} reflection I_{202} (d-f) as a function of NiO_6 octahedra tilt angles (a,d), displacement of the Sm^{3+} cation (b,e), and breathing distortion (c,f). The intensities are normalized to the value in the pristine $SmNiO_3$	202
Figure E.6:	Calculated shift of the XAS peak for H-doped $SmNiO_3$ relative to the peak of the XAS for pristine $SmNiO_3$ (y-axis) for various ratios of H:Ni in the $SmNiO_3$ supercells (x-axis). The experimental shift for H-doped $SmNiO_3$ is shown for reference (dashed line).	205

Figure E.7: Integrated spin density for the E.7a undoped and E.7b H-doped SmNiO_3 system. Dashed (solid) lines indicate the Ni site corresponding to the smaller (larger) NiO_6 polyhedron. The corresponding oxidation state for each Ni-site is shown.

206

LIST OF TABLES

Table 2.1:	The meta data for a particular material.	22
Table 2.2:	Surface properties for a crystal. Properties denoted by * are defined for each distinct surface.	23
Table 2.3:	The possible warnings tagged for each surface calculation.	24
Table 2.4:	Comparison between the calculated unreconstructed and reconstructed surface energies, and experimental surface energies (in $J\ m^{-2}$) for various surfaces of Si. The calculated area fractions based on the Wulff shapes are also provided.	31
Table 2.5:	A comparison of the high-throughput values to experimental and computed values for materials from the literature. A range of values is provided based on the lowest and highest values found in the literature.	32
Table 5.1:	The coordination number, average bond length and polyhedron volume for each site before dopant insertion.	90
Table 6.1:	Phase transition critical temperature T_c of stoichiometric and non-stoichiometric V_2O_3 . Percentage change in T_c relative to that of stoichiometric V_2O_3 is indicated in the last column.	119
Table A.1:	The values of $\bar{\Phi}$ and $\Phi_{hkl}^{\text{lowest}}$ (along with its corresponding Miller index) from high-throughput calculations and the experimental $\Phi_{poly}^{\text{expt}}$ from the literature.	142
Table A.2:	A comparison of the high-throughput values to experimental and computed values for materials from the literature.	146
Table A.3:	The R values for γ_{hkl} and Φ_{hkl} as a function of normalized broken bonds per surface area (\overline{BB}) and Φ_{hkl} as a function of γ_{hkl}	160
Table B.1:	The coefficients and constants, see (Equation B.14), used to calculate the surface energy as a function of $\Delta\mu_i$ for all slab models. Values of Γ_i are the coefficients to $\Delta\mu_i$ in units of \AA^{-2} and represent the coverages of species i at the surface, while the units of the constant b are $eV\text{\AA}^{-2}$. Entries labeled . . .	165
Table B.2:	Dopant concentrations on the TaC powders determined from energy dispersive spectroscopy. The dopant concentrations listed for the Ni/Ti-doped TaC powders represent the concentrations of Ti in the powders. The concentration of Ni for these powders was fixed at 2.5 at.%.	168
Table C.1:	P-values obtained for the multiple linear regressions using ANOVA from Figures 8 and C.5. Tests were conducted with a confidence of 95%.	180
Table C.2:	A table for values of E_{seg}^{FS} , E_{seg}^{GB} and E_{SE} (Unit: eV). E_{seg}^{FS} and E_{seg}^{GB} for all dopants in all sites of the tilt and twist GBs calculated in this study are listed. E_{SE} are listed for each dopant correspond to the lowest E_{seg}^{GB} site in both systems. Dopants (X) are listed in a descending of the metallic radius.	181

Table C.3: Values of the metallic radii (R_X), cohesive energy (E_{coh}) and Pauling electronegativity (χ) for the 29 dopants and the host material (Mo) used in this study.	182
Table D.1: Energy difference (in meV/f.u.) for monoclinic V_2O_3 for a non-magnetic (ΔE_{NM-AFI}) and ferromagnetic (ΔE_{FM-AFI}) configuration relative to an anti-ferromagnetic configuration for 5 different functionals. U_{eff} values of 2.68 eV and 1.35 eV are chosen for the PBE+ U and SCAN+ U functionals respectively.	187
Table D.2: Calculated lattice parameters of the low (I_2/a) and high ($R\bar{3}c$) temperature phases and their experimental counterparts for various functionals. U_{eff} values of 2.68 eV and 1.35 eV are chosen for the PBE+ U and SCAN+ U functionals respectively.	187
Table E.1: Coordinates of the atoms in $SmNiO_3$ orthorhombic unit cell with lattice parameters $a_o = 5.328 \text{ \AA}$, $b_o = 5.437 \text{ \AA}$ and $c_o = 7.568 \text{ \AA}^{15}$. The numbers in brackets next to oxygen atoms indicate an index of Ni atom, relative to which the coordinates of the oxygen atoms are calculated (see	196

ACKNOWLEDGEMENTS

I would like to express my gratitude to my advisor, Prof. Shyue Ping Ong, for his support, guidance, and patience throughout my graduate studies. I would like to thank him for providing me with the opportunities afforded to me to become the scientist that I am today. I will do my best to carry out the professionalism in research and programming that he has taught me. I would also like to express my gratitude to the thesis committee Prof. Jian Luo, Prof. Olivia Graeve, Prof. Andrea Tao and Prof. Francesco Paesani for their assistance and support in the completion of this dissertation.

Secondly, I am grateful to my collaborators, Dr. Zihan Xu, Dr. Balachandran Radhakrishnan, Dr. Chi Chen, Dr. Donald Winston, Prof. Wenhao Sun, Prof. Kristin A. Persson, Dr. Naixie Zhou, Prof. Jian Luo, Dr. Joseph H. Montoya, Dr. Xiang-Guo Li, Prof. Olivia Graeve, Dr. Tianqi Ren, Hui Zheng, Prof. Yoav Kalcheim, Prof. Ivan Schuller, Dr. Ivan A. Zaluzhnyy, Prof. Shriram Ramanathan, Prof. Oleg G. Shpyrko, and Prof. Alex P. Frano. I also would like to thank the Materials Virtual Lab (MAVRL) group members for all the advice and insight they have given me and for helping to bring me out of my shell. Special thanks to Dana Jimenez for keeping me on track with scheduling classes and filing paper work and to Matthew Horton for his help with the Materials Project and Pymatgen.

Finally, I would like to thank my parents and my siblings for their unconditional love and support.

Chapter 2 is, in full, a reprint of the material “Data Descriptor: Surface energies of elemental crystals” as it appears in Scientific Data, Richard Tran, Zihan Xu, Balachandran Radhakrishnan, Donald Winston, Wenhao Sun, Kristin A. Persson and Shyue Ping Ong, 2016, 3 (160080), pp 1-13. The dissertation author was the primary investigator and author of this paper. All calculations and data analysis were performed by the author.

Chapter 3 is, in full, a reprint of the material “Anisotropic work function of elemental crystals” as it appears in Surface Science, Richard Tran, Xiang-Guo Li, Joseph H. Montoya,

Donald Winston, Kristin A. Persson and Shyue Ping Ong, 2019, 687(September), pp 48-55. The dissertation author was the primary investigator and author of this paper. Most calculations and data analysis were performed by the author.

Chapter 4 is, in full, a reprint of the material “Morphology control of tantalum carbide nanoparticles through dopant additions and surface segregation”, Tianqi Ren, Richard Tran, Sebastian Lee, Aric Bandera, Manuel Herrera, Xiang-Guo Li, Shyue Ping Ong and Olivia A. Graeve. This material has been submitted to a peer-reviewed journal and is currently being reviewed for publication. The dissertation author was the primary investigator and author of this paper. All calculations and data analysis for the computational part of this paper were performed by the author. The experimental portion of the work – synthesis and characterization – was done by collaborators Tianqi Ren, Sebastian Lee, Aric Bandera, Manuel Herrera, and Olivia A. Graeve.

Chapter 5 is, in full, a reprint of the material “Computational study of metallic dopant segregation and embrittlement at Molybdenum grain boundaries” as it appears in Acta Materialia, Richard Tran, Zihan Xu, Naixie Zhou, Balachandran Radhakrishnan, Jian Luo and Shyue Ping Ong, 2016, 117 (July), pp 91-99. The dissertation author was the primary investigator and author of this paper. Most calculations and data analysis were performed by the author.

Chapter 6 is, in full, a reprint of the material “Metal insulator transition under intrinsic defects in V_2O_3 ”, Richard Tran, Yoav Kalcheim, Xiang-Guo Li, Ivan Schuller, and Shyue Ping Ong. This material has been submitted to a peer-reviewed journal and is currently being reviewed for publication. The dissertation author was the primary investigator and author of this paper. All calculations and data analysis were performed by the author.

Chapter 7 is, in full, a reprint of the material “Imaging of proton distributions in nickelate-based neuromorphic devices”, Ivan A. Zaluzhnyy, Peter O. Sprau, Richard Tran, Qi Wang, Hai-Tian Zhang, Zhen Zhang, Nelson Hua, Boyan Stoychev, Mathew J. Cherukara, Martin V. Holt, Evgeny Nazaretski, Xiaojing Huang, Hanfei Yan, Ajith Pattammattel, Yong S. Chu,

Shyue Ping Ong, Shriram Ramanathan, Oleg G. Shpyrko, and Alex P. Frano. This material has been submitted to a peer-reviewed journal and is currently being reviewed for publication. All calculations and data analysis for the computational part of this paper were performed by the author. The experimental portion of the work – synthesis and characterization – was done by collaborators Ivan A. Zaluzhnyy, Peter O. Sprau, Qi Wang, Hai-Tian Zhang, Zhen Zhang, Nelson Hua, Boyan Stoychev, Mathew J. Cherukara, Martin V. Holt, Evgeny Nazaretski, Xiaojing Huang, Hanfei Yan, Ajith Pattammattel, Yong S. Chu, Shriram Ramanathan, Oleg G. Shpyrko, and Alex P. Frano.

I would like to acknowledge the following programs under the U.S. Department of Energy for financial support: the Materials Project under Contract no. DE-AC02-05-CH11231 and Quantum Materials for Energy Efficient Neuromorphic Computing (Q-MEEN-C) under Award # DE-SC0019273. I would also like to acknowledge the U.S. Department of Defense for financial support as a part of the National Security Science and Engineering Faculty Fellowship (NSSEFF) under ONR Grant No. N00014-15-1-0030. I like to acknowledge the computing resources provided by the Triton Shared Computing Cluster (TSCC), the National Energy Research Scientific Computing Centre (NERSC), the Extreme Science and Engineering Discovery Environment (XSEDE), and the Center for Nanoscale Materials (CNM).

VITA

2015	B. S. in Nanoengineering, University of California San Diego
2017	M. S. in Nanoengineering, University of California San Diego
2020	Ph. D. in Nanoengineering, University of California San Diego

PUBLICATIONS

1. **Richard Tran**, Zihan Xu, Balachandran Radhakrishnan, Donald Winston, Wenhao Sun, Kristin A. Persson and Shyue Ping Ong “Data Descriptor: Surface energies of elemental crystals”, Scientific Data, 2016, 3 (160080), pp 1-13.
2. **Richard Tran**, Xiang-Guo Li, Joseph H. Montoya, Donald Winston, Kristin A. Persson and Shyue Ping Ong “Anisotropic work function of elemental crystals”, Surface Science, 2019, 687 (September), pp 48-55.
3. **Richard Tran***, Zihan Xu*, Naixie Zhou, Balachandran Radhakrishnan, Jian Luo and Shyue Ping Ong “Computational study of metallic dopant segregation and embrittlement at Molybdenum grain boundaries” Acta Materialia, 2016, 117 (July), pp 91-99. (*These authors contributed equally)

ABSTRACT OF THE DISSERTATION

First principles modeling of planar and point defects in materials

by

Richard Tran

Doctor of Philosophy in NanoEngineering

University of California San Diego, 2020

Professor Shyue Ping Ong, Chair

Defects are a key component in fine tuning the behavior of materials for technological applications. In this thesis, we explore the effect of planar (in the form of surfaces and grain boundaries) and point defects on material properties. We will use density functional theory (DFT) calculations to uncover the physics behind defect modified material properties and develop high-throughput databases. This thesis is broadly divided into three topics.

The first topic (Chapters 2 and 3) focuses on developing a high-throughput database for surface energy and work function. This study covers elemental crystalline solids of over 100 polymorphs and over 70 elements. Our database is rigorously validated against previous experimental and computational data where available. We propose a weighted work function

and surface energy based on the Wulff shape that can be compared to measurements from polycrystalline specimens. We show that the weighted work function can be modeled empirically using simple atomic parameters. Finally, we analyze work function anisotropy with simple bond breaking rules for metallic systems.

The second topic (Chapters 4 and 5) is an investigation of the role of metallic dopant segregation in the planar defects of refractory materials with the intention of reducing room temperature brittleness. We use DFT calculations in conjunction with experimental results to demonstrate dopant induced nanocube formation in TaC which is useful for reducing material porosity during sintering. We also investigate the strengthening/embrittling effects of 29 dopants at the grain boundaries of Mo using DFT and empirical continuum models and assessed several simple atomic parameters as predictors for segregation and embrittlement.

The third topic (Chapters 6 and 7) investigates the role of point defects on the metal insulator transition (MIT) of quantum materials for the purpose of developing energy-efficient neuromorphic devices. Using the PBE+*U* functional, we explore the effect of intrinsic point defects on temperature and electric field induced MIT in V₂O₃. In corroboration with experimental results, we also investigate the use of H-doping to tune the Ni valency of SmNiO₃ which has broad implications in its MIT properties.

Chapter 1

Introduction

1.1 Background

Crystallographic defects are ubiquitous in nature and can act as double-edged swords by hindering or improving the applicability of materials. For example, point defects in semiconductors can lead to the formation of carrier traps. Such traps can decrease the efficiency of devices by causing early carrier recombination via the Shockley-Read-Hall mechanism^{1,2}. At the same time, traps can also act as springboards for carrier conduction via the Poole-Frenkel effect³, reducing the amount of energy needed for electronic switching.

The advent of broad access to supercomputing power coupled with the Kohn-Sham ansatz⁴ to Schrödinger's equation has given birth to the practical application of density functional theory (DFT) for materials design. DFT allows for first principles predictions of various material properties by mapping the many-electron Schrödinger's equation to a functional of the electron density. These developments have aided in furthering our understanding of crystallographic defects by allowing for the accurate and efficient modelling of large interfacial structures and other defect-containing supercells.

In this thesis, we will explore planar and point defects using DFT. A planar defect exists in a two-dimensional space and includes surfaces and grain boundaries. A point defect exists in a zero-dimensional space and includes vacancies, self- and impurity-interstitials, and impurity substitutions. We note that these two classes of defects are not mutually exclusive as some impurities can substitute atoms at a planar defect or bind to existing surface atoms as adsorbates.

The remainder of this thesis is organized into three parts. Chapters 2 and 3 will focus on the construction of a database for the surface energies and work functions of elemental crystalline solids. Chapters 4 and 5 will explore the segregation of substitutional dopants in the grain boundaries and surfaces of refractory materials with the goal of mitigating intrinsic brittleness. Finally Chapters 6 and 7 will explore point defects in quantum materials exhibiting metal insulator transition for the application of energy efficient neuromorphic computing.

1.2 Database of surface properties and Wulff shapes

1.2.1 Surface properties of materials

The surfaces of materials are structurally and chemically more complex relative to the ordered structure of the bulk. Surface properties are of significant interest in the application and engineering of materials. For example, the immediate exposure of the surface to an external environment and the instability brought about by the under-coordination of surface atoms allows for chemical reactions such as corrosion and catalysis to occur. Furthermore, the surface acts as the threshold whereby the electron of a material escapes into the vacuum. The energy required to effect this escape is called the work function (Φ) and is directly dependent upon the properties of the surface. The work function has of key importance in many technological applications, including thermionic electron guns, semiconducting devices, and vacuum chambers.

The surface of a material can be classified by its Miller index or (hkl) plane, *i.e.* the plane in which a material was cleaved to form a facet. Different facets will have different geometrical and chemical makeups on the surface which results in slight variations in thermodynamics, reactivity, and Φ . The ease in which a particular facet will form and its stability is determined by the surface energy (γ), which is the excess energy of the surface relative to the bulk, given by:

$$\gamma = \frac{E_{tot} - E_{bulk}}{A_{slab}} \quad (1.1)$$

where E_{tot} is the total energy of a system containing a surface, E_{bulk} is the energy of the bulk phase of a material and A_{slab} is the surface area generated from cleaving the material.

A crystal will generally facet into the most stable surfaces to reduce its overall surface energy. γ also plays an important role in determining the equilibrium crystal, or Wulff shape, of a material. This shape can be derived from the Wulff construction illustrated in Figure 1.1(left and center) whereby a set of (hkl) planes of the material are arranged at a distance from an origin

proportional to their γ . The convex polyhedron formed from the bisecting planes is the Wulff shape. Although variations in γ can lead to a variety of shapes as seen in Figure 1.1(right), the Wulff shape will always maintain the point group of its parent crystal.

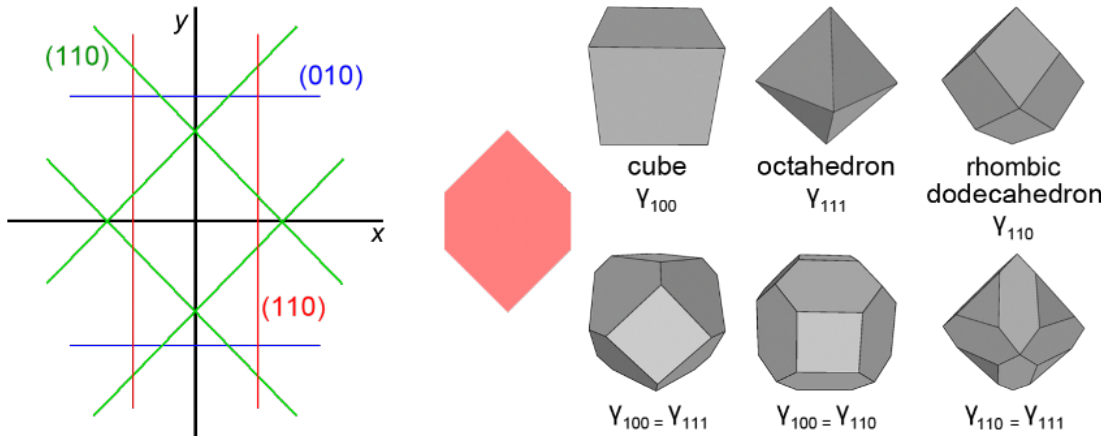


Figure 1.1: Left: 2D projection of the Wulff construction for an orthorhombic crystal with the $x - y$ plane parallel to the (001) plane. Center: Projection of the resulting equilibrium shape on the (001) plane. Right: Examples of Wulff shapes for a cubic crystal with varying γ .⁵

1.2.2 Efficient and accurate predictions of surface properties

DFT calculations have been used extensively to explore a multitude of surface related properties such as surface energy, work function and surface relaxation. However these properties require numerous calculations beginning with the relaxation of the unit cell, followed by the relaxation of several supercell slab models representing multiple possible surfaces with different Miller indices.

As a result, a great deal of computational studies have been dedicated to improving the efficiency and accuracy of these calculations. Some studies coupled DFT with optimization techniques such as Bayesian optimization⁶ and genetic algorithms⁷ to develop efficient means of predicting stable surface structures. Developments in DFT functionals to better model van der Waals forces, such as the SCAN+rVV10⁸ and BEEF-vdW^{9,10}, have also led to more accurate predictions of surface energy, work function, adsorption, and relaxation.

Numerous empirical models^{11,12} have also been proposed to predict surface energy without the use of expensive DFT calculations. The most well known is the broken bond model¹³ given by:

$$\gamma = \frac{N_{BB}E_{coh}}{AN_{CN}} \quad (1.2)$$

where N_{BB} is the number of broken surface bonds, N_{CN} is the bulk coordination number, A is the surface area and E_{coh} is the cohesive energy of the material. Similarly Smoluchowski smoothing¹⁴ proposes an inverse relationship between work function and the number of broken bonds. However, such empirical models fall far short of the accuracy provided by DFT due to the absence of surface relaxation and restriction to elemental metallic systems.

Material databases constructed via high-throughput DFT calculations¹⁵ have provided the necessary data needed to formulate predictive models for material properties using machine learning^{16–18}. A similar database for surface properties can provide the data required to generate such models. Vitos et al.¹⁹ has previously compiled a database for γ for ground state metals up to Pu with the full charge density DFT method under a maximum Miller index (MMI) of 1. Similar data sets for the electronic work function Φ are more scarce with Waele et al.²⁰ having only compiled a data set for 48 elemental crystalline solids under a MMI of 1. More recently, Palizhati et al.²¹ was able to produce a database of surface energies for 3285 intermetallic alloys under a MMI of 2. Neural networks were then used to produce a predictive model for γ with a test mean absolute error of 8.2 meV\AA^{-2} .

1.2.3 Challenges and overview

The recent database and model for γ developed by Palizhati et al.²¹ is a massive leap from the limited bond-breaking models previously proposed. However, there is still much to be desired in when it comes to the modelling of surface properties. For example, few investigations into modeling γ and Φ have yet to be explored for reconstructed surfaces^{22–24} let alone any new

models for Φ in general.

In this thesis we provide the ground work for the database of surface properties. Our database includes the surface energy, work function, and Wulff shape for over 100 polymorphs of over 70 elemental crystalline solids with a MMI of 2 and 3 for non-cubic and cubic crystals respectively. Our database also includes information for well known reconstructed surface structures. Chapter 2 focuses on the construction of our high-throughput workflow which we use to generate the surface energies and Wulff shapes of the elemental crystalline solids. Chapter 3 focuses on expanding our database to include the work functions of these materials and assesses the Smoluchowski model for anisotropic values of Φ as well as propose a new model for Φ for polycrystalline materials. We also investigate the influence of reconstruction on Φ .

1.3 Interfacial dopant segregation to improve the ductility of refractory materials

1.3.1 Refractory materials

Refractory metals are defined by a melting temperatures above 2273 K and exceptional hardness. Such materials are useful in high temperature environments such as those found in scramjet engines, turbine blades, and nuclear reactors. These exceptional properties also lead to excellent creep, sputtering, and corrosion resistance making refractory metals applicable to medical equipment and protective coating materials.

The elemental solids that are classified as refractory metals are Nb, Mo, Ta, W and Re. Additional elements such as silicon, carbon, nitrogen and boron can be added to these metals to form refractory ceramics. These compounds can exhibit increased melting temperatures and hardness due to the hybridization of the metallic *d* and nonmetal *p* orbitals to form strong covalent bonds. For example, the addition of silicon to molybdenum can form MoSi_2 which can increase

the yield strength relative to Mo as much as a factor of six²⁵. Meanwhile the addition of carbon can lead to the formation of transition metal carbides with melting temperatures well above 3200 K²⁶ and as such are referred to as ultra-high temperature ceramics.

Despite the intrinsic hardness of these materials, the formation of microstructural defects in the form of grain boundaries (GBs) and pores leads to an innate brittleness under room temperature conditions, limiting practical application. Furthermore, impurities such as oxygen and bismuth can concentrate at these defects to form precipitants that exacerbate material brittleness.

1.3.2 Nanoparticle morphology control with surface dopant segregation

Although sintering can reduce porosity by compacting individual grains and particles, it is not guaranteed to eliminate them completely. Further reduction in porosity can be accomplished by controlling the nano- and microstructural shape of particles to form more compact geometries such as cubes which allow for uniform stacking during sintering to close existing pores.

Modifying the morphology of these particles begins with changing the surface energy of the material in accordance to the Wulff construction. Methods of tuning the surface energy of refractory ceramics to form specific shapes have been demonstrated by controlling the stoichiometry of the surface for multiple ceramic carbides^{27,28}, nitrides, and diborides²⁹. A similar effect can also be achieved with the addition of impurities such as adsorbates³⁰ and substitutional dopants. Transition metal dopants such as Cr have been shown to change globular WO_3 nanoparticles into octahedrons and cuboids. Meanwhile Fe and Ni doping are effective at forming cubes in NbC and TiC respectively^{27,31}. Nie et al.³¹ postulated that the strong interaction between the dopant-3d and C-2p orbitals on the (100) surface allowed for the formation of cubes.

DFT can be used to determine the surface energy of doped and non-stoichiometric surfaces to provide detailed maps of morphology evolution for nanoparticles. Studies of simple monoatomic adsorption on metallic surfaces such as C on Ru³², N₂ on Fe³³, H on Fe³⁴ and H on Mo³⁵ can reveal the specific surface concentrations of adsorbates required to formed a

particular shape. Calculated Wulff shapes in several works have also successfully corroborated the observed nanoparticle shapes of experiments for materials as simple as elemental silicon^{36,37} and as complex as LiVOPO₄³⁸.

1.3.3 Grain boundary dopant segregation

Grain boundaries also contribute to brittleness in refractory metals and ceramics. These grain boundaries are highly unstable due to the weakened interfacial bonds and can also act as sinks for impurities such as oxygen which increases GB embrittlement. Some impurities however can also be used for GB strengthening in a variety of ways. Grain boundaries can be inoculated with impurities to decrease grain size which increases the yield strength in a process called Hall-Petch strengthening^{39,40}. Dopants called getter materials can also be introduced to capture detrimental impurities, preventing GB segregation^{41–43}. While many dopants, such as bismuth^{44–47}, are known to cause embrittlement via GB segregation, other dopants such as rhenium^{43,48,49} can strengthen GB bonds to reduce material brittleness. DFT has been used extensively to identify dopants as embrittling or strengthening by comparing the dopant potential to segregate into grain boundaries and surfaces^{50–55}.

There have been several empirical models that sought to explain the underlying physics behind interfacial dopant segregation^{56,57} and GB embrittlement^{58,59}. Although it has been known to be inconsistent with experiments for dopants of low solid solubility⁶⁰, DFT has nonetheless aided in expanding upon these models^{55,61,62} to a varying extent.

1.3.4 Objectives and overview

In this thesis we used DFT to explore metallic dopant segregation in the planar defects of two technologically relevant refractory materials in the hopes of mitigating room temperature embrittlement. Chapter 4 is a collaborative effort where we experimentally and computationally

assessed the effect of dopant surface segregation on TaC nanoparticle morphology. Using the Wulff construction, we mapped out the morphology evolution of TaC for each dopant investigated. We explored the notion that dopant enhanced hybridization at the (100) surface will lead to the formation of nanocubes. Chapter 5 explores the segregation and embrittling/strengthening effects of 29 different metallic dopants in Mo GBs. We addressed the disparity between DFT results and continuum empirical models as well as previous experimental results due to the low solubility of specific dopants. We also proposed a model based on site preference and a predictive cohesive energy and atomic strain based model for dopant embrittlement/strengthening in GBs.

1.4 Defect assisted metal insulator transition for neuromorphic computing

1.4.1 Neuromorphic computing

The majority of computers today follow a von Neumann architecture whereby inputs are processed into outputs in a serial fashion. Such devices require vast amounts of computational power and time to accomplish similar cognitive tasks that a human brain can manage with far less time and energy. Neuromorphic computing seeks to replicate the efficiency of the brain using a similar neural network architecture that allows for parallel processing of inputs. Milestones in neuromorphic computing have seen the coupling of devices with software⁶³ and applications in machine learning^{64,65}.

The fundamental device in a neuromorphic system is the neuristor, which like a neuron, produces a non-linear response (*i.e.* a collapse in resistance) only when a signal exceeds a specified threshold. The neuristor will gradually recover its initial state over time once the signal is removed by "leaking" out the response effect to emulate short term memory in a behavior known as "leaky, integrate, and fire". This behavior can be achieved through volatile resistive

switching (VRS) whereby the resistance of a device varies as a hysteretic function of an applied stimulus, *e.g.* an electric field.

1.4.2 Mott insulators

VRS appears in Mott insulators, transition metal oxides (TMO) that are electronically insulating contrary to classical band theory⁶⁶. Nevill Mott believed that the partially filled *d* orbitals of TMOs allows for strong electron-electron interaction (correlation) in the form of Coulombic repulsion⁶⁷. This repulsion separates the electronic bands to open up a band gap allowing for electronic insulation.

Mott insulators can exhibit electronic, structural, magnetic and optical transitions which are coupled together depending on the intrinsic mechanism as shown in Figure 1.2. For the remainder of this thesis, we will focus on the electronic transition of Mott insulators, *i.e.* metal-to-insulator transition (MIT). MIT is coupled to optical and structural transition under an electric field or temperature gradient respectively.

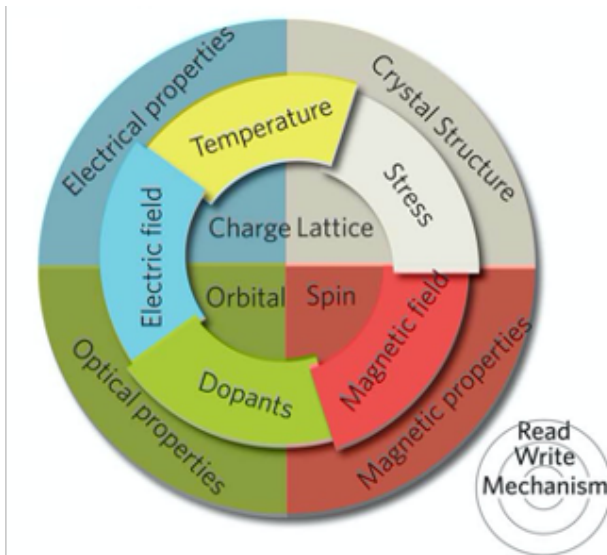


Figure 1.2: Types of phase transitions available to Mott insulators. The inner circle shows the underlying mechanism behind transition. The mid-ring represents various stimuli to trigger transition and the outer ring illustrates the physical properties that can be changed. Note that some property changes are coupled depending on the stimulus.⁶⁸

1.4.3 Use of defects

Defects in the form of impurities, vacancies and self-interstitials are an effective means to tune the writing mechanisms of Mott insulators. Some defects can decrease the necessary electric field strength required to induce VRS which can reduce Joule heating^{69,70}. This is useful for preventing excessive heat dissipation which can also inadvertently lead to VRS. Lowering the threshold stimulus can also reduce the energy consumption of a device during operation. Similarly some defects can decrease critical temperature (T_c) to make temperature induced VRS more accessible (Ti doping in V_2O_3 ⁷¹) or increase T_c to thermally stabilize a material (Cr doping in V_2O_3 ⁷²). On the other hand, the application of temperature gradients^{73,74} and electric fields^{75,76} in Mott insulators are known to introduce point defects such as vacancies and self-interstitials making VRS difficult to reproduce with each cycle. Defects can also change the resistance to tune the electronic threshold of the device such as with H-doping in rare-earth nickelate perovskites (RNiO_3) which can increase resistance by ~ 8 orders of magnitude⁷⁷.

1.4.4 Use of DFT

Standard DFT functionals such as the generalized gradient approximation Perdew-Berke-Ernzerhof (PBE)⁷⁸ and local density approximation⁷⁹ are unable to account for strong electron correlations. This leads to incorrect descriptions of electronic, structural, thermodynamic, and magnetic properties in Mott insulators. The Hubbard-U correction accounts for this by adding a repulsive Coloumbic force between the correlated electrons⁸⁰. However the U-value is empirically fitted to known experimental quantities which reduces the first principles nature of DFT calculations.

In spite of this, PBE+U has been successful in describing the properties of Mott insulators under the presence of defects. Studies in metallic doping in VO_2 ⁸¹ and V_2O_3 ⁸² have provided insight into modulating the phase transitions of Mott insulators with excellent agreement with

previous experiments^{71,72,83}. Similarly, several studies have investigated the influence of hydrogen⁷⁷, lithium⁸⁴, and electron⁸⁵ doping on MIT in RNiO_3 . Studies of the effect of vacancies on resistance change in several transition oxides⁸⁶ such as NiO ⁸⁷ and VO_2 ⁸⁸ have garnered wide success and when coupled with nudged elastic band calculations, provide insight into the role of vacancy diffusion in recovering stoichiometry⁸⁹.

1.4.5 Objectives and project summary

Our objective is to evaluate the influence of defects in different types of highly correlated materials to better tune properties relating to MIT. This will yield insights into manipulating resistive switching in neuromorphic computing devices in an energy efficient manner. For this thesis, we specifically focus on two materials.

Chapter 6 focuses on intrinsic point defects in V_2O_3 . V_2O_3 is widely investigated as a model material for the technological application of MIT due to its structural and chemical simplicity. However, there are difficulties in simultaneously and correctly modelling its structural, magnetic, electronic and thermodynamic properties due to its strongly correlated nature. Subsequently, common defects that occur in V_2O_3 , such as self-interstitials and vacancies, have yet to be explored using DFT. From assessing the performance of various functionals, we conclude that PBE+ U provides the most accurate prediction for the aforementioned properties. We assessed the influence of point defects on these properties with PBE+ U . This work provides the basis for a wider comparative study of point defects in different vanadates^{69,90–93}.

Chapter 7 is a collaborative experimental and computational effort to explore the effect of H-doping in SmNiO_3 , a perovskite structure that is known to exhibit MIT. The underlying tunability of the resistance in this material is related to its change in valency. Although H-doping is known to be an effective means of tuning resistance, its influence on nickel valency is vaguely explored. Here, we evaluated the effect of H-doping on the valency of the Ni cations of SmNiO_3 using experimental and computational x-ray absorption spectroscopy.

Chapter 2

Surface energies of elemental crystals

2.1 Introduction

The surface properties of a crystal are crucial to the understanding and design of materials for many applications. For instance, many technologies such as fuel cells and industrial chemical manufacturing require the use of catalysts to accelerate chemical reactions, which is fundamentally a surface-driven process^{94–102}. Surface effects are especially important in nanomaterials, where relatively large surface area to volume ratios lead to properties that differ significantly from the bulk material^{103–107}. For example, the nanoscale stability of metastable polymorphs is determined from the competition between surface and bulk energy of the nanoparticle^{108–111}.

The stability of a surface is described by its surface energy γ , a measure of the excess energy of surface atoms due to a variety of factors, such as the broken bonds yielding undercoordinated atoms. This fundamental quantity is important in understanding surface structure, reconstruction, roughening and the crystal's equilibrium shape¹¹². Despite its importance, experimental determination of surface energies, especially for specific facets, is difficult and rare.^{37,113–116} Furthermore, experimentally observed Wulff shapes are often inconsistent across studies due to the sensitivity of high energy facets to temperature and impurities¹¹⁷. Niessen et al.¹¹⁸ and Miller and Tyson¹¹³ have accumulated a large set of metallic elemental surface energy data by extrapolating surface tension of liquid phases for solid surfaces. Reviews of such surface tension techniques have been compiled by Mills and Su¹¹⁹ and Keene¹²⁰.

First principles computations such as those based on density functional theory (DFT) methods are important complementary tools to experimental techniques in characterizing surface properties of a material^{121–123}. Computational techniques provide the means to precisely control the surface structure and composition. Indeed, fundamental and application-driven computational studies of surfaces in the literature are extensive^{101,124–126}. On the broader scale, Vitos et al.¹⁹ have previously compiled a database of surface energies for all metals up to Pu using the full charge density (FCD) DFT method, a technique based on the coupling of the linear muffin-tin

orbital method and the atomic-sphere approximation¹²⁷. However, this database is limited to surfaces of ground state crystals up to a maximum Miller index (MMI) of 1 only.

The challenges for DFT determination of surface properties are three-fold. First, the choice of the exchange correlation functional as well as other parameters such as pseudopotentials, integration grid, etc. can significantly affect the accuracy and convergence of surface energies, which in turn leads to values that are generally difficult to compare across different works.¹²⁸ Second, the typical “slab” approach for performing surface energy calculations require the use of large supercells with the introduction of a large vacuum region, which makes such calculations computationally intensive, especially for low symmetry materials and high Miller indices. Finally, some surfaces undergo significant reconstruction to reduce surface energy and increase stability, the most notorious example being the 7×7 reconstruction of the Si (111) surface^{129–131}. In order for the DFT geometry optimization algorithms to identify the global energy minimum surface structure, a reasonable initial guess for the reconstructed surface is needed to avoid relaxation to a local minimum, and such initial guesses are difficult to determine *a priori* without experimental input.

In this work, we present a large database of surface energies and Wulff shapes of more than 100 polymorphs of about 70 elements constructed using high-throughput DFT calculations. The elemental crystals studied include all polymorphs available in the Materials Project (<https://www.materialsproject.org>),¹⁵ and the chemistries covered include both metals and non-metals. All surfaces up to a maximum absolute Miller index (MMI) of 2 and 3 were computed for non-cubic and cubic crystals respectively. To address the first and second challenges outlined above, a robust computational workflow based on the efficient convergence scheme proposed by Sun et al.¹³² was developed to automate the large number of multi-step calculations. To partially address the third challenge, we include well-known reconstructions such as the missing row (110) and hexagonal (111) reconstructions for the face-centered-cubic surfaces^{24,133} in our data set. All data have been made publicly available via the Crystalium web application at the Materials

Virtual Lab website, as well as the Materials Project’s graphical user interface and RESTful Application Programming Interface (API)^{15,134}. The full dataset is also available as a JSON file at the Dryad-repository (Data Citation 1). We show that the calculated surface energies are in excellent agreement with available experimental values. We will also provide an assessment of the effect of surface reconstructions on the accuracy of the data.

2.2 Methods

2.2.1 Slab model generation

The approach used to compute surface energies in this work is the typical slab model, wherein a supercell of the crystal oriented to expose the relevant surface of interest is generated, and atoms are removed from a portion of the supercell to create a vacuum. An example is given in Figure 2.1. Starting from the conventional unit cell, a series of lattice vector transformations is conducted to create an “oriented” unit cell (OUC) where the **a** and **b** lattice vectors are parallel to the plane with Miller indices (hkl) and the **c** lattice vector is not parallel to the plane. It should be noted that **c** vector is not necessarily perpendicular to the plane,¹³² though the “most orthogonal” vector that can be obtained within a reasonable cell size is used. The OUC is then extended by multiples of the **c** lattice vector and atoms are removed to generate the slab model with an desired slab and vacuum thickness. To obtain all symmetrically distinct terminations for a given plane, atoms in the OUC are shifted in the **c** direction prior to extension to generate the slab model. All slabs generated are constrained to have symmetric top and bottom surfaces. The model generation algorithm has been implemented in the Python Materials Genomics (pymatgen) materials analysis library,¹³⁵ with a comprehensive set of unit tests to ensure robust functioning of the code.

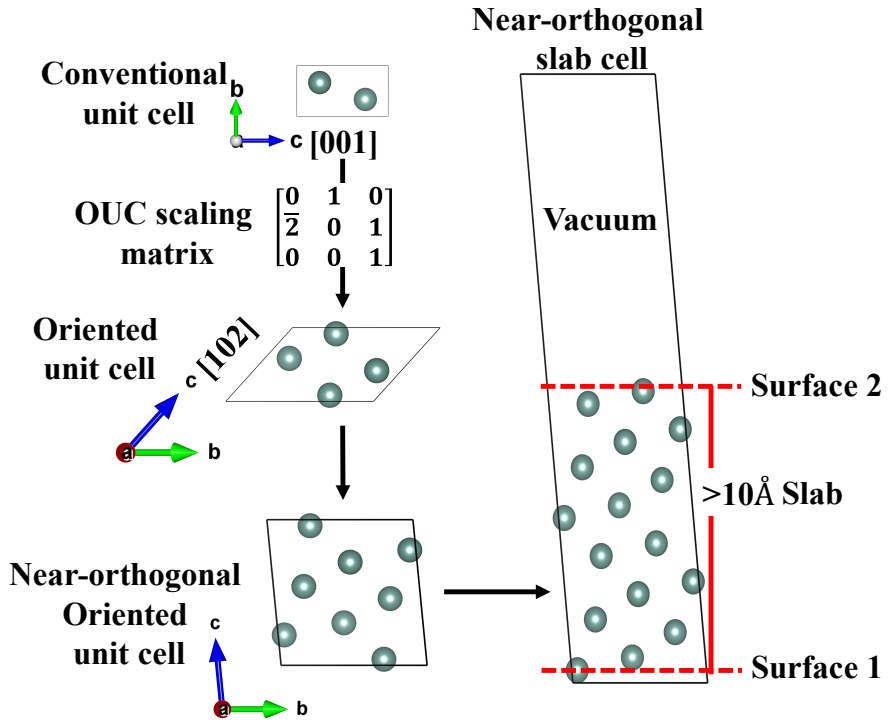


Figure 2.1: Construction of Y (10̄12) slab from the conventional unit cell. Note that the **c** lattice vector does not necessarily need to be perpendicular.

2.2.2 Computational methodology

For a given slab model of a facet with Miller index (hkl) , the surface energy γ_{hkl}^σ is given by the following expression:

$$\gamma_{hkl}^\sigma = \frac{E_{slab}^{hkl,\sigma} - E_{bulk}^{hkl} \times n_{slab}}{2 \times A_{slab}} \quad (2.1)$$

where, $E_{slab}^{hkl,\sigma}$ is the total energy of the slab model with termination σ , E_{bulk}^{hkl} is the energy per atom of the bulk OUC, n_{slab} is the total number of atoms in the slab structure, A_{slab} is the surface area of the slab structure, and the factor of 2 in the denominator accounts for the two surfaces in the slab model. To efficiently converge the surface energy, both the bulk and slab energies were calculated using the OUC, which allows consistent reciprocal integration grids to be used for the bulk and slab calculations.¹³² The OUC was fully relaxed in both cell volume and atomic

positions, while the slabs were relaxed in the atomic positions only.

All DFT^{4,136} energy calculations were performed using the Vienna Ab initio Simulation Package (VASP)^{137–139} within the projector augmented wave (PAW)¹⁴⁰ approach. The exchange-correlation effects were modeled using the Perdew-Berke-Ernzerhof (PBE) generalized gradient approximation (GGA)⁷⁸ functional, and all calculations were spin-polarized with a plane wave cutoff energy of 400 eV. The energies and atomic forces of all calculations were converged to within 6×10^{-6} eV and 0.01 eV Å⁻¹ respectively. The Methfessel-Paxton method¹⁴¹ was chosen as the smearing algorithm, the blocked Davidson iteration scheme¹⁴² was chosen as the electron minimization algorithm, and ions were updated with the conjugated gradient algorithm. Γ-centered k -point meshes of $\frac{50}{a} \times \frac{50}{b} \times \frac{50}{c}$ and $\frac{50}{a} \times \frac{50}{b} \times 1$ were used for OUC and slab calculations respectively with non-integer values rounded up to the nearest integer. Through a series of comprehensive convergence tests, it was determined that vacuum and slab layer sizes of 10 Å were sufficient to ensure that the surface energies were converged to within 0.02 J/m².

2.2.3 Wulff shape

The Wulff construction gives the crystal shape under equilibrium conditions^{112,143,144}. In this construction, the distance of a facet from the crystal center is proportional to the surface energy of that facet, and the inner convex hull of all facets form the Wulff shape. Here, we use the methodology developed by Miracle-Sole¹⁴⁴ to construct the Wulff shape. An example of the Wulff shape of Fe is given in Figure 2.2a, which contains all surfaces up to a MMI of 3. To illustrate the importance of sampling higher Miller index surfaces in obtaining an accurate Wulff shape, the Wulff shape of Fe up to MMI of 1 is shown in Figure 2.2b. It is evident that inclusion of higher-index surfaces is necessary to produce an accurate description of the equilibrium crystal shape.

The area fraction f_{hkl}^A of each symmetrically distinct facet under equilibrium conditions can be determined from the Wulff shape. We define the weighted surface energy $\bar{\gamma}$ using this

fraction as given by the following equation:

$$\bar{\gamma} = \frac{\sum_{\{hkl\}} \gamma_{hkl} A_{hkl}}{\sum_{\{hkl\}} A_{hkl}} = \sum_{\{hkl\}} \gamma_{hkl} f_{hkl}^A \quad (2.2)$$

where γ_{hkl} is the surface energy for a unique facet existing in the Wulff shape, A_{hkl} is the total area of all facets in the $\{hkl\}$ family in the Wulff shape, and f_{hkl}^A is the area fraction of the $\{hkl\}$ family in the Wulff shape. In this work, $\bar{\gamma}$ is used as a basis for comparison to experimentally determined surface energies, for which usually only one value is reported.

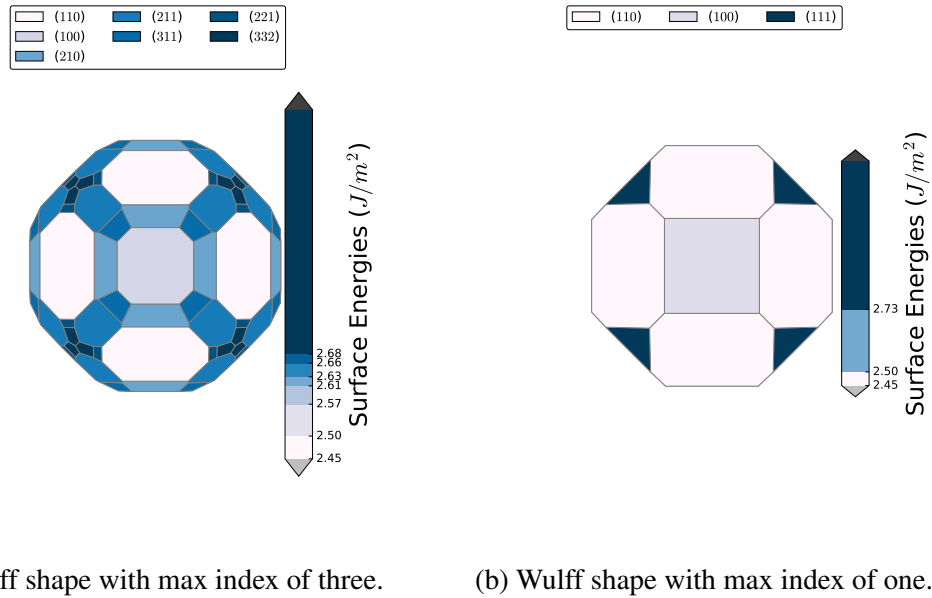


Figure 2.2: The Wulff shape of α -Fe generated with surface energies for facets up to a max Miller index of (a) 3 and (b) 1.

2.2.4 Anisotropy measures

Several measures of surface anisotropy have been proposed in the literature. For instance, the ratio $\gamma_{111}/\gamma_{110}$ is frequently used for fcc and bcc metals, but such surface-specific measures lack general applicability across crystals of different symmetry. The most commonly used general measure of anisotropy is the shape factor η , which is given by the following equation:

$$\eta = \frac{A}{V^{2/3}} \quad (2.3)$$

where A and V are the surface area and volume of the Wulff shape, respectively. The shape factor is a useful quantity in determining the critical nucleus size¹¹². Typically, the shape factor is compared against that of an ideal sphere ($\eta = (36\pi)^{\frac{1}{3}}$), and a larger η indicates greater anisotropy.

Though generally applicable, η does not account for variation in surface energies except indirectly through its impact on the Wulff shape. In the database, we have provided an alternative definition of surface energy anisotropy α_γ given by the following equation:

$$\alpha_\gamma = \frac{\sqrt{\sum_{\{hkl\}} (\gamma_{hkl} - \bar{\gamma})^2 f_{hkl}^A}}{\bar{\gamma}} \quad (2.4)$$

α_γ can effectively be viewed as a coefficient of variation of surface energies that is normalized for comparison across crystals with different weighted surface energies. A perfectly isotropic crystal would have $\alpha_\gamma = 0$. α_γ is comparable across different crystal systems and accounts for all surfaces based on their relative importance (in terms of contribution to the Wulff shape).

2.2.5 Data scope

The current release of the database contains surface energies and Wulff shapes of more than 100 polymorphs of about 70 elements. This database is far larger in scope than previous compilations of surface energies in several important ways:

1. Both metals and non-metals are included.
2. All polymorphs for each element available in the Materials Project database are included. This is in contrast with previous works where only the most stable ground state crystal structures were studied.
3. All surfaces up to a maximum Miller index (MMI) of two and three were calculated for

all non-cubic and cubic crystals respectively. The most common spacegroups among the crystals sampled are $Fm\bar{3}m$, $Im\bar{3}m$, $P6_3/mmc$, and $Fd\bar{3}m$, which contains 13, 13, 12, and 13 symmetrically distinct surfaces respectively up to the MMI used in this work. The only exceptions are the ground state crystals of Mn, S, P, Se and B for which only the terminations and surfaces containing the least number of broken bonds were calculated due to the low symmetry and/or large unit cell sizes.

4. Well-known reconstruction schemes for certain surfaces, such as the 2×1 missing row and 1×1 hexagonal reconstructions for fcc (110) and (111) surfaces respectively, are incorporated.

This database will be systematically improved through continuous updates. Future updates will include higher MMIs and other surface reconstruction schemes. Further expansion to non-elements, e.g., binaries, ternaries, etc. is also planned at a later stage.

2.2.6 Surface calculation workflow

Figure 2.3 shows an outline of the high-throughput workflow used in this work implemented using the FireWorks software package¹⁴⁵. The initial bulk crystals were obtained by querying for all elemental crystals from the Materials Project via the Materials API¹³⁴. All OUCs up to the MMI for each crystal were then automatically generated. For each OUC (corresponding to a specific Miller index (hkl)), a full relaxation was then carried out, and the slab models for distinct terminations were then generated from the fully relaxed OUC and calculated. To handle errors that may arise during calculations, the custodian software package¹³⁵ was used as a wrapper around VASP together with a set of robust error handling rules. The results from successful calculations were then automatically inserted into a MongoDB document-based database. The metadata of the DFT calculations and the surface properties extracted (see Tables 2.1 and 2.2) were subsequently inserted into the Materials Project database and the Dryad repository.

Consistency checks were devised as part of the workflow to detect possible errors and anomalous behavior in the surface calculations. Calculations containing such anomalies are tagged with a warning containing a list of their brief descriptions. The nature of these warnings are detailed in Table 2.3. Entries tagged with such warnings do not automatically indicate that the calculations are invalid. For example, although surface atom displacements on relaxation are typically expected to be less than 5%¹²⁵, the relaxation of the (110) surface of diamond Si exceeds this value due to its tendency to reconstruct to achieve stability.

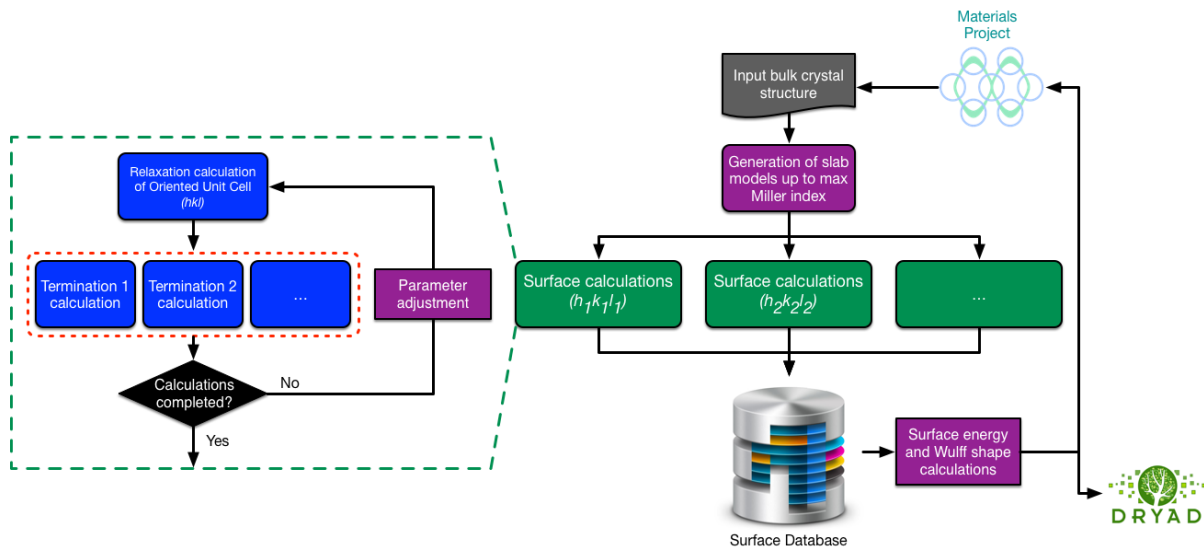


Figure 2.3: A schematic of the high throughput-infrastructure for the calculation the surface energies of elemental crystalline solids. Dashed blocks represent workflow steps performed in parallel.

Table 2.1: The meta data for a particular material.

Key	Datatype	Description
formula	string	Chemical formula
material_id	string	IDs for entries in Materials Project
polymorph	integer	Rank of polymorph stability (0 being ground state)
spacegroup	string	International spacegroup symbol and number
e_above_hull	float	Energy above the hull reported by Materials Project.

Table 2.2: Surface properties for a crystal. Properties denoted by * are defined for each distinct surface.

Property	Key	Datatype	Unit	Description
Weighted surface energy, $\bar{\gamma}$	weighted_surface_energy	float	J m^{-2}	Surface energy weighted by the Wulff shape's facet areas.
	weighted_surface_energy_EV_PER_ANG2	float	eV \AA^{-2}	
Anisotropy, α_{γ}	surface_anisotropy	float	-	Measure of the anisotropy of the surface energies weighted by relative importance.
Shape factor, η_{γ}	shape_factor	float	-	Measure of the anisotropy based on the geometry of the Wulff shape.
Surfaces	surfaces	list		List of sub-entries describing an individual surface.
Surface energy, $\gamma_{hk\ell}^*$	surface_energy	float	J m^{-2}	Surface energy corresponding to the most stable termination or reconstruction.
	surface_energy_EV_PER_ANG2	float	eV \AA^{-2}	
Miller index ($(hk\ell)miller_indexlistMiller index of the slab.$	miller_index	list		Miller index of the slab.
Task ID*	tasks	int		Task ID of the OUC and slab calculation the sub-entry properties were derived from.
Reconstruction*	is_reconstructed	boolean		Indicates whether the sub-entry properties corresponds to a reconstructed slab
Wulff surface area fraction*	area_fraction	float		Fraction of the Wulff shape's surface area occupied by surface's facets.
Slab structure*	structure	string		Slab used to model the surface as a Crystallographic Information File (cif).

Table 2.3: The possible warnings tagged for each surface calculation.

Warning name	Description
$ bulk_vol_rel > 1\%$	Relaxation of the OUC volume is greater than 1%.
$ slab_site_rel > 10\%$	Relaxation of the slab sites is greater than 10%.
$ slab_site_rel > 5\%$	Relaxation of the slab sites is greater than 5%.
negative_surface_energy	The surface energy is negative.

2.2.7 Code availability

Pymatgen is the primary materials analysis code used in this work, and the surface construction and input file generation algorithms are implemented in this package. Both pymatgen and the custodian error recovery library are open-source software under the MIT (Massachusetts Institute of Technology) License. The high-throughput workflow was implemented using the FireWorks library, which is freely accessible under a modified GPL (GNU General Public License)¹⁴⁵. All implemented algorithms, including the model generation and Wulff shape calculation, come with a comprehensive set of unit tests. The open-source software codes are also continuously tested via a continuous integration service. The VASP DFT code used is copyrighted by the University of Vienna, Austria and is accessible under a paid license.

2.3 Data records

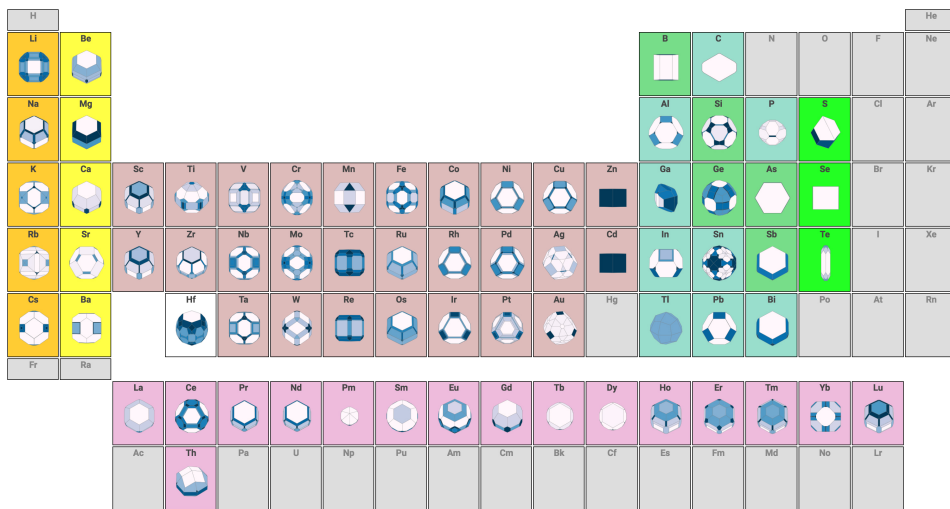
A user-friendly web application, Crystalium, has been developed to allow users to efficiently explore the Wulff shapes, surface energies and slab structures of the polymorphs investigated. This web application is at Crystalium (a screenshot is given in Figure 2.4). In addition, the surface energies and Wulff shapes are also available on the Materials Project website on the detailed data pages of specific crystals. A JSON data file is also available as a Dryad repository (Data Citation 1) which contains the complete set of metadata and surface properties for all materials studied so far.

Crystalium

An Exploration of the Surfaces and Wulff shapes of the Elements.

110 crystals of **72** elements available.

Click on any element to start.



A collaboration between the [Materials Virtual Lab](#) and the [Materials Project](#) powered by [pymatgen](#) and [FireWorks](#). If you use the data, please cite the following work:
R. Tran, Z. Xu, B. Radhakrishnan, D. Winston, W. Sun, K. A. Persson, S. P. Ong, *Surface Energies of Elemental Crystals*, Submitted.

Hf polymorph #0 (mp-103, P6₃/mmc, E_{hull}=0.000 eV/atom)

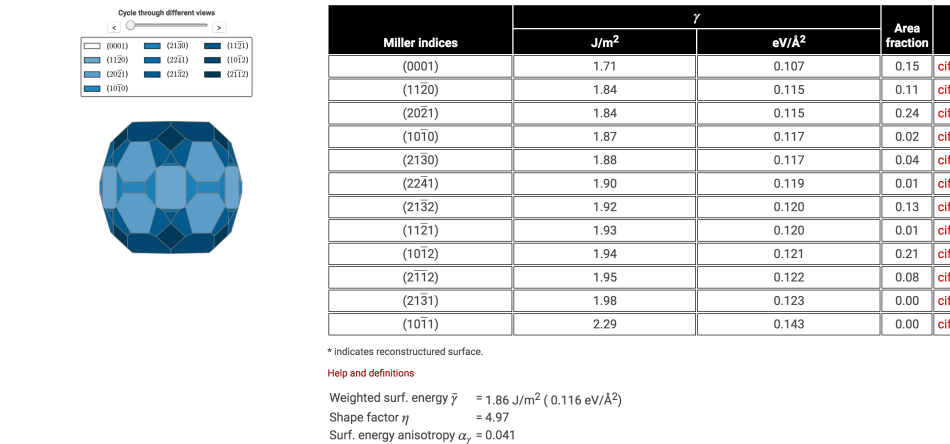


Figure 2.4: Screenshot of the Crystalium web application at Crystalium

2.3.1 File format

The data set for each material is stored as an individual JSON document (Data Citation

- 1). The material is described by its metadata which contains information such as the spacegroup, formula, a unique Materials Project identifier (mp-id), the energy per atom above the hull (a measure of the relative stability of the bulk crystal) and the polymorph number. A description of

the metadata can be found in Table 2.1.

2.3.2 Properties

The JSON document for each entry contains an organized list of sub-entries that describes the properties of each surface in detail. Each sub-entry contains information such as the Miller index, surface energy and the fraction of the Wulff shape's surface area occupied by this facet. For each Miller index, the lowest surface energy termination, including among different reconstructions investigated where applicable, is provided in each sub-entry. The slab structure used to model the surface is available as a Crystallographic Information File (cif). In addition, the weighted surface energy (Equation 2.2), shape factor (Equation 2.3), and surface anisotropy (Equation 2.4) are also given. Table 2.2 provides a full description of all properties available in each entry as well as their corresponding JSON key.

2.4 Technical validation

The data was validated through an extensive comparison with surface energies from experiments and other DFT studies in the literature. Due to limitations in the available literature, only the data on ground state phases were compared.

2.4.1 Comparison to experimental measurements

Experimental determination of surface energy typically involves measuring the surface tension of the material in its liquid phase¹¹³ and subsequent extrapolation to 0K under isotropic approximations. Anisotropy is neglected, and hence, values for individual unique facets are usually not available experimentally. Figure 2.5 compares the weighted surface energies of all crystals (Equation 2.2) to experimental values in the literature^{37,113,118–120}. It should be noted that we have adopted the latest experimental values available for comparison, i.e., values were

obtained from the 2016 review by Mills and Su¹¹⁹, followed by Keene¹²⁰, and finally Niessen et al.¹¹⁸ and Miller and Tyson¹¹³. A one-factor linear regression line $\bar{\gamma}^{DFT} = \bar{\gamma}^{EXP} + c$ was fitted for the data points. The choice of the one factor fit is motivated by the fact that standard broken bond models show that there is a direct relationship between surface energies and cohesive energy, and previous studies have found no evidence that DFT errors in the cohesive energy scale with the magnitude of the cohesive energy itself¹⁴⁶.

We find that the DFT weighted surface energies are in excellent agreement with experimental values, with an average underestimation of only 0.01 J m^{-2} and a standard error of the estimate (SEE) of 0.27 J m^{-2} . The Pearson correlation coefficient r is 0.966. Crystals with surfaces that are well-known to undergo significant reconstruction tend to have errors in weighted surface energies that are larger than the SEE.

The differences between the calculated and experimental surface energies can be attributed to three main factors. First, there are uncertainties in the experimental surface energies. The experimental values derived by Miller and Tyson¹¹³ are extrapolations from extreme temperatures beyond the melting point. The surface energy of Ge, Si¹⁴⁷, Te¹⁴⁸, and Se¹⁴⁹ were determined at 77K, 77K, 432K and 313K respectively while the energy of the (0001) surface of pyrolytic graphite was determined using the sessile drop technique under high temperatures¹⁵⁰. In addition, the possibility of contamination by surface active elements such as oxygen can lead to lower surface tension values. As a result, the higher value of surface tension measured in experiments is often argued to be the more accurate value^{119,120}.

Second, the limitations of the exchange-correlation functional used can also cause discrepancies.^{19,151} Though the average difference between the computed PBE surface energies in this work and experimental surface energies is very small (0.01 J m^{-2}), there is nevertheless non-negligible differences for specific elements. In addition, this study does not take into consideration the effects of Van der Waals forces in materials such as graphite where it is the dominant interaction between graphene layers in the (0001) direction. Of the 1000 different surfaces

studied, only the (0001) surfaces of the two graphite polymorphs have unphysical negative surface energies, which was also previously observed by Ooi et al.¹⁵².

Finally, surface reconstructions could also contribute to differences between the computed and experimental values. To understand the effect of reconstructions on surface energies, we compared the surface energy of the relaxed (110) fcc metal surfaces from the database to the reconstructed configuration described by Zhang et al.¹³³, as shown in Figure 2.6. We find that the missing row reconstruction is predicted to be favored (lower in energy) over the unreconstructed surface for Pt, Au and Ir only, in agreement with previous experimental and computational results^{133,153}. Even for the surfaces that undergo reconstruction, the differences between the reconstructed and unreconstructed surface energies are relatively small ($< 0.2 \text{ J m}^{-2}$) in metals.

Exceptional cases of reconstruction with large differences between the relaxed and reconstructed surface energies do exist. Semiconductors such as Si and Ge are known to have significantly smaller surface energies in their reconstructed state. The experimental, reconstructed and relaxed surface energies for Si are shown in Table 2.4. The reconstructed surface energies are much closer to those found experimentally than the unreconstructed surface energies. The reconstructed (111) surface in particular shows the largest energy difference (0.85 J m^{-2}). It should be noted that this HT work did not explore the well-known 7×7 reconstruction^{154,155} of the Si(111) surface due to the large supercells required.

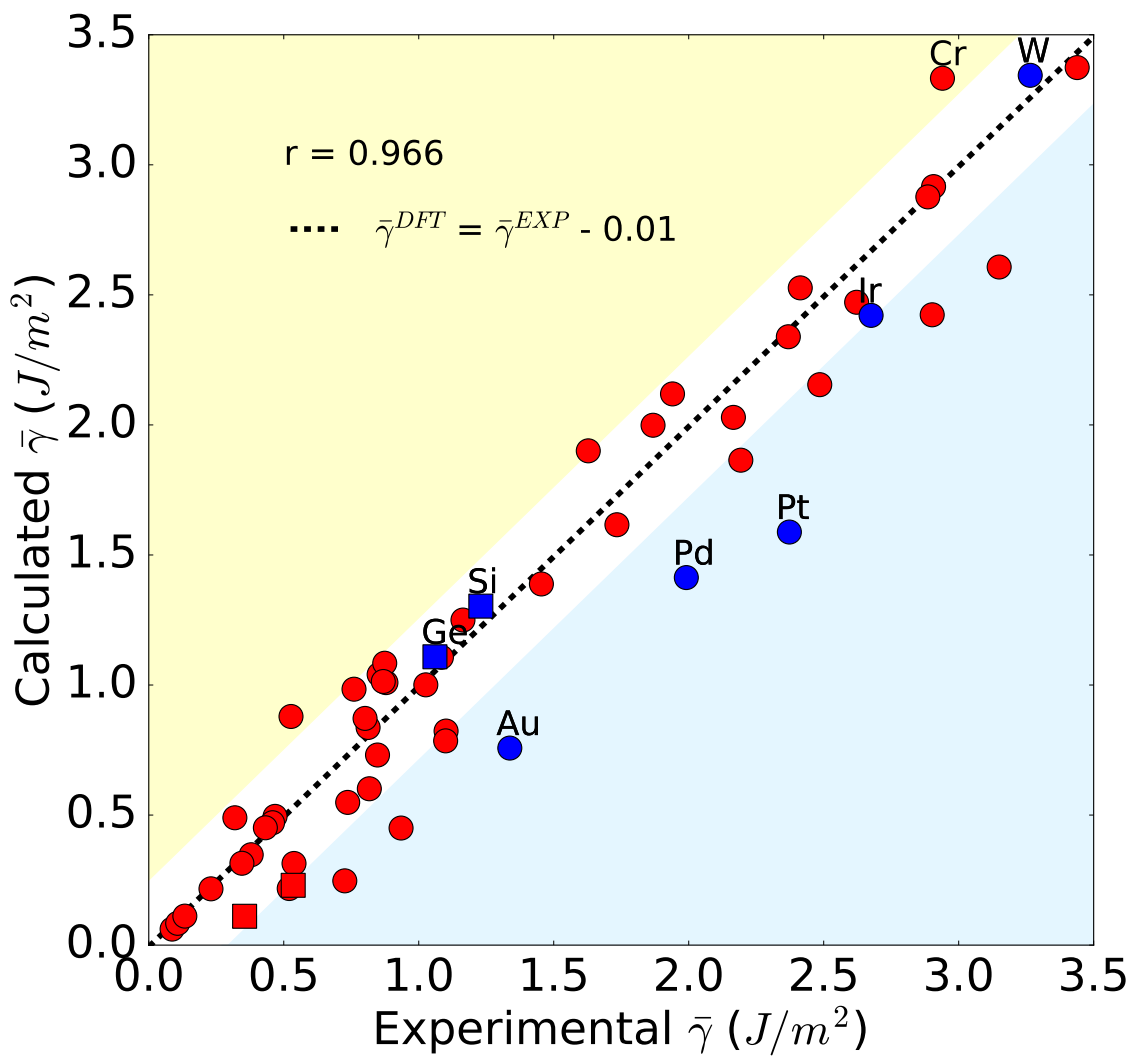
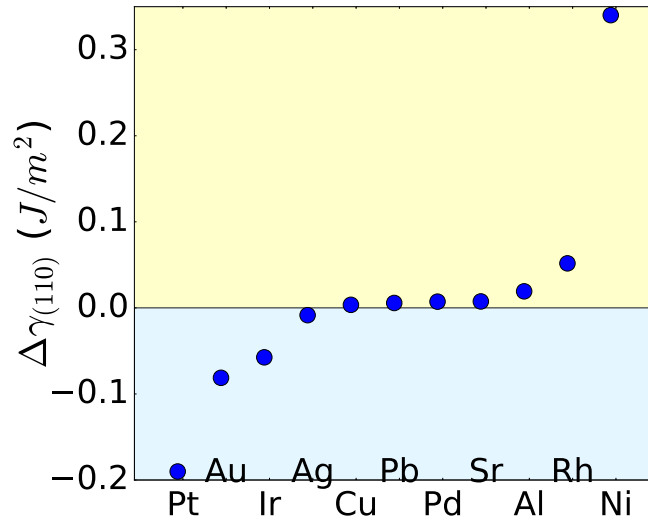
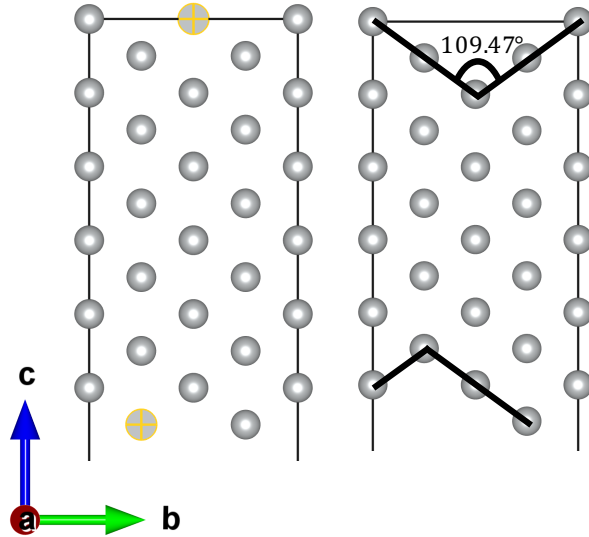


Figure 2.5: Plot of experimental versus calculated weighted surface energies for ground-state elemental crystal. Structures known to reconstruct have blue data points while square data points correspond to non-metals. Points that are within the standard error of the estimate ($\pm 0.27 J m^{-2}$) lie in the white region.



(a) $\Delta\gamma_{110}$ for fcc metals.



(b) Unreconstructed (110) fcc (c) 2x1 missing row (110)
fcc surface.

Figure 2.6: (a) Plot of the difference in surface energy ($\Delta\gamma_{110} = \gamma_{110}^{\text{reconstruct}} - \gamma_{110}^{\text{relaxed}}$) between the reconstructed and unreconstructed (110) surface of fcc metals. Negative values indicate a tendency to reconstruct. (b) Unreconstructed and (c) reconstructed models for a (110) fcc slab are shown.

Table 2.4: Comparison between the calculated unreconstructed and reconstructed surface energies, and experimental surface energies (in J m^{-2}) for various surfaces of Si. The calculated area fractions based on the Wulff shapes are also provided.

Miller index	Unreconstructed		Reconstructed		Experiment	
	γ	f_{hkl}^A	γ	f_{hkl}^A	γ	Reconstruction
(111)	1.57	0.09	1.30	0.45	1.23	(2×1)
(110)	1.76	0.00	1.51	0.00	1.43	(1×1)
(100)	2.13	0.00	1.28	0.36	1.36	$p(2\times 1)$

2.4.2 Comparison with previous computational studies

Table 2.5 presents a comparison of the calculated surface energies in this work with those computed in previous works. Unlike the comparison with experimental data, surface-specific comparisons are presented to demonstrate the accuracy of the data. An “averaged” experimental value is provided where available for reference. Despite the fact that the literature values come from studies with widely different parameters, including choice of exchange-correlation functional, pseudopotential choice / full electron calculations, etc., we find that the calculated values in this work differ from these literature values by only 2-13%^{117,156}. The (111) surface of fcc Pt from Da Silva et al.¹⁵⁶ has the largest (13%) difference. This is largely due to use of pseudopotentials in this study while Da Silva et al.¹⁵⁶ used an all-electron method.

In general, we find that the calculated surface energies in this work are slightly lower than that in the work of Vitos et al.¹⁹. This observation may be attributed to the atomic sphere approximation used in the FCD calculations by Vitos et al.¹⁹, which is known to hinder relaxation at the surface, thus leading to higher surface energy values¹⁵⁶. Also, our calculated surface energies are significantly lower than those computed using the local density approximation (LDA) functional in the literature, which may be attributed to the LDA functional’s propensity to overbind compared to the GGA functional used in this work.^{11,157–159}.

The planes with the highest atomic density per unit area of fcc, bcc and hcp materials are the {111}, {110} and {0001} planes respectively. According to the classic broken bond model,

the minimization of broken bonds in these surfaces leads to these surfaces having the lowest γ .^{160,161} Our results support this empirical model, with a few notable exceptions. For example, the (0001) surfaces for hcp Sc and Y and the (110) surface for Li are not the lowest energy surfaces among the facets investigated. These exceptions are also observed in Vitos et al.¹⁹ for various materials and in other previous first-principle studies for the Li (110) surface^{19,162,163}.

Table 2.5: A comparison of the high-throughput values to experimental and computed values for materials from the literature. A range of values is provided based on the lowest and highest values found in the literature.

Material	Surface	Surface energy γ (J m^{-2})		
		This work	Prev. DFT	Experimental
Ni	(110)	2.29	$2.37^{19} - 2.31^{117}$	2.44^{119*}
	(210)	2.4	2.43^{117}	
	(100)	2.21	$2.25^{117} - 2.43^{19}$	
	(221)	2.17	2.2^{117}	
	(111)	1.92	$2.01^{19} - 1.95^{117}$	
Mg	(10 $\bar{1}$ 0)	0.6	0.78^{19}	0.82^{120*}
	(0001)	0.54	$0.54^{156} - 0.79^{19}$	
Ba	(110)	0.31	$0.38^{19} - 0.37^{164}$	0.34^{120*}
	(100)	0.32	$0.37^{164} - 0.35^{19}$	
	(111)	0.39	$0.45^{164} - 0.4^{19}$	
Pt	(110)	1.68	$2.91^{126} - 2.27^{19}$	2.37^{120*}
	(100)	1.84	$2.73^{19} - 2.23^{164}$	
	(111)	1.48	$2.35^{156*} - 1.47^{156}$	
Sr	(110)	0.41	$0.47^{164} - 0.43^{19}$	0.38^{120*}
	(100)	0.35	$0.41^{19} - 0.39^{164}$	
	(111)	0.34	$0.5^{165} - 0.4^{164}$	
Mo	(110)	2.8	$2.92^{166} - 3.69^{165}$	2.07^{119*}

Table 2.5: A comparison of the high-throughput values to experimental and computed values for materials from the literature. A range of values is provided based on the lowest and highest values found in the literature (continued).

Material	Surface	Surface energy γ (J m^{-2})		
		This work	Prev. DFT	Experimental
	(100)	3.18	$3.34^{166} - 3.84^{19}$	
	(211)	3.4	$3.11^{166} - 3.6^{19}$	
	(111)	2.96	$3.24^{166} - 3.74^{19}$	
Bi	(0001)	0.17	-NA-	0.43^{120*}
Li	(110)	0.5	$0.56^{19*} - 0.3^{162}$	0.7^{120*}
	(100)	0.46	$0.52^{19} - 0.32^{162}$	
	(111)	0.54	$0.62^{19*} - 0.34^{162}$	
Pb	(100)	0.28	$0.64^{128*} - 0.32^{128}$	0.52^{120*}
	(110)	0.33	$0.72^{126} - 0.33^{19}$	
	(111)	0.25	$0.6^{126} - 0.26^{128*}$	
Re	(0001)	2.58	4.21^{19}	2.52^{119*}
	(10 $\bar{1}$ 0)	2.86	4.63^{19}	
Ge	(110)	0.97	1.17^{131}	0.68^{119*}
	(100)	0.87	1.71^{131}	
	(111)	1.11	1.3^{131}	
Lu	(0001)	1.13	1.6^{19}	1.08^{120*}
	(10 $\bar{1}$ 0)	1.05	1.42^{19}	
Fe	(110)	2.45	$3.0^{164} - 2.43^{19}$	2.41^{119*}
	(100)	2.5	$3.12^{164} - 2.22^{19}$	
	(211)	2.61	2.59^{19}	
	(111)	2.73	$3.28^{164} - 2.73^{19}$	
Ga	(001)	0.57	-NA-	0.02^{119*}

Table 2.5: A comparison of the high-throughput values to experimental and computed values for materials from the literature. A range of values is provided based on the lowest and highest values found in the literature (continued).

Material	Surface	Surface energy γ (J m^{-2})		
		This work	Prev. DFT	Experimental
Dy	(10 $\bar{1}$ 2)	1.0	-NA-	0.88 ^{120*}
Sc	(10 $\bar{1}$ 0)	1.2	1.53 ¹⁹	1.16 ^{120*}
	(0001)	1.27	1.83 ¹⁹	

¹²⁸ GGA (Hamann pseudopotentials) ¹⁹ GGA (FCD) ¹²⁶ LDA (FP-KKR) ¹¹⁷ GGA-PBE ¹³¹ LDA (Vanderbilt pseudopotentials) ¹⁶⁴ GGA-PBEsol ¹⁵⁶ GGA-PBE (FP-LAPW) ¹⁶⁵ GGA-PBEsol ¹⁶⁶ Local Density Formulation ¹⁶² PWGGA (LCGTO) * See reference herein

2.5 Conclusion

The database in this study is the most extensive collection of calculated surface energies for elemental crystalline solids to-date. When used with data mining and machine learning techniques, the database can be used to reveal trends in surface phenomena and guide the screening of potentially interesting materials for target surface properties. For instance, the relaxed surface structures and energies of many metals, particularly the noble metals, will be highly useful in the study of surface absorption of molecules, which is of great fundamental relevance in catalysis. Consideration of surfaces is especially crucial in nano-materials design, where surface effects tend to dominate the overall performance and properties. We also anticipate the data presented to be a useful starting point for the study of the interfaces between materials, either within the same material (e.g., grain boundaries) or between different materials. In the near future, we will provide the facility for Materials Project users to upload experimentally proposed reconstructions to further improve the completeness of the database. Furthermore, future

enhancements would include the surface properties of not just elements, but also multicomponent compounds (including alloys).

Chapter 2 is, in full, a reprint of the material “Data Descriptor: Surface energies of elemental crystals” as it appears in Scientific Data, Richard Tran, Zihan Xu, Balachandran Radhakrishnan, Donald Winston, Wenhao Sun, Kristin A. Persson and Shyue Ping Ong, 2016, 3 (160080), pp 1-13. The dissertation author was the primary investigator and author of this paper. All calculations and data analysis were performed by the author.

Chapter 3

Anisotropic work function of elemental crystals

3.1 Introduction

The work function (Φ) is an electronic surface property of crystalline solids and is crucial to the understanding and design of materials in many applications. It can be directly applied to the engineering of device specifications such as the Schottky barrier of semiconductor junctions or the thermionic currents of electron guns. Furthermore, it has been used to guide the engineering of interfacial interactions between metals and monolayer structures for nanoscale self-assembly¹⁶⁷. The work function is also an important parameter in characterization techniques where it can influence the tip tunneling current of scanning tunneling microscopes or correct the binding energy in photo-electron spectroscopy (PES).

The work function has also been explored as a parameter for materials design. For example, previous experimental and computational investigations of Ni-alloys by Lu et al.^{168, 169} have established a correlation between the work function and various mechanical properties such as toughness, hardness, ductility and bulk modulus. A more recent study using first-principle calculations found similar correlations for elemental crystalline solids¹⁷⁰. The work function has also been proposed as a possible parameter for the desorption rate of surface adsorbates¹⁷¹. Calculated work functions of hcp materials have also been used to screen for more effective metallic photocathodes.¹⁷²

Much effort has also been devoted to modelling Φ itself. Michaelson¹⁷³ and Miedema et al.¹⁷⁴, for example, were previously successful in modelling the polycrystalline work function as a linear function of electronegativity. The modeling of the anisotropic work function (Φ_{hkl}) as a function of surface morphology and chemical environment has also garnered much attention. Smoluchowski smoothing is one such model which describes the contributions to the work function of metals as a result of isotropic electron spreading and anisotropic electron smoothing¹⁴. The spreading of negative charges increases the work function while the anisotropic smoothing of negative charges at the surface decreases the work function. Smoothing increases with surface

roughness (defined here as the reciprocal of the surface packing fraction¹⁷⁵) which decreases the work function. This model is supported by previous observations that the anisotropic surface energy (γ_{hkl}) is inversely proportional to Φ_{hkl} via the broken bond surface density^{176,177}. Similarly, the Brodie model attempts to explain Φ_{hkl} for transition metals as a function of (bulk) electron effective mass, surface atomic radius and inter-planar distance^{178,179}. A more recent model using a dielectric formalism has been proposed by Fazylov¹⁸⁰ that describes Φ_{hkl} using surface roughness and surface plasmon dispersion.

An extensive database for Φ_{hkl} would be invaluable for validating and further expanding upon these models. However, experimentally measured work functions are usually for polycrystalline specimens ($\Phi_{\text{poly}}^{\text{expt}}$) instead of single crystals. An example of this is the extensive collection of experimentally measured $\Phi_{\text{poly}}^{\text{expt}}$ for 66 polycrystalline elemental solids compiled by Michaelson¹⁸¹. Though measurements for anisotropic Φ_{hkl} are not uncommon, values often vary due to the many techniques used or non-standardized methods of implementing the same technique (e.g., PES)^{182,183}. The sparsity of Φ_{hkl} and the lack of a comprehensive compilation with a single standardized technique makes it difficult to develop and gain insights into work function anisotropy using experimental measurements.

Here, density functional theory (DFT) has the advantage of calculating Φ_{hkl} for a model of any specific solid surface under a controllable set of parameters, making it possible to create a standardized collection of values. Many authors have attempted such compilations for Φ_{hkl} , which are often times accompanied by the corresponding surface energy γ_{hkl} ^{20,125,176,177,184,185}. For instance, Ji et al.¹⁷⁷ and Wang and Wang¹⁷⁶ have calculated Φ_{hkl} for numerous bcc, fcc and hcp materials. Waele et al.²⁰ created a database of Φ_{hkl} for all elemental crystalline solids, but only for facets up to a max Miller index (MMI) of 1, using the Perdew-Burke-Ernzerhof generalized gradient approximation (PBE-GGA) and localized density approximation (LDA) functionals. More recently, Patra et al.⁸ evaluated the performance of various functionals by calculating Φ_{hkl} for an MMI of one for Al, Cu, Ru, Rh, Pd, Ag, Pt and Au. Despite the wide variety of

computational data, the majority of these studies are limited to small Miller indices (typically MMI of 1). In addition, computational data for lanthanide systems and different polymorphs is sparse^{185–187}. Furthermore, most compilations do not consider possible reconstructions, which can drastically affect the calculated work function²⁰.

Here, we report the development of a comprehensive, validated database of work functions for elemental crystalline solids using DFT calculations that addresses all the above limitations in the following ways:

1. Coverage of 142 polymorphs of 72 elements, including rare earth metals.
2. Facets up to an MMI of three and two for cubic and non-cubic crystals, respectively, are considered.
3. Common reconstruction schemes, such as the missing-row (110) fcc and the diamond-type reconstructions,¹³¹ have been taken into account.

We validate our computed work functions with past experimental and computational data for both Φ_{hkl} and $\Phi_{\text{poly}}^{\text{expt}}$. Finally, we will discuss trends in the work function of the elements, and develop a predictive empirical model for $\Phi_{\text{poly}}^{\text{expt}}$.

3.2 Methods

3.2.1 Definitions

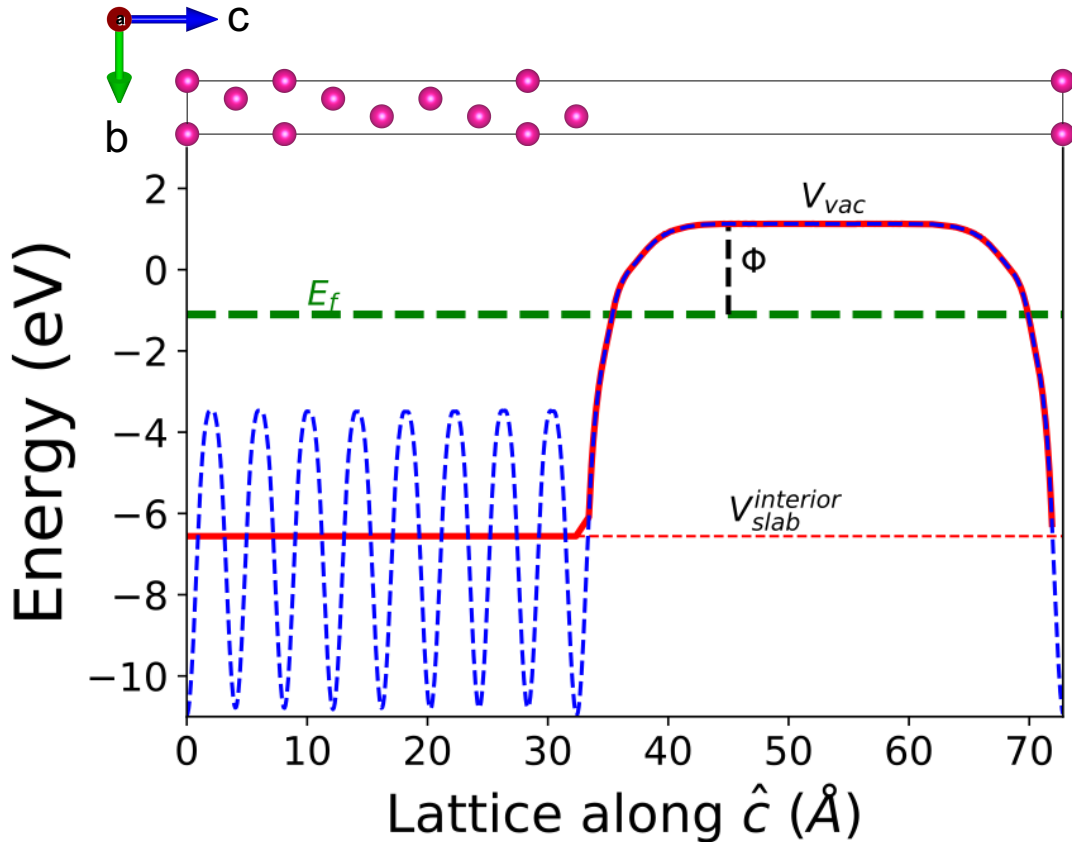


Figure 3.1: Plot of the electrostatic potential along the hcp Rb (0001) slab model. The Fermi energy (E_f), electrostatic potential of the vacuum region (V_{vac}), average electrostatic potential of the slab region ($V_{\text{slab}}^{\text{interior}}$) and work function (Φ) are indicated.

The work function is defined as the energy barrier required to move an electron from the surface of a solid material into free space, as given by the following expression:

$$\Phi = V_{\text{vac}} - E_F \quad (3.1)$$

where V_{vac} is the electrostatic potential of the vacuum region near the surface and E_f is the Fermi energy of the slab. The energy barrier can be visualized in Figure 3.1 where V_{vac} is obtained when the electron is far enough away from the surface, that the potential remains constant over a small distance in the vacuum. This method has been widely used in previous studies for calculating the work function^{20,176,177,185} and has been shown to converge quickly with respect to slab thickness¹⁸⁴.

3.2.2 Modeling non-uniform work functions

For comparison to work functions obtained from polycrystalline specimens, one approach is to calculate the work function of a “patchy” surface by weighting each Φ_{hkl} by the area fraction of its corresponding facet^{171,188} as follows:

$$\bar{\Phi} = \frac{\sum_{\{hkl\}} \Phi_{\text{hkl}} A_{\text{hkl}}}{\sum_{\{hkl\}} A_{\text{hkl}}} = \sum_{\{hkl\}} \Phi_{\text{hkl}} f_{\text{hkl}}^A \quad (3.2)$$

where A_{hkl} and f_{hkl}^A are the total area and the area fraction of all facets in the $\{hkl\}$ family, respectively. A polycrystal is an extreme case of a patchy surface, and as such the same technique can be applied to $\Phi_{\text{poly}}^{\text{expt}}$. The PES signal of the patch with a lower work function will tend to eclipse those with higher work functions leading to an underestimated measurement of $\Phi_{\text{poly}}^{\text{expt}}$. Thus, experimental values of the lowest anisotropic work function ($\Phi_{\text{hkl}}^{\text{lowest}}$) are only ~ 90 meV lower than $\Phi_{\text{poly}}^{\text{expt}}$. Because of this, it has also been suggested that $\Phi_{\text{hkl}}^{\text{lowest}}$ is a good estimate of $\Phi_{\text{poly}}^{\text{expt}}$ ^{20,171,182}. In this study, we use the facets present in the Wulff shape previously calculated by the current authors³⁶ as an estimate of the orientation and area fraction present in a polycrystalline sample to obtain $\bar{\Phi}$ and $\Phi_{\text{hkl}}^{\text{lowest}}$ as estimates for $\Phi_{\text{poly}}^{\text{expt}}$.

As mentioned earlier, Smoluchowski smoothing describes the anisotropic work function of metals as being inversely correlated with the broken bonds per surface area. As such, we model our values for Φ_{hkl} normalized by $\bar{\Phi}$ using the ratio of broken bonds-to-bulk coordination number

$(\frac{N_{\text{BB}}}{CN_{\text{bulk}}})$ in a slab normalized by the surface area-to-atomic area ratio ($\frac{A_{\text{surf}}}{\pi r_A^2}$) in order to compare across all systems:

$$\overline{\text{BB}} = \frac{N_{\text{BB}}}{CN_{\text{bulk}}} \times \frac{A_{\text{surf}}}{\pi r_A^2} \quad (3.3)$$

It is known that for bcc and hcp materials, the first nearest neighbors (1NN) and second nearest neighbors (2NN) are in close proximity to each other, leading to contributions from the latter to the anisotropy of surface energy¹⁸⁹. Hence, when defining $\overline{\text{BB}}$ for a material, we will limit the maximum coordination number to the 1NN for fcc materials and explore both 1NN and 2NN for hcp and bcc materials. For hcp structures, we omitted Φ_{0001} when investigating the effect of the 1NN as the number of broken bonds will always be 0 which is unphysical. The inverse correlation between $\overline{\text{BB}}$ and Φ_{hkl} for each element can be quantified by the Pearson correlation coefficient (r). We will define systems with a negative linear trend between Φ_{hkl} and the normalized broken bonds with $r < -0.75$ as having a strong correlation, $-0.75 < r < -0.5$ as having a moderate correlation and $r > -0.5$ as having a weak correlation. Only ground state metallic fcc, bcc and hcp systems were explored under this context.

3.2.3 Computational details and workflow

For all slab calculations, we performed a full relaxation of the site positions under a fixed volume before obtaining the electrostatic potential of the slabs (see ref 36 for a complete description of computational details). The electrostatic potentials only contains the electrostatic contributions (no contributions from the exchange correlation). All calculations were performed using the Vienna Ab initio Simulation Package (VASP) with the exchange-correlation effects modeled using the PBE-GGA functional. Calculations using the revised PBE (rPBE) functional were performed on a smaller set of data using the same parameters for comparison.

We used the high-throughput workflow proposed by Sun and Ceder¹³² and implemented by Tran et al.³⁶ and Montoya and Persson¹⁹⁰ to obtain all required data. The workflow was

implemented using the open-source software packages Python Materials Genomics,¹³⁵ Fire-Works¹⁹¹ and Atomate¹⁹². The work function is extracted from the calculations and inserted into the same database. To handle errors that may arise during calculations, the custodian software package was used as a wrapper around VASP together with a set of robust error handling rules. The database will be continuously improved and will continue growing as more structural data becomes available on the Materials Project¹⁹³.

3.2.4 Data availability

The data can be accessed from the elemental-surface-data-focused Crystalium¹⁹⁴ website, as well as from the Materials Project website¹⁹⁵ on its detail pages for specific crystals.

3.3 Results

Due to the vast number of data points for Φ_{hkl} when comparing to literature values, we have adopted a consistent marker shape and color scheme for ease of reference (see Figure 3.2) for all subsequent plots. The shape and color represents the row and group of the element in the periodic table, respectively.

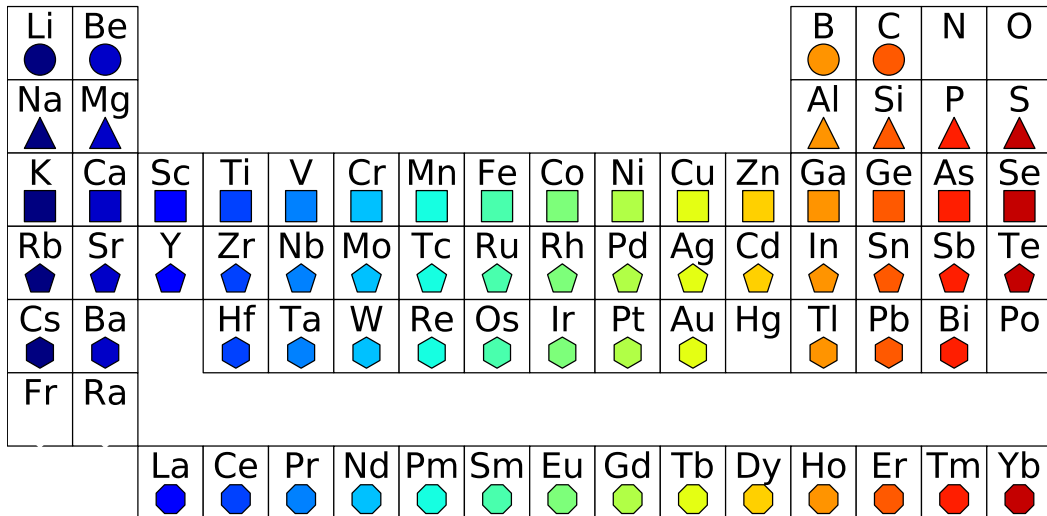


Figure 3.2: Marker shape and color scheme for plots.

All values for Φ reported in this study, including those found in the literature, are listed in the Supplementary Information in Tables A.1 and A.2. Literature values for Φ were taken from the most recent experimental and computational studies available during the writing of this manuscript. Experimental values are explicitly annotated with a “expt” superscript, e.g., $\Phi_{\text{poly}}^{\text{expt}}$, and unless otherwise indicated, all other values are computed values.

3.3.1 Experimental and computational validation

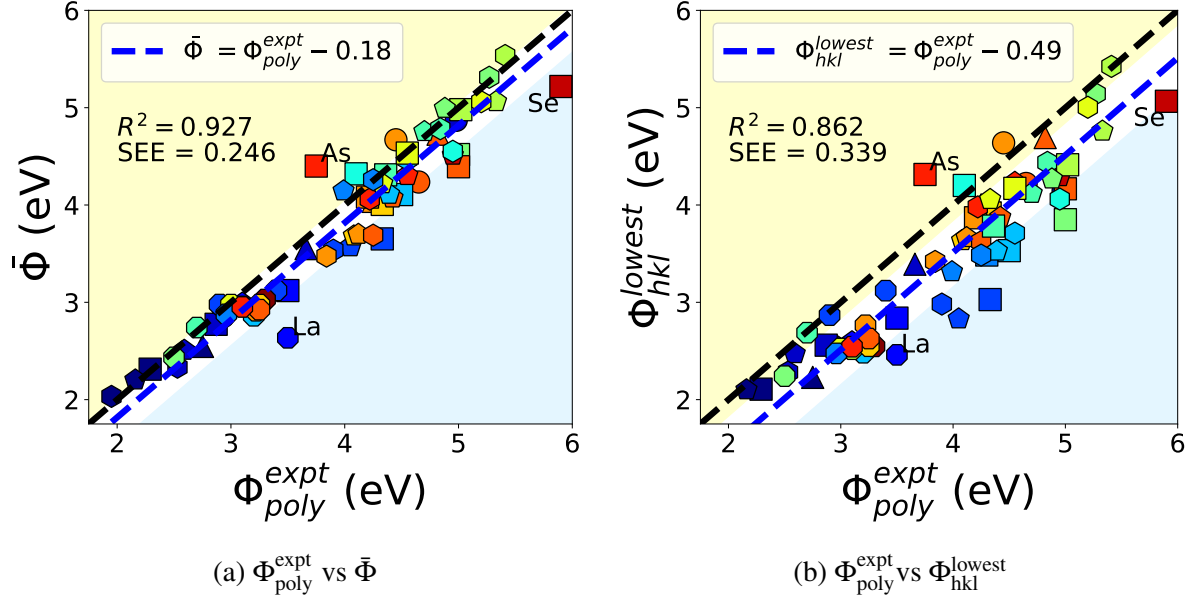


Figure 3.3: Plot of (a) experimentally measured $\Phi_{\text{poly}}^{\text{expt}}$ vs the computed $\bar{\Phi}$ and (b) $\Phi_{\text{poly}}^{\text{expt}}$ vs the computed $\Phi_{\text{hkl}}^{\text{lowest}}$. The single-factor linear regression line $y = x + c$ for both plots are indicated as dashed blue lines along with the R^2 value and standard error of the estimate (SEE). Values within the light blue (light yellow region) are below (above) the SEE. (see refs 171,196,197).

Figures 3.3 shows a single-parameter $y = x + c$ least squares fit for $\bar{\Phi}$ vs $\Phi_{\text{poly}}^{\text{expt}}$ and $\Phi_{\text{hkl}}^{\text{lowest}}$ vs $\Phi_{\text{poly}}^{\text{expt}}$ for the ground state polymorph of each element. We find that the PBE $\bar{\Phi}$ are on average 0.31 eV closer to $\Phi_{\text{poly}}^{\text{expt}}$ than the PBE $\Phi_{\text{hkl}}^{\text{lowest}}$. The linear fit for $\bar{\Phi}$ vs $\Phi_{\text{poly}}^{\text{expt}}$ also yielded a higher R^2 of 0.927 and a lower standard error of the estimate (SEE) of 0.246 eV compared to that of $\Phi_{\text{hkl}}^{\text{lowest}}$ vs $\Phi_{\text{poly}}^{\text{expt}}$ ($R^2 = 0.862$ eV and SEE = 0.339 eV). We find that $\bar{\Phi}$ systematically underestimates $\Phi_{\text{poly}}^{\text{expt}}$ by 0.18 eV on average. Notable outliers include $\Phi_{\text{poly}}^{\text{expt},\text{As}}$ which is underestimated, and $\Phi_{\text{poly}}^{\text{expt},\text{La}}$ and $\Phi_{\text{poly}}^{\text{expt},\text{Se}}$ which are overestimated by more than the SEE. The largest error is for La, with an error of 0.86 eV. Although the Michaelson¹⁸¹ values of $\Phi_{\text{poly}}^{\text{expt,Re}}$ is 0.44 eV closer to our calculated value, the more recent value reported by Kawano¹⁷¹ is reported here.

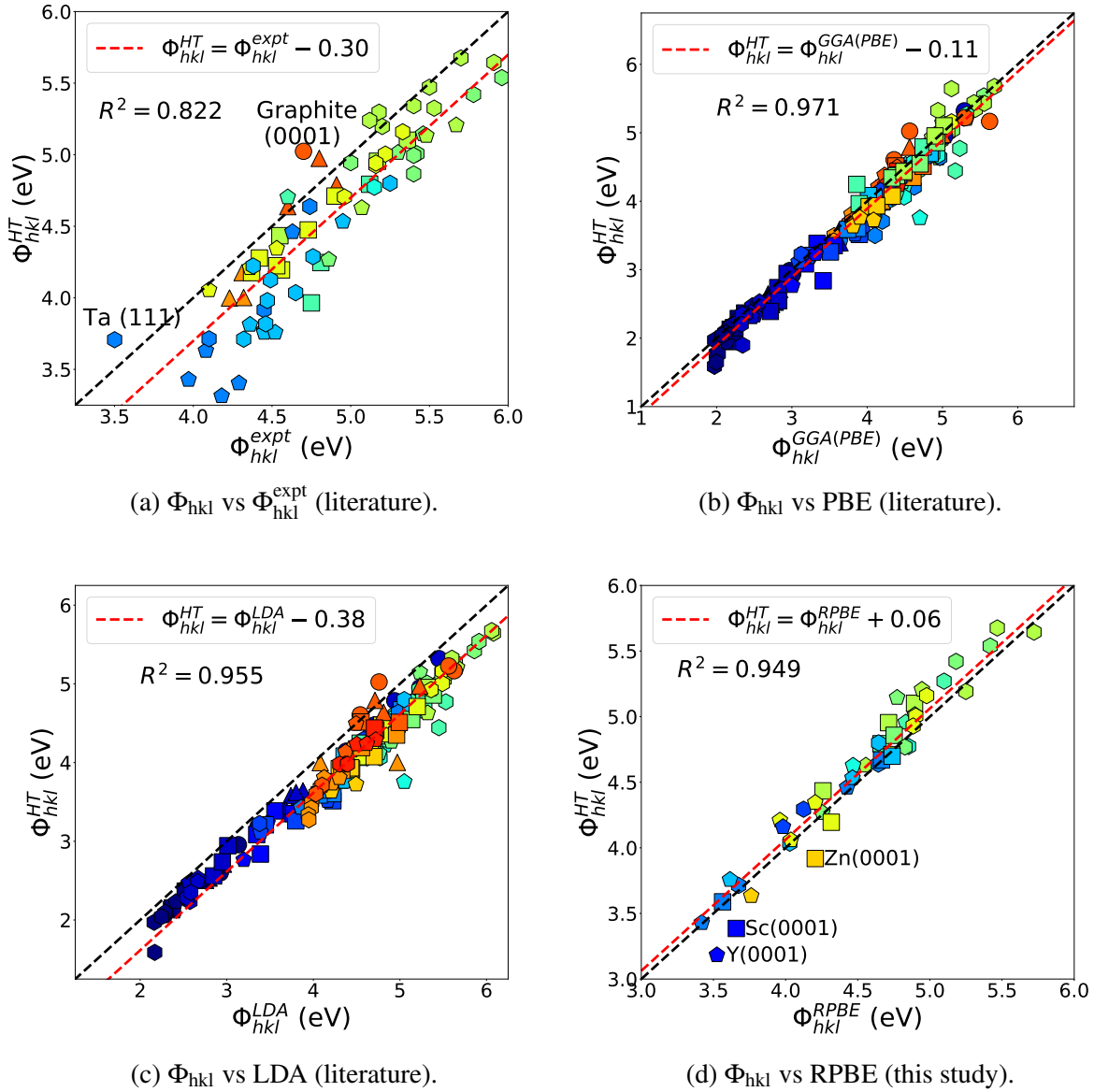


Figure 3.4: Plot of computed facet-dependent Φ_{hkl}^{HT} in this work vs (a) experimental values^{171,183,196} (b) literature PBE values^{8,20,176,177}, (c) literature LDA values^{8,20,177} and (d) RPBE values (this work).

Figure 3.4 compares the facet-dependent work functions obtained in this study to values obtained experimentally from single crystals and from other functionals, including LDA, PBE and RPBE. Again, we find that the experimental values in Figure 3.4a are on average 0.30 eV higher than the computed ones with an increasing deviation for work functions of lower values.

The (100), (310) and (311) facets of the early transition and refractory metals (Mo, W and Nb) have some of the lowest work functions, which also have the greatest deviation between the PBE and experimental values. For the same elements, facets with higher work functions have a smaller deviation ((110) and (210)). An exception to this is Φ_{111}^{Ta} where computed and experimental values are in relative agreement despite having a value lower than other work functions. Meanwhile, the computed value of $\Phi_{0001}^{\text{Graphite}}$ greatly overestimates the experimental value (see ref 171). In general, the qualitative trends in work functions for different facets of each element are in agreement with the experimental trends, with the notable exception of Al. Eastmen and Mee¹⁹⁸ previously reported the order of $\Phi_{\text{hkl}}^{\text{Al}}$ to be $\Phi_{111}^{\text{Al}} > \Phi_{100}^{\text{Al}} > \Phi_{110}^{\text{Al}}$ which is typical of fcc metals while a later work by Grepstad et al.¹⁹⁹ reported that $\Phi_{100}^{\text{Al}} > \Phi_{110}^{\text{Al}} \sim \Phi_{111}^{\text{Al}}$, which is consistent with our results (see Table A.2 for values).

Our values for Φ_{hkl} are in excellent agreement with those calculated using PBE, LDA and RPBE (as shown in Figure 3.4b, 3.4c and 3.4d respectively) with values of R^2 greater than 0.94 in all three cases. Unsurprisingly, there is smaller deviation when comparing our data to other GGA values (0.11 eV for PBE and 0.06 eV for rPBE) than to LDA values which are on average 0.38 eV higher. The major discrepancy between PBE and rPBE are for the (0001) surfaces of Y, Sc and Zn, with the PBE values being higher by 0.34 eV, 0.27 eV and 0.29 eV, respectively. Our values for $\Phi_{21\bar{3}1}^{\text{Sc}}$ and Φ_{210}^{Ba} are significantly lower when compared to PBE values obtained from the literature. Overall, the LDA-computed work functions are on average closer to the experimental values with a deviation of 0.11 eV (see Figure A.1).

3.3.2 Work function of missing-row reconstructions

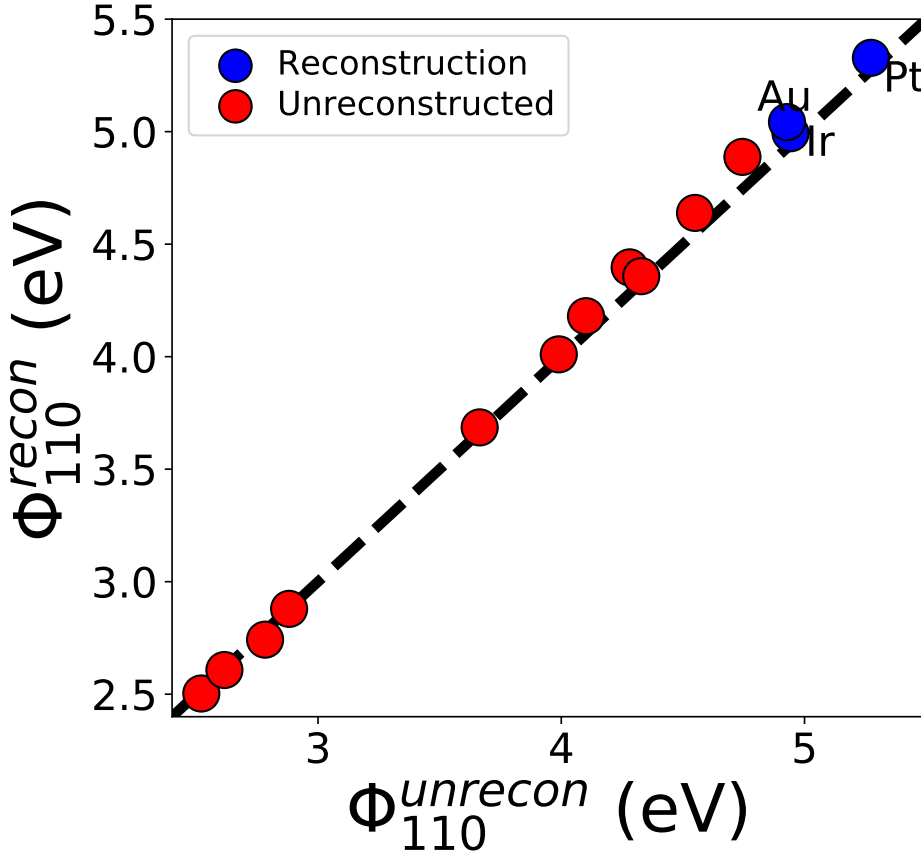


Figure 3.5: Plot of the (110) work function for an unreconstructed ($\Phi_{110}^{\text{unrecon}}$) and 1×2 missing-row reconstructed ($\Phi_{110}^{\text{recon}}$) surface for fcc materials. Data points corresponding to materials where reconstruction is thermodynamically favorable ($-2 \text{ meV\AA}^{-2} < \gamma_{110}^{\text{recon}} - \gamma_{110}^{\text{unrecon}}$) are labelled in blue.

Figure 3.5 compares the work function for the (110) missing-row reconstructed surface of face-centered cubic metals ($\Phi_{110}^{\text{recon}}$) to the work function of the corresponding unreconstructed surface ($\Phi_{110}^{\text{unrecon}}$). As found in our previous work, only Pt, Au and Ir have significantly lower surface energies for the (110) missing-row reconstruction compared to the unreconstructed surface, which is in agreement with experimental observations. In general, we find that reconstruction leads to a relatively small increase in the work functions, though the three fcc metals exhibiting a

thermodynamic driving force to reconstruct also have the largest work functions.

3.4 Discussion

3.4.1 Periodic trends in the work function

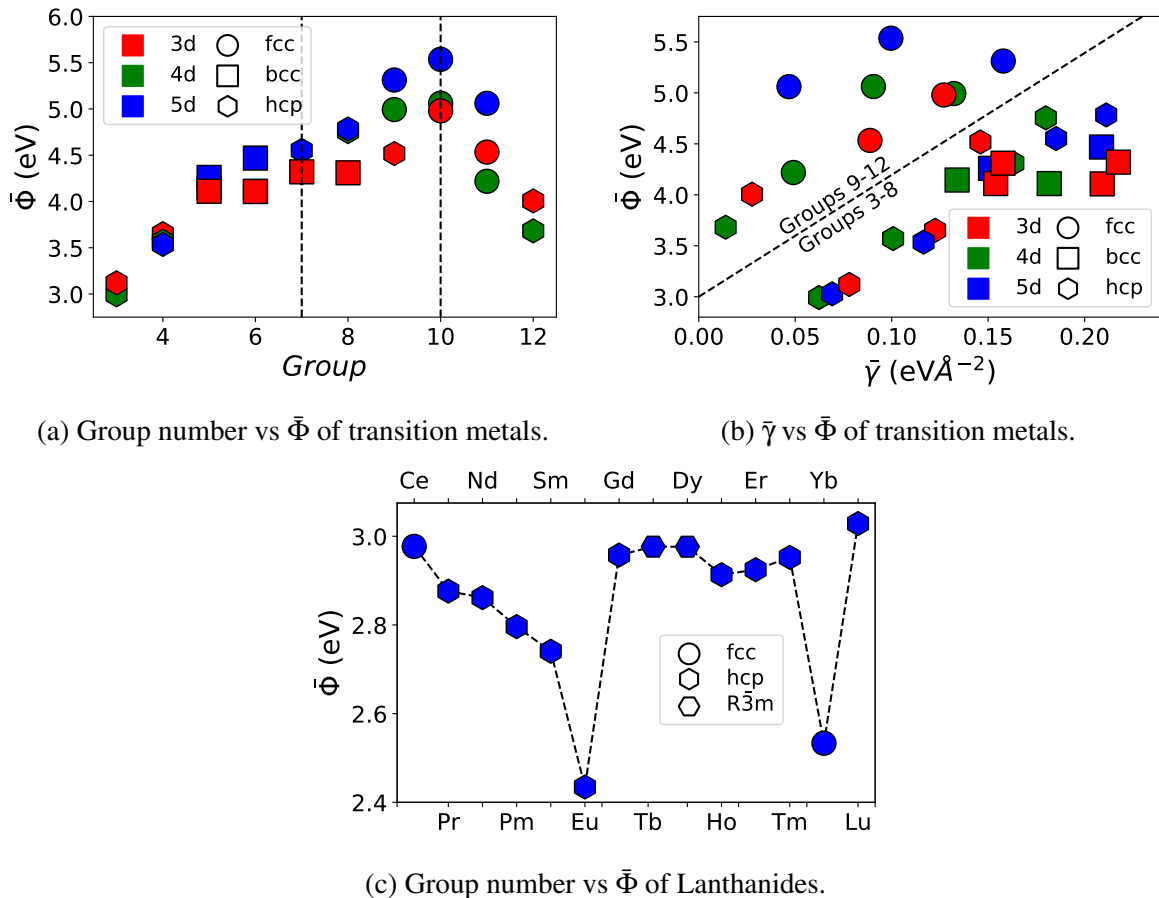


Figure 3.6: Plot of $\bar{\Phi}$ versus (a) group number and (b) $\bar{\gamma}$ for transition metals, and (c) $\bar{\Phi}$ versus group number for lanthanides. The left and right dashed lines in (a) corresponds to the parabolic peak when plotting group number against $\bar{\gamma}$ and $\bar{\Phi}$ respectively.

Figure 3.6a plots $\bar{\Phi}$ against the periodic group number for transition metals which demonstrates a parabolic behavior with the position of the parabolic maxima located at group 10 (Pt group). When plotting $\bar{\Phi}$ against the weighted surface energy ($\bar{\gamma}$) in Figure 3.6b, we observe

a split between elements above and below group 8. A similar parabolic trend when plotting $\bar{\gamma}$ against group number results in a maxima observed at group 7 rather than 10. The position of these parabolic peaks are related to the increasing cohesive energy resulting from the increasing number of half-filled d -orbitals as well as the width of the electronic s , p and d bands. For a more in-depth discussion, the interested reader is referred to the references herein^{125,157}. We further note that cohesive energy and thus surface energy are strongly correlated with mechanical properties which suggests a cohesive energy origin to previously observed trends between $\bar{\Phi}$ and mechanical properties of transition metals^{168,170,200}.

To our knowledge, this work represents the first time DFT has been used to calculate the work functions of the lanthanides. Figure 3.6c plots $\bar{\Phi}$ against the group number. A gradual decrease is observed for the half-filled lanthanides from Ce to Sm with a sharp decrease for Eu. The latter half of the lanthanides has a relatively constant value from Gd to Tm with a sharp decrease for Yb. Afterwards, a sharp increase is observed for Lu. These trends are consistent with trends of the cohesive energies of the lanthanides (see Figure A.2), which in turn may be attributed to the gradual filling of the $4f$ orbitals. The two lowest $\bar{\Phi}$ are observed when the $4f$ orbitals are half filled (Eu) and completely filled (Yb), and these two elements also have the lowest cohesive energy and melting point among the lanthanides. With the exception of Ce, the computed $\bar{\Phi}$ underestimates the experimental values of $\Phi_{\text{poly}}^{\text{expt}}$ for the lanthanides with a standard deviation of 0.136 eV from Ce to Yb (see Table A.1).

3.4.2 Discrepancies in the comparisons

In general, our computed work functions are consistent with previous computational studies^{8,20,176}. It is well known that the GGA(PBE) functional underestimates the intermediate range van der Waals (vdW) forces and Fermi energy while having no long-range vdW forces, which generally leads to an underestimated work function. Although LDA generally yields values closer to experiment than GGA(PBE), this agreement is due to the various errors inherent in LDA

that work in tandem to provide an error cancellation.⁸

LDA/GGA are also known to have errors associated with overbinding/underbinding leading to smaller/larger cell volumes, lattice parameters and atomic distances, which can in turn influence surface properties. Larger atomic distances will decrease 2NN contributions to γ_{hkl} and Φ_{hkl} . This effect is especially prominent in the refractory metals Mo, Ta, Nb and W where the work function is shown to be dependent only on 1NN, but not 2NN (see Table A.3). Without 2NN contributions, the work function will be severely underestimated in these metals when compared to experimental values, thus explaining the increasing deviation for refractory metals. Furthermore, the surface energy scales well with 2NN for Nb and Ta (which have the greatest deviation in Φ_{hkl} of the four refractory metals), indicating that underbinding in GGA(PBE) is more consequential for work function than it is for surface energy.

Experimental error is also a potential source of discrepancies in our comparisons. $\bar{\Phi}^{\text{As}}$ is significantly higher while $\bar{\Phi}^{\text{La}}$ and $\bar{\Phi}^{\text{Se}}$ are significantly lower than that of their corresponding values for $\Phi_{\text{poly}}^{\text{expt}}$. Experimental values for these particular elements were taken from Michaelson¹⁸¹ where surface contamination could lead to inaccuracies of up to 0.5 eV¹⁷³ in the reported measurements. $\Phi_{\text{poly}}^{\text{As}}$ is also known to range from 3.75 to 5.4 eV which our value for $\bar{\Phi}^{\text{As}}$ lies between. Furthermore, the value of $\Phi_{\text{poly}}^{\text{Se}}$ was also determined using a photoelectric method which is known to yield erroneous values of work function for semiconductors. In addition, we opted to use the latest values available from the literature, which for $\Phi_{\text{poly}}^{\text{La}}$ came from Michaelson¹⁸¹, despite measurements from Rozkhov and Ye.¹⁹⁷ being 0.54 eV closer to our DFT and previous linear muffin-tin orbital method values¹⁸⁶.

Although the calculated $\Phi_{\text{hkl}}^{\text{lowest}}$ has previously been suggested as a good approximation of experimentally measured $\Phi_{\text{poly}}^{\text{expt}}$, we have shown that the Wulff-area-weighted $\bar{\Phi}$ provides a much closer estimate. This suggests that the eclipsing effect of lower work functions in PES signals of patchy surfaces may not be as prominent as once thought. Despite this, the values of $\Phi_{\text{poly}}^{\text{expt}}$ are higher than $\bar{\Phi}$ by an average value of 0.18 eV. Kawano¹⁷¹ has argued that the weighted work

function is more likely to follow a Boltzmann distribution with a higher value than that provided by Equation 3.2. In this context, temperature becomes an important factor in determining the work function^{200,201}. However, it is unaccounted for in our calculations which are assumed to take place at 0K.

3.4.3 Effect of reconstruction on work function

In general, the work function of the reconstructed facets are slightly larger than that of the unreconstructed facets. This can be due to the exposure of the {111} facets during reconstruction which generally have larger values of Φ_{hkl} than the (110) facet due to the lack of Smoluchowski smoothing in the flat {111} surfaces. It is not coincidental that the disparity between $\Phi_{110}^{\text{recon}}$ and $\Phi_{110}^{\text{unrecon}}$ for metals with surface reconstruction (Au, Ir, and Pt) is larger than for other metals. Ho and Bohnen²⁰² previously explained that missing row reconstruction was the result of competing forces that contributed to the kinetic energy (KE) contributions to surface energy. A missing-row introduces additional broken *d*-bonds for transition metals which increases KE. At the same time, a larger surface area is created from the newly exposed {111} facets which will better facilitate the spreading of *s* and *p* electrons. This increase in electron spreading will lower the surface KE and for some elements such as Au, Ir and Pt, is enough to overcome the KE increase. Recall that electron spreading will increase work function, a tenet of the Smoluchowski model (see later section), which explains the larger increase in $\Phi_{110}^{\text{recon}}$ for reconstructed surfaces relative to $\Phi_{110}^{\text{unrecon}}$.

3.4.4 Models for the work function

Smoluchowski rule

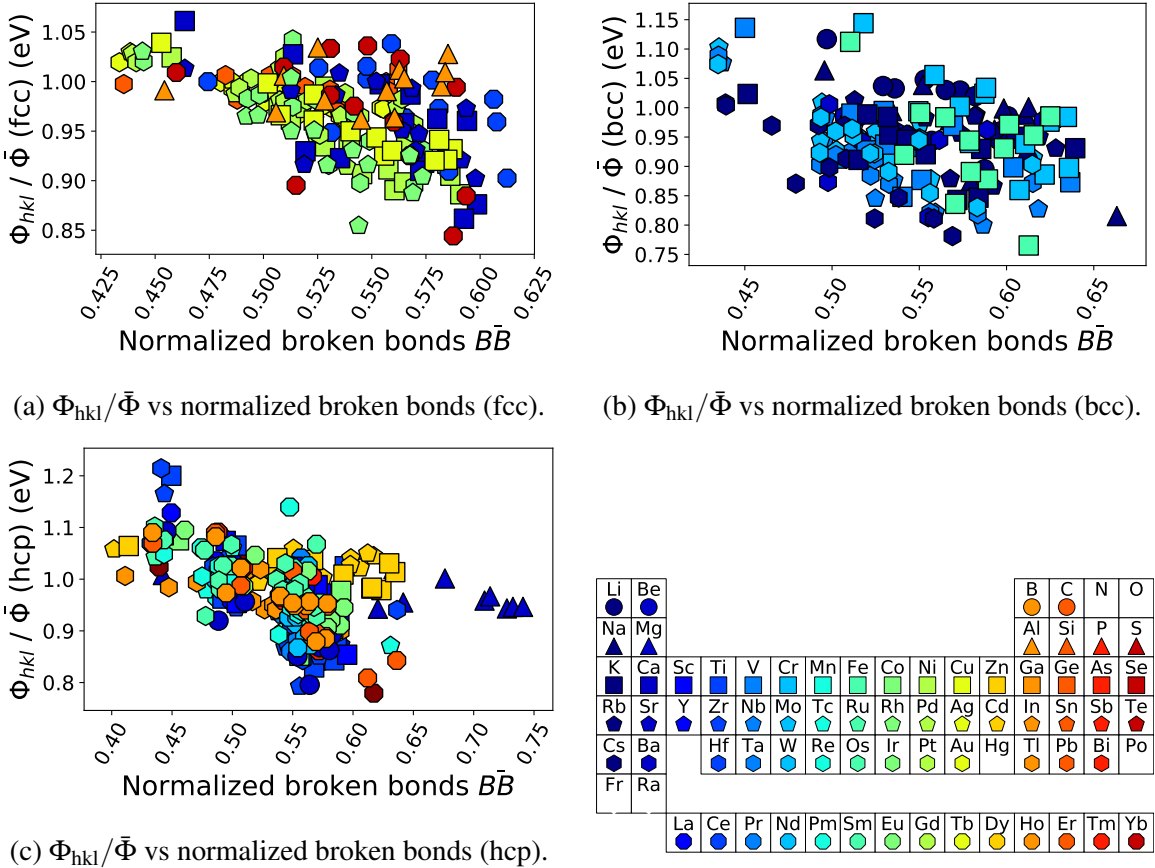


Figure 3.7: Plot of the normalized broken bonds vs $\Phi_{hkl}/\bar{\Phi}$ normalized by average work function for (a) fcc, (b) bcc and (c) hcp structures for elemental crystalline solids commonly observed in literature. A legend indicating the element of each corresponding marker is shown at the bottom right.

Figure 3.7 plots Φ_{hkl} normalized by the average work function for each element $\bar{\Phi}$ as a function of the normalized broken bonds. All r values obtained from comparing Φ_{hkl} and γ_{hkl} to their respective normalized broken bonds and to each other are presented in Table A.3. Strong negative correlations were observed for the anisotropic work functions of 23 metals: Au, Ni, Ag, Pd, Cu, Rh, Nb, Mo, Li, Ta, W, Y, Lu, Ru, Zr, La, Tc, Sc, Re, Eu, Er and Ho. Among

these systems, similar trends have been confirmed in previous studies for Ni, Cu, Ag, Mo and W, but not for Au and Pd^{20,171,176}. Ta and Nb are the only metals where a stronger correlation with surface energy ($r_{\text{Ta}} = 0.96$, $r_{\text{Nb}} = 0.88$) is observed when modelling with 2NN and work function ($r_{\text{Ta}} = -0.78$, $r_{\text{Nb}} = -0.86$) when modelling with 1NN. A moderate negative correlation is observed for 20 metals: Pt, Ir, Ca, Sr, Na, V, Cs, K, Cr, Mg, Ti, Zn, Pr, Hf, Tl, Co, Be, Nd, Sm and Os. The remaining 9 metals have weak negative correlations with Cd and Al having no negative correlation ($r_{\text{Cd}} = 0.01$, $r_{\text{Al}} = 0.22$) at all.

Grepstad et al.¹⁹⁹ has previously suggested that the Smoluchowski rule is valid only for systems with densely packed planes. It is well known that the c/a ratio of Cd is significantly larger than other hcp metals leading to sparsely packed planes along the (0001) direction²⁰³ which can explain why Cd does not follow the Smoluchowski rule. However, although Grepstad et al.¹⁹⁹ was able to show that the computed values of Φ_{211}^{Cu} and $\Phi_{\text{hkl}}^{\text{Al}}$ are consistent with this explanation, our results clearly show that even for facets of Cu with $\text{MMI} > 1$, bond breaking trends are still valid.

Alternatively, Fall et al.²⁰⁴ associates the anomalously low value of Φ_{111}^{Al} with the presence of p orbitals parallel to its surface which are highly favored in electronically dense facets. By decreasing the valence electrons at the surface, the p orbitals perpendicular to the surface become favored over the parallel p orbitals. This leads to an increase in Φ_{111}^{Al} that will eventually lead to an anisotropy consistent with the Smoluchowski rule. It is possible that the same phenomenon can explain the lack of correlation in other p -block systems such as Pb ($r = -0.05$).

An improved model for the work function of metals

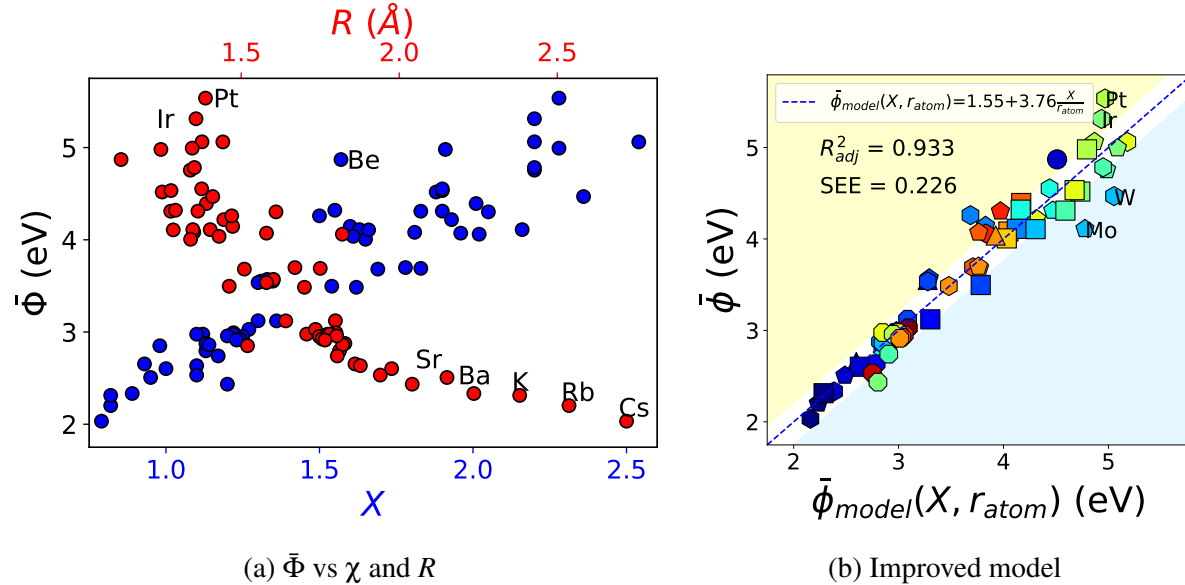


Figure 3.8: Plot for the calculated $\bar{\Phi}$ against (a) Pauling electronegativity χ and metallic radius R , and (b) predictions from improved model for $\bar{\Phi} = 1.55 + 3.76 \frac{\chi}{r_{atom}}$, where $r_{atom} = \sqrt[3]{V_{atom}}$ and V_{atom} is the unit cell volume per atom.

The comprehensive data set presented in this work affords us the ability to develop more robust models for the work function of the elemental metals. It has previously been well-established by Michaelson¹⁷³ and Miedema et al.¹⁷⁴ that the work functions of metals have a positive linear relationship with the electronegativity χ of the metal. This may be explained by the fact that χ is a measure of how strongly electrons are bounded to the atom, and hence, the higher the χ , the greater the energy needed to bring an electron from the bulk to the free vacuum (Φ). Nevertheless, as can be seen from Figure 3.8a, it is clear that χ only explains $R^2 = 85.5\%$ of the variation in $\bar{\Phi}$ across the metals.

We carried an investigation of the relationship between $\bar{\Phi}$ and various atomic properties. As can be seen from Figure 3.8a, a strong, albeit non-linear, negative relationship is observed between $\bar{\Phi}$ and the metallic radius R . From Gauss' law, the potential inside an infinite charged plate is proportional to the bulk charge density times the square of the thickness of the plate,

i.e., it scales charge per unit length of material. We postulate that the average work function is proportional to the electron density per unit length, similar in spirit to the traditional jellum work function model for metals²⁰⁵. We performed a linear regression of $\bar{\Phi}$ against $\frac{\chi}{r_{atom}}$, where χ is related to the electron charge contributed per atom (in line with previous models) and $r_{atom} =^3 \sqrt{V_{atom}}$, where V_{atom} is the unit cell volume per atom. As shown in Figure 3.8b, this optimized model $\bar{\Phi} = 1.55 + 3.76 \frac{\chi}{r_{atom}}$ exhibits a much improved prediction accuracy for $\bar{\Phi}$, with a very high R^2 of 0.933 and a small SEE of 0.226 eV.

3.5 Conclusions

In conclusion we have constructed the largest database of anisotropic work functions to date. We have validated our database by comparing to both experimental and computational results from the literature and by confirming previously observed trends. In addition, we have also developed a technique for estimating the work function of a polycrystalline specimen using the Wulff shape and showed that it is a significantly more accurate estimate for experimental polycrystalline values than the lowest anisotropic work function. Using this large dataset, we have also extensively probed well-known empirical relationships for the work function, such as the Smoluchowski rule, and developed a substantially-improved prediction model for the work function of the metals from atomic properties such as the electronegativity and metallic radius.

Chapter 3 is, in full, a reprint of the material “Anisotropic work function of elemental crystals” as it appears in Surface Science, Richard Tran, Xiang-Guo Li, Joseph H. Montoya, Donald Winston, Kristin A. Persson and Shyue Ping Ong, 2019, 687(September), pp 48-55. The dissertation author was the primary investigator and author of this paper. Most calculations and data analysis were performed by the author.

Chapter 4

**Morphology control of tantalum carbide
nanoparticles through dopant additions
and surface segregation**

4.1 Introduction

Tantalum carbide (TaC) is an ultra-high temperature ceramic (UHTC) with a melting temperature of \sim 4100 K and exceptional hardness, both attributed to its strong Ta-C covalent bonds^{206,207}. Such properties hold great engineering relevance under harsh conditions, resulting in industrial applications such as high-speed cutting tools and hard coatings. TaC also holds great potential in aerospace and advanced energy systems, such as turbine blades, scramjet engines, nuclear reactors and solar absorbers²⁶. Practical limitations of TaC at high temperatures are often due to the degradation of mechanical properties due to porosity and other microstructural defects, as well as problems connected to oxidation²⁰⁸ and creep deformation²⁰⁹.

Improvement of properties begins with control of powder size and shape. Studies have explored the shape control of transition metal carbide nanoparticles to exploit the high surface area-to-volume ratio in applications such as catalysis and chemical sensing whereby specific facets, such as those with steps and kinks, will better facilitate chemical reactions^{210,211}. Modeling studies have looked at the molecular adsorption of H₂O on ZrC, to obtain cubes and octahedrons, and carbon adsorption on Ru to produce nanorods³². Strain effects have also been explored as parameters for morphological modification of copper and nickel particles²¹² and acid etching techniques have been applied for obtaining cubes of borides^{213,214}. Moreover, experimental efforts have investigated shape change in cubic carbides as a function of carbon stoichiometry, which influences the relative growth rate of the dominant {111} and {100} facets^{28–30}.

Recently, doping has been suggested as a possible mechanism to form nanocubes in ceramic materials. For transition metal dopants, the interactions between the d-orbitals of dopants and the p-orbitals of the non-metallic anionic elements (i.e., carbon, nitrogen, boron, etc.) in ceramic compounds are thought to promote adsorption on the {100} facets, especially for metallic dopants with high carbon solubility^{29,31}. With this in mind, the modification of particles from octahedrons to cuboids with an increasing dopant concentration has been successfully

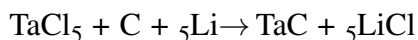
demonstrated for Cr-doped WO₃ and Ni-doped TiC^{29,211}. However, the fundamental principles behind dopant-induced morphological selectivity and control remain largely unknown.

In this study, a combined experimental and computational effort is implemented to demonstrate the effects of dopants on the particle morphology of TaC. We show that morphology modification results from a combination of dopant segregation towards the surface of particles and dopant interaction with surface carbon through orbital hybridization. These effects modify surface energy, slowing crystal growth and facilitating the formation of polyhedrons. Doping with iron and Ni-Ti co-doping results in cubes and cuboctahedrons, while cobalt and nickel doping result in cuboctahedrons. This work provides critical insights into the fundamentals of dopant-induced shape control, which has exceptional potential in tuning the mechanical and catalytic properties of ceramic materials.

4.2 Methods

4.2.1 Synthesis and characterization of TaC powders

The synthesis of TaC particles is based on a modified solvothermal method^{215,216}. Tantalum (V) chloride [No. 14614, 99.8%, anhydrate, Sigma-Aldrich] and carbon black powder [No. 39724, >99.9%, Alfa Aesar] were used as the metal and carbon sources. Lithium granules [No. 499811, 99%, Sigma-Aldrich] were employed as the non-aqueous solvent and reductant, according to the following chemistry:



The amount of each component was calculated based on 3 g theoretical yield of TaC, while two times of excess carbon and lithium were used to ensure phase purity. For different dopant systems, metallic nickel [No. A17943, 99.9% metals basis, Alfa Aesar], iron [No. 267953, >99.9% metals basis, Sigma-Aldrich], cobalt [No. 697745, >99.9% metals basis, Sigma- Aldrich], titanium [No. 43102, 99.5%, metals basis, Alfa Aesar], and niobium [No. 11548, 99.9% metals basis, Sigma-Aldrich] were used as dopants.

basis, Alfa Aesar] were used for synthesis. Their amounts varied based on various atomic ratios between the dopant and the host that were investigated. See Table B.2 for corresponding dopant concentrations in each powder sample. To lower the maximum flame temperature, 30 wt.% of pure TaC powders [No. 12144, 99.5%, Alfa Aesar] were added as reaction diluent. The precursors were weighed and ground manually in a mortar and pestle in an argon-protected glovebox for at least 15 minutes to create a homogeneous mixture. They were then placed in a quartz test tube, after which lithium granules were incorporated. The test tube was then rotated repeatedly to ensure that the surfaces of the lithium granules were fully covered with precursor powders and temporarily sealed with parafilm prior to being transferred out of the glovebox for preheating and ignition. To initialize the reaction, a volumetric external heating apparatus was custom-made using a stainless steel hollow cylinder wrapped with dual-element high-temperature heating tape. The system was preheated to \sim 400°C in order for the reaction to occur. To minimize oxidation during the reaction, the test tube was flushed with ultra-high purity argon gas 5 times before being inserted into the heating cylinder, capped by a rubber stopper and connected to a vacuum pump for outgassing. The reaction self-ignited once the system reached the melting temperature of lithium. The duration of reaction was less than 40 seconds for all reactions. The system was then air-cooled to room temperature. The post-reaction products were rinsed using deionized water to dissolve excess lithium, followed by two wash cycles using hydrochloric acid [H-135, 25 vol%, Spectrum Chemical]. Within each cycle, 15 minutes of magnetic stirring and 30 minutes of ultrasonication were applied for thoroughness of washing and deagglomeration. Finally, the acid-washed powders were cleaned one more time using deionized water and finally rinsed with ethanol. The resulting powders were collected after 24 hours of drying in air.

The phase purity of samples was analyzed by X-ray diffraction on a D2 Phaser instrument [Bruker AXS, Inc., Madison, WI] using CuK α radiation. The morphology of particles was imaged by scanning electron microscopy (SEM) on an Apreo instrument [ThermoFisher Scientific, Hillsboro, OR]. Elemental composition characterization was performed by energy dispersive

spectroscopy (EDS) and X-ray photoelectron spectroscopy (XPS) on a custom designed system [SPECS Surface Nano Analysis GmbH, Berlin, Germany] equipped with a PHOIBOS 150 WAL analyzer with DDL-2 detector and a FOCUS 500/600 ellipsoidal monochromatic X-ray source with a dual anode of Al and Ag. EDS and XPS were employed for determination of bulk and surface chemical composition, respectively. The elemental surface compositions were calculated by deconvolution of individual peaks using CasaXPS software. To statistically determine the morphological modifications, particles were evaluated based on multiple SEM images. At least 900 particles were counted for each sample, ensuring the randomness and statistical significance of the sampling. For each dopant precursor concentration, two individual batches of powders were synthesized and characterized using identical procedures to confirm the repeatability of the results.

4.2.2 Computational methods

All DFT calculations were performed using the Vienna Ab initio Simulation Package (VASP) within the projector augmented wave (PAW) approach^{4,136,138,140}. The exchange-correlation effects were modeled using the Perdew-Berke-Ernzerhof (PBE) generalized gradient approximation (GGA) functional, and all calculations were spin-polarized with a plane wave cutoff of 400 eV⁷⁸. The pseudopotentials used are similar to those used in the Materials Project¹⁵. The energies and atomic forces of all calculations were converged within 10^{-4} eV and $0.02 \text{ eV}\text{\AA}^{-1}$ respectively. Γ -centered k -point meshes of $\frac{50}{a} \times \frac{50}{b} \times \frac{50}{c}$ and $\frac{50}{a} \times \frac{50}{b} \times 1$ were used for the oriented unit cell and slab calculations, respectively, with non-integer values rounded up to the nearest integer¹³². Since there are several possible terminations for the TaC (111) facet, we only investigated segregation in the most stable terminations (Ta-terminated slab in Figure 4.4(c)). Furthermore, when γ has been determined for several facets, it can be used to construct the Wulff shape. Further explanation and details into the surface grand potential can be found in Section B.1 of Appendix B.

By comparing dopant stability in the surface and bulk, defined as the energy difference between a doped and undoped cell, we can determine where the dopant will segregate. This is dictated by the segregation energy, which is given by:

$$E_{seg} = \frac{(E^{slab+X} - E^{slab})}{2} - (E^{bulk+X} - E^{bulk}) \quad (4.1)$$

The difference between E^{slab+X} and E^{slab} , the calculated total energies of the clean and doped slab cells, respectively, represents dopant stability on the surface. Meanwhile, the difference between E^{bulk+X} and E^{bulk} , the calculated total energies of the undoped and doped bulk cells, respectively, represents dopant stability in the bulk. The factor of 2 in the first term accounts for both surfaces being symmetrically doped. $E_{seg} < 0$ indicates a segregation tendency towards the surface, $E_{seg} \sim 0$ indicates no segregation tendency, and $E_{seg} > 0$ indicates a segregation tendency towards the bulk. Only dopants that segregate towards the surface are assumed to influence the surface energy and thus affect the morphology. We investigated dopant segregation in both the top layer and sublayer of the surface (see Figures 4.4(c)-(d)), where the black-dashed box represents the top layer and the red-dashed box represents the sublayer.

TiTa_3C_4 slabs (see Figures 4.4(e)-(f)) were generated from a fully relaxed bulk TiTa_3C_4 structure, which was in turn generated by substituting one Ta atom for Ti in the conventional unit cell of TaC. Dopant substitution of a single Ta atom was performed for TaC slabs. Single substitution for both Ta and Ti atoms, one at a time, was performed for TiTa_3C_4 . We investigated the most dilute coverage of dopants that can be calculated while maintaining slab systems of less than 200 atoms resulting in a coverage of 1/4 and 1/2 monolayers (number of dopants per unit primitive slab) for the TaC and TiTa_3C_4 slabs, respectively. All slabs had a slab and vacuum layer 22 Å and 16 Å thick to prevent periodic interactions between the dopants and the two surfaces. All slab systems, including doped slabs, maintained symmetrically equivalent surfaces by ensuring Laue point group symmetry in the structures to avoid any dipole moments

perpendicular to the surface^{36,132,217}. All computational parameters, structural models, Wulff construction, chemical potential range maps and surface energy analysis were obtained with the aid of the Python Materials Genomics (pymatgen) materials analysis library¹³⁵.

For each dopant-carbon bond, we quantify $p - d$ hybridization as the integration of the negative Crystal Orbital Hamiltonian Population (–ICOHP), which is the covalent bond contribution to the bonding character of the dopant. Similarly, –ICOHP is used to quantify the metallic bond contributions for each dopant-Ta bond. The –COHP is integrated from the valence band to the Fermi level in order to obtain the –ICOHP. In this study, we only consider bonds within a radius of 3.5 Å from the dopant, which encompasses all carbon nearest neighbors and Ta next nearest neighbors (see Figures 4.6(b)-(c)). The –ICOHP is normalized by the number of valence electrons and the sum of the metallic (dopant-Ta) and covalent (dopant-C) contributions, which results in the total bond contribution of the dopant. We normalize –ICOHP for the covalent contributions by this total to obtain the percentage covalent contribution of the dopant given by the table in Figure 4.6(a). For further details, the reader is referred to Maintz et al.²¹⁸ and Sun et al.²¹⁹.

4.3 Results

4.3.1 Undoped TaC nanoparticles

The morphologies of undoped powders of TaC are illustrated in Figure 4.1(a), showing that the nanoparticles are predominantly of random shapes, with minimal amounts of faceted surfaces. X-ray diffraction patterns of the powders can be observed in Figure 4.1(b), where the lattice parameter obtained from Rietveld refinement is 4.4543 ± 0.00003 Å, indicating that the sample is slightly non-stoichiometric^{220,221}. Controlling the particle morphology requires tuning the relative growth rate of different crystal facets. Faster growth for a particular crystal face results in quicker extinction of that face, leaving the slower growing faces as the enclosing surfaces for

the final crystal. The growth rate of a particular face is directly proportional to its corresponding surface energy, γ . Using the Wulff construction, Figure 4.1(c) illustrates how the equilibrium shape for a generic cubic material changes with the growth rate ratio ($R = \gamma_{111}/\gamma_{100}$). Values of R below 0.58 result in octahedrons, values between 0.58 and 1.73 result in cuboctahedrons, and values greater than 1.73 result in cubes. Burton et al.²²² previously proposed that facets with a high growth rate will go through thermodynamic roughening whereby the crystal morphology transitions from its equilibrium crystal shape to a round/irregular shape due to free energy minimization at elevated temperatures. More recently, Jin et al.²⁹ has reported experimental thermodynamic roughening of transition metal carbides. In our case, it is likely that the growth rate of the {100} facets has surpassed the temperature threshold for thermodynamic roughening due to the extremely high synthesis temperatures (>2000 K), thus explaining the lack of cubic particles and the lack of faceting in general in Figure 4.1(a).

The surface energy with respect to the carbon chemical potential ($\Delta\mu_C$) is plotted in Figure 4.1(d) for undoped TaC surfaces (y-axis) for facets with Miller indices of (111), (110) and (100), and the (111) fcc Ta surface. For the stoichiometric slabs, such as (110) and (100), the surface energies are constant with respect to $\Delta\mu_C$. For the non-stoichiometric (111) Ta-terminated slab, however, the C-deficiency relative to the bulk TaC results in a positive linear relationship between γ_{111} and $\Delta\mu_C$ (see Equation B.1 and derivations therein in Appendix B). At high $\Delta\mu_C$, the most stable surface of TaC is the (100) facet, due to the smaller number of broken bonds compared to the (111) facet. At lower $\Delta\mu_C$, the Ta-terminated (111) facet is increasingly stabilized as it becomes more similar to the metallic fcc Ta (111) surface²²³ with greater carbon deficiency. In fact, the calculated work function of the TaC (111) surface (4.62 eV) is close to that of the Ta (111) surface (4.70 eV), while that of the TaC (100) surface is significantly lower (3.61 eV). This stabilization of the (111) facet pushes its growth rate below that of roughening, allowing for minimal formation of cuboctahedrons, but not the formation of cubes.

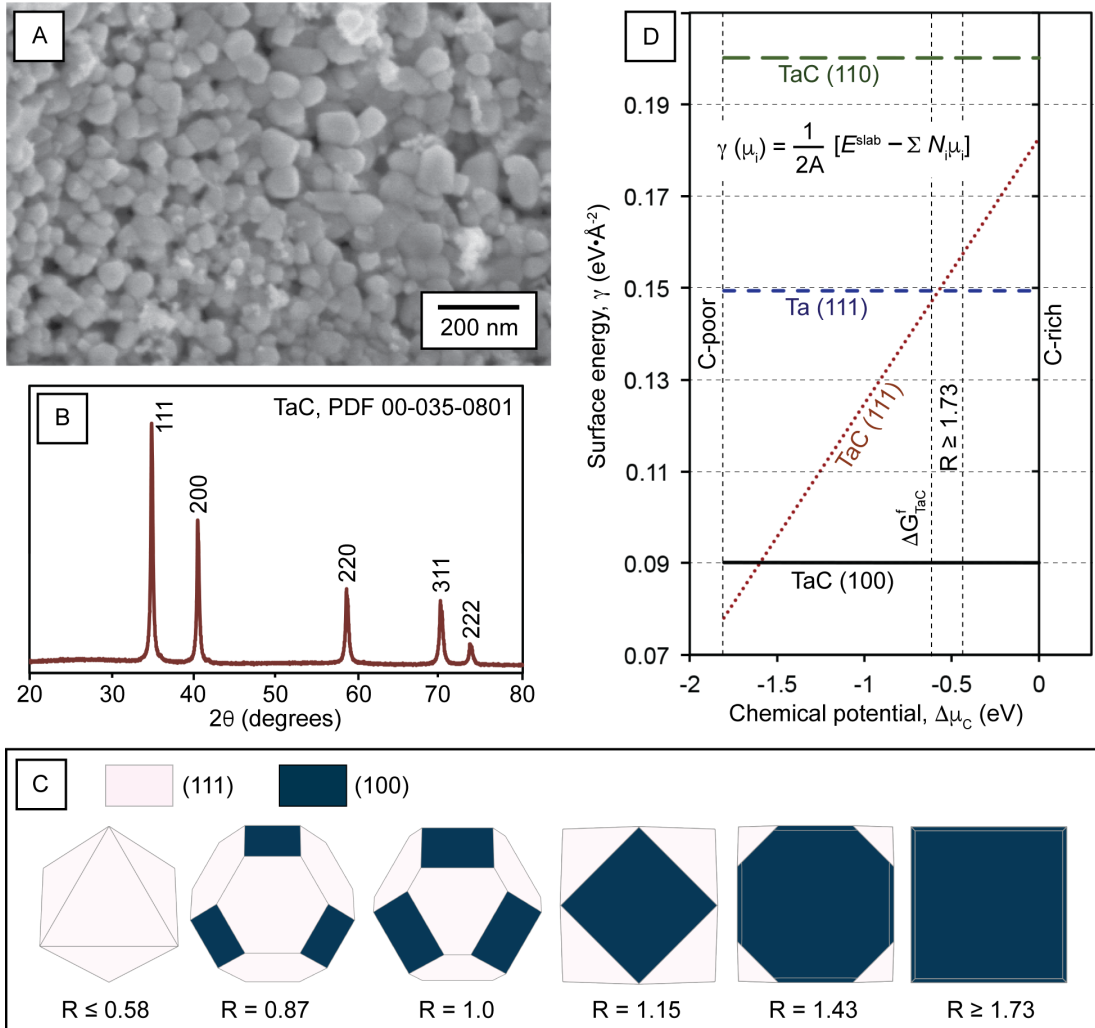


Figure 4.1: Characterization of undoped TaC powders, particle shapes and surface energies. (a) Scanning electron micrograph and (b) X-ray diffraction pattern of undoped TaC powders. (c) Varying morphologies corresponding to the surface energy ratio ($R = \gamma_{111}/\gamma_{100}$) and (D) surface energies for the TaC (100), (111) and (110) slabs and the face-centered cubic Ta (111) slab as a function of the chemical potential of carbon ($\Delta\mu_C$).

4.3.2 Doping efficacy on morphology control

To expose crystal facets and tailor particle morphology, the surface energies of the desired facets must be further decreased. We add metallic dopants with low bulk solubility in TaC, namely Ni, Co, and Fe, as well as mixed Ni/Ti co-dopants, in order to modify its surface thermodynamics and subsequently influence its growth. A metallic dopant with high bulk

solubility in TaC (i.e., Nb) was also added for comparison. The full list of prepared powders, with dopant concentrations determined by energy dispersive spectroscopy, is presented in Table B.2 in Appendix B. Figure 4.2 illustrates the morphology of Fe-doped (Figure 4.2(a)), Ni/Ti- doped (Figure 4.2(b)), and Nb-doped (Figure 4.2(c)) TaC powders. The corresponding XRD patterns are illustrated in Figures B.1 through B.5 for the powders doped with Ni, Co, Fe, Nb, and Ni/Ti, respectively. The SEM micrographs show that a significant portion of the Fe-doped and Ni/Ti- doped particles have been faceted into cubic particles (Figure 4.2(a)-(b)), whereas the Nb-doped powders have not (Figure 4.2(c)).

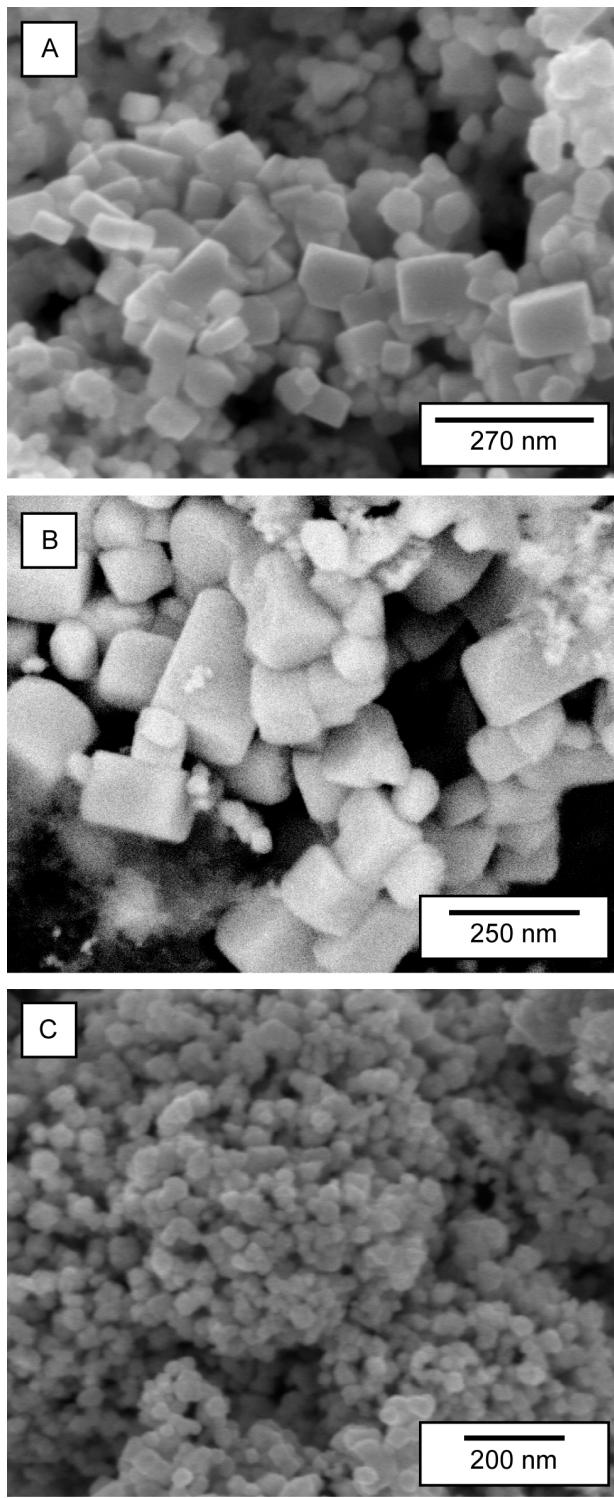


Figure 4.2: Electron microscopy of powders. Scanning electron micrographs for (a) Fe-doped, (b) Ni-Ti co-doped, and (c) Nb-doped TaC powders.

To compare the effectiveness in morphology control, we summarize the overall abundance of particles of different morphologies in Figure 4.3. As the abundance of non-faceted particles decreases (Figure 4.3(a)) in order of undoped, Co-, Ni-, Fe-, and Ni/Ti-doping, there is a corresponding increase in the abundance of faceted polyhedrons (Figure 4.3(b)) and cubic particles (Figure 4.3(c)). Cubic particles are only seen in the Fe- and Ni/Ti-doped powders in abundances of 38% and 42%, respectively. Thus, from the SEM images and the statistical analysis, we have established a causal relationship between the addition of certain dopants and the formation of morphologically-controlled TaC particles.

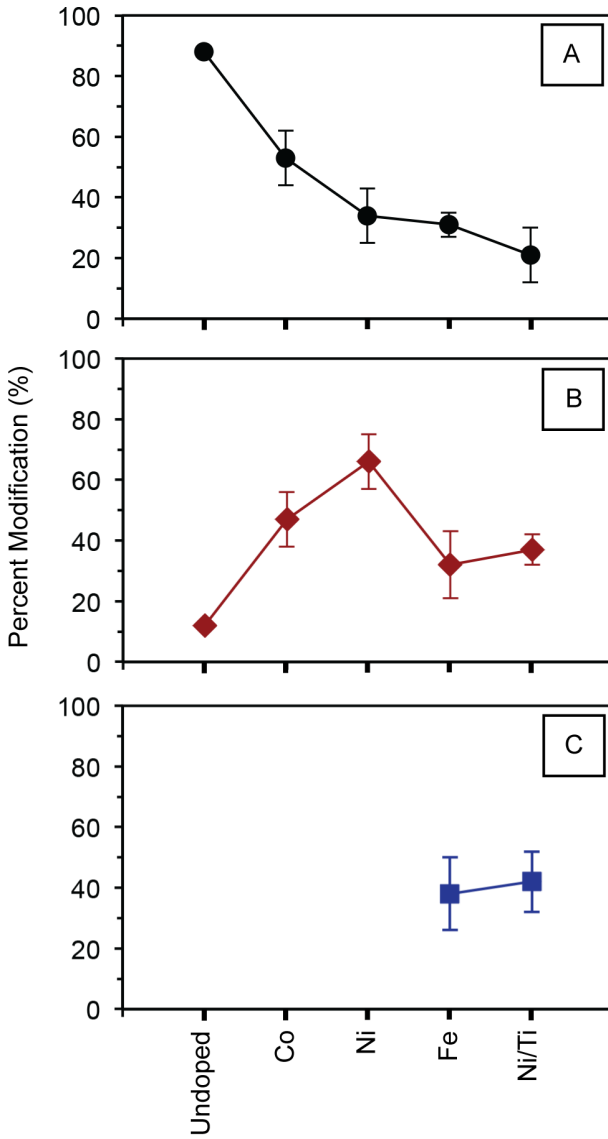


Figure 4.3: Statistical abundance of particle shapes. For the undoped, Co-, Ni-, Fe- and Ni/Ti-doped TaC powders, the resulting morphologies are (a) non-faceted, (b) faceted polyhedrons, and (c) cubic.

4.3.3 Surface segregation of dopants

In order to probe the effect of dopants on the surfaces, we compare the dopant concentrations of the morphology modifiers (Co, Ni, Fe and Ni/Ti) in the bulk using energy dispersive spectroscopy (penetration depth $\sim 1\text{-}2 \mu\text{m}$ below the surface) and near the surface using X-ray

photoelectron spectroscopy (penetration depth <10 nm below the surface) in Figure 4.4(a). The dopant with the greatest surface concentration enrichment (i.e., elemental concentration by XPS is greater than EDS) is Ni followed by Fe and Co. Ti and Nb have a high solubility in the bulk, as shown by the high EDS concentrations. Due to the chemical similarity of Ti and Ta, TiC is expected to be mutually soluble with TaC leading to its high concentration in the bulk. Figure 4.4(b) illustrates the calculated surface segregation energies (E_{seg}^{surf}) for the TaC (111) and (100) facets for all dopants considered in the study. A negative E_{seg}^{surf} indicates a driving force towards segregation to the surface, defined as the layer of atoms inside the black and red boxes in Figure 4.4(c)-(f). In agreement with the experimental observations, Nb and Ti exhibit little to no preference to segregate to any surface, because the segregation energies, illustrated in Figure 4.4(b), show values close to zero for both E_{seg}^{111} and E_{seg}^{100} . In contrast, Ni, Fe, and Co are predicted to strongly segregate to the (111) surfaces. In comparing the E_{seg}^{111} and E_{seg}^{100} , it is clear that the E_{seg}^{111} values are less than -2 eV, whereas E_{seg}^{100} is closer to -1 eV. To investigate how the high bulk solubility of Ti doping affects Ni doping for the case of the Ni/Ti doped samples, we calculated E_{seg}^{surf} for Ni in a $TiTa_3C_4$ solution and demonstrated that Ni will strongly segregate to the (111) surface. This is in qualitative agreement with the experimentally observed higher concentration of these dopants in the surface relative to the bulk.

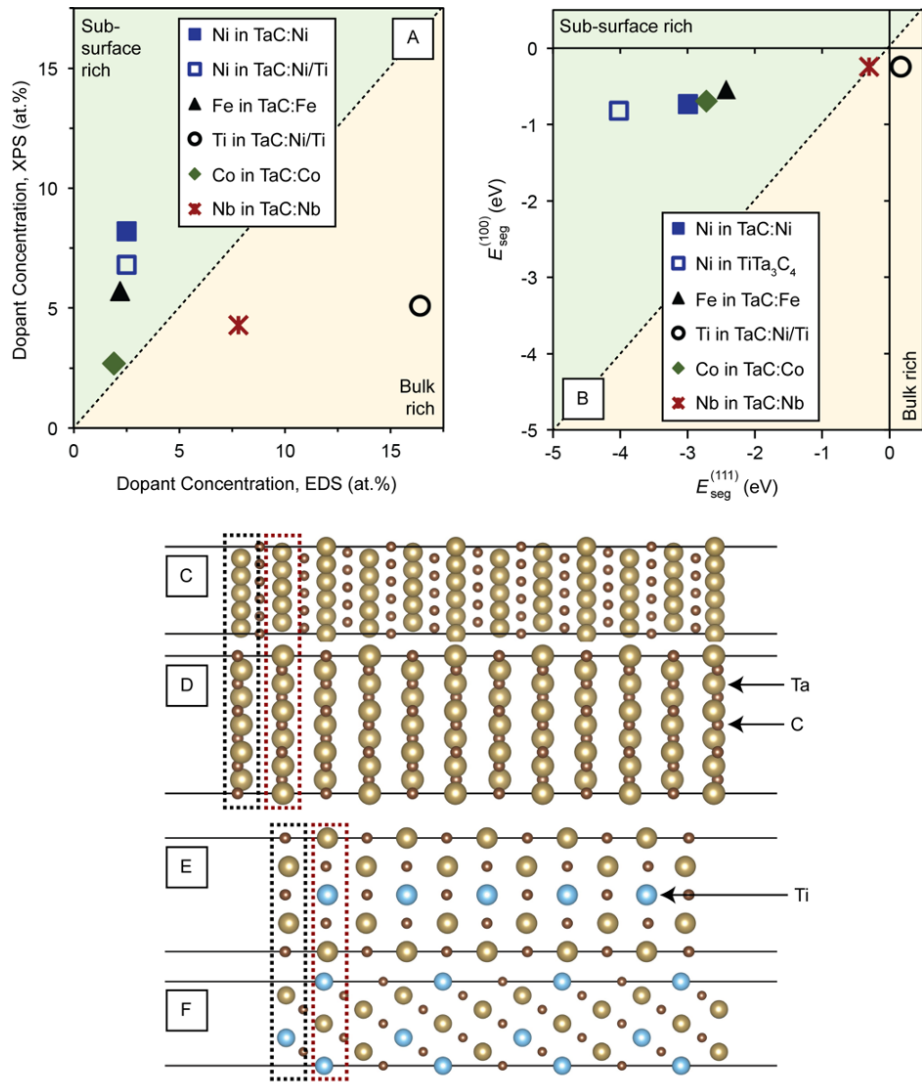


Figure 4.4: Dopant concentrations, surface energies and slab models. (a) Plot of the concentration of dopants detected by X-ray photoelectron spectroscopy with respect to the concentration detected by energy dispersive spectroscopy. The samples chosen for comparison have the highest abundance of modified particles in each system, namely, Ni-4, Co-3, Fe-3 and NiTi-5 (see Table B.2 in Appendix B for sample designations). (b) Calculated segregation energy for the (100) surface with respect to the (111) surface. Slab models for (c) TaC (111) and (d) TaC (100) used to calculate segregation energies in (b). Slab models for (e) TiTa₃C₄ (111) and (f) TiTa₃C₄ (100). The black (surface) and red (sub-surface) dashed boxes indicate the possible metallic (*i.e.*, Ta and/or Ti) sites a dopant can substitute. The slab models were constructed using lattice transformations to orient the basal plane parallel to the Miller index plane of interest. The oriented unit cell was then expanded along the direction normal to the basal plane followed by a removal of half the atoms in the resulting supercell to generate a slab and vacuum layer. The most stable termination for the (111) TaC surface is a Ta-terminated nonstoichiometric slab, while the (100) surface is modeled with a Ta-C terminated stoichiometric slab.

4.3.4 Dopant shape preference and bonding

To rationalize the relative preference of cuboctahedron/cube formation, enthalpy maps of R as a function of $\Delta\mu_C$ (y-axis) and $\Delta\mu_X$ (x-axis) where X is the dopant incorporated into TaC are plotted in Figures 4.5(a)-(c). Dopant segregation has two effects. First, the surface dopants modify the range of $\Delta\mu_C$ and $\Delta\mu_X$ where TaC is stable at the surface, as indicated by the red shaded regions. Second, the surface dopants also modify the surface energies of TaC, and hence R , as a function of $\Delta\mu_C$ and $\Delta\mu_X$. In the case of Ni- and Co-doping (Figures 4.5(a)-(b)), the region where TaC is stabilized overlaps with those where cubes and/or cuboctahedrons will form. For Fe (Figures 4.5(c)), the region where TaC is stabilized overlaps with the region where cubes will form, making Fe a very efficient single dopant. These observations explain the relative abundance of cubes observed under Fe doping, and cuboctahedrons under Ni and Co doping in Figure 4.3.

Similarly, Figures 4.5(d)-(e) describe the enthalpy maps of R for Ni-doped TiTa_3C_4 , our computational analog for Ni/Ti doping. This analog simulates Ni segregation on the surface of a TiTa_3C_4 slab in order to investigate the simultaneous effect of Ti doping in bulk solution and Ni doping on the surface of TaC. We stress that no TiTa_3C_4 was detected in the experimental powders as a separate phase and any interpretation of the computational analog should not be used to imply the formation of this phase in the experimental work. Here, we kept a constant value of $\Delta\mu_{Ni} = -0.4$ eV for Figures 4.5(d) and $\Delta\mu_{Ti} = -2$ eV for Figures 4.5(e), as these values are in the range of chemical potential where TaC is stable under a $\Delta\mu_{Ni}$ with respect to $\Delta\mu_C$ and $\Delta\mu_{Ti}$ with respect to $\Delta\mu_C$, respectively. This leads to a larger chemical potential range that allows for the formation of cubes, in agreement with the statistical abundance of cubic versus faceted polyhedron particles shown in Figure 4.3 for the Ni/Ti-doped powders. Since only dopants that segregate towards the surface will induce morphology modification, surface segregation is a prerequisite for influencing γ . This is further supported by the fact that Nb has little to no segregation preference towards the surface, which results in no signs of morphological modification (Figure 4.2(c)). We

can therefore attribute the considerably lower percentage of faceted particles in the Co-doped system relative to the Ni-, Fe-, and NiTi-doped systems to its comparatively low concentration on the surface (lower than 3 at.%), as revealed by XPS.

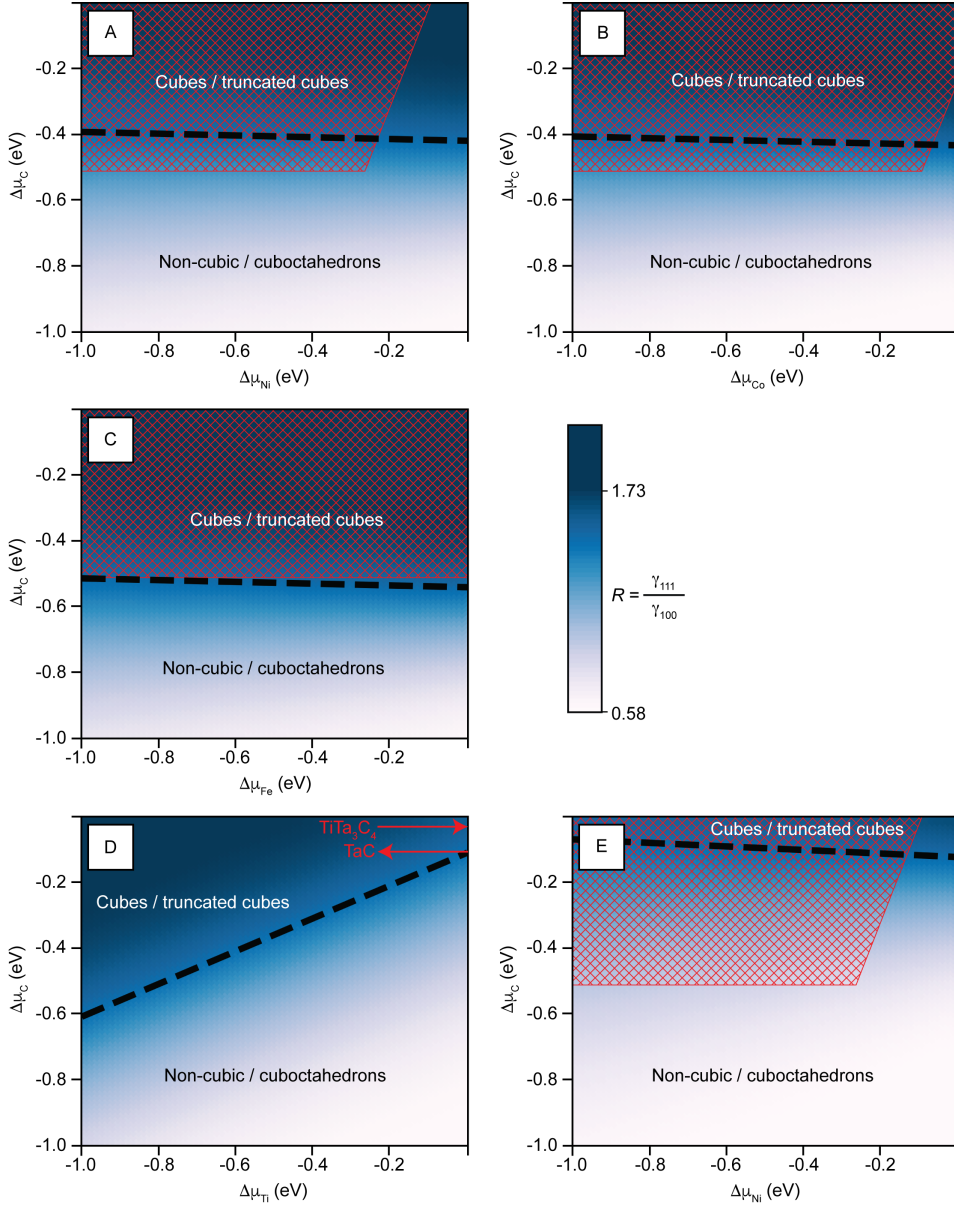


Figure 4.5: Calculated enthalpy maps of R as a function of $\Delta\mu_X$ with respect to $\Delta\mu_C$. (a) Ni in TaC, (b) Co in TaC, (c) Fe in TaC, (d) Ti in TiTa_3C_4 with $\Delta\mu_{Ti} = -0.4$ eV, and (e) Ni in TiTa_3C_4 with $\Delta\mu_{Ti} = -2$ eV at the surface. The dashed line indicates $R = 1.15$ (formation of cuboctahedrons) and partitions the enthalpy map into two regions. The region below is the $\Delta\mu$ window for the formation of (truncated) octahedrons and the region above is the $\Delta\mu$ window for the formation of (truncated) cubes. The red shading indicates the section of the chemical potential map where TaC is stable. Red arrows in (d) indicate the chemical potential of $\Delta\mu_{Ti}$ where TiTa_3C_4 and TaC are stable.

We also calculated the negative integrated Crystal Orbital Hamiltonian Populations (-

ICOHPs) for each dopant bond on the (100) and (111) surfaces^{218,219} to quantitatively gauge the contribution of covalent (dopant *d* and carbon *p*) and metallic (dopant *d* and Ta *d*) interactions to dopant bond strength (see the table in Figure 4.6(a)). We observe that for Fe doping in TaC, the majority of contribution to dopant bond strength is from covalent (over 50%) interactions for the (100) surface and from metallic interactions on the (111) surface. Nie et al.³¹ previously suggested that doping of Ni in TiC may lead to *p* – *d* orbital hybridization between Ni and C at the (100) surface, which will further reduce its surface energy. In the case of Fe-doped TaC, we observe similar *p* – *d* hybridization that stabilizes the (100) surface over the (111) surface, explaining the significantly higher yield of cubic nanoparticles. The significant decrease in γ up to $0.13 \text{ eV}\text{\AA}^{-2}$ when comparing the undoped surfaces to the Ni-, Fe- and Co-doped surfaces at $\Delta\mu_i = 0 \text{ eV}$ will prevent the onset of thermodynamic roughening (see last column of Table B.1 of Appendix B.1 for values of γ). When coupled with dopant and surface atom interactions, this decrease in surface energy is the root cause of the larger yield of faceted particles.

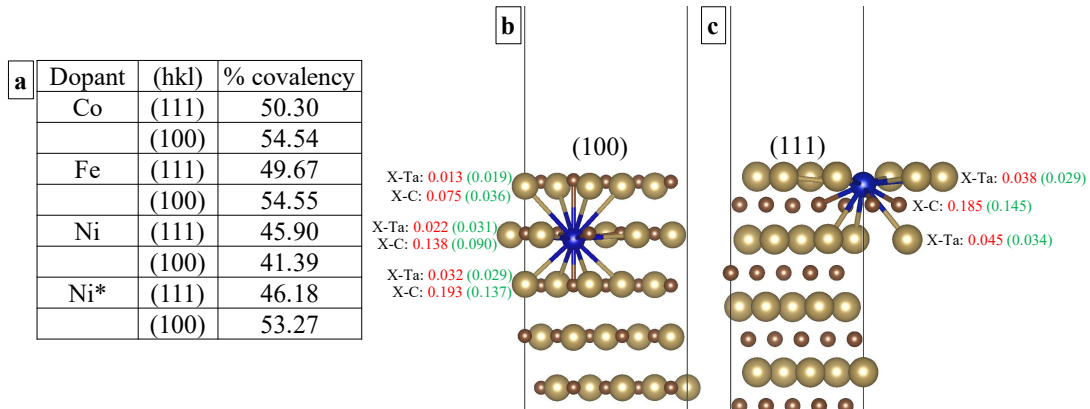


Figure 4.6: -ICOHP bond contributions of dopant bonds at the surface. (a) Table of the percentage of covalency for the dopant bonds at the surface and the corresponding metal atom that was substituted in the undoped surface. The remainder percentage represents metallicity. Ni* indicates Ni substituting Ti in TiTa_3C_4 . The -ICOHP contributions for all nearest X-Ta (metallic bonds) and X-C (covalent bonds) in the (b) (100) and (c) (111) surface are shown where X is the dopant (blue site). -ICOHP values shown in red (green) text are for X=Fe (X=Ni).

4.4 Discussion and conclusion

In summary, the onset of morphology modification is due to surface segregation of dopants and interaction with neighboring carbon via $d - p$ hybridization, which reduces the growth rate to prevent thermodynamic roughening. Ni and Co doping favors faceted polyhedrons, while Fe doping favors both faceted polyhedrons and cubic geometries due to its stronger hybridization effect with neighboring C at the (100) surface. Nb segregates to the surface only minimally and, thus, faceted particles are not formed. Ti dopants will dissolve in the bulk of the TaC host leading to a decrease in surface chemical potential for Ti. This increases the chemical potential window that allows for cube formation. With the addition of Ni and carbon $p - d$ hybridization at the surface, thermodynamic roughening can be prevented leading to cubic and faceted polyhedron geometries in the Ni/Ti doped TaC. We expect the mechanisms explored here can be widely applicable to other combinations of dopants and ceramic powders. For example, if one seeks to produce highly-faceted (V, Hf, Zr)-carbide nanoparticles with fcc crystal structure, doping strategies reported here can be applied. Other rare earth elements may also be effective in changing the growth habits of crystals based on surface segregation and dopant-host atomic orbital hybridization.

Chapter 4 is, in full, a reprint of the material “Morphology control of tantalum carbide nanoparticles through dopant additions and surface segregation”, Tianqi Ren, Richard Tran, Sebastian Lee, Aric Bandera, Manuel Herrera, Xiang-Guo Li, Shyue Ping Ong and Olivia A. Graeve. This material has been submitted to a peer-reviewed journal and is currently being reviewed for publication. The dissertation author was the primary investigator and author of this paper. All calculations and data analysis for the computational part of this paper were performed by the author. The experimental portion of the work – synthesis and characterization – was done by collaborators Tianqi Ren, Sebastian Lee, Aric Bandera, Manuel Herrera, and Olivia A. Graeve.

Chapter 5

Computational study of metallic dopant segregation and embrittlement at Mo grain boundaries

5.1 Introduction

Mo¹⁶⁶ and its alloys²²⁴ have been widely used in high temperature applications²²⁵ owing to their excellent stability, strength, high thermal and electrical conductivity²²⁶, and a low coefficient of thermal expansion²²⁷. In addition, its high creep, corrosion, and sputtering resistance opens up applications in medical devices²²⁸ and coatings for aerospace and defense components²²⁹. However, Mo still suffers from low ductility at near room temperatures^{43,230}.

It is well known that segregation of alloying elements or impurities at grain boundaries (GBs) leads to embrittling effects in Mo as well as many other alloys^{44,231–234}. Nonetheless, doping with certain other elements can also be a promising approach to mitigate the low ductility of Mo, as demonstrated by Miller et al.²³⁵ for Zr, Al, C and B dopants in 2002 Charai et al.²³⁶. also investigated liquid metal wetting embrittlement (LME) of Pb, Sn and Ni on Mo GBs and showed that the wettability by Pb and Ni is dependent on crystallography or GB types. More recently Liu et al.⁴³, reported a nanostructuring technique that involves a molecular-level liquid-liquid mixing/doping to achieve yield strengths over 800 MPa and tensile elongation as large as 40% at room temperature in Mo alloys. On the computational front, first principles investigations of dopant segregation and diffusion in Mo GBs have been carried out with light elemental dopants such as B, C, N, O and H^{110,237}. In particular Janisch and Elsässer²³⁷, used local-density functional theory (LDFT) to confirm one of the predictions made by the empirical Contrell model²³⁸ by showing that the bonding strength between Mo GBs and its interstitial dopants depends the strength of hybridization due to the relative position of electronic bands and thus on the valence configuration of the elements.

GBs in metals critically affect their mechanical properties by acting as centers of dopant segregation^{55,239} and system stabilization²⁴⁰. Although GB segregation in other metals, such as Fe²⁴¹, W⁵⁰, and Ni^{242,243}, have been extensively studied, a systematic first principles investigation of metallic dopant segregation in Mo GBs is yet to be carried out.

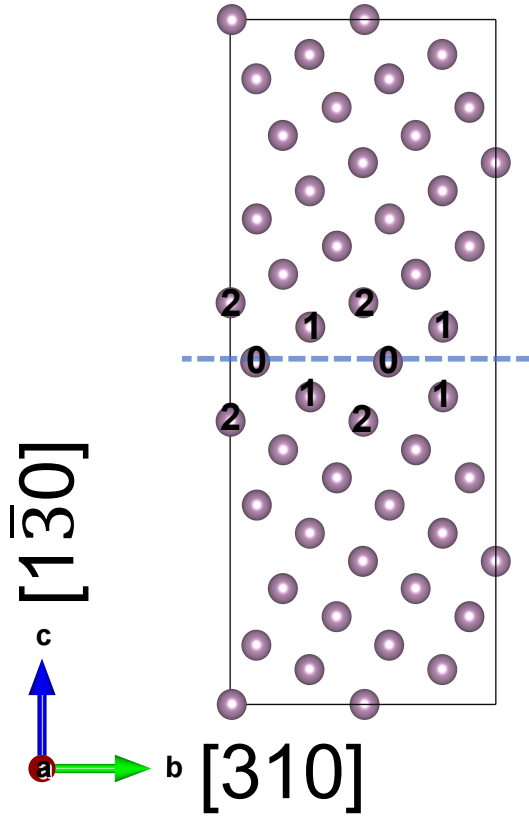
In this work, we performed density functional theory (DFT) calculations to investigate segregation and strengthening phenomena in the $\Sigma 5(310)$ symmetric tilt and $\Sigma 5(100)$ twist GBs of Mo for 27 metallic dopants. We compared the results of our investigation with those computed from the empirical Miedema²⁴⁴ and McLean²⁴⁵ models. We will discuss whether segregation and strengthening/embrittling effects can be explained using simple models based on strain and cohesive energy, and the reasons for observed deviations from these models.

5.2 Methods

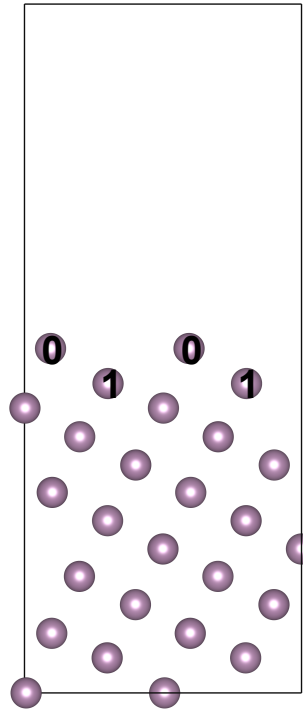
For brevity, the terms “twist GB” and “tilt GB” will henceforth be used to refer to the $\Sigma 5(100)$ twist and $\Sigma 5(310)$ tilt GBs investigated in this work. All GB model construction, input file generation and analyses were performed using the Python Materials Genomics (pymatgen) library¹³⁵. The following subsections outline the various structural models and calculation parameters used. Comprehensive convergence tests were carried out (see Figure C.1 in Appendix C) to ensure that the relevant properties of interest (*e.g.*, segregation energy) were converged to within 0.02 eV using these models and parameters.

5.2.1 Grain boundary structural models

GB structures were generated from the fully relaxed body-centered cubic (bcc) Mo unit cell with cubic lattice parameter $a = 3.167\text{\AA}$. The tilt GB model (Figure 5.1a) had dimensions $9.443\text{\AA} \times 9.956\text{\AA} \times 24.760\text{\AA}$ with 144 atoms, and the twist GB model (Figure 5.2) had dimensions $7.083\text{\AA} \times 7.083\text{\AA} \times 25.343\text{\AA}$ with 80 atoms. The twist GB model was generated in accordance to coincidental site lattice (CSL) theory²⁴⁶. Free surface calculations were performed using cells of the same cell sizes as the GB models, but with approximately half the numbers of atoms.



(a) View along a axis.



(b) (310) surface slab.

Figure 5.1: Structure model for (a) the Mo $\Sigma 5(310)$ tilt GB and (b) the Mo (310) surface slab. Symmetrically distinct sites in the tilt GB are numbered with increasing integers representing increasing distance from the mirror plane.

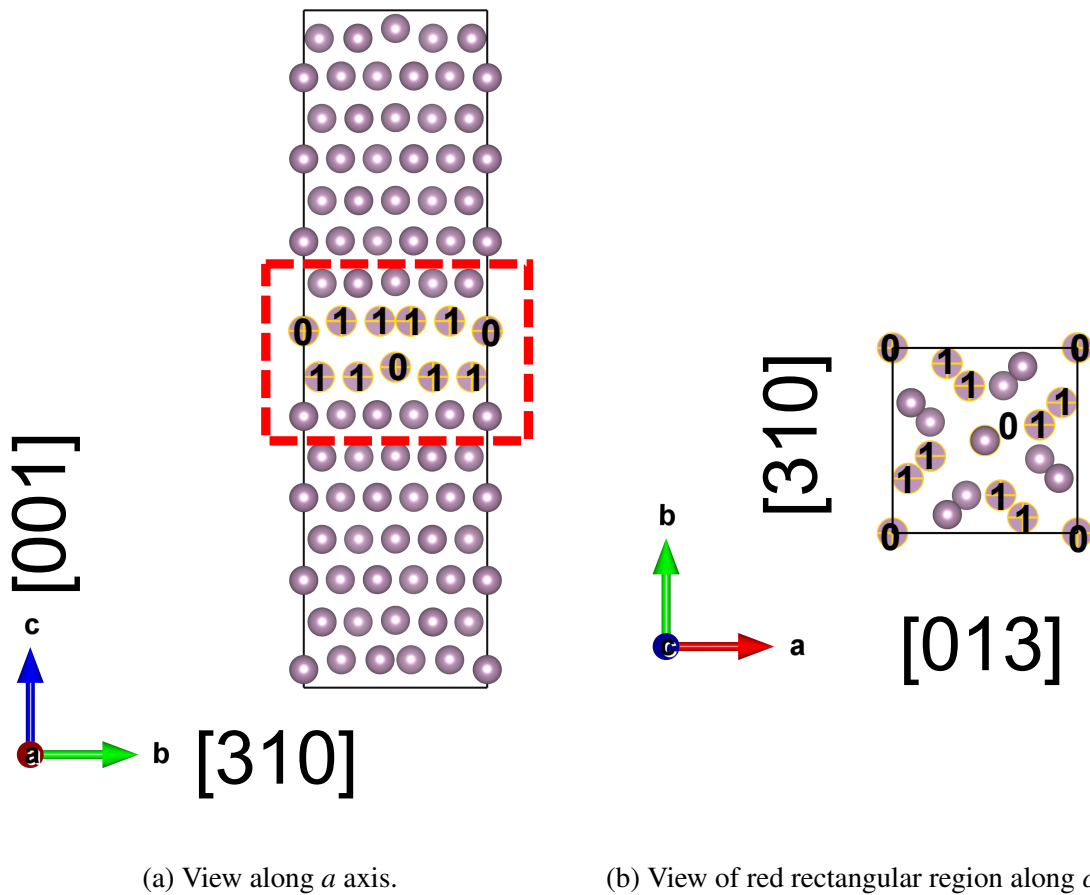


Figure 5.2: Structure model for Mo $\Sigma_5(100)$ twist GB. Coincident sites are labeled with the number 0, while non-coincident sites are labeled as 1.

5.2.2 DFT calculations

All DFT calculations^{4,136} were performed using the Vienna Ab initio Simulation Package (VASP)¹³⁷ within the projector augmented wave (PAW)¹⁴⁰ approach. The exchange-correlation effects were modeled using the Perdew-Berke-Ernzerhof (PBE) generalized gradient approximation (GGA)⁷⁸ functional, and all calculations were spin-polarized. A plane wave cutoff energy of 400 eV and a Gamma-centered k -point mesh were used for all calculations. The energies and atomic forces of all calculations were converged to within 5×10^{-4} eV and 0.02 eV Å⁻¹ respectively. The Methfessel-Paxton method¹⁴¹ was chosen as the smearing algorithm, the blocked Davidson iteration scheme¹⁴² was chosen as the electron minimization algorithm, and

ions were updated with the conjugated gradient algorithm. Γ -centered k -point meshes of $6 \times 6 \times 1$ and $7 \times 7 \times 1$ were chosen for the tilt and twist boundary structures, respectively.

5.2.3 Key parameters for segregation studies

From DFT calculations, the grain boundary (GB) and free surface (FS) energies are given by the following equation:

$$\gamma_{GB/FS} = \frac{E_{GB/FS} - E_{bulk/atom} \times n_{GB/FS}}{2 \times A_{GB/FS}} \quad (5.1)$$

where $\gamma_{GB/FS}$ is the GB/FS energy, $E_{GB/FS}$ is the energy of the supercell containing the GB or FS, and $E_{bulk/atom}$ is bulk energy per atom in the Mo bcc structure, $A_{GB/FS}$, is the cross-section area and $n_{GB/FS}$ is the number of atoms in the GB/FS supercell.

The propensity of the dopant to segregate into the GB/FS is characterized by its segregation energy $E_{seg}^{GB/FS}$, which is given by the relative difference in energy between the dopant in the GB/FS and in the bulk. The segregation energy of a dopant X can be computed using the following equation:

$$E_{seg}^{GB/FS} = (E_{GB/FS+X} - E_{GB/FS}) - (E_{bulk+X} - E_{bulk}) \quad (5.2)$$

where $E_{GB/FS/bulk+X}$ is the energy for the doped GB/FS/bulk structure and $E_{GB/FS/bulk}$ is the energy of the undoped GB/FS/bulk structure. In this work, all doped structures were obtained by substituting a single Mo atom with a dopant atom and then relaxing the atomic positions with the lattice parameters fixed at those of the fully-relaxed undoped structures. Interstitial doping was not investigated. A negative $E_{seg}^{GB/FS}$ indicates dopant segregation into the GB/FS is energetically favorable, in line with the convention used in literature^{50,241–243}.

From E_{seg}^{GB} and E_{seg}^{FS} , the strengthening energy, E_{SE} can be obtained from the following equation

$$E_{SE} = E_{seg}^{GB} - E_{seg}^{FS} = (E_{GB+X} - E_{GB}) - (E_{FS+X} - E_{FS}) \quad (5.3)$$

A positive/negative E_{SE} indicates that the grain boundary is weakened/strengthened by the dopant.

5.2.4 Empirical continuum models

In this work, we compared the DFT predictions with two empirical GB thermodynamic models: the McLean model²⁴⁵ and the Miedema model²⁴⁴. The McLean model only considers strain energy of the solute, which in this case is derived from the Friedel model²⁴⁷, as the major factor in GB segregation, and the segregation enthalpy (ΔH^{seg}) is given by the following equation:

$$\Delta H_{el}^{seg} = \frac{24\pi K_{Mo} G_X r_{Mo} r_X (r_{Mo} - r_X)^2}{3K_{Mo} r_{Mo} + 4G_X r_X} \quad (5.4)$$

where K and G are the bulk modulus and shear modulus, respectively, the subscript X denoting the dopant, and r is the atomic radius.

The Miedema model posits that the bonding energy differences between dopant and bulk atoms contribute to GB segregation enthalpy, with ΔH^{seg} given by the following equation:

$$\Delta H^{seg} = -0.71 \times \frac{1}{3} \times v \times (-\Delta H_{sol}^{Mo} c_0 \gamma_{Mo}^S V_{Mo}^{2/3} + c_0 \gamma_X^S V_X^{2/3}) + \Delta E_{el} \quad (5.5)$$

where v is the ratio of lost bonds at GB core, $c_0 \gamma^S V^{2/3}$ represents the molar surface enthalpy of pure metal (Mo or X) by the definition of Miedema, ΔH_{sol}^{Mo} is the enthalpy of solution of X in Mo and ΔE_{el} is the solute strain energy.

Because the empirical continuum models assume that changes in volume and entropy due to segregation are negligible, segregation energy E_{seg}^{GB} is approximately equals to segregation enthalpy, we will use the former term in the remainder of this article for consistency. Also, E_{seg}^{GB} calculated using the empirical models assume the reverse convention whereby a positive value indicates segregation preference towards the GB while a negative value indicates the dopant tends to stay in the bulk. To maintain consistency when comparing to the DFT values, E_{seg}^{GB} derived

from these models will be presented with the reverse sign.

5.3 Results

Given the relatively large number of dopants explored in this work, we have adopted a consistent marker shape and color scheme for all figures for ease of reference. The marker type indicates the type of dopant (circle: 3d transition metal; square: 4d transition metal; triangle: 5d transition metal; pentagon: other s/p metals), and the marker colors are assigned in order of increasing atomic number within each group of dopants, *i.e.*, for the transition metals, dopants in the same periodic group share the same color.

5.3.1 Site preference for dopants in Mo twist and tilt GBs

For both the tilt and twist GBs, there are multiple distinct sites close to the GBs that may be potentially occupied by the dopant:

1. In the tilt GB, we considered three distinct sites: the site lying on the mirror plane (Site 0) and the two sites that are nearest to the mirror plane (Sites 1 and 2), as shown in Figure 5.1a. As seen in Table 5.1, Sites 0 and 2 have larger average nearest neighbor distances and coordination numbers than Site 1. The polyhedron volume of Site 1 is the smallest among the three sites.
2. In the twist GB, we investigated two distinct sites: (i) the coincidental site (Site 0) and (ii) the non-coincidental site (Site 1), as shown in Figure 5.2. As seen in Table 5.1, Site 0 has a larger coordination number, average nearest neighbor distance, and polyhedron volume than Site 1.

Figure 5.3 plots the energy differences between GBs doped at different sites against the relative metallic radius R_X/R_{Mo} of the dopant. We find that larger dopants generally prefer larger

sites (Site 0 in the twist GB and Sites 0 and 2 in the tilt GB), and vice versa. In the tilt GB, dopants with radii smaller than Mo tend to favor the site just above the mirror plane (Site 1), while dopants with radii larger than Mo show a clear preference for the mirror plane site (Site 0), as shown in Figures 5.3a. An outlier is Pt, which shows a strong preference for the larger Sites 0 and 2 relative to the smaller Site 1 despite having a metallic radius slightly smaller than Mo. None of the dopants prefer Site 2 over Site 0. For the twist GB (Figure 5.3c), dopants with radii smaller than Mo clearly prefer the non-coincidental site (Site 1) while dopants with radii larger than Mo present little to no site preference.

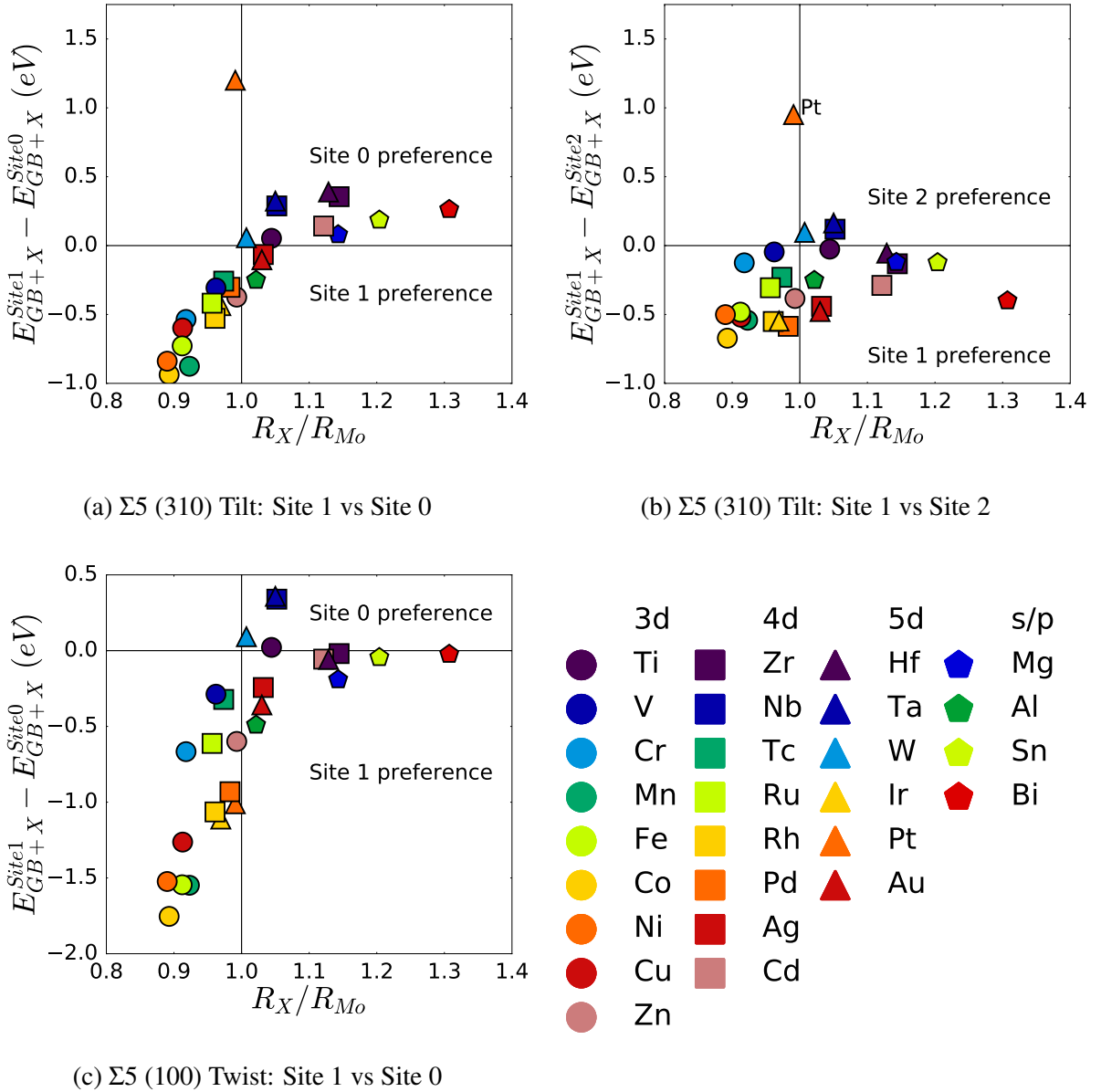


Figure 5.3: Plot of energy difference between GBs doped at different sites $E_{GB+X}^{SiteM} - E_{GB+X}^{SiteN}$ against relative radius R_X/R_{Mo} . (a) $E_{GB+X}^{Site1} - E_{GB+X}^{Site0}$ of the $\Sigma 5$ (310) tilt GB; (b) $E_{GB+X}^{Site1} - E_{GB+X}^{Site2}$ of the $\Sigma 5$ (310) tilt GB; (c) $E_{GB+X}^{Site1} - E_{GB+X}^{Site0}$ of the twist $\Sigma 5$ (100) GB.

Table 5.1: The coordination number, average bond length and polyhedron volume for each site before dopant insertion.

Site	$\Sigma 5$ (100) Twist			$\Sigma 5$ (310) Tilt		
	0	1	0	1	2	
Coordination number	8	6	7	8	8	
Average bond length (\AA)	2.835	2.667	2.840	2.717	2.747	
Polyhedron volume (\AA^3)	39.041	20.116	31.976	26.726	31.869	

5.3.2 Dopant segregation energy

Figure 5.4 plots the segregation energy for the lowest energy sites of the twist GB $E_{seg}^{X, \text{twist}}$ against that for the tilt GB $E_{seg}^{X, \text{tilt}}$. In general, we find that the segregation energies of most dopants to either type of GB are within ± 0.25 eV of each other, with the exception of the magnetic 3d transition metals, Pd and Pt. Of the 27 dopants investigated, only W, Ti and V are predicted to have a small positive $E_{seg}^{X, \text{twist}}$, and only Ti is predicted to have a small positive $E_{seg}^{X, \text{tilt}}$. All other dopants are predicted to have negative segregation energy for both types of GBs, *i.e.*, there is a thermodynamic driving force towards segregation. Given that $E_{seg}^{X, \text{twist}}$ and $E_{seg}^{X, \text{tilt}}$ are relatively similar, and the tilt GB has a lower calculated energy ($\gamma_{tilt} = 1.83 \text{ Jm}^{-2}$) than the twist GB ($\gamma_{twist} = 2.43 \text{ Jm}^{-2}$), we will henceforth present mainly the results for the $\Sigma 5(310)$ tilt GB and use E_{seg}^X to refer to $E_{seg}^{X, \text{tilt}}$ for brevity. Interested readers are referred to the Supplementary Information for the corresponding plots and results for the $\Sigma 5(100)$ twist GB.

Figure 5.5 compares the DFT segregation energy for all dopants in the $\Sigma 5(310)$ tilt GB with those predicted from the empirical McLean and Miedema models. Again, we note here that we have inverted the sign of the E_{seg}^X from the empirical models such that a negative E_{seg}^X always implies a driving force to segregate. We observe that both empirical models tend to predict E_{seg} that are less negative compared to DFT. In particular, the E_{seg}^X of the noble metals (Rh, Ir, Pt, Ru, Pd, Ag, Au), 3d transition metals (Co, Ni, Fe) and Tc predicted by both empirical models are much less negative than that predicted in DFT. On the other hand, Mg and Ti are both predicted

by the empirical models to have more negative E_{seg}^X compared to the DFT predictions.

Figure 5.6a plots E_{seg}^X against normalized difference in metallic radii $\frac{R_X - R_{Mo}}{R_{Mo}}$ for all dopants. We may observe that there is a somewhat parabolic-like relationship between E_{seg}^{tilt} and relative metallic radii, which indicates that the strain energy is likely a significant contributing factor to segregation. However, the noble metals and 3d transition metals are again outliers, predicted by DFT to have relatively large E_{seg}^X , despite having relatively small metallic radii mismatch with Mo.

Figure 5.6b plots E_{seg}^X against the square of the Pauling electronegativity difference $(\chi_X - \chi_{Mo})^2$ between each dopant and Mo, which is proportional to the difference in the dissociation energy of the dopant X and the average dissociation energy of X and Mo²⁴⁸. We find that there is a reasonably strong monotonic relationship between E_{seg}^X and $(\chi_X - \chi_{Mo})^2$, with increasing electronegativity difference generally leading to less negative E_{seg}^X .

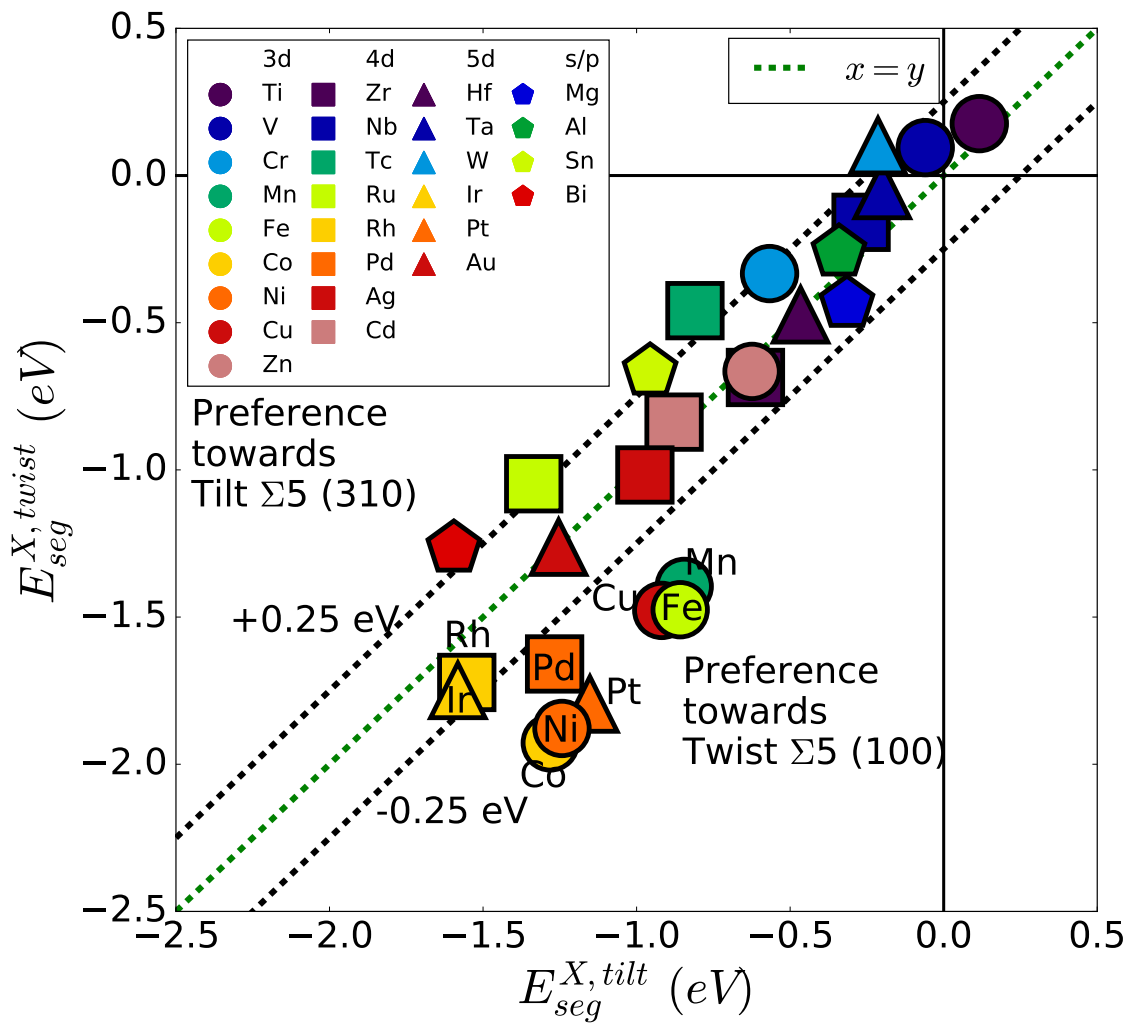


Figure 5.4: Comparison between the lowest E_{seg}^X of the tilt and twist GBs of Mo.

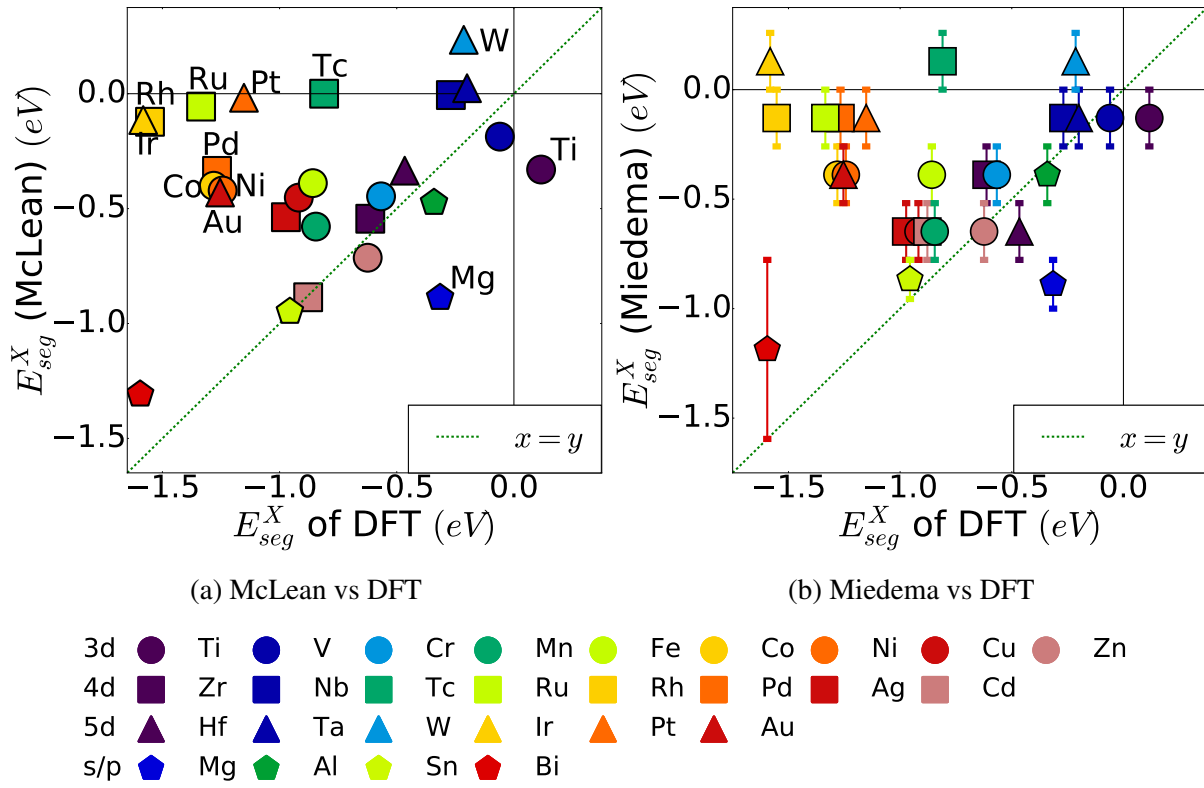


Figure 5.5: Comparison of the E_{seg}^X calculated using (a) the McLean model and (b) the Miedema model with the lowest DFT predicted values for the $\Sigma 5(310)$ tilt GB. For the Miedema model, E_{seg}^X is given as a range, and E_{seg}^X for Bi, Mg and Sn have no minimum value stated in the literature⁵⁵.

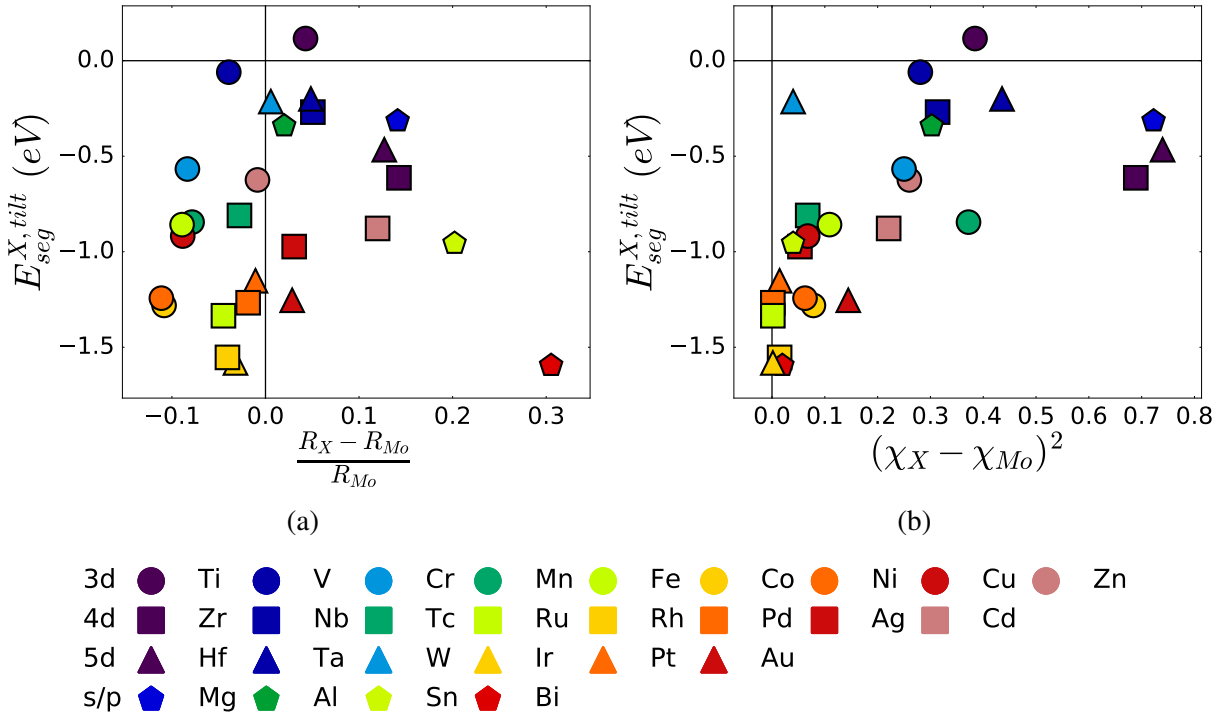


Figure 5.6: Plot of the lowest tilt segregation energy E_{seg}^X against (a) the relative metallic radius difference $\frac{R_X - R_{Mo}}{R_{Mo}}$ for each dopant X , and (b) the square of the relative Pauling electronegativity $(\chi_X - \chi_{Mo})^2$ for each dopant X .

5.3.3 Strengthening energy

In Figure 5.7, the strengthening energy E_{SE}^X is plotted against the segregation energy E_{seg}^X for the 27 dopants in the $\Sigma 5$ (310) tilt GB. The dopants can be classified into three zones of interest: dopants that have positive E_{seg}^X (white region) would prefer to stay in the bulk, and hence would have no effect on GB strength. For dopants that segregate, those with negative E_{SE}^X (blue region) tend to strengthen the GB while those with positive E_{SE}^X tend to embrittle it.

For Figure 5.7a, E_{SE}^X and E_{seg}^X were determined based on the lowest energy dopant site in the GB and FS (henceforth, referred to as the “l-to-l” approach), while for Figure 5.7b, they were determined based on Site 0 in both the GB and FS, *i.e.*, the mirror plane site in the GB and surface site in the FS (henceforth, referred to as the “m-to-s” approach). We find that the site preference has a significant influence on the DFT predictions. Using the l-to-l approach,

the DFT calculations predict that Pd, Cu, Ta, Cr, Tc, W, Fe, Ni, Ru, Rh, Co, Mn and Ir would strengthen the Mo tilt GB. Using the m-to-s approach, only Ta and Hf are predicted to have a weak strengthening effect, and all other dopants are predicted to embrittle or have no effect on the GB. Among the dopants that embrittle Mo, Bi has by far the greatest tendency to segregate and the most positive E_{SE}^X .

Instead of the traditional one-factor bond-breaking model that relates E_{SE}^X with relative cohesive energy ΔE_{coh}^X ^{55,58}, we investigated the following two-factor linear model:

$$E_{SE}^X = k_{coh}\Delta E_{coh}^X + k_R \frac{R_X - R_{Mo}}{R_{Mo}} \quad (5.6)$$

where $\frac{R_X - R_{Mo}}{R_{Mo}}$ is the relative metallic radii (a measure of strain), ΔE_{coh}^X is the relative difference in cohesive energy, and k_{coh} and k_R are constant coefficients fitted using least squares regression.

We find that this two-factor model is able to account for most of the variation in the E_{SE}^X ($R^2 > 0.8$, see Figure 5.8), though the two coefficients differ significantly depending on whether the l-to-l or m-to-s approach is used in determining E_{SE}^X . For the l-to-l approach (Figure 5.8a), the relative radii accounted for a much larger proportion of the E_{SE}^X ($k_R = 7.37 \pm 0.578$), and the contribution of ΔE_{coh}^X , k_{coh} , is much smaller than the 1/3 expected from the Seah bond-breaking model. For the m-to-s approach (Figure 5.8b), $k_{coh} = 0.39 \pm 0.042$, which is close to the 1/3 value expected from the traditional bond-breaking model of Seah⁵⁸, though the relative radii still accounts for a significant proportion of the variation in E_{SE}^X .

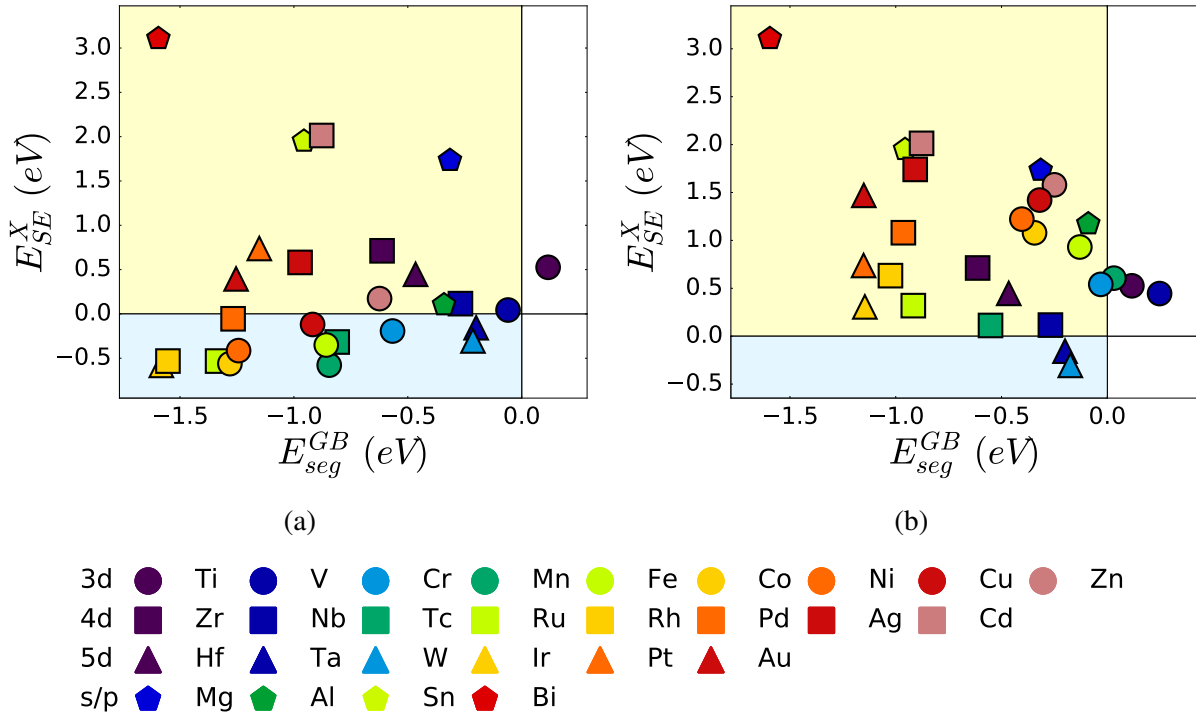


Figure 5.7: Plots of the strengthening energy E_{SE}^X versus segregation energy E_{seg}^X for the 27 dopants in the $\Sigma 5$ (310) tilt GB. (a) based on lowest energy dopant site in GB and free surface (l-to-l approach); (b) based on Site 0 (m-to-s approach). Dopants in the white region (positive E_{seg}^X) prefer to stay in the bulk. For dopants that segregate, those with negative E_{seg}^X (blue region) tend to strengthen the GB.

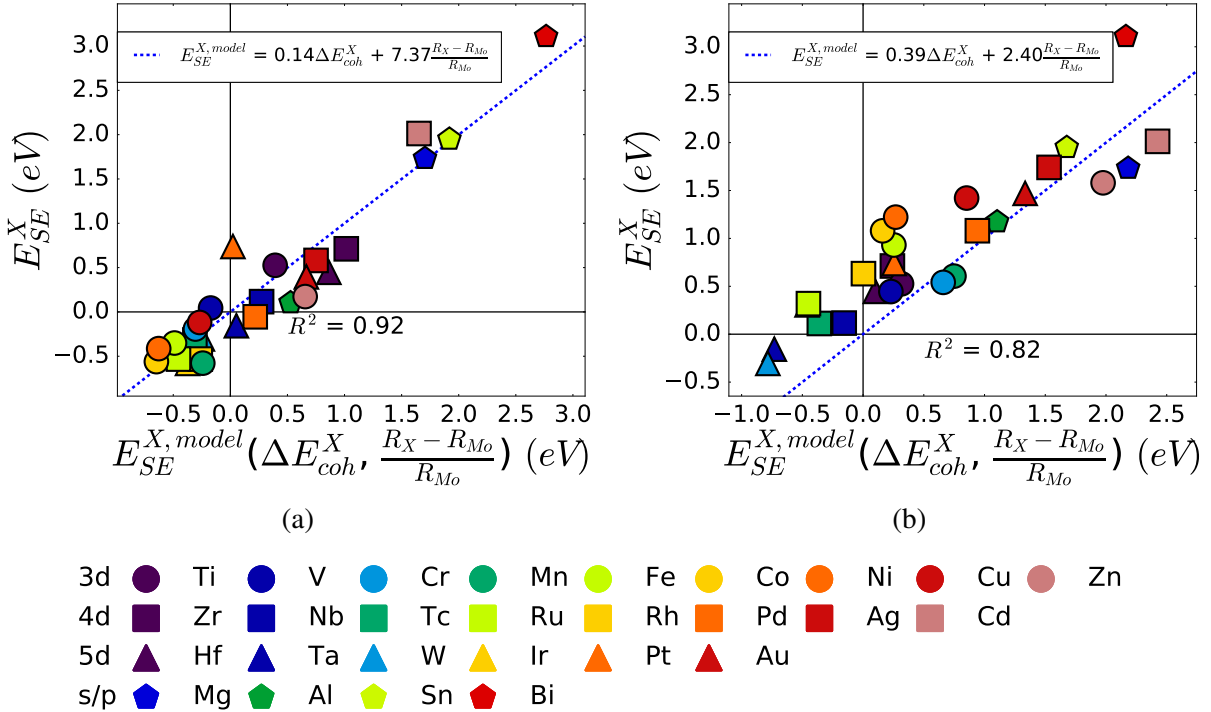


Figure 5.8: Plot of the observed strengthening energy E_{SE}^X for the site with the lowest E_{seg}^{GB} versus the two factor linear model for $E_{SE}^{X, \text{model}}(E_{coh}^X, \frac{R_X - R_{Mo}}{R_{Mo}})$ for the 27 dopants in the $\Sigma 5$ (310) tilt GB. (a) Fitting performed based on the l-to-l approach. $k_{coh} = 0.14 \pm 0.023$, $k_R = 7.37 \pm 0.578$. (b) Fitting performed based on the m-to-s approach. $k_{coh} = 0.39 \pm 0.042$, $k_R = 2.40 \pm 1.076$. In all fittings, the p -value for all coefficients are < 0.05 .

5.4 Discussion

The segregation and strengthening/embrittling effects of dopants on Mo GB are of fundamental importance in a wide variety of applications. In this work, we performed a comprehensive DFT investigation of these effects for 27 dopants in the symmetric $\Sigma 5(310)$ tilt and $\Sigma 5(100)$ twist GBs of Mo.

We find that the type of GB generally has a small effect on the DFT-predicted dopant segregation energy. This is likely because both the twist and tilt GBs studied in this work are $\Sigma 5$ GBs with GB sites of relatively similar sizes (see Table 5.1). For the twist GB, most dopants prefer to segregate to the non-coincidental sites, which is in good agreement with the experimental work

of Pénisson and Vystavel²⁴⁹, which showed that Ni in Mo GBs prefer to segregate into random and high Σ Mo GBs where there are more non-coincident sites for dopants to segregate into. We recognize that the behavior of general (random or high Σ) GBs can be somewhat different; yet the relative trends of segregation for 27 dopants at two special $\Sigma 5$ (twist and tilt) GBs can still represent some useful trends in relative segregation behaviors of different alloy elements.

Historically, dopant segregation is attributed to the effect of strain and/or bond breaking arguments based on simple lattice models, which forms the basis for the McLean²⁴⁵ and Miedema models²⁴⁴. We find significant disagreements between the more rigorous DFT segregation energies and those predicted by these empirical models for certain chemical classes, most notably the noble metals and the $3d$ transition metals. The dopants for which there is the most significant disagreement are those that tend to form intermetallic compounds with Mo. For example, Co, Pt, Ni, Ir, Pt, Tc, Zr, Hf, and Fe form at least one intermetallic compound with Mo²⁵⁰, and the empirical models significantly underestimate the magnitude of the segregation energy for these dopants. Elements for which the empirical models are in good agreement with the DFT results, such as W, Nb, Cr, Cd, Ta, V, generally do not form intermetallic compounds with Mo. Precipitation of the GB due to compound formation is a chemical effect not accounted for in the empirical models. Moreover, it has been demonstrated generally for many metallic and ceramic materials (see several reviews by Cantwell et al.²⁴⁰, Kaplan et al.²⁵¹, Harmer²⁵², Luo²⁵³ and references therein) and specifically for several binary^{233,254} and ternary Mo based alloys^{68,255} as well as W-based alloys^{256,257} that GBs can undergo 2-D phase-like structural transitions, which are more likely to form in systems with strong, negative mixing enthalpies. These systems also tend to form intermetallic compounds and have less agreement with the current DFT computations which do not consider interfacial structural transitions.

Similarly Seah⁵⁸, argued that the strengthening effect of dopants on GBs can be modeled with a simple bond-breaking argument, and is related to the difference in cohesive energies. More recently Gibson and Schuh⁵⁵, performed a survey of first principles calculations to show

that segregation-induced grain boundary embrittlement is generally predicted by bond-breaking arguments. While the general trends observed in this work support these previous findings, we find that dopant site preference also has a significant impact on the relative influence of relative radii $\frac{R_X - R_{Mo}}{R_{Mo}}$ and relative cohesive energies ΔE_{coh}^X on the E_{SE}^X . In general, the relative radius drives site preference, more so in the GB than in the free surface. As a result, a model that assumes cleavage of the lowest energy tilt GB configuration to form the lowest energy free surface configuration (Figure 5.8a) finds a weak dependence of E_{SE}^X on ΔE_{coh}^X , and a stronger dependence on $\frac{R_X - R_{Mo}}{R_{Mo}}$. On the other hand, a model that assumes cleavage of a tilt GB with the dopant at the mirror plane site to form a free surface with the dopant on the corresponding surface site shows a much stronger dependence of E_{SE}^X on ΔE_{coh}^X , which is in line with the bond-breaking model⁵⁸. In essence, the bond-breaking argument applies when the dopant site environment remains consistent between the GB and free surface, *i.e.*, at the mirror plane in the tilt GB or either of the investigated sites in the twist GB. We also recognize that the bond-breaking arguments may work (even) better with general (random/non-lattice-matching or high Σ) GBs where bonds are less satisfied.

There are some disagreements between the predicted E_{SE}^X using the l-to-l approach and previous experimental data. For instance, the predicted E_{SE}^X suggests that Ni is a good candidate dopant for strengthening Mo GBs, but experimentally, it is well-known that Ni tends to embrittle Mo GBs. More recent experimental and phenomenological thermodynamic modeling studies find that the mechanism leading to the embrittlement of Mo GBs due to Ni doping is likely due to the formation of premelting-like (disorderd) complexions (*i.e.* 2-D interfacial phases)^{233,254}. While Hwang and Huang^{234,258,259} earlier proposed the formation of δ -NiMo intermetallic compounds at the Mo GB as the cause of embrittlement, more recent work by one of the co-authors of the present work has shown that δ -NiMo intermetallic compounds does not wet the general GBs of Mo, as the dihedral angles are $> 100^\circ$; yet, a nanoscale disordered, Ni-enriched interfacial complexion was observed in well-quenched specimens²³³. Thus, it is possible that those δ -

NiMo intermetallic compounds formed via recrystallization of disordered complexions which were formed at high temperatures. This can also be a contributing factor to the embrittlement of slowly-cooled Mo-Ni specimens, making Hwang and Huang's observations relevant to the embrittlement mechanism. These studies can adequately explain the discrepancy between the DFT predictions and the experimental data, since the current DFT calculations do not consider interfacial disordering or structural transitions.

We also note that the alternative m-to-s model predicts that Ni embrittles the Mo GB which is consistent with experimental observations. For a rapid fracture process where atoms do not have the time to equilibrate to the preferred low energy sites, the m-to-s model may be more appropriate. Moreover, the DFT predictions (whether l-to-l or m-to-s) are premised on a simple cleavage model where a GB separates to form two free surfaces. Such a model would not be appropriate for a mechanism of embrittlement via intermetallic compound formation. Finally, previous experimental work suggests that Ni tends to segregate at random and high Σ Mo GBs. The GBs investigated in this work are low Σ , which may present different dopant site energetics. It is also known that general or high Σ GBs are more prone to disorder at high temperatures²⁵³.

Based on the m-to-s model for the tilt GB, only Ta and W are predicted to have a weak strengthening effect on Mo. For the $\Sigma 5(100)$ twist GB, Mn, Fe, Co and Nb are predicted to have reasonable strengthening effects (see Figure C.4 in the SI).

5.4.1 Conclusions

In conclusion, we have studied the segregation and strengthening effects of 27 metallic dopants on the $\Sigma 5(100)$ twist and $\Sigma 5(310)$ tilt GB in Mo using DFT calculations. In comparison with the empirical McLean and Miedema models, DFT predicts significantly larger in magnitude segregation energies for the noble and 3d transition metals, especially those that are known to form intermetallic compounds with Mo. In terms of the strengthening energy, we find that dopant site preference and strain effects have a significant influence, in addition to the difference in

cohesive energy based on traditional bond-breaking considerations. Assuming a fast cleavage model for fracture, only Ta and W are predicted to have a weak strengthening effect on Mo for the $\Sigma 5(310)$ tilt GB, and Mn, Fe, Co and Nb are predicted to have reasonable strengthening effects for the $\Sigma 5(100)$ twist GB.

Chapter 5 is, in full, a reprint of the material “Computational study of metallic dopant segregation and embrittlement at Molybdenum grain boundaries” as it appears in Acta Materialia, Richard Tran, Zihan Xu, Naixie Zhou, Balachandran Radhakrishnan, Jian Luo and Shyue Ping Ong, 2016, 117 (July), pp 91-99. The dissertation author was the primary investigator and author of this paper. Most calculations and data analysis were performed by the author.

Chapter 6

Metal insulator transition under intrinsic defects in V₂O₃

6.1 Introduction

Neuromorphic computers, which aim to mimic the computational functionality found in biological brains, have the potential to be far more efficient than traditional von Neumann architectures in a variety of tasks, including data processing and cognition. One potential implementation of a neuromorphic computer can be achieved using a sequence of neuristors that can process electric signals in response to time dependent excitations. This signal must exceed a threshold and maintain its excited state for a period of time in a behavior referred to as “leaky, integrate, and fire” to emulate the short term memory needed to sum inputs.

Quantum materials that undergo metal insulator transition (MIT) are ideal for such devices as they exhibit a sudden collapse of insulating behavior under an external stimuli and can gradually recover its insulating state over time in the absence of the stimuli. This behavior is known as volatile resistive switching. Vanadium oxides such as V_2O_3 and VO_2 are known to exhibit this functionality²⁶⁰ and are considered model materials for studying such properties due to their chemical simplicity. Below a critical temperature (T_c) of 165 K, V_2O_3 is an anti-ferromagnetic insulator (AFI) with monoclinic space group I_2/a and a band gap (E_g) of 0.6 eV²⁶¹. Above T_c , it is a paramagnetic metal (PM) adopting the corundum structure with trigonal space group $R\bar{3}c$.

Varying the temperature of a material to achieve MIT can consume a lot of energy when scaled to an actual computing device. From an engineering standpoint, it is desirable to reduce this energy consumption as much as possible, either by decreasing the energy barrier (temperature) required to trigger the MIT or by avoiding temperature-induced MIT altogether. Previous experiments^{262,263} and density functional theory (DFT) calculations⁹¹ have shown that V_2O_3 may be more suitable for such applications than VO_2 due to its lower energy barrier for MIT, resulting in faster switching speed. Further, introducing defects is a pathway to modulate the MIT behavior of V_2O_3 .

While many defect studies in V_2O_3 have been focused on transition metal doping, most

notably for Cr and Ti doping^{71,72,91}, intrinsic defects have garnered less attention. One such study was done by Ramirez et al.⁹³ who demonstrated that while the resistance change is more or less stable, the transition temperature does go down substantially with the dose of defect-induced ion bombardment. However, they observed a sudden and complete breakdown in MIT and structural phase transition (SPT) at a concentration of 2×10^{14} ions. Wickramaratne et al.⁹² used DFT to study Frenkel defects in V₂O₃ to explain the origins of these effects. He demonstrated that the V-Frenkel defect reduced the spin-flip energy by a factor of 3, thus reducing the energy barrier for the Slater AFI to PM transition. Ueda et al.⁷⁴ explored the effect of non-stoichiometry in V₂O_{3+x} and compared it to Ti-doped V₂O₃ and pressurized V₂O₃. They showed that non-stoichiometry reduces the transition temperature of the AFI phase as x increases up to 0.03, beyond which the AFI phase breaks down to an anti-ferromagnetic metallic phase. Similarly, Bao et al.²⁶⁴ used neutron diffraction to find this phase for V_{2-y}O₃ with a Neel temperature (T_N) of 9 K. More recently it has been experimentally shown that V₂O₃ exhibits non-thermal switching when defects are introduced⁶⁹. This is achieved via the Poole-Frenkel effect whereby trapped carriers occupying in-gap states can hop into the conduction band whose energy barrier has been reduced by an external potential.

DFT methods have been used to study the MIT in vanadium oxides. Due to their Mott insulating nature,^{68,265,266}, a Hubbard U correction, typically fitted to reproduce the experimental band gaps, needs to be applied for semi-local functionals such as the Perdew-Berke-Ernzerhof (PBE) generalized gradient approximation (GGA)⁷⁸ to account for the repulsion arising from electron correlation. Alternatively, hybrid functionals that include a fraction of exact exchange have also been found to successfully predict an insulating state for low temperature (LT) V₂O₃ and VO₂^{267,268}. However, the Heyd-Scuseria-Ernzerhof (HSE) functional in particular has also been shown to incorrectly predict an insulating high temperature (HT) and magnetically ordered LT phase for VO₂²⁶⁹. Stahl and Bredow²⁷⁰ had recent success using the meta-GGA strongly constrained and appropriately normed (SCAN) functional to simultaneously predict four key

properties - a band gap in the LT non-magnetic phase, a metallic state for the HT phase, and the correct energy difference between the HT and LT phases in VO₂.

In this work, we perform a comprehensive evaluation of different DFT functionals - PBE and SCAN, with and without Hubbard U, as well as HSE - in reproducing the key energetic and electronic structure properties of LT and HT V₂O₃. This will be followed by an in-depth investigation of defects in the LT and HT phases of V₂O₃ and how they introduce carrier traps and influence the band gap of the LT phase which can yield potential insights into the origins of non-thermal MIT in V₂O₃.

6.2 Methods

6.2.1 DFT calculations

All DFT^{4,136} calculations were performed using the Vienna Ab initio Simulation Package (VASP)¹³⁷ within the projector augmented wave (PAW)¹⁴⁰ approach. The plane wave cutoff energy was 400 eV²⁶⁷, and the energies and atomic forces were converged to within 10⁻⁴ eV and 0.02 eVÅ⁻¹, respectively. Gaussian and Methfessel-Paxton¹⁴¹ smearing were used for the insulating LT and metallic HT phases, respectively. Γ-centered k-point densities per unit reciprocal length of 30 Å⁻¹ and 85 Å⁻¹ were used for the relaxation of supercells and for density of states (DoS) calculations, respectively. The exchange-correlation functionals tested in this work are PBE, PBE+U, SCAN, SCAN+U and HSE. The *U* parameter was set at 2.68 eV and 1.35 eV for PBE+U and SCAN+U, respectively, which were found to reproduce the experimental band gap of LT V₂O₃, i.e., 0.6 eV (see Figure D.1a)^{73,261,271}.

All analysis and input generation was performed with the Python Materials Genomics (pymatgen) library¹³⁵.

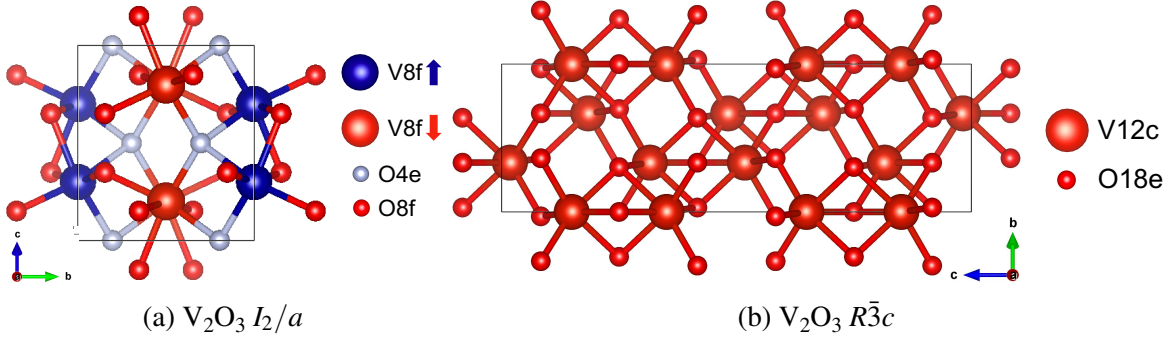


Figure 6.1: Conventional unit cells of (a) the LT monoclinic (large red/blue spheres correspond to opposite spins) (b) and HT corundum phases of V_2O_3 . The Wyckoff symbols and spin directions of each symmetrically distinct site is given on the right of each structure.

6.2.2 Initial structures and magnetic configurations

As with previous experimental and computational works^{272,273}, we found that the most stable anti-ferromagnetic configuration of LT V₂O₃ has V atoms ferromagnetically aligned on the (010) planes with each consecutive plane being oppositely aligned along the [010] direction as shown in Figure 6.1a.

The HT phase is known to be paramagnetic. In this work, we investigated both ferromagnetic and non-magnetic initializations as it was found that an anti-ferromagnetic initialization causes the HT corundum phase to automatically relax to the LT monoclinic phase.

6.2.3 Intrinsic defects

In this work, we focus on vacancies and interstitials. Using the Kröger-Vink notation, vacancies and interstitials are indicated by v_A and A_i respectively where A is the species of the defect. Note that a lower case v is used to denote vacancies to distinguish from the symbol for vanadium. Negative and positive charges are indicated by \bullet and $/$ superscripts respectively. V and O interstitial sites were found using the Interstitialcy Finding Tool (InFiT)²⁷⁴. The algorithm found four symmetrically distinct interstitial sites in the LT phase and one symmetrically distinct site in the HT phase.

We investigated both charged and neutral defects using the method described by Broberg et al.²⁷⁵. A nominal oxidation state of -2 was assumed for the oxygen anion, and charges ranging from 0 to -2 (0 to +2) for O_i (v_O) were introduced by adding (subtracting) an integer number of electrons. The same method, *mutatis mutandis*, was applied for charged defects involving V_i and v_V assuming an oxidation state of +3 for the vanadium cation. Charged defects were investigated only for the insulating LT phase.

All defect calculations were performed using $2 \times 2 \times 2$ (160 atoms) and $2 \times 2 \times 1$ (120 atoms) supercells of the conventional unit cells for the LT and HT phases, respectively.

6.2.4 Thermodynamic analysis

The defect formation energy is calculated with the following equation:

$$E_{form}[X^q] = E_{tot}[X^q] - E_{tot}[\text{bulk}] - \sum n_i(E_i + \Delta\mu_i(T, P_0)) + q\epsilon_F + E_{corr}^q \quad (6.1)$$

where $E_{tot}[X^q]$ and $E_{tot}[\text{bulk}]$ are the total DFT energies of the supercell with and without the defect X respectively. n_i is the number of species i added ($n_i > 0$) or removed ($n_i < 0$) from the supercell. $\Delta\mu_i(T, P)$ is the chemical potential for species i relative to the energy per atom of species i . The chemical potentials of Equation 6.1 can be rewritten in terms of $\Delta\mu_O$ only by substituting μ_V for Equation S1. As such all calculations of E_{form} will be done with respect to $\Delta\mu_O$ as a function of temperature T and partial pressure P_0 . It should be noted that an anion correction ($E_{corr}^O = -0.702$ eV) is applied to $\Delta\mu_O$ to compensate for the overbinding of O_2 under PBE and PBE+U¹³⁴. As such, the relative chemical potential of oxygen is in reference to the DFT calculated energy of O_2 per atom and the correction:

$$\Delta\mu_O(T, P_0) = \mu_O - \frac{1}{2}E_{O_2} - E_{corr}^O \quad (6.2)$$

with the allowed range of $\Delta\mu_O(T, P_0)$) being

$$-4.35eV = \Delta G_{V_2O_3} < \Delta\mu_O(T, P_0) < 0 eV \quad (6.3)$$

where $\Delta G_{V_2O_3}$ is the formation energy of V_2O_3 (see Appendix D.1.1 for more details in regards to the chemical potential).

For charged defects, the fourth term, $q\varepsilon_F$, compensates for the charge where ε_F is the Fermi level and ranges between the valence band maximum (VBM) and conductance band minimum (CBM) in the DoS (see Figure 6.4(a)). E_{corr}^q is the Freysoldt correction term for charged defects in a supercell²⁷⁶. A more detailed discussion of these quantities is given in Appendix D.1.

From E_{form} , the thermodynamic transition level between charged states q_1 and q_2 , which determines the Fermi level of carrier traps, is given as follows:

$$\varepsilon_F(q_1, q_2) = \frac{E_{form}[X^{q_1}] - E_{form}[X^{q_2}]}{q_2 - q_1} \quad (6.4)$$

The MIT temperature T_c in the presence of a defect can be calculated with the following equation²⁷⁷:

$$T_c = T_{c,0} \frac{\Delta H}{\Delta H_0} \quad (6.5)$$

where $T_{c,0} = 165$ K is the experimental MIT temperature of stoichiometric V_2O_3 , and ΔH_0 and ΔH are the changes in enthalpy during LT and HT phase transition for stoichiometric and non-stoichiometric V_2O_3 , respectively. Here, the enthalpy (H) is approximated using the total relaxed DFT energy on the assumption that the pV and TS terms are negligible.

6.3 Results

6.3.1 Functional assessment of bulk properties

Figure 6.2 summarizes the ability of five functionals - PBE, PBE+ U , SCAN, SCAN+ U and HSE - to reproduce the correct band gap (6.2a) and relative energetics (6.2b) of LT and HT V₂O₃. All functionals predict the HT phase to be metallic ($E_g^{HT} = 0$ eV). However, the PBE functional incorrectly predicts the LT phase to be metallic, while the SCAN and HSE functionals lead to severe underestimation and overestimation of the band gap E_g^{LT} , respectively. For the PBE+ U and SCAN+ U functionals, the Hubbard U parameter were calibrated to reproduce the experimental band gap of LT V₂O₃, i.e., 0.6 eV exactly (see Figure D.1a).

All functionals predict the LT phase to have an anti-ferromagnetic ground state (see Table D.1). While all functionals also predict the AFI LT phase to be more stable than the ferromagnetic metallic (FM) HT phase, there are substantial differences in the energy difference of up to 100 meV/f.u. between the HT and LT phase ($\Delta E_{V_2O_3}^{HT-LT}$). It is known experimentally that the energy difference between HT and LT VO₂, $\Delta E_{VO_2}^{HT-LT}$ is approximately 44 meV/f.u.²⁷⁸. Since $T_c^{VO_2} > T_c^{V_2O_3}$ ($T_c^{VO_2} = 340K$), $\Delta E_{V_2O_3}^{HT-LT} < \Delta E_{VO_2}^{HT-LT} \sim 44$ meV/f.u. The PBE, PBE+ U and HSE functionals produce values of $\Delta E_{V_2O_3}^{HT-LT}$ that satisfy this additional constraint as shown in the blue shaded region. The SCAN and SCAN+ U functionals overestimates $\Delta E_{V_2O_3}^{HT-LT}$ by a significant margin.

We also investigated the accuracy of each functional in reproducing the experimental lattice parameters of the LT and HT phases^{83,279}, as shown in Table D.2. For the monoclinic LT phase, the calculated lattice lengths are within 0.07Å of the experimental values for the PBE+ U , SCAN, SCAN+ U and HSE functionals. The PBE functional, however, leads to errors of $> 0.1\text{\AA}$ for the a and b lattice parameters and 2° for β . For the HT phase in the hexagonal setting, the PBE+ U functional has the largest deviation from the experimental lattice parameters with an

overestimation of 0.17\AA and 0.1\AA for a and c respectively. In both phases, the SCAN functional yielded lattice parameters that are closest to the experimental values with errors of $< 0.03\text{\AA}$ for the lattice lengths. The space group of both phases are preserved in all cases after structural relaxation.

Based on the above results, we have elected to use the PBE+ U functional with $U_{eff} = 2.68$ eV to study the MIT in stoichiometric and non-stoichiometric V_2O_3 . This functional choice yields values of ΔE^{HT-LT} and E_g^{LT} consistent with experimental observations, albeit at the expense of somewhat larger errors in the lattice parameters. The subsequent results in this work are based on this functional choice.

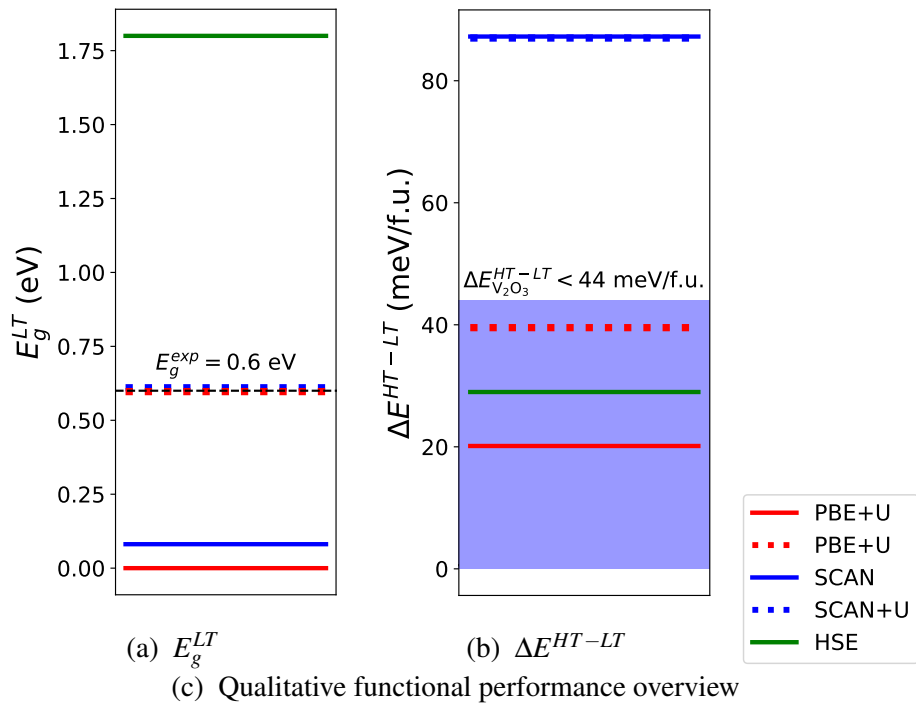


Figure 6.2: Plots of the (a) band gap of the LT AFI phase of V_2O_3 and (b) energy difference per formula unit relative to the HT FM phase for the PBE, PBE+U, SCAN, SCAN+U and HSE functionals. The U parameters of 2.68 eV and 1.35 eV for PBE+U and SCAN+U, respectively, were calibrated to reproduce the experimental band gap of LT V_2O_3 . The dashed black line indicates the experimental band gap and the blue shaded region indicates the expected energy difference for V_2O_3 . (c) Overview of the ability of the five functionals in reproducing the four key qualitative properties of V_2O_3 : (1) LT phase is more stable than the HT phase ($E^{LT} < E^{HT}$); (2) LT phase is insulating (i.e. $E_g^{LT} > 0$ eV); (3) HT phase is metallic (i.e. $E_g^{HT} = 0$ eV); (4) LT phase is anti-ferromagnetic (AFM). * indicates a caveat in fulfilling a criteria.

6.3.2 Charged defects in LT AFI V_2O_3

The calculated defect phase diagram in LT AFI V_2O_3 as a function of oxygen chemical potential $\Delta\mu_O$ (temperature) and Fermi energy ϵ_F is given in Figure 6.3. Under less reducing

conditions, vanadium vacancies v_V are the most stable defects (red regions). At the most oxidizing conditions of $\Delta\mu_O > -2.1$ eV ($T < 1754$ K at standard atmospheric conditions), vanadium-deficient V_2O_3 is predicted to be stable relative to stoichiometric V_2O_3 ($E_{form} < 0$ eV). As conditions become more reducing (blue regions), oxygen vacancies v_O on the $4e$ site become the most stable defects. Previous annealing experiments performed under ultrahigh-vacuum by Simic-Milosevic et al.⁷³ found the formation of v_O in bulk V_2O_3 between 600 K and 700 K. While our computed temperatures for the formation of v_O are far above these temperatures, it should be noted that these temperatures are only estimates that neglect any entropic contributions from solid phases. Nevertheless, our results are in qualitative agreement with experiments where v_O is predicted to form well above above T_c . Finally, under the most reducing conditions (cyan regions), vanadium interstitials V_i are the most stable. Given the lack of any previous experimental evidence of vanadium interstitial formation, the remainder of this work will be primarily focused on vacancy defects.

The transition between different defect charge states can be determined using Equation 6.4. For example, the neutral vanadium vacancy v_V is predicted to be stable at ϵ_F of 5.44 eV, but the negatively charged v_V^\cdot is predicted to be stable above 5.44 eV. Similarly, the oxygen vacancy transitions from v'_O to v_O at $\epsilon_F \approx \frac{VBM+CBM}{2}$.

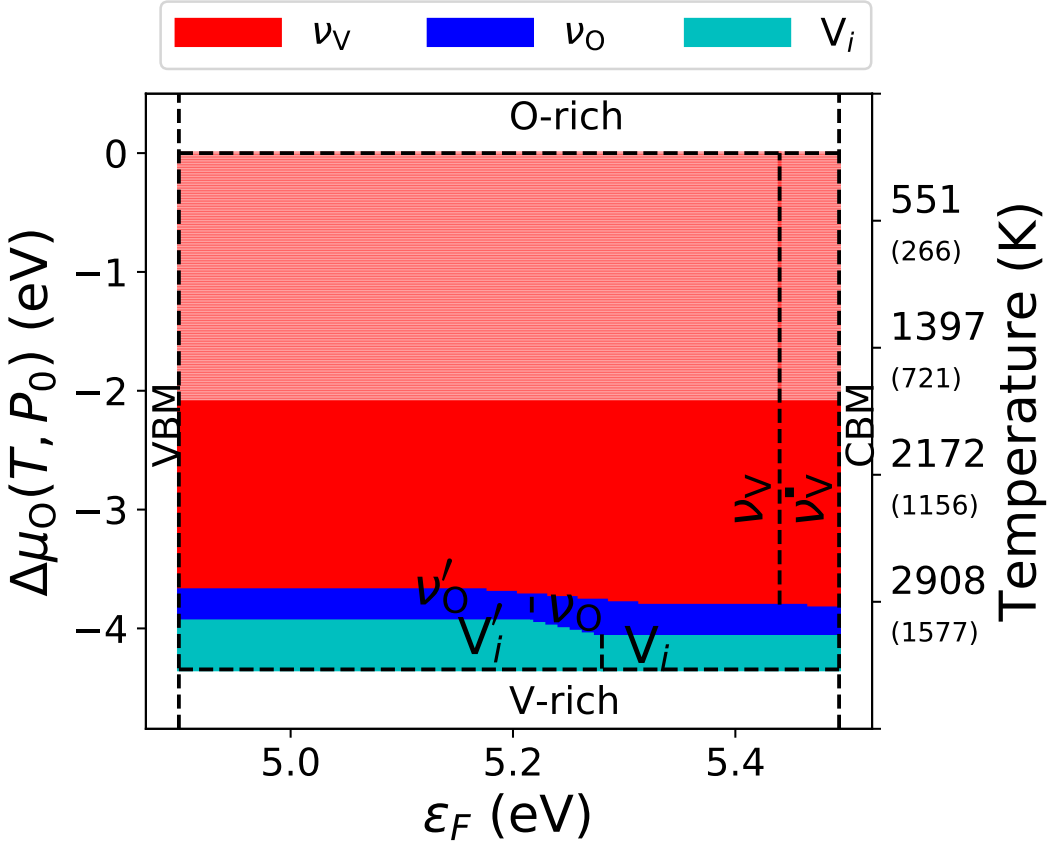


Figure 6.3: Stability map for charged and neutral defects in LT V_2O_3 as a function of ϵ_F and $\Delta\mu_O$. The legend at the top indicates the colors representing defect types. The lighter red region indicates where the formation of vanadium-deficient V_2O_3 is favorable relative to stoichiometric V_2O_3 , i.e., $E_{form} < 0$ eV, while the solid red region $E_{form} > 0$ eV. Vertical dashed lines indicate a transition between charged states in a defect. Two corresponding temperature scales derived from the JANAF thermochemical tables²⁸⁰ are provided as the secondary y axis on the right (see Equation D.6). The temperature scales are based on two partial pressures of oxygen: $p_0 = 0.1$ MPa, i.e., standard atmospheric conditions, and $p_0 = 10^{-13}$ MPa, i.e., ultra-high-vacuum conditions (parentheses).

Figure 6.4 shows the DoS of LT AFI V_2O_3 with vacancies with the stoichiometric DoS as a reference (Figure 6.4(a)) along with the charge transition levels of v_V and v_O . All vacancy defects lead to a decrease in the band gap relative to stoichiometric V_2O_3 . The v_V defect lowers the CBM and VBM by 0.23 eV and 0.11 eV, respectively, leading to a decrease in E_g from 0.59 to 0.53 eV as shown in Figure 6.4(b). In Figure 6.4(c), v_V^\bullet introduces additional spin polarized

states that slightly raises the VBM level while lowering CBM by 0.12 eV, leading to a significant reduction in E_g to 0.45 eV. As ϵ_F increases, the charge carrier is trapped at a localized in-gap state as it transitions from v_V to v_V^\bullet . The activation energy for the conductivity of the trapped carrier (E_a) is about 73 meV relative to the CBM of stoichiometric V_2O_3 . The transition state exists above the lowered CBM of vanadium vacancies allowing the trapped carrier to immediately conduct.

In Figure 6.4(d), the CBM and VBM remain relatively unchanged when v'_O is introduced, leaving E_g for the most part unchanged (0.56 eV). The most significant decrease in E_g comes from the introduction of v_O as shown in Figure 6.4(e) where additional spin polarized states raises the VBM level by 0.37 eV to significantly reduces E_g to 0.22 eV. The transition of the oxygen vacancy from v'_O to v_O occurs in the middle of the band gap with $E_a = 296$ meV relative to the CBM of stoichiometric V_2O_3 . However, the transition to v_O results in the charge carrier falling below the valence band of v_O .

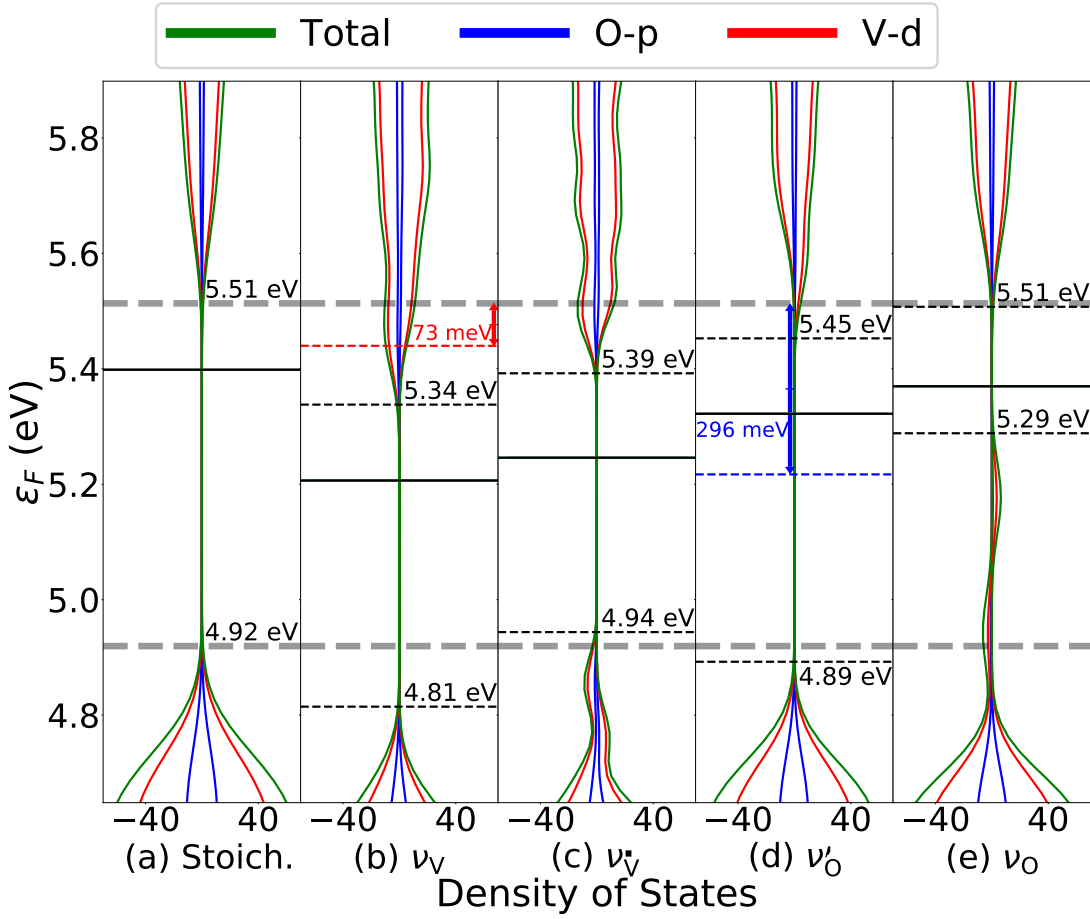


Figure 6.4: Total (green), O-2p (blue), and V-3d (red) orbital DoS for a $2 \times 2 \times 2$ supercell of (a) LT stoichiometric V_2O_3 and non-stoichiometric V_2O_3 containing a (b) ν_{V} , (c) ν_{V}^{\bullet} , (d) ν_{O}' or (e) ν_{O} defect. The VBM and CBM of the non-stoichiometric V_2O_3 (black dashed lines) as well as the Fermi level (black solid line) are also provided for each DoS. The stoichiometric VBM and CBM (grey dashed lines) is also provided for reference. The corresponding activation energies for carrier conductivity (E_a), i.e., the energy difference between the stoichiometric CBM and transition levels (dashed lines), are also annotated in (b) (red) and (d) (blue).

We performed Bader charge analysis to assess the effect of vacancies on the charges of atoms surrounding the defects²⁸¹. Figure 6.5 shows the change in Bader charge in the V_2O_3 supercell containing ν_{V} and ν_{O} . Using the Bader charges of stoichiometric V_2O_3 as a reference, we find that the charge on the oxygen nearest neighbors of ν_{V} (Figure 6.5(a)) become less negative from -1.24 to -1.12. We also observe a positive charge increase from +1.87 to +2.07 on three neighboring vanadium atoms within 3.4 Å from the vacancy. This is consistent with

previous observations that LT V_2O_3 is a p -type semiconductor as a consequence of vanadium vacancies^{73,282}.

In contrast, the charge on the nearest neighbor vanadium of v_{O} becomes less positive from +1.87 to +1.67. Furthermore, the electron carriers are confined to these nearest neighbors while the hole carriers of vanadium vacancies are present in the nearest neighbors as well as three additional surrounding vanadium atoms within 3.4 Å from the vacancy. This hints to holes being more delocalized than electrons making hole carriers more conductive which explains the lower E_a for v_{V} .

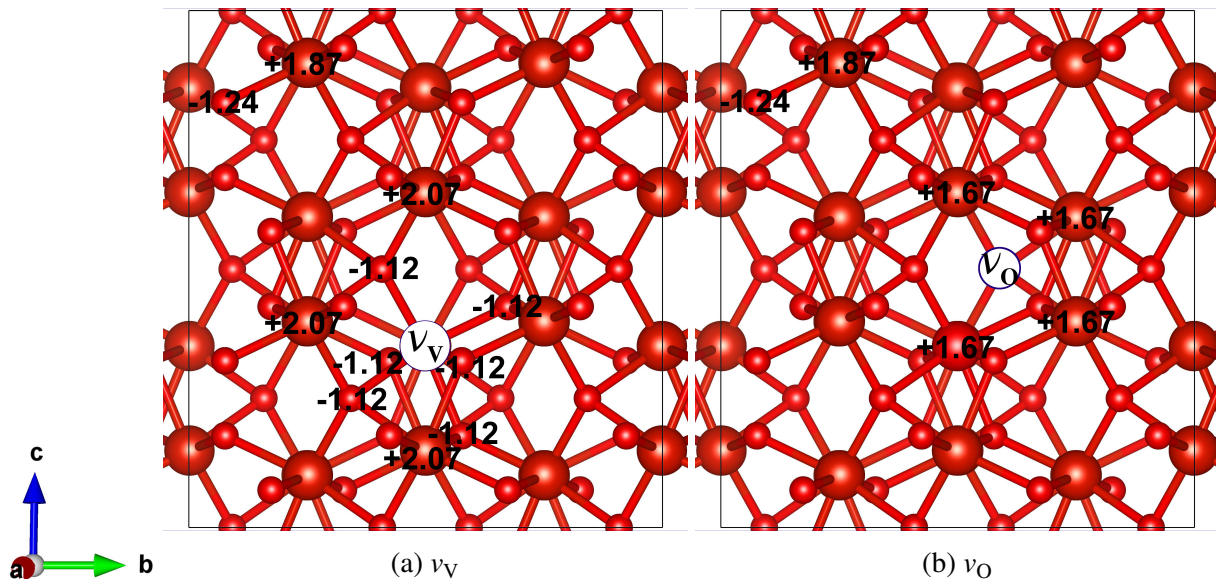


Figure 6.5: The $2 \times 2 \times 2$ supercell of V_2O_3 containing v_{V} (a) and v_{O} (b). All sites with Bader charges that differ from bulk-like charges are labelled while all other sites have bulk-like charges. Bulk-like charges are labelled on the top left sites for oxygen (-1.24) and vanadium (+1.87).

6.3.3 Effect of defects on MIT

Figure 6.6 plots the formation energy for neutral defects E_{form} as a function of $\Delta\mu_{\text{O}}$ in the LT monoclinic AFI and HT corundum FM phases of V_2O_3 . As the stoichiometric FM HT V_2O_3 is 2.08 eV/f.u. lower in energy than the NM HT V_2O_3 , we will focus on the AFI LT and FM HT phases here. The corresponding plots for the NM phase are presented in Figure D.2

and the relative stability of defects are the same in both the FM and NM configurations. Like with the LT phase, the vanadium vacancy is more stable than the other defects in the HT phase. The formation energy of v_V in the HT FM phase is lower (more stable) than that of the LT phase by 0.26 eV. As such, the stabilization of v_V over stoichiometric V_2O_3 also occurs when $\Delta\mu_O > -2.255$ eV. v_O becomes the most stable defect at $\Delta\mu = -3.87$ eV in the HT phase, but never more stable than stoichiometric HT V_2O_3 .

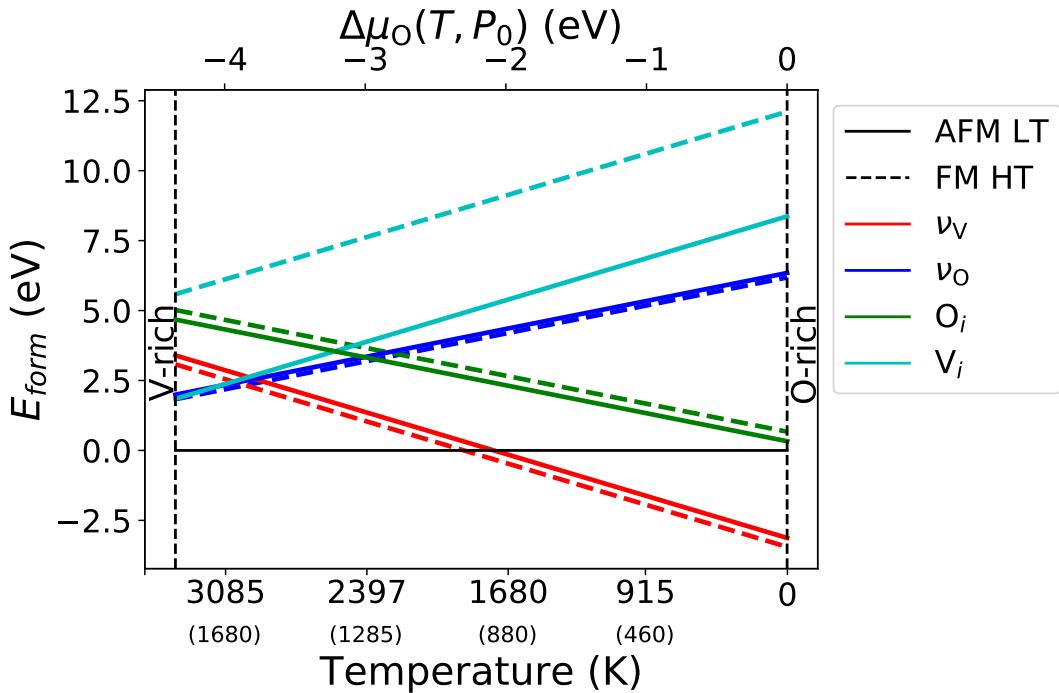


Figure 6.6: The neutral defect formation energy (E_{form}) for O_i , V_i , v_V and v_O in LT AFI (solid) and HT FM (dashed) V_2O_3 as a function of the oxygen chemical potential ($\Delta\mu_O$, top x axis). The temperature scales based on $p_0 = 0.1$ ($p_0 = 10^{-13}$ MPa in parenthesis) is provided on the bottom x axis.

Table 6.1 shows the calculated transition temperature T_c between the LT AFI phase and the HT FM phase for stoichiometric and non-stoichiometric V_2O_3 using Equation 6.5. Oxygen vacancies increase the LT AFI \rightarrow HT FM T_c from 165 K to 168 K (1.6% change). In contrast a vanadium vacancy will significantly decrease T_c from 165 K to 119 K (-27.9%).

Table 6.1: Phase transition critical temperature T_c of stoichiometric and non-stoichiometric V_2O_3 . Percentage change in T_c relative to that of stoichiometric V_2O_3 is indicated in the last column.

LT → HT transition	Defect	$T_c(K)$	Percentage change
AFI→PM	-	165	-
AFI→FM	v_V	119	-27.9%
AFI→FM	v_O	168	1.6%

6.4 Discussion

Here, we will provide a discussion of our computed results in the context of previous experiments on the application of V_2O_3 MIT for neuromorphic computing. Using the PBE+ U functional, we have clearly demonstrated that v_V are the most stable defects under a reasonable device operation temperatures, which is consistent with past experiments^{73,74}. Further, we have shown that v_V decreased T_c of MIT for V_2O_3 by 28% when transitioning from the AFI to the FM phase at a stoichiometric ratio of $\text{V}_{1.98}\text{O}_3$ (one vanadium vacancy in a 160-atom system), which is very close to the T_c decrease of 23.4% observed by Ueda et al.⁷⁴ for $\text{V}_{1.99}\text{O}_3$.

One proposed mechanism for the non-thermal MIT observed by Kalcheim et al.⁶⁹ is the Poole-Frenkel effect whereby the electric field reduces the energy barrier for excitation of trapped carriers from in-gap states into the conduction band³. Our calculations provide support for this mechanism. As shown in Figure 6.4, vanadium vacancies result in the formation of trapped charge carriers around $E_a = 73$ meV below the CBM of V_2O_3 . An applied field can decrease this barrier for carriers to hop into the energetically lowered conduction band of V_2O_3 thereby allowing for a purely electric field-induced MIT. Our calculated activation energy for carrier conductivity under vanadium vacancies is similar to that observed by Kalcheim et al.⁶⁹ ($E_a = 60$ meV).

The calculated formation energies predict that the FM HT phase is more stable than the AFI phase in the presence of v_V . This is consistent with the results of Ramirez et al.⁹³ who demonstrates a sudden breakdown of MIT in V_2O_3 at an ion bombardment concentration above

$2 \times 10^{14} \text{ ions/cm}^2$. This was accompanied by a breakdown in structural phase transition (SPT) whereby the corundum phase is stable even below the stoichiometric critical temperature of 165 K. The ions were not found to be embedded in the actual V_2O_3 sample which is an indicator of intrinsic defects being introduced. In contrast, VO_2 exhibits no SPT or MIT breakdown despite having a higher concentration of ion bombardment. Past computational results of VO_2 ⁸⁸ showed O_i and v_{O} to be the dominant defects in VO_2 with LT VO_2 being able to easily recover its stoichiometric state via the diffusion of oxygen from the air⁸⁹. However, such a recovery would not be possible with the vanadium defects in V_2O_3 , which could explain the breakdown of SPT and MIT in V_2O_3 but not VO_2 .

6.5 Conclusion

To conclude, we explored the performance of five DFT functionals in assessing the bulk properties of HT and LT V_2O_3 in regards to Mott insulation and concluded that the PBE+ U functional provides the best compromise in computational accuracy and efficiency. It was shown that vanadium vacancies are the most s defects under typical device operation temperatures. Vanadium vacancies can influence MIT in two ways. It can decrease the critical temperature required to induce transition from the monoclinic low temperature AFI phase and corundum high temperature FM phase. It can also lead to a non-thermal transition whereby a hole carrier hops from an in-gap state to the CBM whose energetic barrier is decreased due to an external potential (the Poole-Frenkel effect). These mechanisms can help reduce the energy consumption of neuromorphic devices.

Chapter 6 is, in full, a reprint of the material “Metal insulator transition under intrinsic defects in V₂O₃”, Richard Tran, Yoav Kalcheim, Xiang-Guo Li, Ivan Schuller, and Shyue Ping Ong. This material has been submitted to a peer-reviewed journal and is currently being reviewed for publication. The dissertation author was the primary investigator and author of this paper. All calculations and data analysis were performed by the author.

Chapter 7

Imaging of proton distributions in nickelate-based neuromorphic Devices

7.1 Introduction

In a quest to overcome the imminent slowdown of Moore's law, quantum materials are actively being explored as platforms for transformative computational paradigms. Standing at the forefront of these is neuromorphic computing, wherein a new level of computational efficiency can be achieved by using biologically inspired electronics^{283,284}. A hardware realization of this paradigm requires materials whose electrical resistance can change under external stimuli, thus emulating synaptic memory links between neurons^{260,285}. Various strongly correlated materials exhibiting a metal-insulator transition are being investigated for this purpose, including transition metal oxides^{286,287}, rare-earth compounds²⁸⁵, and organic-inorganic perovskites²⁸⁸. To successfully mimic the synaptic behavior of neuromorphic architectures, candidate materials must have the following features: (i) can be electrically switched by a small external stimulus, (ii) have a wide range of achievable electrical resistances for easy readability, (iii) can both increase and decrease their resistance, and (iv) can operate under normal conditions.

It was recently shown that SmNiO_3 (SNO) films doped with H^+ satisfy these conditions, displaying synaptic functionalities^{285,289} that can develop decision-tree-like resistance trajectories²⁹⁰. These behaviors which demonstrate the feasibility of these materials for neuromorphic computing devices fundamentally rely on the motion and redistribution of light ions influenced by electric field pulses. Generally, doping transition metal oxides with light ions like H^+ is a promising area of research. However, the microscopic mechanism behind the resistive switching in hydrogenated SNO films (H-SNO) remains unknown, particularly the spatially varying interplay between the structural and electronic degrees of freedom. X-ray absorption and scattering have been instrumental tools in determining these properties in pristine nickelate heterostructures^{169,291}, but in small synaptic devices, the key challenge is determining with spatial resolution how the light ions affect the electrical properties. Additionally, x-rays do not directly detect light ions easily. To overcome these challenges, we present a study of the electronic and

structural properties of H-SNO devices using a synchrotron x-ray beam focused to \sim 30 nm. By studying the x-ray fluorescence spectra near the Ni K-edge supported by *ab initio* simulations, we are able to spatially resolve how proton doping affects the valency of nickel. We also use spatially resolved diffraction from a judiciously chosen Bragg reflection to study subtle changes in the lattice structure to resolve the correlations to the electronic structure. The methodology we present can be used to detect the light ion dopants in other transition metal oxides.

Pristine SNO has a distorted perovskite structure characterized by corner-connected NiO_6 octahedra with Sm^{3+} ions filling the cavities between the octahedra (Figure 7.1a). Since the ionic radius of Sm^{3+} is smaller than the size of the cavity, NiO_6 octahedra are tilted²⁹² and distorted and the rare-earth ions are slightly displaced from the central position (Fig. 7.1b-d). The structure can be described by the orthorhombic *Pbnm* symmetry with the unit cell parameters $a_o = 5.328 \text{ \AA}$, $b_o = 5.437 \text{ \AA}$ and $c_o = 7.568 \text{ \AA}$ ¹⁵. The electronic properties of SmNiO_3 are determined to a large extent by hybridization between Sm^{3+} $3d$ orbitals and O^{2-} $2p$ orbitals^{293,294}. Since both the $3d$ and $2p$ orbitals have highly directional lobes, the spatial overlap strongly depends on the Ni-O-Ni angle, which is determined by the NiO_6 octahedral tilt pattern. Although SNO is a paramagnetic insulator at room temperature²⁹³, doping it with H^+ further decreases its electrical conductivity by eight orders of magnitude²⁹⁵. The proposed mechanism has been attributed to the addition of an extra electron into the system that opens a large gap at the Fermi level^{295–297}. A similar effect is observed when SNO is doped with other small ions, such as Li^+ or Na^+ ^{295,298}. Also, possible changes in the crystal lattice (e.g., the unit cell parameters^{296,299} and the NiO_6 tilt pattern^{296,300}) have been shown to directly influence the conductivity of the nickelates. In addition to that, the random defects in the crystal lattice caused by H^+ can result in a decrease of conductivity via Anderson localization³⁰¹. The goal of this work is to disentangle these effects with spatial resolution inside a functioning nanodevice.

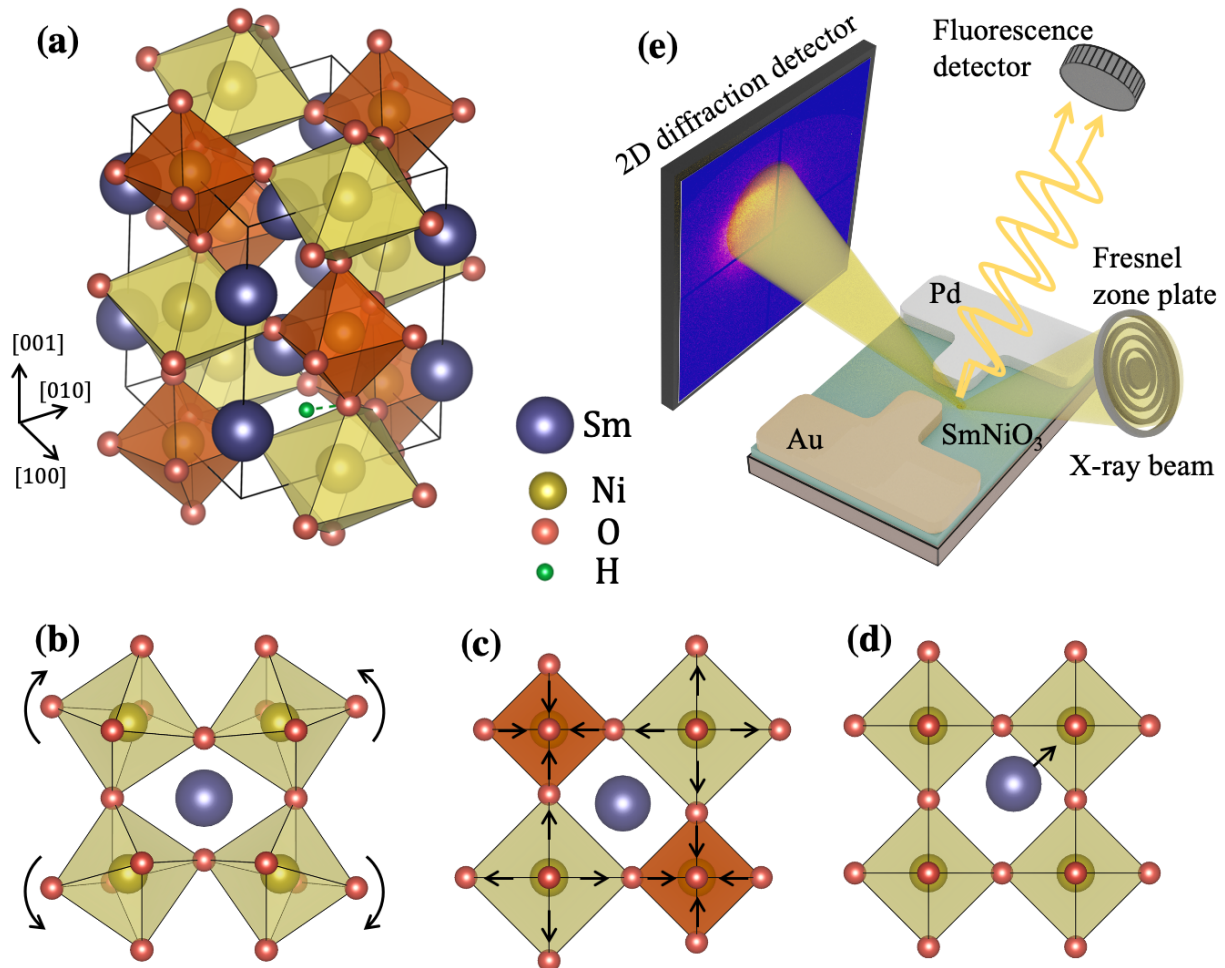


Figure 7.1: (a) Orthorhombic crystal structure of SNO. The breathing mode is shown by color: expanded NiO_6 octahedra are yellow and contracted are orange. (b) Rotation of the NiO_6 octahedra described by three angles α , β , and γ (c) breathing mode with magnitude B , (d) displacement $\mathbf{d} = (d_x, d_y, d_z)$ of the rare-earth cation from the centrosymmetric position inside the cavity between NiO_6 octahedra. (e) Scheme of the nanofocused x-ray experiment. The focused beam is used for raster scanning of the device where the diffraction signal is recorded by a 2D detector in reflection geometry, and the fluoresce signal is collected by a point energy-resolving detector oriented perpendicular to the sample surface

7.2 Experimental details

The SNO-based nanodevices studied here consist of a 150 nm thick SNO film epitaxially grown with a high vacuum sputtering system on (101)-oriented LaAlO₃ substrate. This orientation was chosen such as to be able to access Bragg peaks associated with octahedral distortions of the kind (101)^{302–304}. 5 μm-wide electrodes of Pd and Au were fabricated over the film with a lateral gap of 1 – 2 μm. The Pd electrode serves as a catalyst to incorporate H⁺ in the SNO film during annealing in the forming gas. The annealing was performed for 5 minutes at 100 °C in H₂/N₂ mixture (5%/95%). Ideally, the fully doped H-SNO should have the H⁺ concentration H:Ni=1:1 (atomic ratio), however due to escape of the hydrogen from the device into air, the actual concentration is happen to be about two times lower.

The nanofocused x-ray experiments were performed at the 26-ID-C beamline of the Advanced Photon Source (APS) and 3-ID beamline of the National Synchrotron Light Source II (NSLS II), using photons with energy of 8.3-8.4 keV to measure around the Ni K-edge near 8345 eV. At this energy, the resolution was about 0.5 eV achieved by a double-crystal monochromator. The XAS data were taken using a fluorescence detector placed above the device. The diffraction data were acquired with a two-dimensional photon counting detector with 55 μm pixels oriented perpendicular to the diffracted beam. A Fresnel zone plate was placed upstream from the sample to focus the beam down to ~30 nm at the sample. To scan the beam over the sample, the zone plate optics was moved in order to ensure stability of the sample. The gold and palladium contacts served as fiducials such as to easily locate the device using their fluorescence.

7.3 Computational Details

All DFT^{4,136} calculations were performed using the Vienna Ab initio Simulation package (VASP)¹³⁷ within the projector augmented wave (PAW)¹⁴⁰ approach. The exchange-correlation

effects were modeled using the Perdew-Berke-Ernzerhof (PBE) generalized gradient approximation (GGA)⁷⁸ functional under the Hubbard correction with $U = 2$ eV^{84,305}. We used a plane wave cutoff energy of 520 eV with the energies and atomic forces converged to within 10^{-4} eV and -0.02 eV/Å respectively. We performed full relaxation for the pristine and H-doped structures of SmNiO_3 and all calculations were spin-polarized.

We modelled the pristine and H-doped SmNiO_3 system using the low temperature monoclinic insulating phase with space group $P2_1/n$. SmNiO_3 is known to be paramagnetic, however DFT is only able to simulate magnetically ordered phases (e.g. ferromagnetic (FM) and antiferromagnetic (AFM)) or non-magnetic (NM) phases. As such we investigated the FM and AFM phases adopting the T-type AFM configuration described by Yoo and Liao⁸⁴. We ignore H-doping for the NM configuration as the pristine structure automatically relaxes to the high temperature orthorhombic phase. For further details of the magnetic and structural configurations, the reader is directed to the Supplementary Information.

We found the interstitial sites for H-doping using the Interstitialcy Finding Tool (InFiT)²⁷⁴. We investigated H doping in SmNiO_3 with the following H-to-formula-unit ratio: 1:32, 1:8, 1:4, and 1:2 by doping a single H atom in the $2 \times 2 \times 2$ supercell, $2 \times 1 \times 2$ supercell, conventional unit cell and primitive unit cell respectively.

All analysis and input generation was performed with the aid of the Python Materials Genomics (pymatgen) package¹³⁵.

7.4 Results

The device and experimental geometry are shown schematically in Figure 7.1e. Simultaneous diffraction and fluorescence measurements were taken while scanning the focused ~ 30 nm x-ray beam across the device. The spatially resolved fluorescence map near the Ni resonance energy $E = 8345$ eV across the device is shown in Figure 7.2a. This energy corresponds to the

highest slope of the x-ray absorption spectrum (XAS), and thus is most sensitive to shifts of the absorption edge caused by a different electronic valency. While the region of the increased fluorescence signal extends several hundred nanometers outside of the Pd electrode, a clear boundary can be resolved near this electrode. To understand the increase in fluorescence, we compared the spectra measured in the region between the two electrodes to the region directly under the Pd electrode, shown in Figure 7.2b. A clear shift in the spectra can be seen between these two regions, suggesting an accumulation of charge in that vicinity.

The K-edge transition of Ni corresponds to the promotion of the $1s$ core-level electron into the valence $4p$ shells. The energy difference between these levels depends on the number of electrons at the Ni $3d$ shells (split into t_{2g} triplet and e_g doublet), which screen the Coulomb interaction. In other words, the position of the Ni K-edge peak depends on the valence of Ni ions – the decrease of the Ni valence leads to a shift of the K-edge towards the lower energies^{306–308}. However, in contrast to other transition metals, the K-edge transition of Ni depends only weakly on the oxidation state. Namely, the difference in the peak position between Ni^{2+} and Ni^{3+} is less than 3 eV^{306,307}. Nonetheless, we experimentally resolved the position of the Ni K-edge by identifying the zero point of the second derivative of the two spectra, which gave us an estimate of 1.2 ± 0.4 eV for the energy shift (Figure 7.2b).

To find the corresponding change of the Ni oxidation state, we simulated the structure of H-SNO using the Vienna *ab initio* simulation package (VASP)^{309,310} and calculated the theoretical XAS spectra with the FEFF package³¹¹. The H^+ ion inside the SNO unit cell attaches to the oxygen with a bond length of $\simeq 1 \text{ \AA}$, consistent with the expected bond length of OH^- . There are two nonequivalent oxygen ions to which the doped H^+ might be chemically bonded: the basal oxygen in the Ni-O (001) plane and the apical oxygen in the Sm-O (001) plane. Our simulations show that the bonding with the basal oxygen is significantly energetically more favorable by 0.13 eV. This is in agreement with published results⁸⁴ showing that, in the stable H-SNO configurations, H^+ is bonded to the oxygen in the Ni-O planes and occupies the void

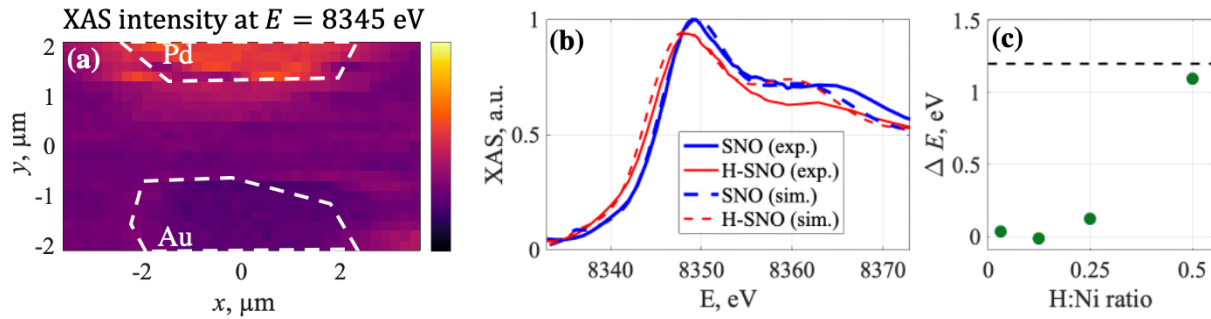


Figure 7.2: (a) Spatially-resolved map of the fluorescence signal at $E=8345$ eV. The white dashed lines outline the Pd and Au electrodes. Bright areas next to the Pd electrode correspond to the reduced valence of nickel ions due to the presence of H^+ . (b) Experimentally measured normalized XAS spectra at K-edge of Ni in the pristine SNO away from the Pd electrode and the doped H-SNO under the Pd electrode (solid lines) and FEFF-simulated XAS spectra for the doped H-SNO and undoped SNO (dashed lines). The simulated spectra were additionally convoluted with a Gaussian function to match the same energy resolution as in the experiment. (c) Dependence of the absorption peak shift ΔE on H^+ concentration for the simulated XAS spectra. Horizontal dashed line marks the experimentally observed value of $\Delta E = 1.2$ eV.

between the rare-earth cations as shown in Fig. 7.1a.

In pristine SNO, the integrated charge density³¹² calculations from DFT (see SI for computational details) reveal that the nickel ions exhibit two oxidation states: $Ni^{2.75+}$ inside the expanded NiO_6 octahedra and $Ni^{3.5+}$ inside the contracted NiO_6 octahedra³¹³. This lead to the average valence of $Ni^{3.125+}$ in pristine SNO. In doped H-SNO, the oxidation state of the nickel ion closest to the implanted H^+ is reduced to approximately $Ni^{2.66+}$, while the farther nickel ions are not affected so much, so the average oxidation state being reduced to $Ni^{2.85+}$. Indeed, the broadening of the experimental XAS peak may suggest a distribution of Ni ions with different oxidation states (Figure 7.2b).

The theoretical XAS spectra for SNO and H-SNO shown in Figure 7.2b exhibit the same shift $\Delta E \approx 1.2$ eV as was observed in the experiment. Our simulation confirms that this shift increases with doping concentration as shown in Figure 7.2c (see Supplementary Information for more details). This allowed us to estimate the doping level to be at the atomic ratio of H:Ni=1:2 in our experiment.

The changes of the crystal structure in the nanodevice upon H^+ doping can be studied

by considering the spatially resolved maps of the diffraction signal. In Figure 7.3a the intensity of the {101} reflection is shown measured on a second device. The striking feature of this map is the dark region below the Pd electrode which extends over more than 1 μm towards the Au electrode. The intensity in this region is approximately four times smaller than under the Au electrode. Nevertheless, the Q -position of the {101} and {202} reflections barely changed across the device, indicating that the lattice parameters did not change with doping (see Figure 7.3b). In previous computational^{77,84} and experimental²⁹⁶ works, an increase of the lattice parameter up to 4% was reported; however, other experimental data²⁹⁵ showed no visible changes in the lattice constant. This discrepancy might be explained by the different concentration of implanted H⁺ and by the influence of the substrate, which may not allow the SNO crystal lattice to expand. Nonetheless, the combined results strongly suggests a weaker role of the lattice in generating the changes in resistance.

Since the unit cell parameters are essentially unchanged, only a rearrangement of the atoms *within* the unit cell can cause a change of the diffraction peak intensity. The intensity of a Bragg reflection is proportional to the squared modulus of the form factor

$$I(\mathbf{q}) \propto |F(\mathbf{q})|^2 = \left| \sum_j O_j f_j(q) \exp(i\mathbf{qr}_j) \right|^2, \quad (7.1)$$

where \mathbf{q} is a scattering vector, index j numerates atoms in the unit cell (see Figure 7.1a), O_j is occupancy, $f_j(q)$ is atomic form factor, and \mathbf{r}_j is the position of each atom. In the ideal perovskite structure, the {101} reflection is forbidden, i.e., the contribution from different atoms in Equation (7.1) cancel out. The deviations from the ideal structure in pristine SNO that result in the non-zero intensity of the {101} reflection include NiO₆ octahedra rotations²⁹², Ni-O bond disproportionation (breathing of the NiO₆ octahedra)^{314,315}, and displacement of the rare-earth cations³¹⁶ (Fig. 7.1b-d).

In order to understand the individual contributions to the intensity of the {101} reflection,

we considered a model of the SNO structure in which the position of Ni ions is fixed in the orthorhombic unit cell (Figure 7.1a), since the distance between Ni ions defines the lattice parameters that are constant. The oxygen ions form ideal octahedra around the nickel ions where the length of the Ni-O bond is $d_{\text{Ni}-0} = d_{\text{Ni-Ni}}(1 \pm B)/2$: $d_{\text{Ni-Ni}}$ is the distance between two Ni^{3+} ions and $B \approx 1.3\%$ is the magnitude of the breathing mode^{313,315}. The alternating expanded and contracted octahedra form a three-dimensional checkerboard pattern^{293,315}. Furthermore, each NiO_6 octahedron rotates about the [100], [010], and [001] directions in the orthorhombic unit cell¹ over angles α , β , and γ to form the tilt pattern inherent to rare-earth nickelates²⁹². In this notation, the rotations $\alpha = 0^\circ$, $\beta = 15.26^\circ$, and $\gamma = 7.9^\circ$ correspond to the reported values of the Ni-O-Ni angles $\theta_{ap} = 149.5^\circ$ and $\theta_b = 154.2^\circ$ for the apical and basal oxygen atoms, respectively^{15,303}. The displacement of Sm^{3+} ions from the symmetric position between the NiO_6 octahedra was described by three parameters, d_x , d_y , and d_z , corresponding to the shift along the [100], [010], and [001] orthorhombic directions (Figure 7.1a). In pristine SNO, the values of d_x and d_y are reported to be 0.06 Å and 0.28 Å, while d_z equals zero^{15,302}.

Since it was not possible to distinguish between the a_o and b_o lattice parameters of the orthorhombic structure due to twinning, the measured intensity of the {101} reflection is actually averaged over four possible orientations of the unit cell, namely (101), (10 $\bar{1}$), (011), and (01 $\bar{1}$)³⁰². In our diffraction simulations, we varied the values of the above-listed distortions of the orthorhombic crystal lattice around the values reported for pristine SNO by the following amounts: $\Delta\alpha, \Delta\beta, \Delta\gamma = \pm 2^\circ$, $B = 0 - 3\%$, and $\Delta d_x, \Delta d_y, \Delta d_z = \pm 0.3$ Å. Our calculations show that the intensity of the {101} reflection is determined mainly by the displacement of the rare-earth cation, while the combined contribution from the breathing mode and tilt pattern constitutes only $\sim 5\%$ of the total intensity. This can be understood since two latter effects include movement of oxygen atoms that are weak x-ray scatters ($|f_{O^{2-}}|/|f_{\text{Sm}^{3+}}| \sim 0.1$ at $E = 8345$ eV); however, strictly speaking, this argument is valid only for the {101} reflection³⁰². Neglecting the contribution

¹Historically these rotations were introduced for the pseudocubic symmetry

from oxygen ions in Equation (7.1), the intensity of the {101} reflection depends only on the cation displacements along [100] and [001] directions

$$I_{101} \propto \exp \left[- \left(\frac{2\pi\sigma_x}{a_o} \right)^2 - \left(\frac{2\pi\sigma_z}{c_o} \right)^2 \right] \sin^2 \frac{2\pi d_x}{a_o} \cos^2 \frac{2\pi d_z}{c_o}. \quad (7.2)$$

Here σ_x and σ_z are the root-mean-square displacement of the Sm^{3+} ions along the [100] and [001] directions from the equilibrium positions dictated by d_x and d_z . In pristine SNO, $\sigma_x \sim \sigma_z \sim 0.05 \text{ \AA}$. The dependence of the {101} reflection intensity on σ_x , σ_z , d_x , and d_z is shown as a contour map in Figure 7.3c,d, to illustrate the combined impact of each parameter in Equation (7.2). The strongest decrease of the {101} reflection intensity is caused by the shift of the Sm^{3+} cations towards the symmetric position along the [100] direction (i.e., $d_x \rightarrow 0$). Notwithstanding, in our calculations the intensity of the {202} reflection remains practically constant, which coincides with the experimental x-ray data in Figure 7.3b. This also allows one to directly map the intensity of the {101} reflection into the displacement of the rare-earth cation. In Figure 7.3e, the intensity of the {101} is plotted with the corresponding variation of the displacement parameter d_x shown along the $x = 0$ line cut of the intensity map (Figure 7.3a). The proportionality coefficient between intensity and d_x was determined by assigning the maximum intensity of the {101} peak below the Au electrode to the literature values of SNO ($d_x \approx 0.06 \text{ \AA}$). The outstanding feature of this plot is a nonmonotonic change of the d_x parameter between the electrodes: the minimum value of d_x is reached approximately 250 nm away from the Pd electrode. This suggests that the diffusion coefficient of H^+ in SNO may depend on H^+ concentration, which leads to accumulation and stagnation of dopants next to the Pd electrode. This also shows that H^+ doping can affect the structure of SNO up to 1 μm away from the Pd electrode, through which the protons were initially introduced. This information is important for optimization of the electrode shape and scaling of the device and requires a dedicated investigation. Finally, our results are in agreement with DFT calculations which predict that incorporating H^+ in SNO can cause a rare-earth-cation

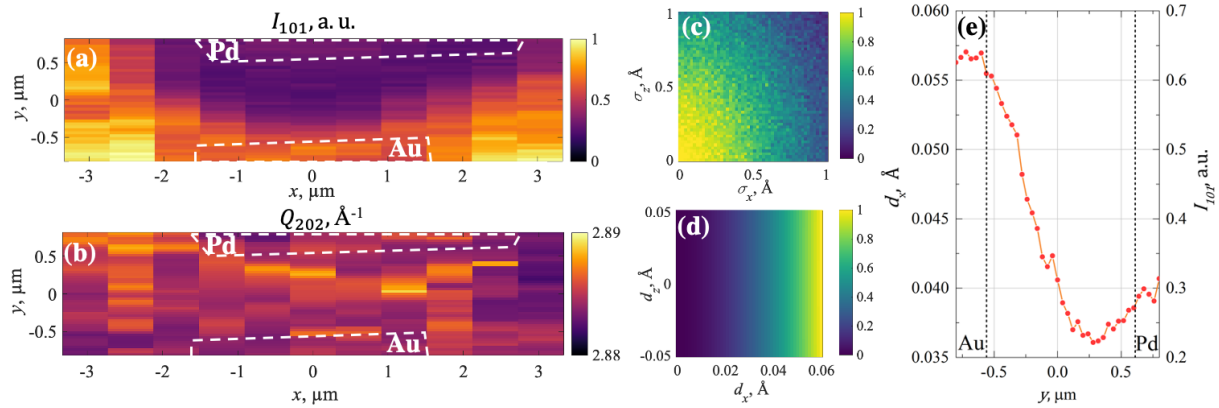


Figure 7.3: (a) Normalized intensity map of the $\{101\}$ reflection. The white dashed lines outline Pd and Au electrodes. The dark region between the electrodes corresponds to the area where H^+ doping results in structural changes in the film. (b) Spatially-resolved map of the Q -position (\AA^{-1}) of the $\{202\}$ reflection. (c-d) Dependence of the $\{101\}$ peak intensity on the root-mean-square displacement (c) and mean position of the Sm^{3+} ions (d). The intensity was evaluated by fixing the positions of all ions in the SNO unit cell and allowing only Sm^{3+} to move. For each value of the parameters the result was statistically averaged over 10^4 realizations. (e) Mean shift of the Sm^{3+} ions and the corresponding change of intensity along the $x = 0$ line in the spatially resolved map in Figure 7.3(a) using Equation (7.2). Vertical lines mark Au and Pd electrodes.

displacement sufficient to decrease the $\{101\}$ -peak intensity.

7.5 Discussion

To understand and further improve the performance of the H-SNO devices^{290,295,317} one should address two questions: how the hydrogenation changes the properties of the bulk SNO and how H^+ is spatially distributed within a device. Nanofocused x-ray diffraction and spectroscopy are among a few techniques that can probe the distribution of H^+ ^{299,318}. Technically, the x-rays are not directly sensitive to the implanted H^+ ions, but they are a perfect tool to study the influence of doping on electronic and crystal structure of SNO. In this context, the spatially resolved maps in Figures 7.2a and 7.3a-b provide valuable information on the changes in SNO with hydrogenation. The main effects of the H^+ doping are the reduction of nickel from $\text{Ni}^{3.125+}$ to $\text{Ni}^{2.85+}$ and decrease of the Sm^{3+} displacement from the symmetric position between the nickel ions. The

rare-earth cation displacement is known to be coupled with the tilt of the NiO₆ octahedra³¹⁶, so we anticipate that the rotation angles of the NiO₆ octahedra are also slightly decreased with hydrogenation.

At first glance, the shift of the rare-earth cation towards the centrosymmetrical position in the unit cell and the decrease of the oxygen octahedra rotations seem to be a counterintuitive result of the H⁺ implantation, because these structural changes actually make the SNO crystal lattice closer to the ideal perovskite structure. On the other hand, the rare-earth nickelates with large rare-earth cations are known to have less distorted crystal structures (i.e., exhibit smaller octahedral tilts), than the nickelates with small cations²⁹³. Therefore, implantation of H⁺ next to the rare-earth cation may effectively increase the radius of the latter, which would result in a decrease of the NiO₆ tilt angles, causing the system to be more metallic. We should also note that, even with our spatial resolution, our probe measures an average structure across the beam footprint. However, the implanted H⁺ can produce local lattice distortions that do not affect the intensity of the measured diffraction peaks (see Figure 7.3c). A hint that these local distortions are averaged out in diffraction can be seen in the slight broadening of the H-SNO absorption spectra as compared to the pristine SNO (Figure 7.2). Together, our data suggest that the dramatic changes in resistance upon hydrogenation come from the change in electronic valency, not from structural distortions. This further implies that hydrogenating other transition metal oxides with different crystal structures might also yield changes in resistance and possibly other neuromorphic functionalities.

7.6 Conclusion

In summary, we used a nano-focused x-ray beam to perform spatially resolved spectroscopic and structural studies of the H-SNO-based nanodevice. As a result of H⁺ doping, we observed the 1.2 eV shift of the Ni K-edge towards the lower energies. Our DFT simulations

account for this shift by a reduction of the nickel $\text{Ni}^{3.125+}$ to $\text{Ni}^{2.85+}$. We also observed the decrease of the {101} Bragg peak intensity next to the Pd electrode. Structural modeling revealed that this can be caused by a shift of the Sm^{3+} cations over ~ 0.03 Å towards the centrosymmetrical position inside the voids between the NiO_6 octahedra. Combining the x-ray spectroscopy and diffraction, we elucidate how H^+ doping changes the structure and electronic properties of an SNO device. Since the increase in resistance likely comes from the valency change rather than the structural distortions, we speculate the hydrogenation of other oxides could also display similar behavior. Our methods pave the way for future x-ray nanoscale studies of devices based on transition metal oxides for neuromorphic computing.

Chapter 7 is, in full, a reprint of the material “Imaging of proton distributions in nickelate-based neuromorphic devices”, Ivan A. Zaluzhnyy, Peter O. Sprau, Richard Tran, Qi Wang, Hai-Tian Zhang, Zhen Zhang, Nelson Hua, Boyan Stoychev, Mathew J. Cherukara, Martin V. Holt, Evgeny Nazarertschi, Xiaojing Huang, Hanfei Yan, Ajith Pattammattel, Yong S. Chu, Shyue Ping Ong, Shriram Ramanathan, Oleg G. Shpyrko, and Alex P. Frano. This material has been submitted to a peer-reviewed journal and is currently being reviewed for publication. All calculations and data analysis for the computational part of this paper were performed by the author. The experimental portion of the work – synthesis and characterization – was done by collaborators Ivan A. Zaluzhnyy, Peter O. Sprau, Qi Wang, Hai-Tian Zhang, Zhen Zhang, Nelson Hua, Boyan Stoychev, Mathew J. Cherukara, Martin V. Holt, Evgeny Nazarertschi, Xiaojing Huang, Hanfei Yan, Ajith Pattammattel, Yong S. Chu, Shriram Ramanathan, Oleg G. Shpyrko, and Alex P. Frano.

Chapter 8

Summary and outlook

Planar and point defects are a key component in fine tuning the behavior of materials for technological applications. In this thesis, we demonstrated how DFT calculations can be used to uncover the physics behind defect modified material properties as well as develop high-throughput databases for such properties. This thesis is broadly divided into three topics.

In the first topic we developed a high-throughput database for the surface energies, work function and Wulff shapes of 145 crystals of 74 elements with an MMI of 2 and 3 for non-cubic and cubic space groups respectively. We proposed a new method of comparing the average surface energy and polycrystalline work function of materials by weighting the facet specific quantities with the corresponding fractional surface areas of the Wulff shapes. These weighted averages provided an effective comparison to experimental quantities. We also assessed the Smoluchowski smoothing model for calculating anisotropic work function as well as proposed a new model for predicting the polycrystalline work function based on Gauss's law for a potential inside an infinitely charged plate.

In the second topic we investigated the effect of metallic dopant segregation in the planar defects of refractory materials with the intention of reducing room temperature brittleness. We used DFT calculations in conjunction with experimental results to assess the effect of metallic dopant segregation on the nanoparticle morphology of TaC. Fe and Ni/Ti co-doping were shown to be effective at producing nanocubes due to its enhanced $p - d$ hybridization on the (100) facets. These shapes are promising in reducing porosity through compact sintering. We also investigated the segregation of 29 dopants in Mo GBs. We compared our calculated results to previously developed empirical models. We also assessed the effect of dopant site preference on GB embrittlement and developed a new model using the relative cohesive energy and atomic strain of the dopants.

Our database of elemental surface properties provides the foundation for further expansion into other quantities related to planar defects. As an example, we have recently expanded the database to include the properties of grain boundaries³¹⁹. The next logical step in expansion is

the inclusion of dopant segregation in surfaces and GBs. Such a database will be invaluable for screening materials with dopant enhanced mechanical properties as well as crystal shapes for nanocatalysts and enhanced sintering. Furthermore, the inclusion of GB energy allows for the investigation of nanoparticles beyond the Wulff shape such as twinned nanoparticles and other exotic shapes³²⁰.

There is still room for further improvement for our models of surface and GB properties. Our model of GB embrittlement and assessment of dopant induced morphology is limited to two types of GBs and surfaces respectively and one host material. As such, our assessments can not account for the influence of different structural geometries and host chemistries. The calculation of every possible combination of surface, grain boundary and dopant is a computationally daunting task. Expanding to a larger, but not necessarily complete, data set will provide testing data for the construction of predictive machine learning models that can account for host chemistry, interface geometry, and other unforeseen factors without the need of further DFT calculations.

In the third topic we investigated the influence of point defects on MIT in strongly correlated materials. We assessed various DFT functionals for predicting the bulk properties of insulating and metallic V₂O₃ and concluded that the PBE+U functional provided the best compromise in accuracy and efficiency. We used this functional to assess the effect of vacancies and self-interstitials on the electronic and thermodynamic properties of V₂O₃. Our results demonstrated vanadium vacancies to be the most stable defect and that it decreased T_c which is consistent with past experimental observations. Furthermore, our analysis of the in-gap states provided insight into the underlying mechanisms of non-thermal MIT in V₂O₃. We also assessed the effects of H-doping in SmNiO₃. Using our calculated XAS spectrum and integrated spin density, we were able to confirm that H-doping decreased the overall Ni oxidation state. We also predicted a 1:2 H:Ni concentration in SmNiO₃ thin films by comparing the calculated XAS features to those found in the experimental spectrum.

These calculations constitute an important validation of an integrated computational and

experimental approach to investigating defects in materials. We note that there remains significant scope for improvements in the computational methodology used for assessing MIT in strongly correlated materials. As of yet, the method used in this study has been the PBE+*U* method which requires an empirical fitting of the *U*-value to reproduce known experimental quantities. Future studies will need to improve upon DFT functionals in order to predict these properties without fitting in order to provide true first principles prediction of MIT in materials. Our studies into charged defects and its influence on electronic properties in V₂O₃ can be expanded into other vanadate materials, especially Magnelli phase vanadates which are known for exhibiting MIT. Such studies will yield a more generalized understanding of how MIT works in vanadates as well as TMOs as a whole which will provide for better screening of materials to be used in constructing energy efficient neuromorphic devices.

Appendix A

Supporting information: Anisotropic work function of elemental crystals

Table A.1: The values of $\bar{\Phi}$ and $\Phi_{\text{hkl}}^{\text{lowest}}$ (along with its corresponding Miller index) from high-throughput calculations and the experimental $\Phi_{\text{poly}}^{\text{expt}}$ from the literature.

Material	$\bar{\Phi}$ (eV)	Surface	$\Phi_{\text{hkl}}^{\text{lowest}}$ (eV)	$\Phi_{\text{poly}}^{\text{expt}}$ (eV)
Li	2.85	(2, 2, 1)	2.55	2.93^{196*}
Al	4.04	(3, 3, 1)	3.88	4.25^{171*}
Be	4.87	(1, 1, -2, 0)	3.88	4.98^{181*}
B	4.67	(1, 0, -1, 1)	4.64	4.45^{181*}
C	4.24	(0, 0, 1)	4.22	4.65^{171*}
Na	2.55	(2, 1, 1)	2.08	2.75^{181*}
Mg	3.55	(2, 0, -2, 1)	3.35	3.66^{181*}
Si	4.73	(3, 1, 1)	4.23	4.82^{171*}
K	2.31	(2, 1, 0)	1.95	2.29^{196*}
Ca	2.77	(3, 1, 0)	2.39	2.87^{181*}
Sc	3.12	(2, 0, -2, 1)	2.66	3.50^{181*}
Ti	3.65	(1, 1, -2, 0)	3.03	4.33^{181*}
V	4.11	(3, 2, 2)	3.49	4.30^{181*}
Cr	4.11	(3, 1, 1)	3.53	4.50^{181*}
Mn	4.32	(1, 1, 0)	4.20	4.10^{181*}
Co	4.52	(1, 0, -1, 2)	3.85	5.00^{181*}
Zn	4.01	(1, 0, -1, 1)	3.91	4.33^{181*}
Ga	4.08	(2, 1, 0)	3.87	4.20^{181*}
Ge	4.39	(3, 1, 0)	4.05	5.00^{181*}
As	4.40	(2, 2, -4, 1)	4.31	3.75^{181*}
Se	5.22	(0, 0, 1)	5.07	5.90^{181*}

Table A.1: The values of $\bar{\Phi}$ and $\Phi_{\text{hkl}}^{\text{lowest}}$ (along with its corresponding Miller index) from high-throughput calculations and the experimental $\Phi_{\text{poly}}^{\text{expt}}$ from the literature (continued).

Material	$\bar{\Phi}$ (eV)	Surface	$\Phi_{\text{hkl}}^{\text{lowest}}$ (eV)	$\Phi_{\text{poly}}^{\text{expt}}$ (eV)
Rb	2.20	(2, 1, 1)	1.91	2.16^{181*}
Sr	2.51	(2, 1, 0)	2.26	2.59^{181*}
Y	2.99	(2, 2, -4, 1)	2.57	3.10^{181*}
Zr	3.57	(1, 1, -2, 0)	2.83	4.05^{181*}
Ru	4.75	(1, 1, -2, 1)	4.12	4.70^{171*}
Cd	3.68	(0, 0, 0, 1)	3.63	4.08^{196*}
In	3.70	(1, 0, 1)	3.67	4.12^{181*}
Sn	4.07	(3, 2, 1)	3.87	4.42^{181*}
Sb	4.30	(2, 2, -4, 1)	4.20	4.55^{181*}
Te	4.51	(1, 0, -1, 1)	4.29	4.95^{181*}
Cs	2.03	(1, 1, 1)	1.59	1.95^{196*}
Ba	2.33	(2, 1, 0)	1.90	2.53^{196*}
La	2.64	(2, 2, -4, 1)	2.42	3.50^{181*}
Hf	3.54	(1, 1, -2, 0)	2.98	3.90^{181*}
W	4.47	(3, 1, 0)	3.71	4.55^{171*}
Re	4.55	(1, 1, -2, 1)	4.06	4.95^{171*}
Os	4.78	(1, 1, -2, 1)	4.44	4.84^{171*}
Tl	3.47	(1, 0, -1, 1)	3.13	3.84^{181*}
Pb	3.69	(1, 1, 0)	3.60	4.25^{181*}
Bi	4.06	(2, 2, -4, 1)	3.93	4.22^{181*}
Th	3.12	(1, 1, 1)	2.99	3.40^{181*}

Table A.1: The values of $\bar{\Phi}$ and $\Phi_{\text{hkl}}^{\text{lowest}}$ (along with its corresponding Miller index) from high-throughput calculations and the experimental $\Phi_{\text{poly}}^{\text{expt}}$ from the literature (continued).

Material	$\bar{\Phi}$ (eV)	Surface	$\Phi_{\text{hkl}}^{\text{lowest}}$ (eV)	$\Phi_{\text{poly}}^{\text{expt}}$ (eV)
Ce	2.98	(2, 1, 0)	2.69	2.90^{181*}
Nd	2.86	(2, 2, -4, 1)	2.48	3.20^{181*}
Sm	2.74	(1, 1, -2, 1)	2.54	2.70^{181*}
Eu	2.43	(1, 0, -1, 0)	2.08	2.50^{181*}
Gd	2.96	(2, 1, -3, 0)	2.38	3.10^{181*}
Tb	2.98	(2, -1, -1, 2)	2.53	3.00^{181*}
Lu	3.03	(2, 1, -3, 0)	2.36	3.30^{181*}
Fe	4.31	(3, 2, 2)	3.30	4.36^{171*}
Ni	4.98	(2, 1, 0)	4.41	5.02^{171*}
Cu	4.53	(3, 1, 0)	4.17	4.55^{171*}
Nb	4.15	(3, 1, 0)	3.31	3.99^{171*}
Mo	4.11	(3, 1, 0)	3.53	4.39^{171*}
Rh	4.99	(1, 1, 0)	4.27	4.88^{171*}
Pd	5.06	(1, 1, 0)	4.63	5.33^{171*}
Ag	4.22	(2, 1, 1)	3.97	4.33^{171*}
Ta	4.26	(3, 1, 0)	3.49	4.25^{171*}
Ir	5.31	(3, 2, 0)	4.75	5.27^{171*}
Pt	5.54	(1, 1, 0)	5.19	5.41^{171*}
Au	5.06	(2, 1, 0)	4.71	5.20^{171*}
Pr	2.88	(2, 2, -4, 1)	2.48	2.96^{197*}

Table A.1: The values of $\bar{\Phi}$ and $\Phi_{\text{hkl}}^{\text{lowest}}$ (along with its corresponding Miller index) from high-throughput calculations and the experimental $\Phi_{\text{poly}}^{\text{expt}}$ from the literature (continued).

Material	$\bar{\Phi}$ (eV)	Surface	$\Phi_{\text{hkl}}^{\text{lowest}}$ (eV)	$\Phi_{\text{poly}}^{\text{expt}}$ (eV)
Dy	2.98	(2, -1, -1, 2)	2.55	3.25^{197*}
Ho	2.91	(2, 1, -3, 1)	2.56	3.22^{197*}
Er	2.92	(2, 1, -3, 0)	2.37	3.25^{197*}
Tm	2.95	(2, 1, -3, 1)	2.54	3.10^{197*}

* See reference herein

Table A.2: A comparison of the high-throughput values to experimental and computed values for materials from the literature.

Material	Surface	Work function Φ (eV)				
		HT	GGA(RPBE)	GGA(PBE)	LDA	Experiment
Ru	(0001)	4.96	4.83	4.97 ¹⁷⁷	5.31 ¹⁷⁷	
	(10\bar{1}0)	4.7		4.79 ¹⁷⁷	5.13 ¹⁷⁷	4.6 ^{183*}
	(10\bar{1}1)	4.84		4.91 ¹⁷⁷	5.26 ¹⁷⁷	
	(10\bar{1}2)	4.45		4.5 ¹⁷⁷	4.85 ¹⁷⁷	
	(11\bar{2}1)	4.12		4.39 ¹⁷⁷	4.76 ¹⁷⁷	
	(21\bar{3}0)	4.28		4.47 ¹⁷⁷	4.86 ¹⁷⁷	
Pt	(100)	5.68	5.47	5.69 ⁸	6.06 ²⁰	5.7 ^{183*}
	(111)	5.64	5.72	5.12 ⁸	6.08 ²⁰	5.91 ^{183*}
	(110)	5.33	5.25	4.94 ⁸	5.6 ²⁰	5.53 ^{183*}
	(321)	5.34		5.44 ¹⁷⁶		5.4 ^{171*}
	(211)	5.43		5.55 ¹⁷⁶		
	(310)	5.44		5.42 ¹⁷⁶		
	(210)	5.3				5.18 ^{171*}
	(311)	5.47				5.5 ^{171*}
	(320)	5.2				5.2 ^{171*}
	(331)	5.24				5.12 ^{171*}
Ni	(100)	4.95	4.71	4.9 ²⁰	5.33 ²⁰	5.17 ^{183*}
	(111)	5.1	4.89	5.02 ²⁰	5.5 ²⁰	5.36 ^{183*}
	(110)	4.43	4.26	4.49 ²⁰	4.95 ²⁰	4.55 ^{183*}
Nb	(100)	3.43	3.42	3.55 ¹⁷⁶	3.86 ²⁰	3.97 ^{183*}
	(110)	4.46	4.43	4.49 ¹⁷⁶	4.77 ²⁰	4.63 ^{183*}

Table A.2: A comparison of the high-throughput values to experimental and computed values for materials from the literature (continued).

Material	Surface	Work function Φ (eV)				
		HT	GGA(RPBE)	GGA(PBE)	LDA	Experiment
	(111)	3.63		3.77 ¹⁷⁶	4.15 ²⁰	4.08 ^{183*}
	(210)	3.86		3.97 ¹⁷⁶		
	(331)	4.08		4.15 ¹⁷⁶		
	(311)	3.4		3.64 ¹⁷⁶		4.29 ^{171*}
	(310)	3.31				4.18 ^{171*}
	(211)	3.77				4.45 ^{171*}
Y	(0001)	3.18		3.18 ²⁰	3.44 ²⁰	
	(10 $\bar{1}$ 0)	3.23		3.31 ²⁰	3.47 ²⁰	
	(21 $\bar{3}$ 0)	2.76		3.0 ²⁰	3.2 ²⁰	
Pd	(111)	5.21	4.94	5.32 ⁸	5.66 ⁸	5.67 ^{183*}
	(110)	4.63	4.56	4.95 ⁸	5.32 ⁸	5.07 ^{183*}
	(100)	5.13		5.12 ⁸	5.54 ⁸	5.48 ^{183*}
	(321)	4.86		4.89 ¹⁷⁶		
	(211)	4.92		4.99 ¹⁷⁶		
	(310)	4.93		4.86 ¹⁷⁶		
Rh	(100)	5.01	4.9	5.04 ⁸	5.44 ⁸	5.3 ^{183*}
	(111)	5.15	4.77	5.0 ⁸	5.23 ⁸	5.46 ^{183*}
	(110)	4.27	4.25	4.53 ⁸	4.9 ⁸	4.86 ^{183*}
	(321)	4.57		4.65 ¹⁷⁶		
	(211)	4.75		4.87 ¹⁷⁶		
	(310)	4.62		4.74 ¹⁷⁶		

Table A.2: A comparison of the high-throughput values to experimental and computed values for materials from the literature (continued).

Material	Surface	Work function Φ (eV)				
		HT	GGA(RPBE)	GGA(PBE)	LDA	Experiment
Tc	(0001)	4.63	4.47	4.69 ¹⁷⁷	4.95 ¹⁷⁷	
	(10̄10)	4.22		4.5 ¹⁷⁷	4.83 ¹⁷⁷	
	(10̄11)	3.76		4.7 ¹⁷⁷	5.05 ¹⁷⁷	
	(10̄12)	4.35		4.31 ¹⁷⁷	4.67 ¹⁷⁷	
	(11̄21)	3.8		4.09 ¹⁷⁷	4.44 ¹⁷⁷	
	(21̄12)	4.19		4.28 ¹⁷⁷	4.63 ¹⁷⁷	
	(21̄30)	4.05		4.26 ¹⁷⁷	4.58 ¹⁷⁷	
Ta	(100)	3.71	3.67	4.1 ¹⁷⁶	4.12 ²⁰	4.1 ^{183*}
	(110)	4.64	4.64	4.96 ¹⁷⁶	4.98 ²⁰	4.74 ^{183*}
	(111)	3.71		4.2 ¹⁷⁶	4.22 ²⁰	3.5 ^{183*}
	(210)	4.04		4.34 ¹⁷⁶		
	(331)	4.21		4.62 ¹⁷⁶		
	(311)	3.5		4.1 ¹⁷⁶		
	(211)	3.92				4.45 ^{171*}
Fe	(110)	4.79	4.66	4.74 ²⁰	5.28 ²⁰	5.12 ^{183*}
	(111)	4.25		3.86 ²⁰	4.54 ²⁰	4.81 ^{183*}
	(100)	3.96		3.89 ²⁰	4.41 ²⁰	4.75 ^{183*}
Hf	(0001)	4.29	4.12	4.34 ²⁰	4.58 ²⁰	
	(10̄10)	3.62		3.94 ²⁰	4.21 ²⁰	
	(21̄30)	3.23		3.12 ²⁰	3.38 ²⁰	
Mo	(100)	3.76	3.61	3.84 ¹⁷⁶	4.36 ²⁰	4.45 ^{183*}

Table A.2: A comparison of the high-throughput values to experimental and computed values for materials from the literature (continued).

Material	Surface	Work function Φ (eV)				
		HT	GGA(RPBE)	GGA(PBE)	LDA	Experiment
	(110)	4.53	4.46	4.51 ¹⁷⁶	4.86 ²⁰	4.95 ^{183*}
	(111)	3.76		3.94 ¹⁷⁶	4.34 ²⁰	4.52 ^{183*}
	(210)	4.0		4.11 ¹⁷⁶		
	(331)	4.15		4.25 ¹⁷⁶		
	(311)	3.61		3.89 ¹⁷⁶		
	(211)	3.81				4.36 ^{171*}
W	(100)	4.04	4.03	4.09 ¹⁷⁶	4.44 ²⁰	4.65 ^{183*}
	(110)	4.8	4.64	4.76 ¹⁷⁶	5.05 ²⁰	5.25 ^{183*}
	(111)	3.98		4.24 ¹⁷⁶	4.41 ²⁰	4.47 ^{183*}
	(210)	4.22		4.29 ¹⁷⁶		4.38 ^{171*}
	(331)	4.39		4.46 ¹⁷⁶		
	(311)	3.82		4.1 ¹⁷⁶		4.46 ^{171*}
	(211)	4.29				4.76 ^{183*}
	(321)	4.13				4.49 ^{171*}
	(310)	3.71				4.32 ^{171*}
V	(100)	3.59	3.56	3.74 ²⁰	4.07 ²⁰	
	(110)	4.67	4.66	4.74 ²⁰	5.02 ²⁰	
	(111)	3.6		3.87 ²⁰	4.23 ²⁰	
Sc	(0001)	3.39	3.66	3.33 ²⁰	3.56 ²⁰	
	(10 $\bar{1}$ 0)	3.35		3.56 ²⁰	3.77 ²⁰	
	(21 $\bar{3}$ 0)	3.09		3.18 ²⁰	3.35 ²⁰	

Table A.2: A comparison of the high-throughput values to experimental and computed values for materials from the literature (continued).

Material	Surface	Work function Φ (eV)			
		HT	GGA(RPBE)	GGA(PBE)	LDA
	(21̄31)	2.84		3.42 ²⁰	3.39 ²⁰
Os	(0001)	5.27	5.1	5.32 ¹⁷⁷	5.64 ¹⁷⁷
	(10̄10)	4.44		5.17 ¹⁷⁷	5.45 ¹⁷⁷
	(10̄11)	4.77		5.23 ¹⁷⁷	5.53 ¹⁷⁷
	(10̄12)	4.78		4.85 ¹⁷⁷	5.15 ¹⁷⁷
	(11̄21)	4.44		4.67 ¹⁷⁷	4.98 ¹⁷⁷
	(21̄12)	4.93		4.9 ¹⁷⁷	5.22 ¹⁷⁷
	(21̄30)	4.68		4.87 ¹⁷⁷	5.2 ¹⁷⁷
Zn	(0001)	3.92	4.21	4.08 ²⁰	4.44 ²⁰
	(10̄10)	4.08		4.33 ²⁰	4.7 ²⁰
	(21̄30)	3.92		4.03 ²⁰	4.3 ²⁰
	(21̄31)	3.93		4.13 ²⁰	4.43 ²⁰
Co	(0001)	4.86	4.75	4.92 ²⁰	5.39 ²⁰
	(10̄10)	4.55		4.7 ²⁰	5.14 ²⁰
	(21̄30)	4.37		4.39 ²⁰	4.81 ²⁰
	(21̄31)	4.34		4.33 ²⁰	4.76 ²⁰
Ag	(100)	4.21	3.96	4.26 ⁸	4.68 ²⁰
	(111)	4.34	4.21	4.49 ⁸	4.84 ²⁰
	(110)	4.05	4.04	4.16 ⁸	4.55 ²⁰
	(321)	4.01		4.14 ¹⁷⁶	
	(211)	3.97		4.24 ¹⁷⁶	

Table A.2: A comparison of the high-throughput values to experimental and computed values for materials from the literature (continued).

Material	Surface	Work function Φ (eV)				
		HT	GGA(RPBE)	GGA(PBE)	LDA	Experiment
	(310)	4.06		4.08 ¹⁷⁶		
Re	(0001)	4.77	4.85	4.88 ¹⁷⁷	5.17 ¹⁷⁷	5.15 ^{171*}
	(10 $\bar{1}$ 0)	4.58		4.62 ¹⁷⁷	4.93 ¹⁷⁷	
	(10 $\bar{1}$ 1)	4.67		4.94 ¹⁷⁷	5.25 ¹⁷⁷	
	(10 $\bar{1}$ 2)	4.42		4.55 ¹⁷⁷	4.86 ¹⁷⁷	
	(11 $\bar{2}$ 1)	4.06		4.33 ¹⁷⁷	4.62 ¹⁷⁷	
	(21 $\bar{1}$ 2)	4.38		4.48 ¹⁷⁷	4.79 ¹⁷⁷	
	(21 $\bar{3}$ 0)	4.06		4.49 ¹⁷⁷	4.77 ¹⁷⁷	
Ir	(100)	5.54	5.42	5.55 ¹⁷⁶	5.91 ²⁰	5.96 ^{183*}
	(111)	5.42	5.18	5.5 ¹⁷⁶	5.86 ²⁰	5.78 ^{183*}
	(110)	5.01	4.83	4.96 ¹⁷⁶	5.31 ²⁰	5.42 ^{183*}
	(321)	5.0		5.07 ¹⁷⁶		5.4 ^{171*}
	(211)	5.21		5.28 ¹⁷⁶		
	(310)	5.04		5.13 ¹⁷⁶		
	(210)	4.94				5.0 ^{171*}
	(331)	4.87				5.4 ^{171*}
Cd	(0001)	3.63	3.76	3.81 ²⁰	4.21 ²⁰	
	(10 $\bar{1}$ 0)	3.72		4.08 ²⁰	4.49 ²⁰	
	(21 $\bar{3}$ 0)	3.76		3.9 ²⁰	4.21 ²⁰	
Au	(100)	5.0	4.9	5.07 ⁸	5.49 ⁸	5.22 ^{183*}
	(111)	5.16	4.98	5.12 ⁸	5.49 ⁸	5.33 ^{183*}

Table A.2: A comparison of the high-throughput values to experimental and computed values for materials from the literature (continued).

Material	Surface	Work function Φ (eV)				
		HT	GGA(RPBE)	GGA(PBE)	LDA	Experiment
	(110)	4.93	4.88	4.94 ⁸	5.36 ⁸	5.16 ^{183*}
	(321)	4.89		4.98 ¹⁷⁶		
	(211)	4.96		5.01 ¹⁷⁶		
	(310)	4.93		4.92 ¹⁷⁶		
	(210)	4.71				4.96 ^{171*}
	(311)	4.94				5.16 ^{171*}
Cu	(111)	4.71	4.74	4.88 ⁸	5.2 ⁸	4.9 ^{183*}
	(110)	4.2	4.32	4.38 ⁸	4.68 ⁸	4.56 ^{183*}
	(100)	4.47		4.42 ⁸	4.79 ⁸	4.73 ^{183*}
	(321)	4.22		4.35 ¹⁷⁶		
	(211)	4.22		4.45 ¹⁷⁶		4.53 ^{171*}
	(310)	4.17		4.26 ¹⁷⁶		
	(210)	4.18				4.37 ^{171*}
	(311)	4.28				4.42 ^{171*}
Cr	(110)	4.7	4.74	4.83 ²⁰	5.13 ²⁰	
	(111)	4.04		4.09 ²⁰	4.39 ²⁰	
	(100)	4.08		4.02 ²⁰	4.36 ²⁰	
Zr	(0001)	4.16	3.98	4.18 ²⁰	4.46 ²⁰	
	(10 $\bar{1}$ 0)	3.52		3.84 ²⁰	4.16 ²⁰	
	(21 $\bar{3}$ 0)	3.11		3.09 ²⁰	3.39 ²⁰	
Li	(100)	2.96		2.99 ¹⁷⁶	3.13 ²⁰	

Table A.2: A comparison of the high-throughput values to experimental and computed values for materials from the literature (continued).

Material	Surface	Work function Φ (eV)			
		HT	GGA(RPBE)	GGA(PBE)	LDA
	(110)	3.18		3.22 ¹⁷⁶	3.36 ²⁰
	(111)	2.6		2.75 ¹⁷⁶	2.92 ²⁰
	(210)	2.99		2.97 ¹⁷⁶	
	(331)	2.94		3.01 ¹⁷⁶	
	(311)	2.91		3.0 ¹⁷⁶	
Na	(100)	2.53		2.64 ¹⁷⁶	2.8 ²⁰
	(110)	2.71		2.84 ¹⁷⁶	2.96 ²⁰
	(111)	2.5		2.58 ¹⁷⁶	2.76 ²⁰
	(210)	2.65		2.68 ¹⁷⁶	
	(331)	2.49		2.73 ¹⁷⁶	
	(311)	2.45		2.69 ¹⁷⁶	
K	(100)	2.15		2.22 ¹⁷⁶	2.37 ²⁰
	(110)	2.37		2.37 ¹⁷⁶	2.52 ²⁰
	(111)	2.13		2.18 ¹⁷⁶	2.36 ²⁰
	(210)	1.95		2.23 ¹⁷⁶	
	(331)	2.29		2.29 ¹⁷⁶	
	(311)	2.15		2.24 ¹⁷⁶	
Rb	(100)	2.1		2.12 ¹⁷⁶	2.29 ²⁰
	(110)	2.23		2.24 ¹⁷⁶	2.41 ²⁰
	(111)	2.05		2.1 ¹⁷⁶	2.29 ²⁰
	(210)	1.94		2.13 ¹⁷⁶	

Table A.2: A comparison of the high-throughput values to experimental and computed values for materials from the literature (continued).

Material	Surface	Work function Φ (eV)			
		HT	GGA(RPBE)	GGA(PBE)	LDA
	(331)	2.18		2.18 ¹⁷⁶	
	(311)	2.08		2.13 ¹⁷⁶	
Cs	(100)	1.97		1.97 ¹⁷⁶	2.16 ²⁰
	(110)	2.04		2.07 ¹⁷⁶	2.25 ²⁰
	(111)	1.59		1.97 ¹⁷⁶	2.17 ²⁰
	(210)	1.77		2.0 ¹⁷⁶	
	(311)	1.65		2.0 ¹⁷⁶	
Ca	(100)	2.56		2.76 ¹⁷⁶	2.85 ²⁰
	(110)	2.74		2.81 ¹⁷⁶	2.95 ²⁰
	(111)	2.94		2.94 ¹⁷⁶	3.01 ²⁰
	(321)	2.52		2.78 ¹⁷⁶	
	(211)	2.55		2.83 ¹⁷⁶	
Sr	(310)	2.39		2.71 ¹⁷⁶	
	(100)	2.47		2.47 ¹⁷⁶	2.56 ²⁰
	(110)	2.49		2.54 ¹⁷⁶	2.66 ²⁰
	(111)	2.53		2.57 ¹⁷⁶	2.67 ²⁰
	(321)	2.33		2.51 ¹⁷⁶	
Ba	(211)	2.37		2.45 ¹⁷⁶	
	(310)	2.31		2.47 ¹⁷⁶	
	(100)	2.28		2.31 ¹⁷⁶	2.54 ²⁰
	(110)	2.35		2.38 ¹⁷⁶	2.58 ²⁰

Table A.2: A comparison of the high-throughput values to experimental and computed values for materials from the literature (continued).

Material	Surface	Work function Φ (eV)			
		HT	GGA(RPBE)	GGA(PBE)	LDA
	(111)	2.24		2.29 ¹⁷⁶	2.58 ²⁰
	(210)	1.9		2.35 ¹⁷⁶	
	(331)	2.35		2.34 ¹⁷⁶	
	(311)	2.21		2.33 ¹⁷⁶	
Be	(0001)	5.32		5.29 ¹⁷⁷	5.45 ¹⁷⁷
	(10 $\bar{1}$ 0)	4.48		4.52 ¹⁷⁷	4.71 ¹⁷⁷
	(10 $\bar{1}$ 1)	4.95		5.03 ¹⁷⁷	5.23 ¹⁷⁷
	(10 $\bar{1}$ 2)	4.71		4.81 ¹⁷⁷	5.04 ¹⁷⁷
	(11 $\bar{2}$ 1)	4.35		4.58 ¹⁷⁷	4.82 ¹⁷⁷
	(21 $\bar{1}$ 2)	4.79		4.81 ¹⁷⁷	4.94 ¹⁷⁷
	(21 $\bar{3}$ 0)	4.14		4.17 ¹⁷⁷	4.38 ¹⁷⁷
Mg	(0001)	3.61		3.76 ¹⁷⁷	3.89 ¹⁷⁷
	(10 $\bar{1}$ 0)	3.39		3.64 ¹⁷⁷	3.76 ¹⁷⁷
	(10 $\bar{1}$ 1)	3.64		3.7 ¹⁷⁷	3.88 ¹⁷⁷
	(10 $\bar{1}$ 2)	3.58		3.63 ¹⁷⁷	3.74 ¹⁷⁷
	(11 $\bar{2}$ 1)	3.4		3.56 ¹⁷⁷	3.68 ¹⁷⁷
	(21 $\bar{1}$ 2)	3.62		3.67 ¹⁷⁷	3.8 ¹⁷⁷
	(21 $\bar{3}$ 0)	3.35		3.49 ¹⁷⁷	3.72 ¹⁷⁷
Al	(111)	4.0		4.2 ⁸	4.97 ⁸
	(100)	4.18		4.27 ⁸	4.41 ⁸
	(110)	4.0		3.96 ⁸	4.08 ⁸
					4.23 ^{183*}

Table A.2: A comparison of the high-throughput values to experimental and computed values for materials from the literature (continued).

Material	Surface	Work function Φ (eV)			
		HT	GGA(RPBE)	GGA(PBE)	LDA
Ga	(001)	3.9		4.01^{20}	4.33^{20}
	(100)	4.19		4.22^{20}	4.56^{20}
	(010)	4.35		4.61^{20}	4.96^{20}
In	(001)	3.74		3.88^{20}	4.22^{20}
	(100)	3.81		3.79^{20}	4.12^{20}
	(110)	3.81		3.92^{20}	4.3^{20}
Tl	(0001)	3.5		3.56^{20}	3.98^{20}
	(10 $\bar{1}$ 0)	3.42		3.56^{20}	3.98^{20}
	(21 $\bar{3}$ 0)	3.34		3.52^{20}	3.94^{20}
	(21 $\bar{3}$ 1)	3.27		3.52^{20}	3.95^{20}
C($P6_3/mmc$)	(0001)	5.02		4.57^{20}	4.76^{20}
C($Fd\bar{3}m$)	(111)	4.61		4.36^{20}	4.54^{20}
	(100)	5.17		5.63^{20}	5.63^{20}
	(110)	5.22		5.3^{20}	5.56^{20}
Si	(111)	4.64		4.67^{20}	4.81^{20}
	(100)	4.79		4.56^{20}	4.71^{20}
	(110)	4.97		5.0^{20}	5.23^{20}
Ge	(111)	4.52		4.38^{20}	4.55^{20}
	(100)	4.41		4.48^{20}	4.72^{20}
	(110)	4.51		4.74^{20}	4.99^{20}
Sn	(111)	4.21		4.15^{20}	4.37^{20}

Table A.2: A comparison of the high-throughput values to experimental and computed values for materials from the literature (continued).

Material	Surface	Work function Φ (eV)			
		HT	GGA(RPBE)	GGA(PBE)	LDA
Pb	(100)	4.38		4.23^{20}	4.49^{20}
	(110)	4.5		4.4^{20}	4.71^{20}
Pb	(111)	3.68		3.76^{20}	4.08^{20}
	(100)	3.71		3.8^{20}	4.1^{20}
As	(110)	3.6		3.73^{20}	4.03^{20}
	(0001)	4.44		4.41^{20}	4.71^{20}
Sb	(0001)	4.23		4.24^{20}	4.5^{20}
	(10 $\bar{1}$ 0)	4.29		4.39^{20}	4.72^{20}
Bi	(11 $\bar{2}$ 0)	4.24		4.41^{20}	4.62^{20}
	(0001)	3.98		4.07^{20}	4.37^{20}
Ti	(11 $\bar{2}$ 0)	3.98		4.14^{20}	4.39^{20}
	(0001)	4.38		4.42^{20}	4.67^{20}
Ti	(10 $\bar{1}$ 0)	3.51		3.9^{20}	4.23^{20}
	(21 $\bar{3}$ 0)	3.21		3.19^{20}	3.45^{20}
Ti	(21 $\bar{3}$ 1)	3.26		3.51^{20}	3.8^{20}

* See reference herein

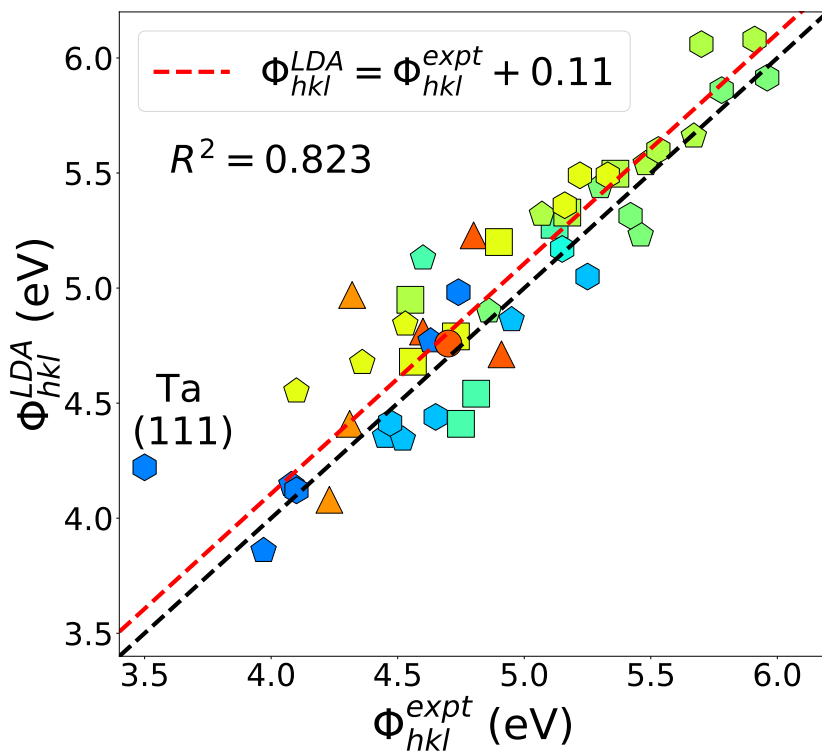


Figure A.1: Plot of computed facet-dependent Φ_{hkl} using LDA from the literature^{8,20,177} vs experimental values^{171,183,196}.

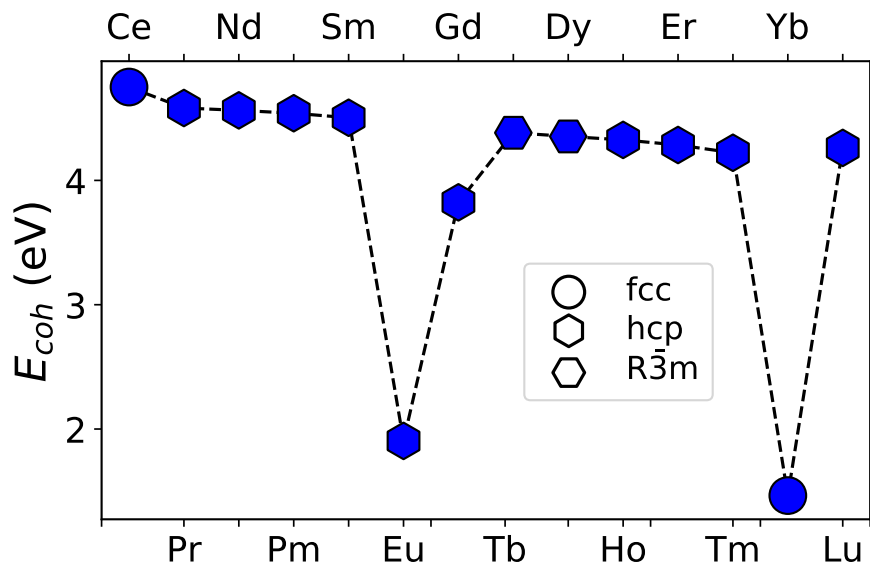


Figure A.2: Plot of the cohesive energy (E_{coh}) versus the group number for lanthanides.

* See reference herein

Table A.3: The R values for γ_{hkl} and Φ_{hkl} as a function of normalized broken bonds per surface area ($\bar{B}\bar{B}$) and Φ_{hkl} as a function of γ_{hkl} .

Material	spacegroup	R values				
		γ_{hkl} vs $\bar{B}\bar{B}$		Φ_{hkl} vs $\bar{B}\bar{B}$		Φ_{hkl} vs γ_{hkl}
		1stNN	2ndNN	1stNN	2ndNN	
Cu	$Fm - 3m$	0.99	–	-0.93	–	-0.93
Er	$P6_3/mmc$	-0.06	0.84	0.24	-0.90	-0.77
La	$P6_3/mmc$	0.53	0.98	-0.72	-0.89	-0.73
Re	$P6_3/mmc$	0.57	0.79	0.02	-0.89	-0.28
Ag	$Fm - 3m$	0.96	–	-0.89	–	-0.88
Ni	$Fm - 3m$	1.00	–	-0.89	–	-0.85
Ru	$P6_3/mmc$	-0.40	0.95	0.64	-0.88	-0.91
Ho	$P6_3/mmc$	0.35	0.75	-0.24	-0.88	-0.70
Zr	$P6_3/mmc$	0.52	0.73	-0.15	-0.87	-0.48
Nb	$Im - 3m$	0.47	0.88	-0.86	-0.43	-0.72
Au	$Fm - 3m$	0.92	–	-0.86	–	-0.74
Eu	$P6_3/mmc$	-0.02	0.77	0.20	-0.84	-0.74
Tc	$P6_3/mmc$	0.80	0.92	-0.18	-0.84	-0.42
Y	$P6_3/mmc$	-0.07	0.78	0.23	-0.83	-0.61
Lu	$P6_3/mmc$	-0.01	0.70	0.05	-0.82	-0.70
Rh	$Fm - 3m$	0.97	–	-0.82	–	-0.68
W	$Im - 3m$	0.94	-0.00	-0.81	-0.52	-0.65
Tm	$P6_3/mmc$	0.34	0.69	-0.15	-0.80	-0.47
Li	$Im - 3m$	-0.38	0.77	-0.34	-0.79	-0.43

Table A.3: The R values for γ_{hkl} and Φ_{hkl} as a function of normalized broken bonds per surface area ($\overline{\text{BB}}$) and Φ_{hkl} as a function of γ_{hkl} (continued).

Material	spacegroup	R values				
		γ_{hkl} vs $\overline{\text{BB}}$		Φ_{hkl} vs $\overline{\text{BB}}$		Φ_{hkl} vs γ_{hkl}
		1stNN	2ndNN	1stNN	2ndNN	
Sc	$P6_3/mmc$	0.67	0.67	-0.23	-0.79	-0.66
Ta	$Im-3m$	0.19	0.96	-0.78	-0.51	-0.60
Mo	$Im-3m$	0.47	0.21	-0.78	-0.53	-0.55
Pd	$Fm-3m$	0.95	–	-0.78	–	-0.71
Cr	$Im-3m$	0.87	0.17	-0.61	-0.74	-0.38
Ti	$P6_3/mmc$	0.67	0.21	0.34	-0.74	0.42
V	$Im-3m$	-0.27	0.89	-0.74	-0.67	-0.40
Cs	$Im-3m$	0.87	0.89	-0.73	-0.65	-0.83
Be	$P6_3/mmc$	0.45	0.88	0.43	-0.73	-0.15
Hf	$P6_3/mmc$	0.80	0.82	0.11	-0.73	0.07
Ir	$Fm-3m$	0.93	–	-0.72	–	-0.50
Co	$P6_3/mmc$	0.57	0.95	-0.68	-0.71	-0.47
Pt	$Fm-3m$	0.88	–	-0.71	–	-0.51
Ca	$Fm-3m$	0.86	–	-0.70	–	-0.41
Nd	$P6_3/mmc$	0.07	0.94	0.22	-0.70	-0.23
Pr	$P6_3/mmc$	0.03	0.95	0.28	-0.65	-0.15
Tl	$P6_3/mmc$	0.79	0.83	-0.19	-0.65	-0.57
Mg	$P6_3/mmc$	0.30	0.82	-0.64	-0.26	-0.23
Na	$Im-3m$	0.38	0.97	-0.49	-0.62	-0.62

Table A.3: The R values for γ_{hkl} and Φ_{hkl} as a function of normalized broken bonds per surface area ($\overline{\text{BB}}$) and Φ_{hkl} as a function of γ_{hkl} (continued).

Material	spacegroup	R values				
		γ_{hkl} vs $\overline{\text{BB}}$		Φ_{hkl} vs $\overline{\text{BB}}$		Φ_{hkl} vs γ_{hkl}
		1stNN	2ndNN	1stNN	2ndNN	
Os	$P6_3/mmc$	-0.10	0.94	0.24	-0.60	-0.30
Sm	$P6_3/mmc$	0.10	0.70	-0.32	-0.58	0.09
Sr	$Fm - 3m$	0.85	–	-0.56	–	-0.46
K	$Im - 3m$	0.22	0.95	-0.55	-0.44	-0.38
Zn	$P6_3/mmc$	0.59	0.48	-0.51	0.44	-0.20
Ce	$Fm - 3m$	0.96	–	-0.49	–	-0.49
Fe	$Im - 3m$	0.40	0.23	-0.44	-0.48	-0.49
Pm	$P6_3/mmc$	0.46	0.88	-0.40	-0.44	-0.21
Yb	$Fm - 3m$	0.76	–	-0.44	–	-0.23
Rb	$Im - 3m$	0.22	0.94	-0.35	-0.39	-0.45
Ba	$Im - 3m$	-0.01	0.98	-0.20	-0.04	0.01
Pb	$Fm - 3m$	0.94	–	-0.05	–	0.02
Cd	$P6_3/mmc$	0.53	0.51	0.01	0.41	0.24
Al	$Fm - 3m$	0.97	–	0.22	–	0.09

* See reference herein

Appendix B

**Supporting information: Morphology
control of tantalum carbide nanoparticles
through dopant additions and surface
segregation**

B.1 Surface energy

In general, the surface energies of undoped TaC can be obtained from the following expression:

$$\gamma(\Delta\mu_C) = \frac{E^{slab} - N_{Ta}g_{TaC}^{bulk}}{2A} + \Gamma_C(\Delta\mu_C + E_C^{graphite}) \quad (\text{B.1})$$

where $\gamma(\Delta\mu_C)$ is the surface energy as a function of the carbon chemical potential, $\Delta\mu_C$ relative to the energy of graphite per atom ($E_C^{graphite}$), g_{TaC}^{bulk} is the Gibbs free energy of bulk TaC per formula unit, A is the cross-sectional area, E_{slab} is the total DFT energy of the slab, $\Gamma_C = \frac{1}{2A}(N_{Ta} - N_C)$ is the number of excess or deficient C atoms per surface area (coverage), which is negative for excess C and positive for deficient C, and N_{Ta} and N_C is the number of Ta and C atoms in the slab, respectively. For a stoichiometric system, such as the undoped (100) slab of TaC (Table B.1: row 1), $\Gamma_C = 0$ and the surface energy becomes a constant value given by:

$$\gamma = \frac{1}{2A}[E^{slab} - N_{Ta}g_{TaC}^{bulk}] \quad (\text{B.2})$$

Equation B.1 can be derived from its more generalized form:

$$\gamma(\Delta\mu_i) = \frac{1}{2A}[E^{slab} - \sum_i N_i \mu_i] \quad (\text{B.3})$$

where the chemical potential accounts for excess or deficient atomic species exchanged between the surface and an external reservoir (*i.e.*, the surrounding environment in the form of a gas, liquid or bulk phase). All coefficients and constants for surface energy provided in Table B.1 can be derived from this expression. For the case of an undoped TaC surface, we can expand Equation B.3 to:

$$\gamma = \frac{1}{2A}[E^{slab} - N_{Ta}\mu_{Ta} - N_C\mu_C] \quad (\text{B.4})$$

Assuming the surface phase is in equilibrium with the bulk, the chemical potential for all

species in the undoped system is connected via Gibbs free energy by:

$$g_{\text{TaC}}^{\text{bulk}} = \sum_i n_i = \mu_{\text{Ta}} + \mu_C \quad (\text{B.5})$$

where n_i is the stoichiometry of species i per formula unit ($n_{\text{Ta}} = n_C = 1$ in TaC). Assuming there is no configurational entropy or pressure-volume effects, g^{bulk} can be calculated as the total bulk DFT energy per formula unit. We can therefore simplify Equation B.4 as a function of μ_C by substituting Equation B.5 for μ_{Ta} to obtain:

$$\gamma = \frac{1}{2A} [E^{\text{slab}} - N_{\text{Ta}}(g_{\text{TaC}}^{\text{bulk}} - \mu_C) - N_C \mu_C] \quad (\text{B.6})$$

Table B.1: The coefficients and constants, see (Equation B.14), used to calculate the surface energy as a function of $\Delta\mu_i$ for all slab models. Values of Γ_i are the coefficients to $\Delta\mu_i$ in units of \AA^{-2} and represent the coverages of species i at the surface, while the units of the constant b are eV\AA^{-2} . Entries labeled with * correspond to values for TiTa_3C_4 .

(hkl)	Dopant (X)	Site	Γ_C	Γ_X	Γ_{Ti}	Constant (b)
1	(100)	Undoped	–	–	–	0.0915
2	(111)	Undoped	–	0.0576	–	0.1849
3	(100)	Ni	sub	-0.0199	-0.0199	–
4	(111)	Ni	surf	0.0346	-0.0230	–
5	(100)	Co	sub	-0.0199	-0.0199	–
6	(111)	Co	surf	0.0346	-0.0230	–
7	(100)	Fe	sub	-0.0199	-0.0199	–
8	(111)	Fe	surf	0.0346	-0.0230	–
11	(100)	Nb	sub	-0.0199	-0.0199	–
12	(111)	Nb	surf	0.0346	-0.0230	–
15*	(100)	Undoped	–	0.0169	–	0.0169
16*	(111)	Undoped	–	0.0584	–	0.1960
17*	(100)	Ni	sub	-0.0169	-0.0253	0.0084
18*	(111)	Ni	surf	0.0195	-0.0292	-0.0097
						0.0141

An upper and lower bound is needed for μ_C to allow a reasonable range for the surface energy due to the exchange of C atoms between the surface and the external reservoir. The upper

bound is set by the assumption that an excess amount of C at the surface will eventually lead to the formation of surface graphite, while the lower bound is set by the assumption that a surface deficiency of C (or equivalently an excess of Ta) will lead to the formation of Ta₂C. This range for μ_C is expressed as:

$$E_{\text{Ta}_2\text{C}} - 2E_{\text{Ta}}^{\text{bcc}} - E_C^{\text{graphite}} \leq \mu_C \leq E_C^{\text{graphite}} \quad (\text{B.7})$$

where $E_{\text{Ta}_2\text{C}}$ is the energy per formula unit of Ta₂C, $E_{\text{Ta}}^{\text{bcc}}$ and E_C^{graphite} are the energies per atom of body-centered Ta and graphite, respectively. For convenience, we set the upper bound as a zero reference by subtracting E_C^{graphite} from μ_C leaving:

$$\Delta G_{\text{Ta}_2\text{C}}^f \leq \Delta \mu_C \leq 0 \quad (\text{B.8})$$

where $\Delta G_{\text{Ta}_2\text{C}}^f = E_{\text{Ta}_2\text{C}} - 2E_{\text{Ta}}^{\text{bcc}} - E_C^{\text{graphite}}$ is the formation energy of Ta₂C and $\mu_C = \Delta \mu_C + E_C^{\text{graphite}}$. Substituting our expression for μ_C into Equation B.6 will yield an expression for the surface energy of an undoped, non-stoichiometric slab (Table B.1: row 2) in Equation B.1.

With the addition of an external component (*e.g.*, a dopant), a new chemical potential term (μ_X) is added to Equation B.1. As with μ_C , we need an appropriate upper bound, which we set as E_X^{atom} , the total energy of an atom X isolated in a vacuum. We choose this reference assuming the dopant atoms will interact similarly to a metallic gas with the surface. We substitute μ_X into Equation B.1 in a manner similar to μ_C to yield an expression for the surface energy of a doped slab as a function of $\Delta \mu_i$ (Table B.1: row 3 to 14):

$$\gamma(\Delta \mu_C, \Delta \mu_X) = \frac{E^{\text{slab}+X} - N_{\text{Ta}} g_{\text{TaC}}^{\text{bulk}}}{2A} + \Gamma_C(\Delta \mu_C + E_C^{\text{graphite}}) - \Gamma_X(\Delta \mu_X + E_X^{\text{atom}}) \quad (\text{B.9})$$

where $\Gamma_X = \frac{1}{2A} N_X$ is the coverage of dopant X in the slab and $E^{\text{slab}+X}$ is the total energy of a slab with dopant X.

Similar to Equation B.5, for an undoped non-stoichiometric TiTa_3C_4 slab (Table B.1: row 15 to 16), we can solve for μ_{Ta} :

$$\mu_{Ta} = \frac{g_{\text{TiTa}_3\text{C}_4}^{\text{bulk}} - 4\mu_C - \mu_{Ti}}{3} \quad (\text{B.10})$$

The numbers 4 and 3 in this equation are the values of n_C and n_{Ta} , respectively. We set the upper bound of n_{Ti} as the energy per atom of a hexagonal close packed Ti bulk system (E_{Ti}^{hcp}) and again rewrite Equation B.3 as a function of $\Delta\mu_i$:

$$\gamma(\Delta\mu_C, \Delta\mu_{Ti}) = \frac{E^{\text{slab}} - \frac{N_{Ta}}{3} g_{\text{TiTa}_3\text{C}_4}^{\text{bulk}}}{2A} + \Gamma_C(\Delta\mu_C + E_C^{\text{graphite}}) - \Gamma_{Ti}(\Delta\mu_{Ti} + E_{Ti}^{\text{hcp}}) \quad (\text{B.11})$$

with $\Gamma_C = \frac{1}{2A}(\frac{4}{3}N_{Ta} - N_C)$ and $\Gamma_{Ti} = \frac{1}{2A}(\frac{1}{3}N_{Ta} - N_{Ti})$. For a slab where only one species is non-stoichiometric, such as C in the (111) slab of TiTa_3C_4 (Table B.1: row 16), Equation B.11 simplifies to:

$$\gamma(\Delta\mu_C, \Delta\mu_{Ti}) = \frac{E^{\text{slab}} - \frac{N_{Ta}}{3} g_{\text{TiTa}_3\text{C}_4}^{\text{bulk}}}{2A} + \Gamma_C(\Delta\mu_C + E_C^{\text{graphite}}) \quad (\text{B.12})$$

For a doped slab of TiTa_3C_4 (Table B.1: row 17 and 18), we again add an $N_X\mu_X$ term to Equation B.11 to obtain:

$$\gamma(\Delta\mu_C, \Delta\mu_{Ti}) = \frac{E^{\text{slab}} - \frac{N_{Ta}}{3} g_{\text{TiTa}_3\text{C}_4}^{\text{bulk}}}{2A} + \Gamma_C(\Delta\mu_C + E_C^{\text{graphite}}) - \Gamma_{Ti}(\Delta\mu_{Ti} + E_{Ti}^{\text{hcp}}) - \Gamma_X(\Delta\mu_X + E_X^{\text{atom}}) \quad (\text{B.13})$$

In summary, we can generalize the surface energy of all systems as a linear equation with a constant value, b , as follows:

$$\gamma(\Delta\mu_i) = b + \sum_i \Gamma_i \Delta\mu_i \quad (\text{B.14})$$

All values of b and Γ_i for the surface energy of each slab are listed in Table B.1.

B.2 Compositions and X-ray diffraction patterns

Table B.2: Dopant concentrations on the TaC powders determined from energy dispersive spectroscopy. The dopant concentrations listed for the Ni/Ti-doped TaC powders represent the concentrations of Ti in the powders. The concentration of Ni for these powders was fixed at 2.5 at.%.

Sample Number	Ni (at.%)	Co (at.%)	Fe (at.%)	Nb (at.%)	Ni/Ti (at.%)
1	0.9	0.9	0.5	4.4	2.2
2	1.4	1.6	1.2	7.8	4.1
3	1.7	1.9	2.2	-	8.0
4	2.5	2.3	2.7	-	12.4
5	4.1	2.6	4.0	-	16.4
6	5.7	3.4	4.2	-	18.5
7	-	-	4.8	-	-

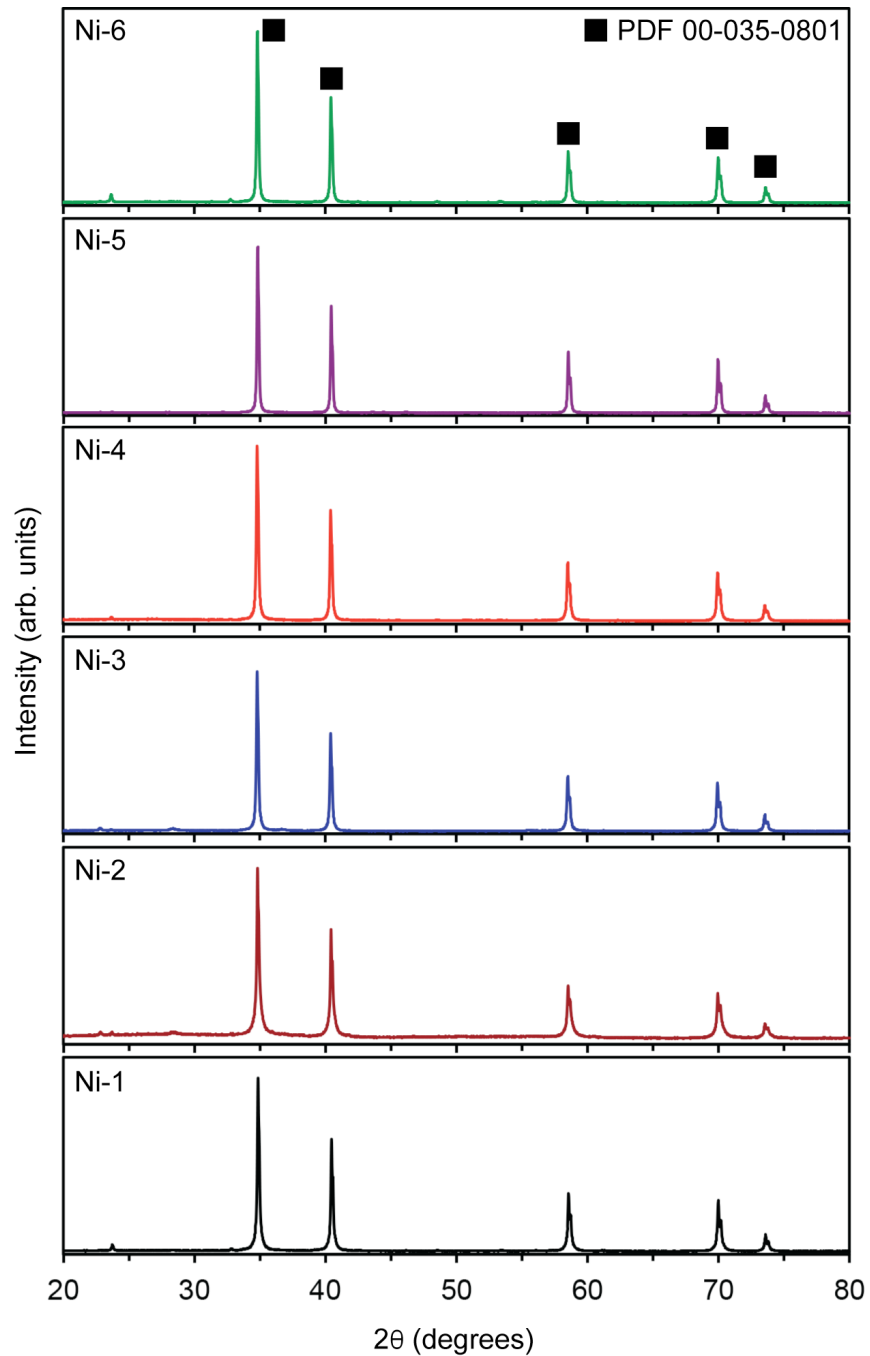


Figure B.1: X-ray diffraction patterns of Ni-doped TaC powders.

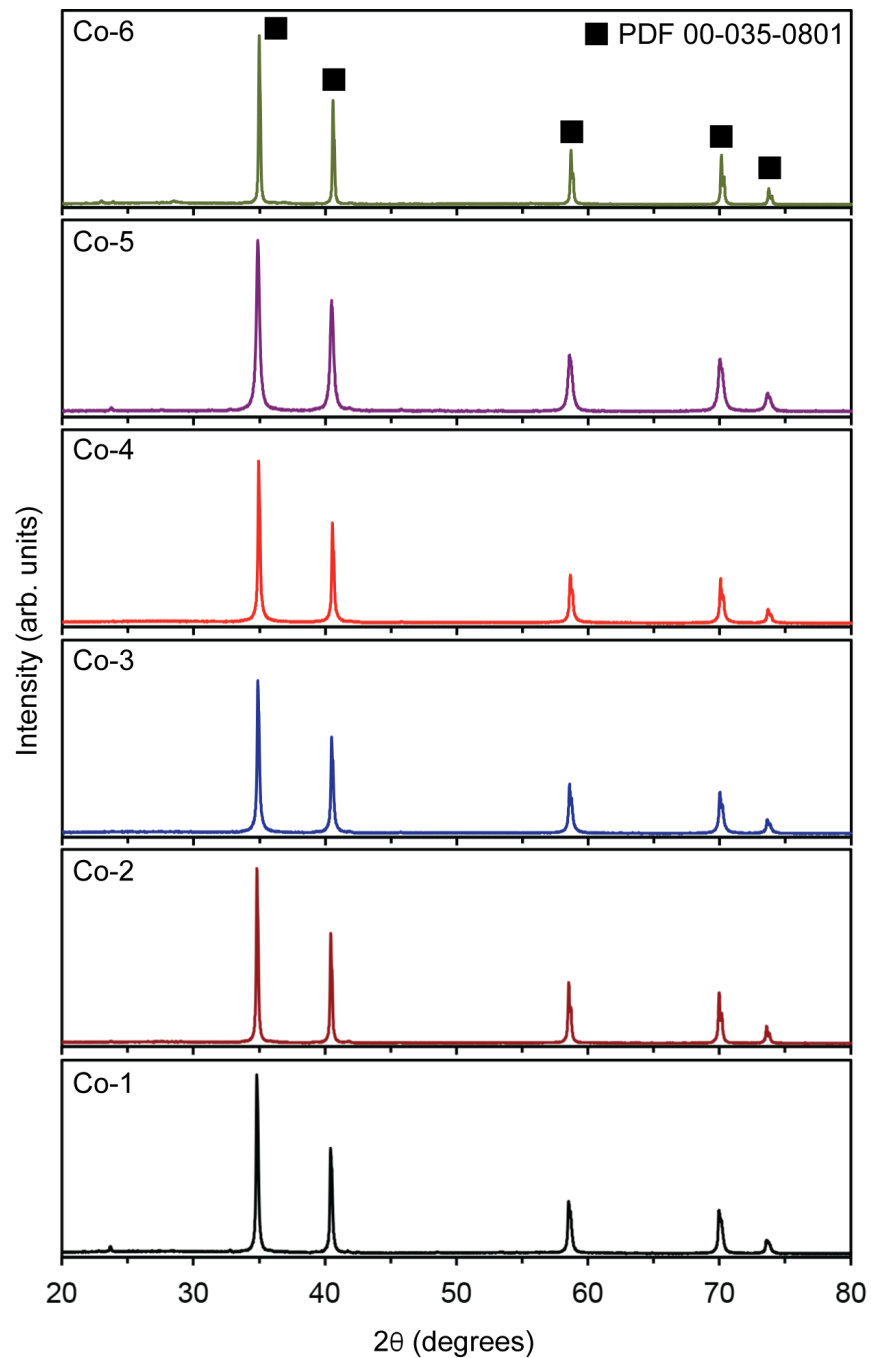


Figure B.2: X-ray diffraction patterns of Co-doped TaC powders.

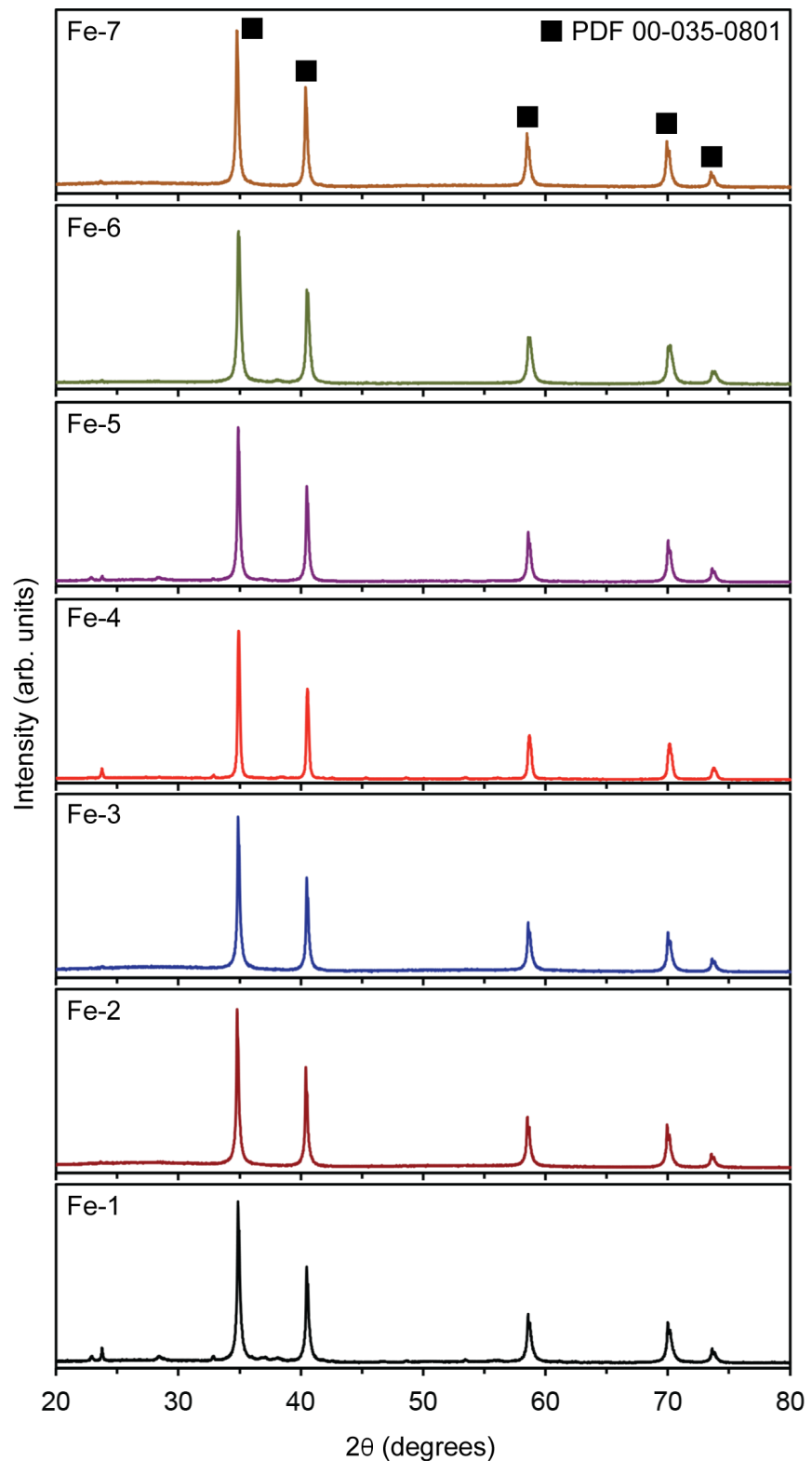


Figure B.3: X-ray diffraction patterns of Fe-doped TaC powders.

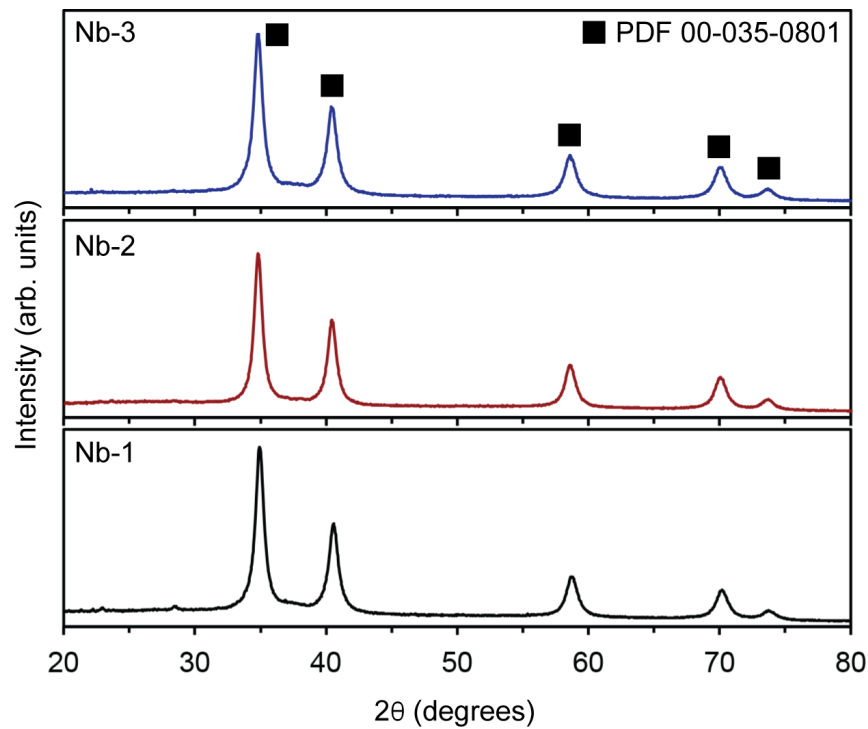


Figure B.4: X-ray diffraction patterns of Nb-doped TaC powders.

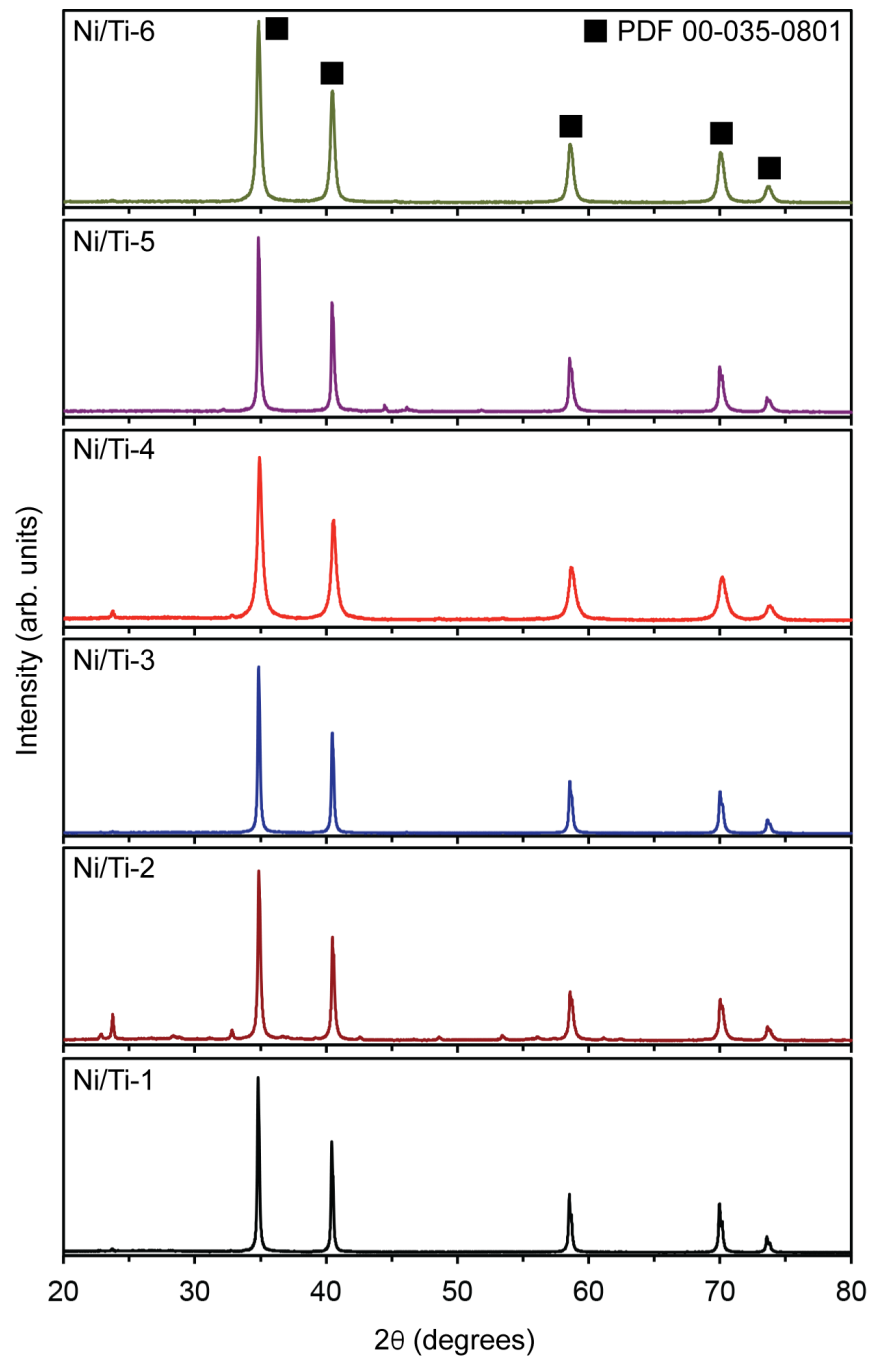


Figure B.5: X-ray diffraction patterns of Ni/Ti-doped TaC powders.

Appendix C

**Supporting information: Computational
study of metallic dopant segregation and
embrittlement at molybdenum grain
boundaries**

C.1 Convergence tests

Figure C.1 presents a set of convergence tests that were performed for both the tilt and twist GB to optimize the parameters for efficient and accurate calculations. Figures C.1a and C.1b varies the size of the GB in the direction normal to their GB planes to find the minimum distance required to minimize interaction with their periodic images. Here, we choose Nb as the dopant in both GBs and Site 0 of the tilt and twist GBs were substituted with the dopant. Figures C.1c and C.1d show the k -point convergence. k -point along the c lattice parameter is set to be 1.

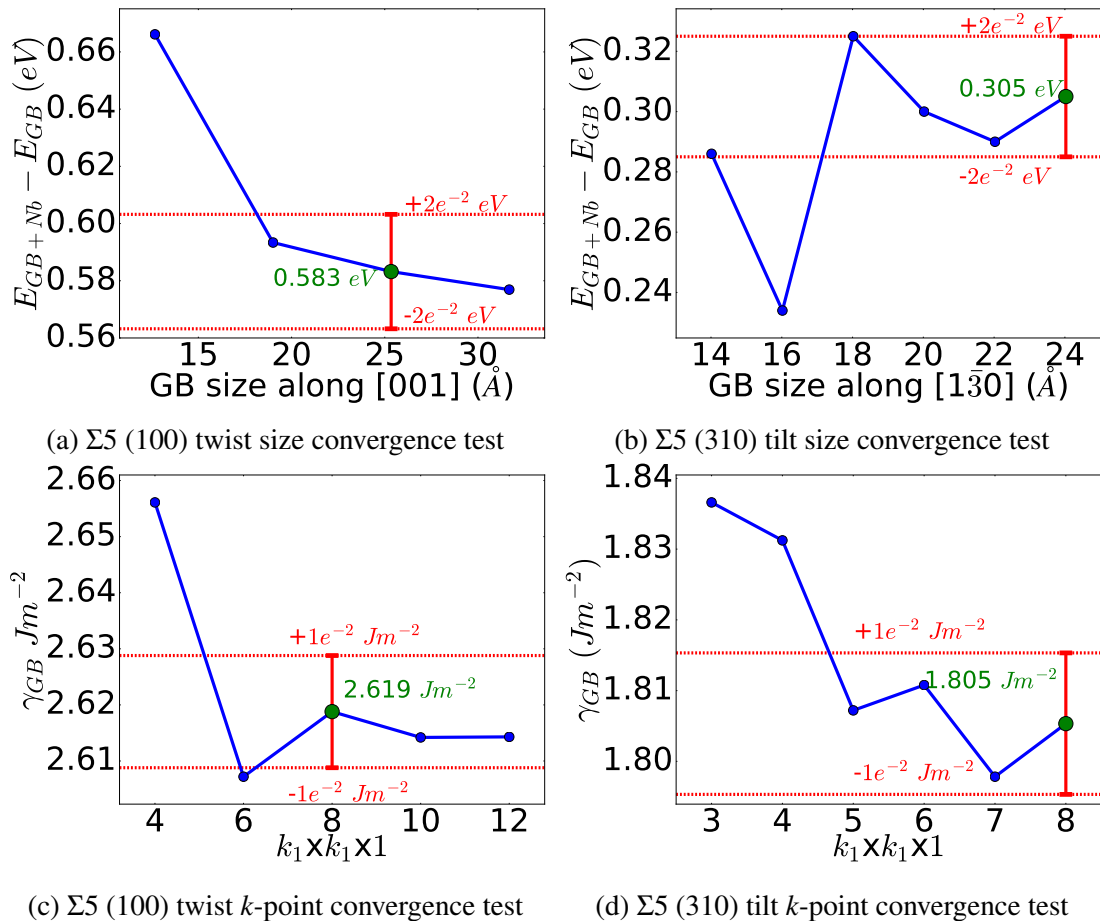


Figure C.1: Convergence tests for validating GB size and k -points. $E_{GB+Nb} - E_{GB}$ is converged with respect to the lattice size along the [001] and [1̄30] direction for the twist GB C.1a and tilt GB C.1b. The GB energy (γ_{GB}) is converged with respect to k_1 ($k_1 = k_2$) for the twist GB C.1c and the tilt GB C.1d.

C.2 Comparison of E_{seg}^X for Mo and W grain boundaries

To validate our calculations, we compared the trends of various dopants in relation to their E_{seg}^X in the Mo twist and tilt GBs with W $\Sigma 3(111)$ tilt GB system from literature⁵⁰. Mo and W are both refractory materials from the same group in the periodic table with similar chemical behaviors. We expect the dopant interactions with the host material to be similar. Figure C.2 shows that among the dopants considered, the site preferences, magnitude of the preference and the sign (GB or bulk preference) of the E_{seg}^X values in the three systems are consistent with each other.

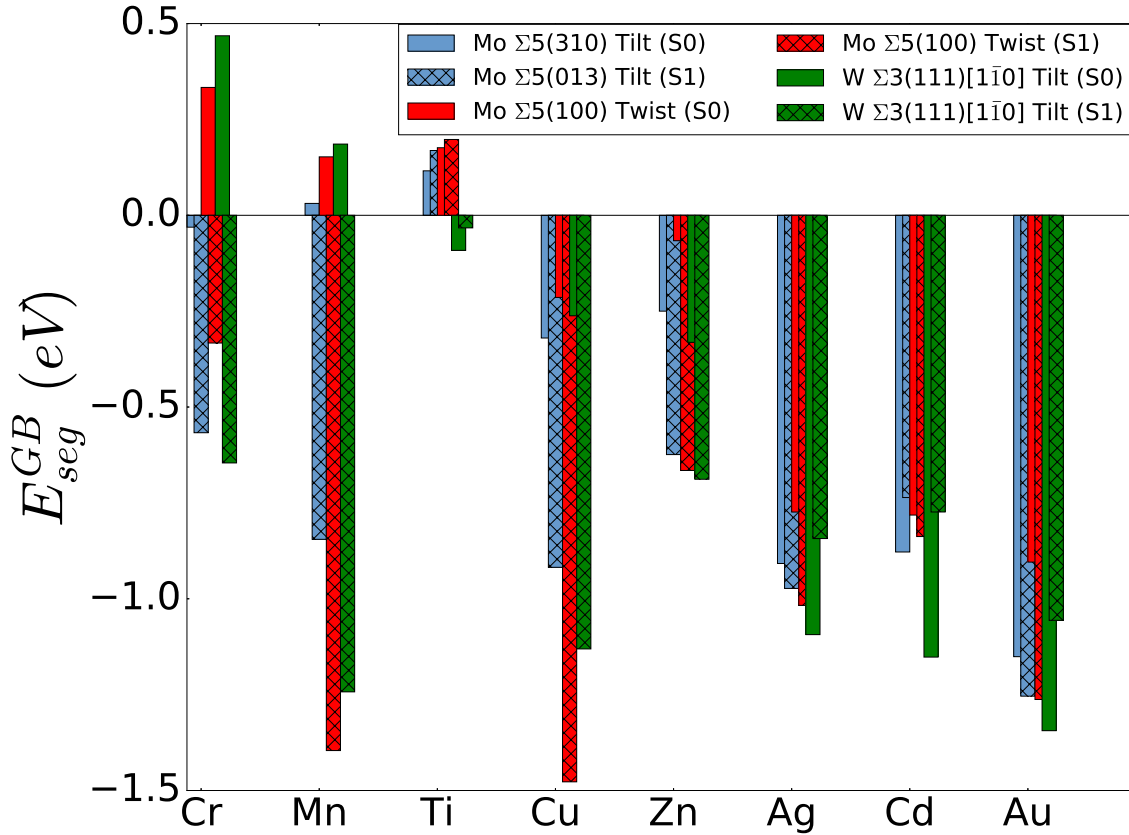


Figure C.2: Comparison of E_{seg}^X for selected dopants in Mo tilt and twist and W GB. The values for the W system are obtained from a study by Li et al.⁵⁰

C.3 Solubility of dopants in Molybdenum

The formation of intermetallic compounds occurs when the solubility of a dopant in the host structure is high. It is therefore axiomatic that when a dopant is more likely to form an intermetallic compound with the host, it is also less likely to segregate into the grain boundary³²¹. Here we quantitatively demonstrate the dependence of E_{seg}^X on dopant solubility in Figure C.3. It is clear that less soluble dopants in Mo tend to segregate into the grain boundary which is in agreement with the previous model for GB segregation proposed by Hondros et al.⁵⁹.

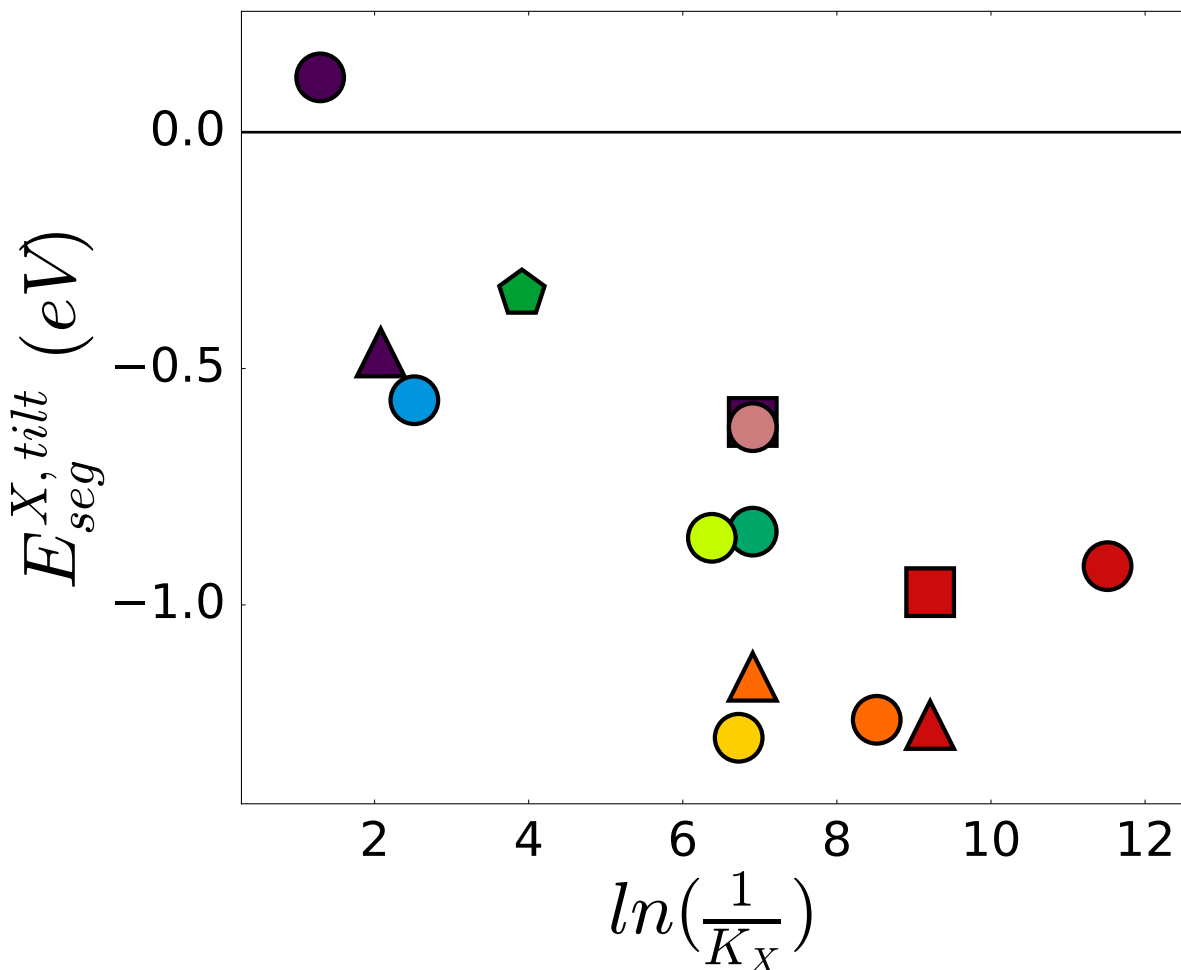


Figure C.3: The dependence of the segregation energy E_{seg}^X on the solubility of the dopants (K_X) in bulk Mo. Values for K_X were extrapolated at 800 K from experimentally derived phase diagrams^{322–325}.

C.4 Corresponding figures for $\Sigma 5$ (100) twist GB

For completeness, the figures for the twist GB corresponding to the figures presented for the tilt GB in regards to E_{SE} from the main article are shown in this section.

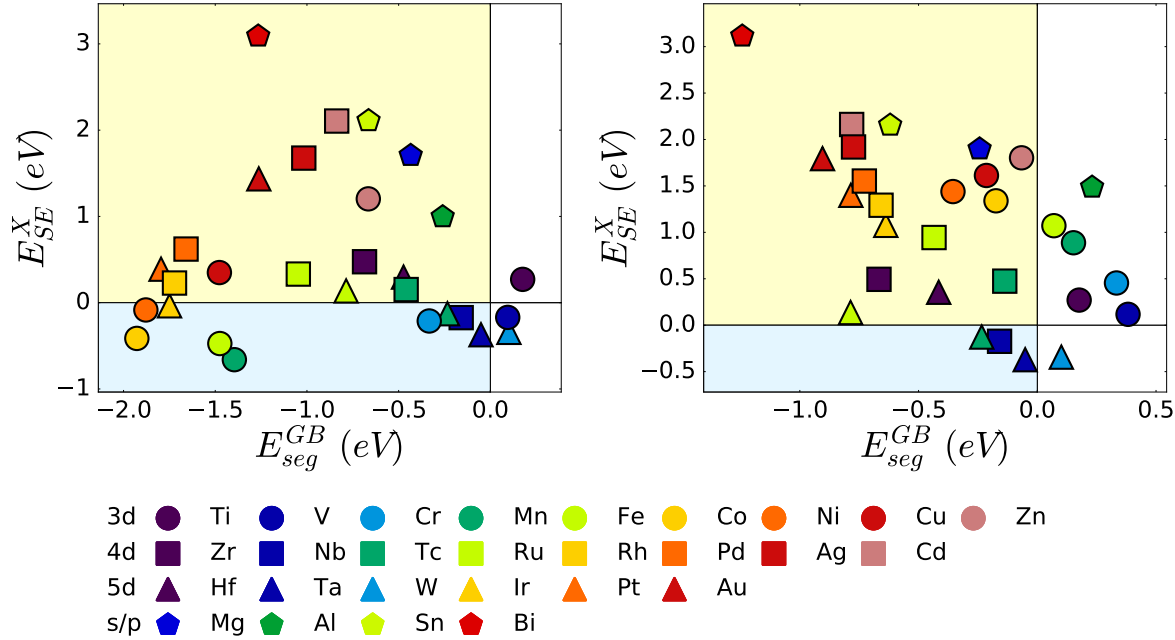


Figure C.4: Plot of the strengthening energy E_{SE}^X versus segregation energy E_{seg}^X for the 29 dopants in the $\Sigma 5$ (100) twist GB. (a) based on the site with the lowest E_{seg}^X ; (b) based on Site 0. Dopants in the white region (positive E_{seg}^X) prefer to stay in the bulk. For dopants that segregate, those with negative E_{seg}^X (blue region) tend to strengthen the GB.

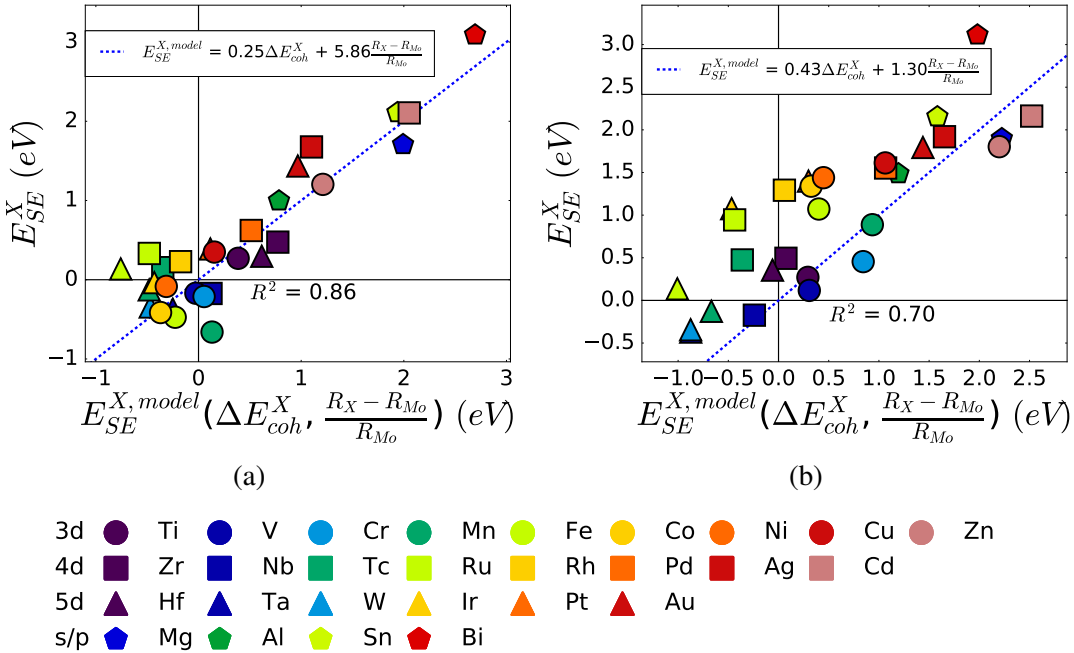


Figure C.5: Plot of the observed strengthening energy E_{SE}^X for the site with the lowest E_{seg}^{GB} versus the two factor linear model for $E_{SE}^{X, \text{model}}(E_{coh}^X, \frac{R_X - R_{Mo}}{R_{Mo}})$ for the 29 dopants in the $\Sigma 5$ (100) twist GB. (a) Fitting performed based on the site with the lowest E_{seg}^{GB} . $k_{coh} = 0.259 \pm 0.029$, $k_R = 5.898 \pm 0.730$. (b) Fitting performed based on Site 0. $k_{coh} = 0.448 \pm 0.059$, $k_R = 1.346 \pm 1.496$. In all fittings, the analysis of variance (ANOVA) finds that the p -value for all coefficients are < 0.05 with the exception of $\frac{R_X - R_{Mo}}{R_{Mo}}$ for C.5b.

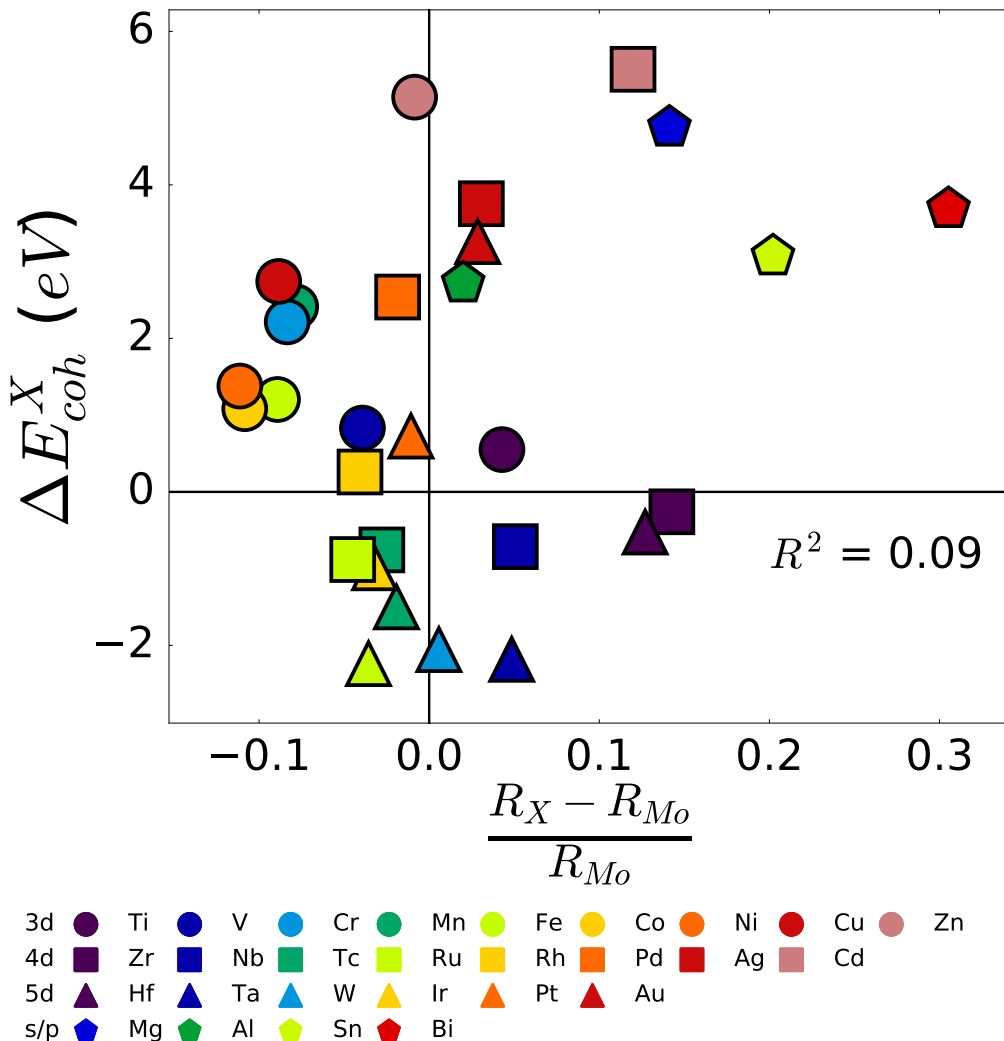


Figure C.6: Plot of the relative difference in atomic size versus the difference in the cohesive energy between the dopant X and host Mo.

Table C.1: P-values obtained for the multiple linear regressions using ANOVA from Figures 8 and C.5. Tests were conducted with a confidence of 95%.

	P> t			
	$\Sigma 5$ (310) Tilt		$\Sigma 5$ (100) Twist	
	1-to-1	m-to-s	Site 0	Lowest E_{seg}^{GB}
$\frac{R_X - R_{Mo}}{R_{Mo}}$	0.000	0.035	0.000	0.401
ΔE_{coh}^X	0.000	0.000	0.000	0.000

Table C.2: A table for values of E_{seg}^{FS} , E_{seg}^{GB} and E_{SE} (Unit: eV). E_{seg}^{FS} and E_{seg}^{GB} for all dopants in all sites of the tilt and twist GBs calculated in this study are listed. E_{SE} are listed for each dopant correspond to the lowest E_{seg}^{GB} site in both systems. Dopants (X) are listed in a descending of the metallic radius.

	Σ_5 (310) Tilt						Σ_5 (100) Twist			
	Site 0		Site 1		Site 2		Site 0	Site 1	E_{seg}^{FS}	E_{SE}
X	E_{seg}^{GB}	E_{seg}^{FS}	E_{seg}^{GB}	E_{seg}^{FS}	E_{seg}^{GB}	E_{SE}	E_{seg}^{GB}	E_{seg}^{GB}	E_{seg}^{FS}	E_{SE}
Bi	-1.595	-4.702	-1.332	-2.933	-0.932	3.107	-1.242	-1.266	-4.356	3.090
Sn	-0.956	-2.905	-0.770	-1.705	-0.647	1.949	-0.620	-0.664	-2.774	2.109
Zr	-0.613	-1.325	-0.258	-0.802	-0.126	0.712	-0.667	-0.686	-1.161	0.475
Mg	-0.315	-2.047	-0.235	-0.977	-0.114	1.732	-0.243	-0.434	-2.141	1.707
Hf	-0.466	-0.913	-0.077	-0.507	-0.022	0.447	-0.415	-0.473	-0.770	0.297
Cd	-0.878	-2.891	-0.736	-1.768	-0.447	2.013	-0.782	-0.838	-2.943	2.106
Nb	-0.269	-0.385	0.019	-0.269	-0.100	0.116	-0.159	0.181	0.014	-0.173
Ta	-0.200	-0.044	0.123	-0.091	-0.041	-0.156	-0.051	0.307	0.320	-0.371
Ti	0.116	-0.410	0.169	-0.088	0.195	0.526	0.176	0.198	-0.094	0.270
Ag	-0.908	-2.649	-0.973	-1.554	-0.532	0.581	-0.774	-1.017	-2.693	1.676
Au	-1.151	-2.621	-1.254	-1.649	-0.775	0.395	-0.904	-1.263	-2.698	1.436
Al	-0.090	-1.263	-0.341	-0.444	-0.089	0.103	0.231	-0.260	-1.256	0.996
W	-0.175	0.130	-0.118	-0.078	-0.214	-0.305	0.101	0.193	0.445	-0.344
Zn	-0.250	-1.830	-0.624	-0.797	-0.240	0.173	-0.066	-0.665	-1.869	1.204
Pt	-1.152	-1.890	0.048	-1.224	-0.903	0.738	-0.785	-1.796	-2.184	0.389
Pd	-0.964	-2.044	-1.267	-1.212	-0.681	-0.055	-0.728	-1.659	-2.281	0.622
Re	-0.568	-0.310	-0.770	-0.444	-0.674	-0.326	-0.234	0.002	-0.106	-0.128
Tc	-0.552	-0.664	-0.810	-0.493	-0.580	-0.317	-0.137	-0.459	-0.611	0.152
Ir	-1.146	-1.452	-1.582	-1.001	-1.034	-0.581	-0.638	-1.749	-1.713	-0.036
Os	-0.934	-0.879	-1.310	-0.734	-0.963	-0.576	-0.786	-0.302	-0.923	0.137
V	0.247	-0.198	-0.060	-0.104	-0.014	0.044	0.382	0.095	0.265	-0.170
Rh	-1.025	-1.657	-1.553	-1.021	-1.002	-0.532	-0.658	-1.722	-1.950	0.228
Ru	-0.917	-1.236	-1.335	-0.803	-1.029	-0.532	-0.435	-1.047	-1.379	0.332
Mn	0.031	-0.575	-0.845	-0.267	-0.303	-0.578	0.152	-1.396	-0.735	-0.660
Cr	-0.031	-0.572	-0.567	-0.374	-0.442	-0.193	0.333	-0.333	-0.121	-0.212
Cu	-0.320	-1.741	-0.918	-0.799	-0.398	-0.119	-0.214	-1.477	-1.827	0.349
Fe	-0.130	-1.061	-0.858	-0.507	-0.375	-0.351	0.070	-1.475	-1.002	-0.473
Co	-0.344	-1.423	-1.281	-0.720	-0.609	-0.561	-0.174	-1.927	-1.514	-0.414
Ni	-0.404	-1.626	-1.243	-0.829	-0.742	-0.414	-0.355	-1.878	-1.794	-0.084

Table C.3: Values of the metallic radii (R_X), cohesive energy (E_{coh}) and Pauling electronegativity (χ) for the 29 dopants and the host material (Mo) used in this study.

Dopants (X)	R_X Å	E_{coh} (eV)	χ
Bi	183.0	2.556	2.02
Sn	168.5	3.174	1.96
Zr	160.2	6.505	1.33
Mg	160.0	1.496	1.31
Hf	158.0	6.769	1.30
Cd	157.0	0.739	1.69
Nb	147.3	6.959	1.60
Ta	147.0	8.427	1.50
Ti	146.2	5.694	1.54
Ag	144.5	2.491	1.93
Au	144.2	2.985	2.54
Al	143.0	3.526	1.61
W	141.0	8.300	2.36
Zn	139.0	1.102	1.65
Pt	138.7	5.519	2.28
Pd	137.6	3.707	2.20
Re	137.5	7.744	1.90
Tc	136.3	7.001	1.90
Ir	135.7	7.235	2.20
Os	135.2	8.483	2.20
V	134.7	5.413	1.63
Rh	134.5	5.986	2.28
Ru	133.9	7.126	2.20
Mn	129.2	3.833	1.55
Cr	128.5	4.030	1.66
Cu	127.8	3.503	1.90
Fe	127.7	5.041	1.83
Co	125.0	5.162	1.88
Ni	124.6	4.867	1.91

Appendix D

Supporting Information: Metal insulator transition under intrinsic defects in V₂O₃

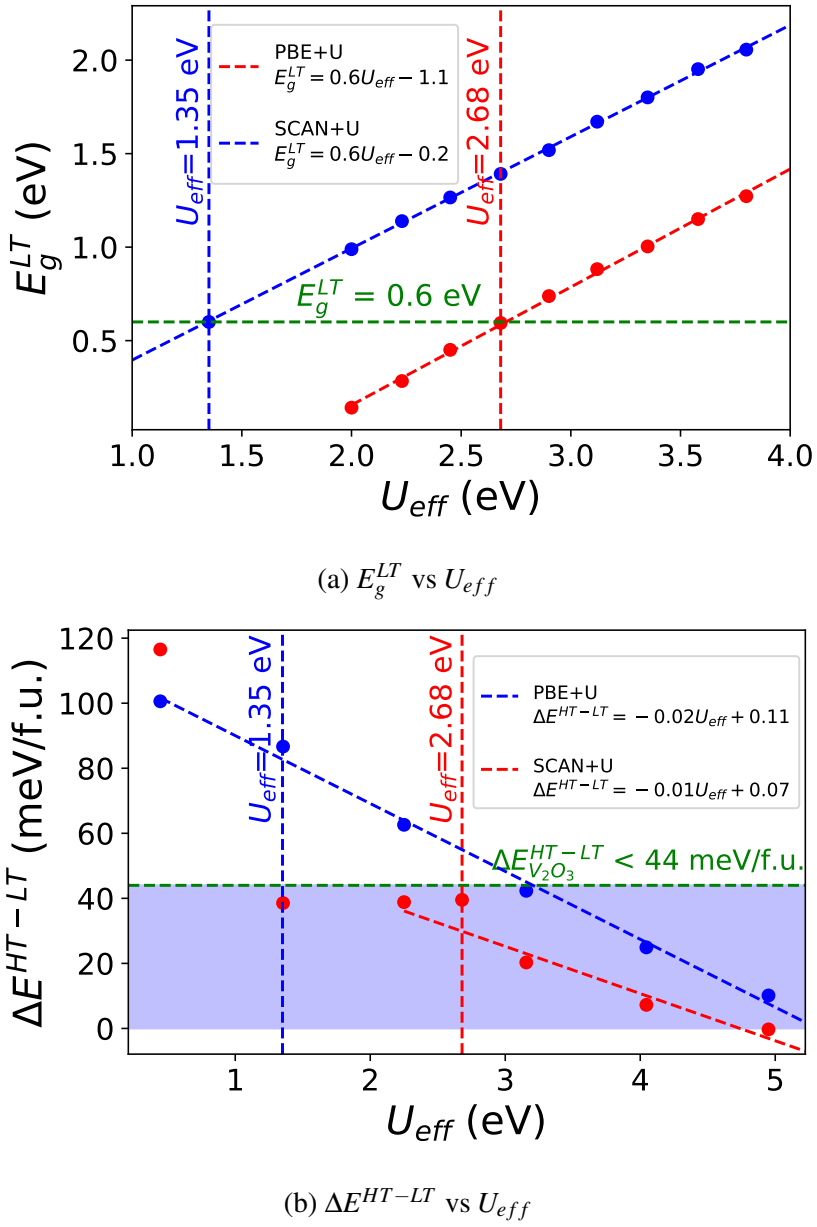


Figure D.1: Plots of the (a) band gap of the LT AFI phase of V_2O_3 and (b) energy difference per formula unit relative to the HT FM phase for the PBE+U (red) and SCAN+U (blue) functionals as a function of the effective Hubbard U (U_{eff}) correction value (x-axis). Dashed lines depict a linear fitting for E_g^{LT} and ΔE_{HT-LT} in (a) and (b) respectively (see legend). Data points with $U_{eff} < 2$ eV are not considered in the linear fitting for PBE+U as the LT phase loses its insulating properties under this value.

D.1 Derivation of thermodynamic quantities for the calculation of the defect formation energy

D.1.1 Chemical potential

The relationship between the bulk DFT energy of V_2O_3 per formula unit and chemical potentials μ_O and μ_V is given by the following:

$$E_{\text{V}_2\text{O}_3}^{\text{bulk}} = \sum_i n_i \mu_i = 2\mu_V + 3\mu_O \quad (\text{D.1})$$

We can substitute this relationship into Equation 1 to rewrite the formation energy in terms of oxygen chemical potential:

$$E_{\text{form}}[X^q] = E_{\text{tot}}[X^q] - E_{\text{tot}}[\text{bulk}] - n_V \frac{E_{\text{V}_2\text{O}_3}^{\text{bulk}} - 3\mu_O}{2} - n_O \mu_O + q\epsilon_F + E_{\text{corr}}^q \quad (\text{D.2})$$

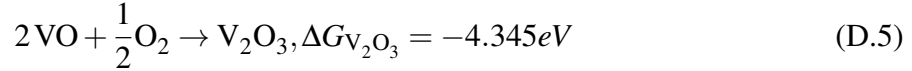
The upper limit of values for μ_O can be set to the computed energy of O_2 gas per atom:

$$\mu_O \leq \frac{1}{2}E_{\text{O}_2} + E_{\text{corr}}^O \quad (\text{D.3})$$

where $E_{\text{corr}}^O = -0.702$ eV is a correction to the overbinding of O_2 in the PBE and PBE+ U functionals³²⁶. Using $\frac{1}{2}E_{\text{O}_2} + E_{\text{corr}}^O$ as a reference, we get:

$$\mu_O - \frac{1}{2}E_{\text{O}_2} - E_{\text{corr}}^O = \Delta\mu_O \leq 0 \quad (\text{D.4})$$

which we substitute for μ_O in Equation SD.2. The lower limit of $\Delta\mu_O$ is generally determined by the enthalpy of reaction of the most stable V-O compounds given by the following:



Here $\Delta G_{\text{V}_2\text{O}_3}$ is the lower limit of the chemical potential where V_2O_3 is stable relative to VO.

To put the chemical potential into context, $\Delta\mu_O$ can be written as a function of temperature (T) and pressure (P):

$$\Delta\mu(T, P) = g(T, H, S) + k_B T \ln\left(\frac{P}{P_0}\right) \quad (\text{D.6})$$

where H and S are determined experimentally from the JANAF thermodynamics tables at temperature T, k_B is the Boltzmann constant and $P_0 = 0.1$ MPa is the standard pressure of oxygen.

D.1.2 Freysoldt correction

The Freysoldt correction²⁷⁶ for charged defects in a supercell is given by:

$$E_{corr}^q = [1 + C_{sh}(1 - \epsilon^{-1})] \frac{q^2 \alpha_M}{2\epsilon L} \quad (\text{D.7})$$

Here C_{sh} is a supercell factor determined by the electrostatic potential along the defect system. ϵ is the dielectric constant for V_2O_3 which we adopted as 8.5³²⁷. α_M is the Madelung constant of the structure. $L = V^{-1/3}$ is the supercell dimension where V is the cell volume.

Table D.1: Energy difference (in meV/f.u.) for monoclinic V_2O_3 for a non-magnetic (ΔE_{NM-AFI}) and ferromagnetic (ΔE_{FM-AFI}) configuration relative to an anti-ferromagnetic configuration for 5 different functionals. U_{eff} values of 2.68 eV and 1.35 eV are chosen for the PBE+ U and SCAN+ U functionals respectively.

Functional	ΔE_{NM-AFI}	ΔE_{FM-AFI}
HSE06	14	54
SCAN	1078	76
SCAN+ U	2265	87
PBE	217	13
PBE+ U	940	39

Table D.2: Calculated lattice parameters of the low (I_2/a) and high ($R\bar{3}c$) temperature phases and their experimental counterparts for various functionals. U_{eff} values of 2.68 eV and 1.35 eV are chosen for the PBE+ U and SCAN+ U functionals respectively.

Phase	Functional	a (Å)	b (Å)	c (Å)	α (°)	β (°)	γ (°)
I_2/a (AFI) ²⁷⁹	Exp	7.27	5.00	5.54	90	96.76	90
I_2/a (AFI)	HSE06	7.22	5.01	5.50	90	96.23	90
I_2/a (AFI)	SCAN	7.27	5.00	5.55	90	96.81	90
I_2/a (AFI)	SCAN+ U	7.29	5.11	5.55	90	96.32	90
I_2/a (AFI)	PBE	7.37	4.90	5.54	90	98.47	90
I_2/a (AFI)	PBE+ U	7.32	5.07	5.58	90	96.52	90
$R\bar{3}c$ (PM) ⁸³	Exp	4.95	4.95	14.01	90	90	120
$R\bar{3}c$ (FM)	HSE06	5.05	5.05	13.86	90	90	120
$R\bar{3}c$ (FM)	SCAN	4.98	4.98	14.04	90	90	120
$R\bar{3}c$ (FM)	SCAN+ U	5.07	5.07	13.90	90	90	120
$R\bar{3}c$ (FM)	PBE	4.86	4.86	14.35	90	90	120
$R\bar{3}c$ (FM)	PBE+ U	5.12	5.12	14.11	90	90	120
$R\bar{3}c$ (NM)	PBE+ U	4.84	4.84	14.28	90	90	120

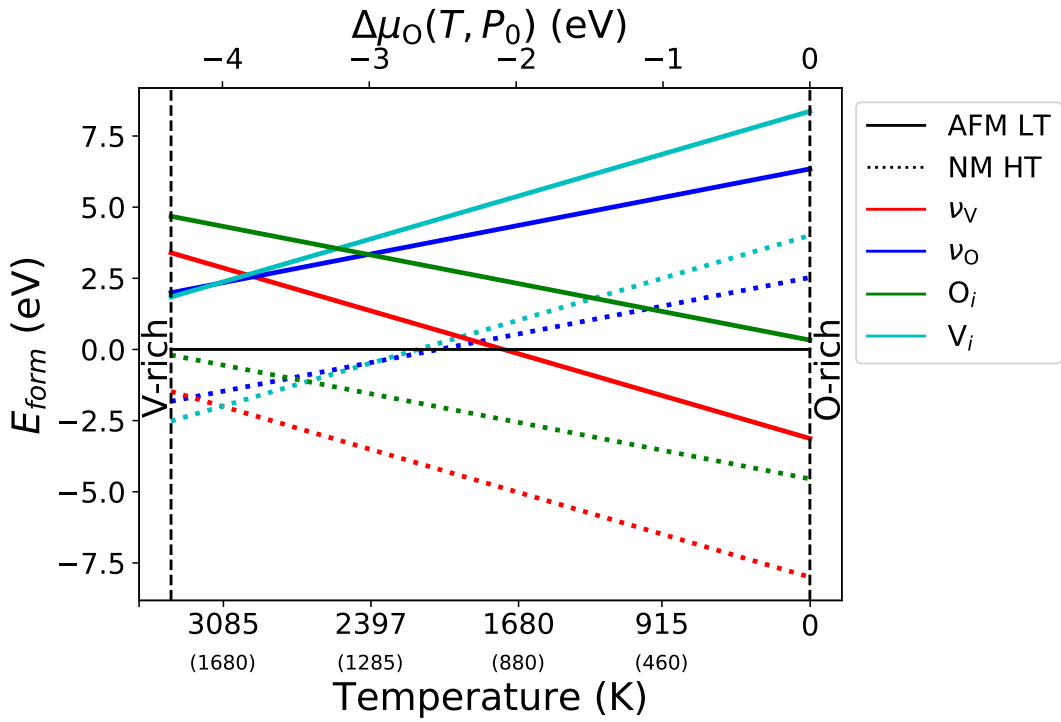


Figure D.2: Neutral defect formation energy (E_{form}) for O_i , V_i , v_V and v_O in LT AFI (solid) and HT NM (dotted) V_2O_3 as a function of the oxygen chemical potential ($\Delta\mu_O$, top x axis). The temperature scales based on $p_0 = 0.1$ ($p_0 = 10^{-13}$ MPa in parenthesis) is provided on the bottom x axis.

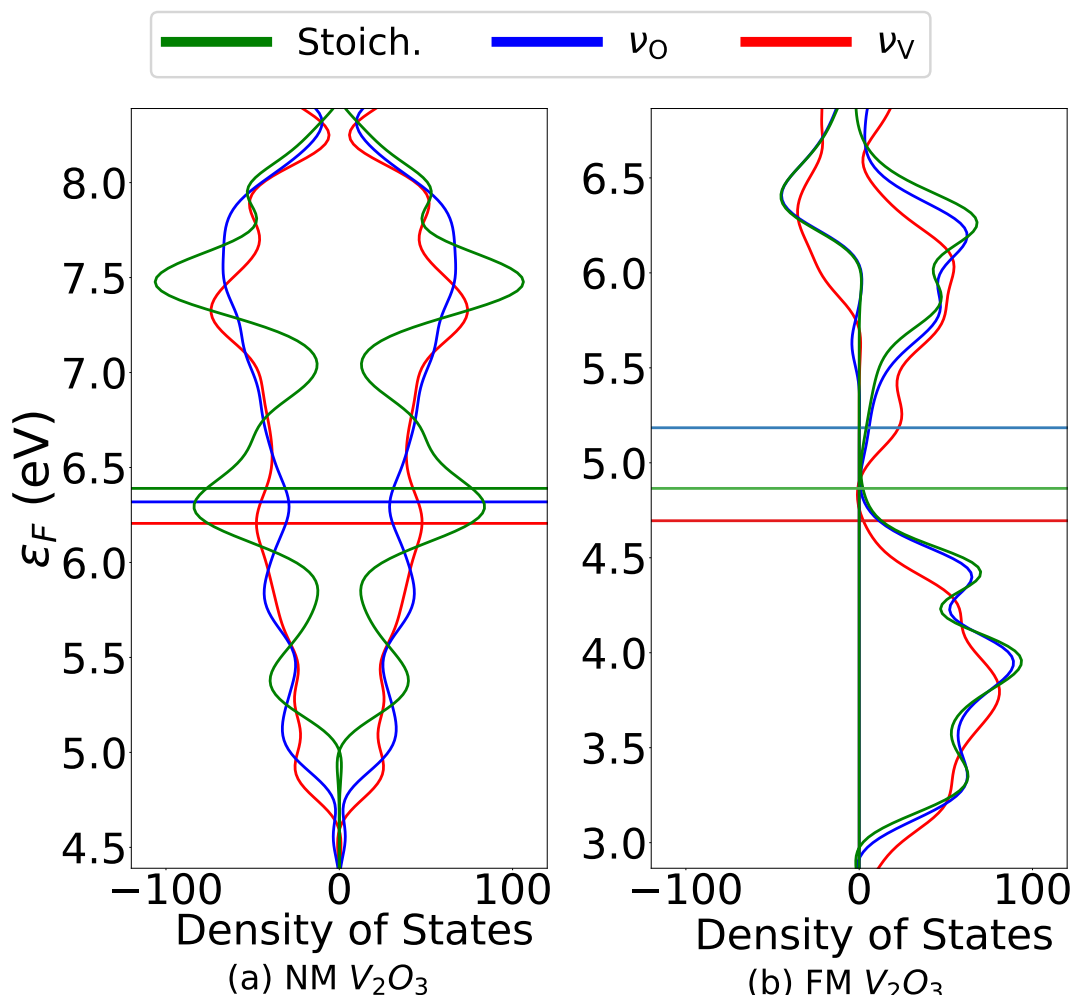


Figure D.3: Total density of states for corundum phase V_2O_3 containing v_V (red), v_O (blue) and no defects (green) under a (a) FM and (b) NM configuration.

Appendix E

Supporting Information: Proton distribution visualization in nickelate neuromorphic devices

E.1 Spatially resolved diffraction studies

The SNO-based device with 1 μm gap between the Au and Pd contacts was scanned by a nanofocused x-ray beam with an exposure time of 10 s ($\{101\}$ reflection) and with an exposure time of 1 s ($\{202\}$ reflection). The footprint of the x-ray beam for the $\{101\}$ reflection was approximately $170 \times 30 \text{ nm}^2$, and for the $\{202\}$ reflection - $90 \times 30 \text{ nm}^2$. The averaged diffraction patterns are shown in Fig. E.1(a,b). The 2θ increases from right to left and the dispersion along the vertical direction is due to the Fresnel zone plate used for focusing. The projected signal along the 2θ -direction is shown in Fig. E.1(c,d).

In Fig. E.2 spatially resolved maps of the intensity, position and width of the $\{202\}$ reflection from SNO (film) and $\{111\}$ reflection from LAO (substrate) are shown. These maps show no clear changes of the parameters induced by H^+ doping, in contrast to the $\{101\}$ intensity map (see the main text). The variation of intensity in Fig. E.2(a,d) are attributed to the heterogeneity of the substrate and almost complete overlap between the film and substrate peaks, which doesn't allow to reliably separate two signals (see Fig. E.1(c,d)).

The position of electrodes was determined by fluorescence signal from Au and Pd, as it is shown in Fig. E.3(a,b). The Ni fluorescence map at $E = 8395 \text{ eV}$ (away from the K-edge resonance, hence not sensitive to valence state of Ni) shows that the SNO film is uniform.

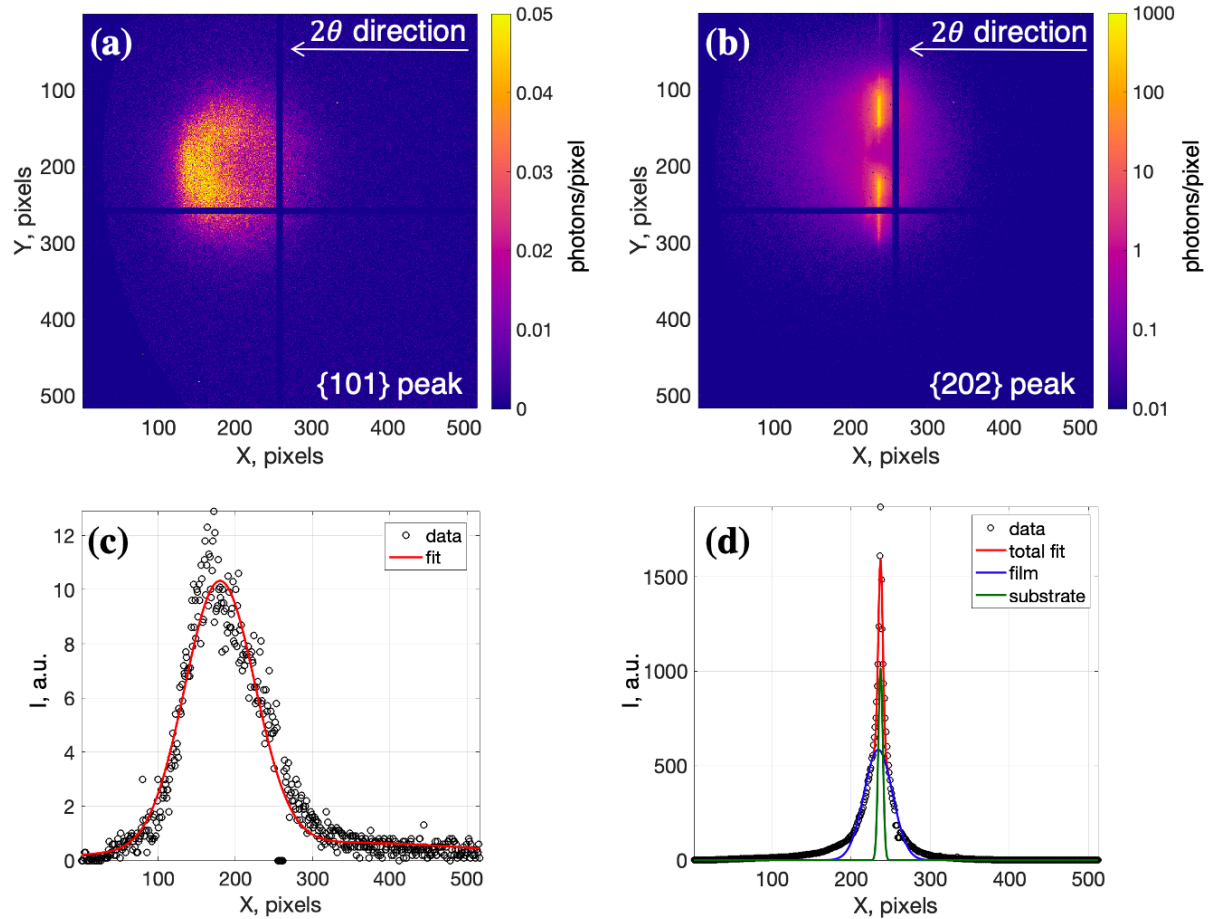


Figure E.1: Averaged diffraction pattern for the $\{101\}$ reflection (a) and the $\{202\}$ reflection (b). Projection of the averaged diffraction pattern along the vertical direction is shown in (c,d). The signal from the $\{101\}$ reflection can be fitted by a single Gaussian function (c), while the signal from the $\{202\}$ reflection can be approximated by a sum of two Gaussian function that correspond to the scattering from the SNO film and the LAO substrate (d).

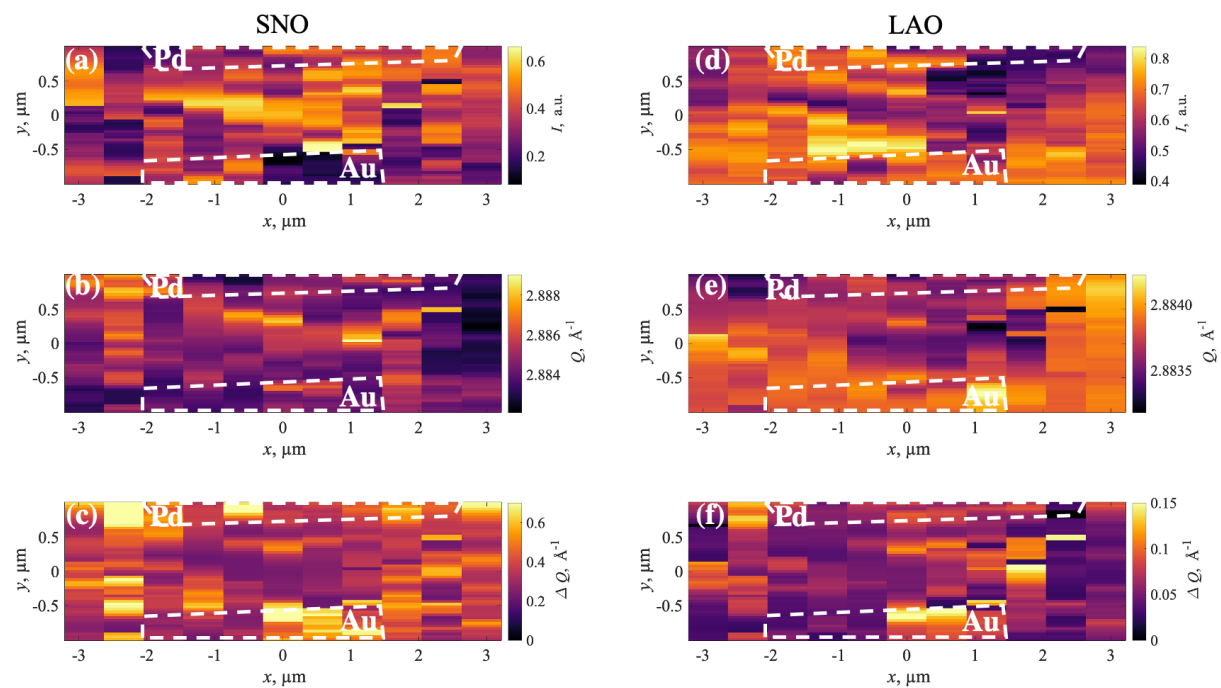


Figure E.2: (a-c) Intensity (a), Q -position (b), and the width (c) of the {202} reflection from the SNO film. (d-f) Intensity (d), Q -position (e), and the width (f) of the LAO {111} substrate reflection. The electrodes are outlined with dashed lines.

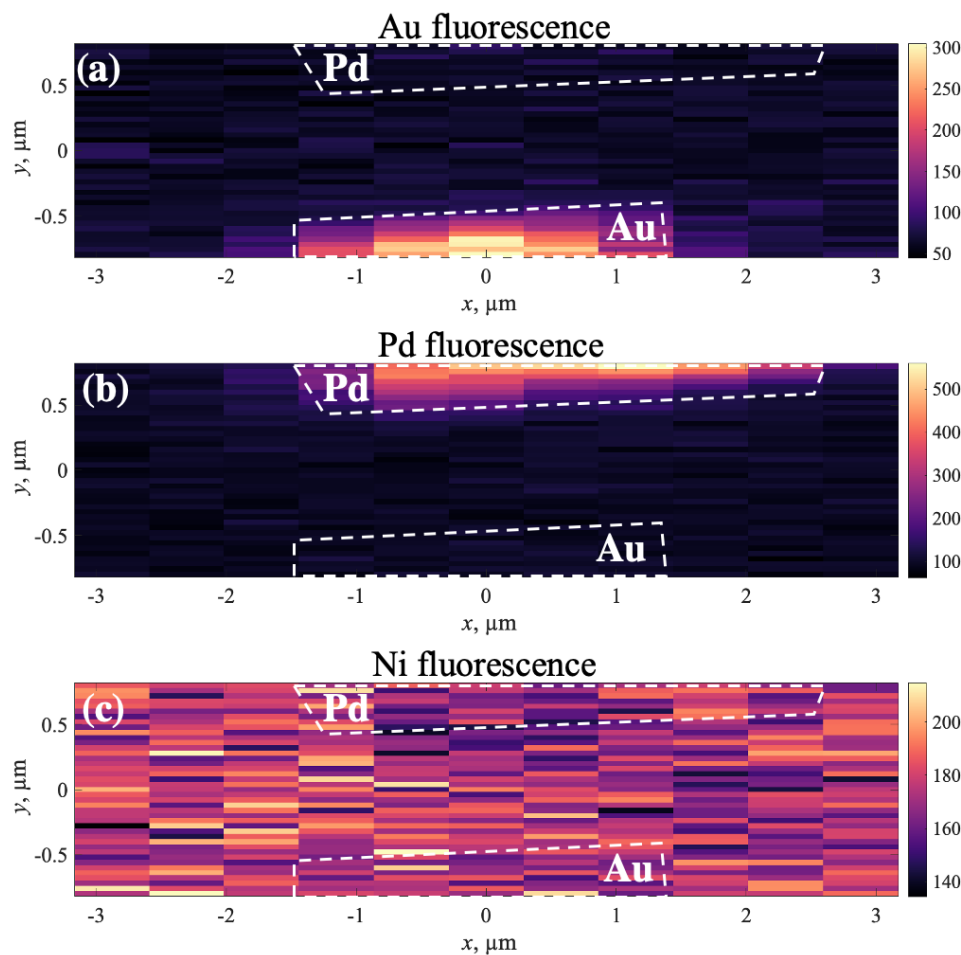


Figure E.3: (a-b) Fluorescence signal from Au (a) and Pd (b) indicates position of electrodes. (c) Non-resonant fluorescent signal from Ni shows the uniform SNO film across the device.

E.2 Simulation of RNO crystal lattice

An orthorhombic unit cell of a perovskite SmNiO_3 lattice was constructed in several steps. In our analysis, we assumed that Ni atoms do not move with hydrogen doping, so the positions of 12 Ni atoms was fixed within a unit cell. Then 4 Sm atoms were placed inside a unit cell and allowed to be shifted from the centrosymmetric positions over d_x , d_y , and d_z in such a way, that the orthorhombic $Pbnm$ symmetry was preserved. Finally, we placed 6 O atoms in the corners of octahedra centered at every Ni atom (20 oxygen atoms in total, if counting only atoms within a unit cell). The position of each oxygen atom was calculating according to the following procedure:

1. For each oxygen atom, a nesting nickel atom was selected, around which the rotations will be performed.
2. The position of the oxygen atom was calculated as

$$\mathbf{r}_O = \mathbf{r}_{\text{Ni}} + \tilde{\mathbf{u}} , \quad (\text{E.1})$$

where $\mathbf{r}_O = (x_O, y_O, z_O)$ are coordinates of the oxygen atom and $\mathbf{r}_{\text{Ni}} = (x_{\text{Ni}}, y_{\text{Ni}}, z_{\text{Ni}})$ are coordinates of the corresponding nickel atom. The relative coordinates $\tilde{\mathbf{u}} = (\tilde{x}, \tilde{y}, \tilde{z})$ were calculated as

$$\tilde{\mathbf{u}} = (1 \pm B) \cdot \hat{R}(\pm\alpha, \pm\beta, \pm\gamma) \mathbf{u}_0 . \quad (\text{E.2})$$

Here $\mathbf{u}_0 = (x_0, y_0, z_0)$ are the relative coordinates of the oxygen atom in an ideal perovskite structure (in which each oxygen atom located exactly in the middle in between two nickel atoms), $\hat{R}(\alpha, \beta, \gamma)$ is an operator of rotation over the angles α , β and γ about x -, y - and z -axis, respectively, and the pre-factor $(1 \pm B)$ takes the breathing distortion with a magnitude B into account ('+' corresponds to the expanded NiO_6 octahedra, and '-' to the contracted).

3. The signs of rotation angles α , β and γ for each octahedra are selected in such a way that the final structure corresponds to the $a^-a^-c^+$ tilt pattern in Glazer notation²⁹².

We assigned an occupation number O_j to each atom, which takes into account that atom might be shared between several neighboring unit cells. For example, $O_j = 1$ for an atom that is completely inside a unit cell, while $O_j = 1/4$ for an atom placed on the edge of a unit cell, since this atom is shared between 4 different unit cells.

The parameters of the structural model are summarized in Table E.1. The first column contains an index of an atom j , the second column - type of an atom. Columns 3–5 contain coordinates x , y and z of an atom, and column 6 - occupation number O_j . For each Ni the signs of rotation angles α , β and γ and the breathing distortion are specified in columns 7 and 8, respectively (this information is duplicated for each oxygen atom). The values of $\tilde{\mathbf{u}} = (\tilde{x}, \tilde{y}, \tilde{z})$ for each oxygen atom are calculated with Eq. E.2, using the undistorted coordinates $\mathbf{u}_0 = (x_0, y_0, z_0)$ specified in columns 9–11. The crystal structure of pristine SmNiO_3 constructed with our model using the parameter values $\alpha = 0^\circ$, $\beta = 15.26^\circ$, and $\gamma = 7.9^\circ$, $d_x = 0.06 \text{ \AA}$, $d_y = 0.28 \text{ \AA}$, $d_z = 0 \text{ \AA}$, and $B = 0.013$ coincides with the literature data^{15,314} (see Fig. E.4).

Table E.1: Coordinates of the atoms in SmNiO_3 orthorhombic unit cell with lattice parameters $a_o = 5.328 \text{ \AA}$, $b_o = 5.437 \text{ \AA}$ and $c_o = 7.568 \text{ \AA}$ ¹⁵. The numbers in brackets next to oxygen atoms indicate an index of Ni atom, relative to which the coordinates of the oxygen atoms are calculated (see Eq. E.1). The coordinates $\tilde{\mathbf{u}} = (\tilde{x}, \tilde{y}, \tilde{z})$ for each oxygen atom are calculated according to Eq. E.2, in which the signs of rotation angles α , β and γ and the breathing distortion are specified in columns 7 and 8, and the values (x_0, y_0, z_0) for undistorted lattice are specified in columns 9–11.

	x_j	y_j	z_j	O_j	Rot.	Brth.	x_0	y_0	z_0
Ni	$a_o/2$	0	0	1/4	– +	+			
Ni	0	$b_o/2$	0	1/4	+ –	–			
Ni	$a_o/2$	b_o	0	1/4	– +	+			
Ni	a_o	$b_o/2$	0	1/4	+ –	–			

Table E.1: Coordinates of the atoms in SmNiO_3 orthorhombic unit cell with lattice parameters $a_o = 5.328 \text{ \AA}$, $b_o = 5.437 \text{ \AA}$ and $c_o = 7.568 \text{ \AA}$ ¹⁵. The numbers in brackets next to oxygen atoms indicate an index of Ni atom, relative to which the coordinates of the oxygen atoms are calculated (see Eq. E.1). The coordinates $\tilde{\mathbf{u}} = (\tilde{x}, \tilde{y}, \tilde{z})$ for each oxygen atom are calculated according to Eq. E.2, in which the signs of rotation angles α , β and γ and the breathing distortion are specified in columns 7 and 8, and the values (x_0, y_0, z_0) for undistorted lattice are specified in columns 9–11 (continued).

	x_j	y_j	z_j	O_j	Rot.	Brth.	x_0	y_0	z_0
Ni	$a_o/2$	0	$c_o/2$	1/2	+++	–			
Ni	0	$b_o/2$	$c_o/2$	1/2	–––	+			
Ni	$a_o/2$	b_o	$c_o/2$	1/2	+++	–			
Ni	a_o	$b_o/2$	$c_o/2$	1/2	–––	+			
Ni	$a_o/2$	0	c_o	1/4	––+	+			
Ni	0	$b_o/2$	c_o	1/4	++–	–			
Ni	$a_o/2$	b_o	c_o	1/4	––+	+			
Ni	a_o	$b_o/2$	c_o	1/4	++–	–			
Sm	$a_o - d_x$	d_y	$c_0/4 + d_z$	1					
Sm	$a_o/2 + d_x$	$b_o/2 + d_y$	$c_0/4 + d_z$	1					
Sm	$a_o/2 - d_x$	$b_o/2 - d_y$	$3c_0/4 - d_z$	1					
Sm	d_x	$b_o - d_y$	$3c_0/4 - d_z$	1					
O (1)	$a_o/2 + \tilde{x}$	\tilde{y}	\tilde{z}	1/2	––+	+	$a_o/4$	$b_o/4$	0
O (1)	$a_o/2 + \tilde{x}$	\tilde{y}	\tilde{z}	1/2	––+	+	0	0	$c_o/4$
O (2)	\tilde{x}	$b_o/2 + \tilde{y}$	\tilde{z}	1/2	++–	–	$a_o/4$	$-b_o/4$	0
O (2)	\tilde{x}	$b_o/2 + \tilde{y}$	\tilde{z}	1/2	++–	–	$a_o/4$	$b_o/4$	0
O (2)	\tilde{x}	$b_o/2 + \tilde{y}$	\tilde{z}	1/2	++–	–	0	0	$c_o/4$
O (3)	$a_o/2 + \tilde{x}$	$b_o + \tilde{y}$	\tilde{z}	1/2	––+	+	$a_o/4$	$-b_o/4$	0
O (3)	$a_o/2 + \tilde{x}$	$b_o + \tilde{y}$	\tilde{z}	1/2	––+	+	0	0	$c_o/4$

Table E.1: Coordinates of the atoms in SmNiO_3 orthorhombic unit cell with lattice parameters $a_o = 5.328 \text{ \AA}$, $b_o = 5.437 \text{ \AA}$ and $c_o = 7.568 \text{ \AA}$ ¹⁵. The numbers in brackets next to oxygen atoms indicate an index of Ni atom, relative to which the coordinates of the oxygen atoms are calculated (see Eq. E.1). The coordinates $\tilde{\mathbf{u}} = (\tilde{x}, \tilde{y}, \tilde{z})$ for each oxygen atom are calculated according to Eq. E.2, in which the signs of rotation angles α , β and γ and the breathing distortion are specified in columns 7 and 8, and the values (x_0, y_0, z_0) for undistorted lattice are specified in columns 9–11 (continued).

	x_j	y_j	z_j	O_j	Rot.	Brth.	x_0	y_0	z_0
O (4)	$a_o + \tilde{x}$	$b_o/2 + \tilde{y}$	\tilde{z}	1/2	++-	-	0	0	$c_o/4$
O (5)	$a_o/2 + \tilde{x}$	\tilde{y}	$c_o/2 + \tilde{z}$	1	+++	-	$a_o/4$	$b_o/4$	0
O (5)	$a_o/2 + \tilde{x}$	\tilde{y}	$c_o/2 + \tilde{z}$	1/2	+++	-	0	0	$c_o/4$
O (6)	\tilde{x}	$b_o/2 + \tilde{y}$	$c_o/2 + \tilde{z}$	1	---	+	$a_o/4$	$-b_o/4$	0
O (6)	\tilde{x}	$b_o/2 + \tilde{y}$	$c_o/2 + \tilde{z}$	1	---	+	$a_o/4$	$b_o/4$	0
O (6)	\tilde{x}	$b_o/2 + \tilde{y}$	$c_o/2 + \tilde{z}$	1/2	---	+	0	0	$c_o/4$
O (7)	$a_o/2 + \tilde{x}$	$b_o + \tilde{y}$	$c_o/2 + \tilde{z}$	1	+++	-	$a_o/4$	$b_o/4$	0
O (7)	$a_o/2 + \tilde{x}$	$b_o + \tilde{y}$	$c_o/2 + \tilde{z}$	1/2	+++	-	0	0	$c_o/4$
O (8)	$a_o + \tilde{x}$	$b_o/2 + \tilde{y}$	$c_o/2 + \tilde{z}$	1/2	---	+	0	0	$c_o/4$
O (9)	$a_o/2 + \tilde{x}$	\tilde{y}	$c_o + \tilde{z}$	1/2	--+	+	$a_o/4$	$b_o/4$	0
O (10)	\tilde{x}	$b_o/2 + \tilde{y}$	$c_o + \tilde{z}$	1/2	+-	-	$a_o/4$	$-b_o/4$	0
O (10)	\tilde{x}	$b_o/2 + \tilde{y}$	$c_o + \tilde{z}$	1/2	+-	-	$a_o/4$	$b_o/4$	0
O (11)	$a_o/2 + \tilde{x}$	$b_o + \tilde{y}$	$c_o + \tilde{z}$	1/2	--+	+	$a_o/4$	$-b_o/4$	0

E.2.1 Rotation operator $\hat{R}(\alpha, \beta, \gamma)$

In this work we assumed that the tilt of the NiO_6 octahedron can be described as a rotation of a rigid body. This allowed us to calculate the coordinates of each O atom by stretching the Ni–O bond (breathing mode) and rotating it relative to its position in the pristine structure. It

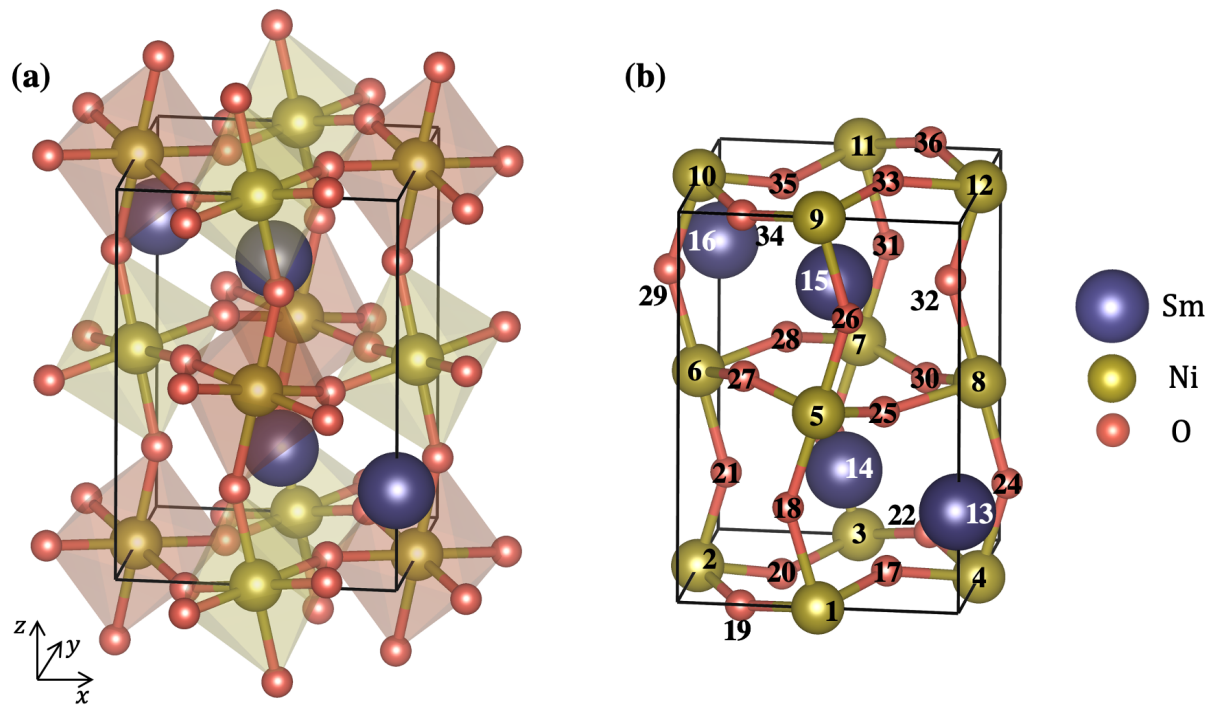


Figure E.4: (a) Orthorhombic unit cell of SmNiO_3 taken from the literature¹⁵. For better visualization, NiO_6 octahedra are shown around each Ni atom. The contracted octahedra are orange, and expanded are yellow (the breathing mode). (b) An identical unit cell of SmNiO_3 consisting of 36 atoms (see atomic coordinates in Table E.1). Only the atoms within a unit cell are shown. The numbers corresponds to the index j .

is known that rotations are not commutative, therefore the rotation operator $\hat{R}(\alpha, \beta, \gamma)$ can not be represented as three consecutive rotations around x -, y - and z -axis, because the final result will depend on the order of rotations. However for small angles, the rotation operators can be interchanged with the final result remaining constant up to the second-order terms³⁰³. Therefore, the rotation operator $\hat{R}(\alpha, \beta, \gamma)$ can be represented as a product of small commutative (Abelian) rotations around three orthogonal axes

$$\hat{R}(\alpha, \beta, \gamma) = \prod_{i=1}^N \hat{R}_x\left(\frac{\alpha}{N}\right) \hat{R}_y\left(\frac{\beta}{N}\right) \hat{R}_z\left(\frac{\gamma}{N}\right). \quad (\text{E.3})$$

Here N is a large number (in our simulations we used $N = 100$), and $\hat{R}_x(\theta)$, $\hat{R}_y(\theta)$, and $\hat{R}_z(\theta)$ are operators of rotation about x -, y - and z -axis, respectively, with matrices

$$\hat{R}_x(\theta) = \begin{bmatrix} 1 & 0 & 0 \\ 0 & \cos\theta & -\sin\theta \\ 0 & \sin\theta & \cos\theta \end{bmatrix}, \quad (\text{E.4})$$

$$\hat{R}_y(\theta) = \begin{bmatrix} \cos\theta & 0 & \sin\theta \\ 0 & 1 & 0 \\ -\sin\theta & 0 & \cos\theta \end{bmatrix}, \quad (\text{E.5})$$

$$\hat{R}_z(\theta) = \begin{bmatrix} \cos\theta & -\sin\theta & 0 \\ \sin\theta & \cos\theta & 0 \\ 0 & 0 & 1 \end{bmatrix}. \quad (\text{E.6})$$

We want to emphasize here that since we use the orthorhombic symmetry, all rotations in this work are performed about orthorhombic axes, and not about traditionally used pseudocubic axes²⁹³.

E.2.2 Simulation of diffraction

The intensity of the diffracted beam I_{hkl} was calculated as the squared modulus of the form factor $F(\mathbf{q})$

$$I_{hkl} \propto |F(\mathbf{q})|^2 , \quad (\text{E.7})$$

where

$$F(\mathbf{q}) = \sum_{j=1}^{36} O_j f_j(q, E) \exp(i\mathbf{qr}_j) , \quad (\text{E.8})$$

and index j runs over all atoms in the unit cell (see Tab. E.1). The atomic form factors $f_j(q, E)$ at x-ray energy $E = 8345$ eV were calculated for Sm^{3+} , Ni^{3+} and O^{2-} ions using Cromer-Mann parameterization³²⁸ and tabulated energy-dependent corrections³²⁹. The components of the scattering vector $\mathbf{q} = (q_x, q_y, q_z)$ for the reflection (hkl) equal to $(2\pi h/a_o, 2\pi k/b_o, 2\pi l/c_o)$. In the manuscript we considered two groups of symmetry equivalent reflections: $\{101\}$ and $\{202\}$ – that corresponds to the $\{\frac{1}{2}\frac{1}{2}\frac{1}{2}\}_{pc}$ and $\{111\}_{pc}$ reflections in pseudocubic notation, correspondingly. Due to orthorhombic twinning, it is impossible to distinguish between the individual reflections within each class, so the intensity of the $\{101\}$ reflection was evaluated as the averaged value of (101) , $(10\bar{1})$, (011) , and $(01\bar{1})$ intensities³⁰². In a similar way, the intensity of the $\{202\}$ is averaged over (202) , $(20\bar{2})$, (022) , and $(02\bar{2})$ reflections.

Direct evaluation of the $\{101\}$ and $\{202\}$ peaks intensity showed that the first peak is approximately 250 times weaker and its intensity strongly depends on d_x component of the rare-earth cation displacement (Fig. E.5). At the same time the intensity of the $\{202\}$ reflection is not strongly affected by these parameters. Neglecting the weak contribution from Ni and O atoms

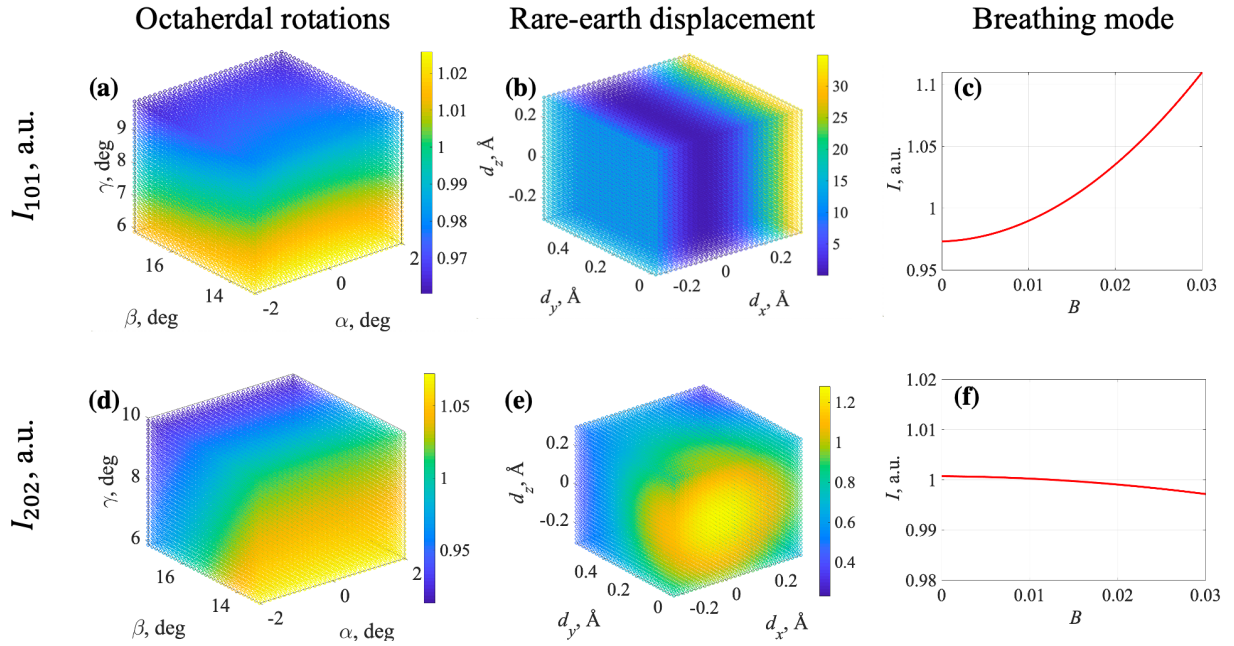


Figure E.5: Intensity of the $\{101\}$ reflection I_{101} (a-c) and $\{202\}$ reflection I_{202} (d-f) as a function of NiO_6 octahedra tilt angles (a,d), displacement of the Sm^{3+} cation (b,e), and breathing distortion (c,f). The intensities are normalized to the value in the pristine SmNiO_3 .

in Eq. E.8, the form factors can be simplified to

$$F_{101,10\bar{1}} \propto \sin \frac{2\pi d_x}{a_o} \cos \frac{2\pi d_z}{c_o}, \quad (\text{E.9})$$

$$F_{011,01\bar{1}} = 0, \quad (\text{E.10})$$

$$F_{202,20\bar{2}} \propto \cos \frac{4\pi d_x}{a_o} \cos \frac{4\pi d_z}{c_o}, \quad (\text{E.11})$$

$$F_{022,02\bar{2}} \propto \cos \left(\frac{4\pi d_y}{b_o} \pm \frac{4\pi d_z}{c_o} \right), \quad (\text{E.12})$$

If the displacements d_x and d_z follow a normal distribution with standard deviation σ_x and σ_z ,

respectively, the intensity of the corresponding reflections can be estimated as

$$I_{\{101\}} \propto \exp \left[- \left(\frac{2\pi\sigma_x}{a_o} \right)^2 - \left(\frac{2\pi\sigma_z}{c_o} \right)^2 \right] \sin^2 \frac{2\pi d_x}{a_o} \cos^2 \frac{2\pi d_z}{c_o}, \quad (\text{E.13})$$

$$\begin{aligned} I_{\{202\}} \propto & \exp \left[- \left(\frac{4\pi\sigma_x}{a_o} \right)^2 - \left(\frac{4\pi\sigma_z}{c_o} \right)^2 \right] \cos^2 \frac{4\pi d_x}{a_o} \cos^2 \frac{4\pi d_z}{c_o} + \\ & + \exp \left[- \left(\frac{4\pi\sigma_y}{b_o} \right)^2 - \left(\frac{4\pi\sigma_z}{c_o} \right)^2 \right] \cos^2 \left(\frac{4\pi d_y}{b_o} + \frac{4\pi d_z}{c_o} \right) + \\ & + \exp \left[- \left(\frac{4\pi\sigma_y}{b_o} \right)^2 - \left(\frac{4\pi\sigma_z}{c_o} \right)^2 \right] \cos^2 \left(\frac{4\pi d_y}{b_o} - \frac{4\pi d_z}{c_o} \right). \end{aligned} \quad (\text{E.14})$$

These results agree with the direct calculations shown in Fig. E.5(b,e): the intensity of the $\{101\}$ reflection can be estimated as $I_{\{101\}} \propto d_x^2$ for a small cation displacement.

E.3 Theoretical results

E.3.1 Structural and magnetic considerations

The LT insulating phase of SmNiO_3 is known to be paramagnetic, however, our DFT calculations are limited to magnetically ordered (e.g. ferromagnetic or antiferromagnetic) or nonmagnetic systems. As such, we need to select a proxy magnetic configuration based on structural consistency with experimental observations and H-doping stability. We start by relaxing the orthorhombic phase of SmNiO_3 shown in Figure SE.4 under a nonmagnetic (NM), ferromagnetic (FM) and antiferromagnetic (AFM) configuration. Full structural relaxation of the NM phase preserves the space group of the $Pbnm$ orthorhombic phase while a FM and T-AFM (see reference herein⁸⁴) ordering of Ni atoms will decrease the β lattice parameter by 0.038° to form a monoclinic structure with a space group of $P2_1/n$. Only the magnetically ordered phases demonstrated a checkered-pattern breathing distortion among the NiO_6 octahedrons consistent with our experimental observations. As such, we only investigated H-doping in the FM and T-AFM configurations. We used the InFit algorithm²⁷⁴ to locate all possible interstitial sites for

H under a 1:32 H:Ni ratio in both phases and observed that the formation energy of H-doping in the FM phase was 70 meV more stable than in the T-AFM phase. Hence all investigations of the effect of H-doping concentration on the oxidation state and XAS spectrum will be done in the FM phase.

E.3.2 H-doping concentration from XAS shift

To evaluate the approximate concentration of H in the experimentally doped SmNiO_3 sample, we calculated the theoretical shift in the XAS peaks between the doped and undoped system for 4 different ratios of H to Ni (H:Ni): 1:32, 1:8, 1:4, and 1:2 using the FEFF software³¹¹. The shift in the XAS spectrum is plotted as a function of the corresponding H:Ni ratio in Figure E.6. We observed that overall, the shift gradually increases as the H content increases from a ratio of 1:8 to a maximum ratio of 1:2 where the XAS peak shifts by 1.1 eV which is within the range of the experimentally evaluated shift of 1.2 ± 0.4 eV. We can then infer that the H concentration in the experiment must be highly concentrated at a ratio of 1 H dopant for every 2 Ni cations.

E.3.3 Integrated charge density analysis

To quantify the change in oxidation state upon H-doping, we plotted the spherically integrated spin-polarized charge density of our Ni cation in our FM SmNiO_3 system as a function of the radial distance from the Ni site in Figure SE.7³¹². We set our cutoff distance at 1.75 Å where the integrated spin density converges. We assume a spin density of 0 corresponds to an oxidation state of Ni^{4+} (empty degenerate e_g orbitals in the crystal field). As such, any increase in the spin density corresponds to a reduction of the Ni^{4+} cation. The integrated spin density is plotted for both the undoped and H-doped SmNiO_3 in Figures E.7a and E.7b respectively. In the pristine SmNiO_3 , we have two symmetrically distinct Ni atoms corresponding to the smaller (Ni_S) and

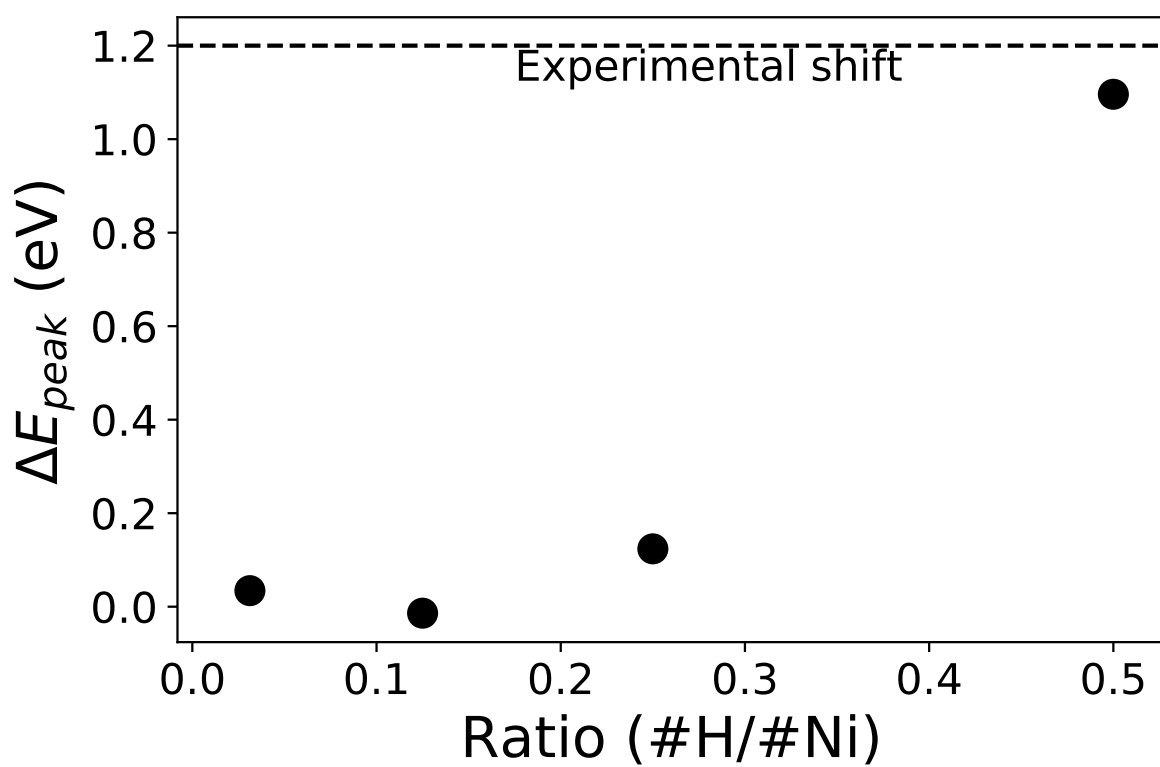


Figure E.6: Calculated shift of the XAS peak for H-doped SmNiO_3 relative to the peak of the XAS for pristine SmNiO_3 (y-axis) for various ratios of H:Ni in the SmNiO_3 supercells (x-axis). The experimental shift for H-doped SmNiO_3 is shown for reference (dashed line).

larger (Ni_L) NiO_6 polyhedrons as a result of the checkered-pattern breathing distortion. As a result, the electrons amongst the Ni cations are redistributed with Ni_S being the electron donor to Ni_L reflected in the lower (higher) integrated spin density of Ni_S (Ni_L). This is consistent with previous calculations using maximally-localized Wannier function³³⁰. Hence the final oxidation states are $Ni_L^{2.75+}$ and $Ni_S^{3.5+}$ and for the overall system, $Ni^{3.125+}$. The introduction of 1 H for every 2 Ni atoms will modify the oxidation states of the Ni cations according to Figure E.7b. The oxidation state of one Ni_L site will remain unaffected while the other becomes more oxidized with its oxidation state increasing from $Ni_L^{2.75}$ to $Ni_L^{3.1}$. On the other hand, both Ni_S sites will be reduced with the site closest to the H-dopants having its oxidation state reduced from $Ni_S^{3.5+}$ to $Ni_S^{2.66+}$. The magnitude of this reduction is in line with the expected reduction of Ni^{3+} to Ni^{2+} upon H-doping. For the entire system, the oxidation state of Ni will reduced from $Ni^{3.125+}$ to $Ni^{2.85+}$.

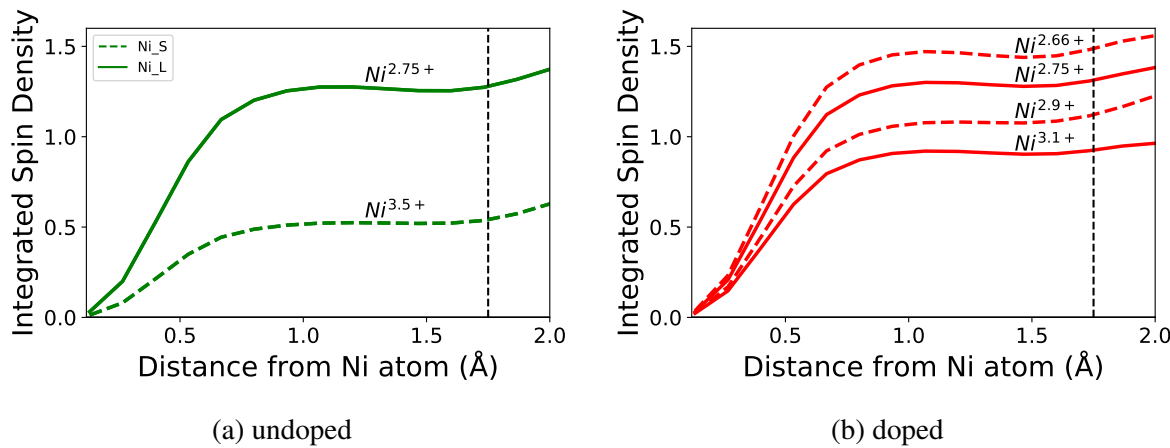


Figure E.7: Integrated spin density for the E.7a undoped and E.7b H-doped SmNiO_3 system. Dashed (solid) lines indicate the Ni site corresponding to the smaller (larger) NiO_6 polyhedron. The corresponding oxidation state for each Ni-site is shown.

Bibliography

Bibliography

- [1] R. N. Hall. Electron-hole recombination in germanium. *Phys. Rev.*, 87(July):387, 1952.
- [2] W. Shockley and W. T. Read. Statistics of the recombinations of holes and electrons. *Physical Review*, 87(5):835–842, 1952. ISSN 0031899X. doi: 10.1103/PhysRev.87.835.
- [3] J. Frenkel. On pre-breakdown phenomena in insulators and electronic semi-conductors. *Physical Review*, 54(8):647–648, 1938. ISSN 0031899X. doi: 10.1103/PhysRev.54.647.
- [4] W. Kohn and L. J. Sham. Self-Consistent Equations Including Exchange and Correlation Effects*. *Physical Review B*, 140(1951), 1965. ISSN 0031899X. doi: 10.1103/PhysRev.140.A1133.
- [5] Georgios D. Barmparis, Zbigniew Lodzianna, Nuria Lopez, and Ioannis N. Remediakis. Nanoparticle shapes by using Wulff constructions and first-principles calculations. *Beilstein Journal of Nanotechnology*, 6(1):361–368, 2015. ISSN 21904286. doi: 10.3762/bjnano.6.35.
- [6] Shane Carr, Roman Garnett, and Cynthia Lo. BASC: Applying Bayesian Optimization to the Search for Global Minima on Potential Energy Surfaces. *Icml*, 48(2012), 2016.
- [7] Jian Zhang. *A genetic algorithm approach in interface and surface structure optimization*. PhD thesis, Iowa State University, 2010.
- [8] Abhirup Patra, Jefferson Bates, Jianwei Sun, and John P. Perdew. Properties of real metallic surfaces: Effects of density functional semilocality and van der Waals nonlocality. *Arxiv*, pages 1–17, 2017.
- [9] Jess Wellendorff, Trent L. Silbaugh, Delfina Garcia-Pintos, Jens K. Nørskov, Thomas Bligaard, Felix Studt, and Charles T. Campbell. A benchmark database for adsorption bond energies to transition metal surfaces and comparison to selected DFT functionals. *Surface Science*, 640:36–44, 2015. ISSN 00396028. doi: 10.1016/j.susc.2015.03.023.
- [10] Olga Vinogradova, Dilip Krishnamurthy, Vikram Pande, and Venkatasubramanian Viswanathan. Quantifying Confidence in DFT-Predicted Surface Pourbaix Diagrams of Transition-Metal Electrode-Electrolyte Interfaces. *Langmuir*, 34(41):12259–12269, 2018. ISSN 15205827. doi: 10.1021/acs.langmuir.8b02219.

- [11] Q Jiang, H M Lu, and M Zhao. Modelling of surface energies of elemental crystals. *Journal of Physics: Condensed Matter*, 16(4):521–530, 2004. ISSN 0953-8984. doi: 10.1088/0953-8984/16/4/001.
- [12] Judit Ruvireta, Lorena Vega, and Francesc Viñes. Cohesion and coordination effects on transition metal surface energies. *Surface Science*, 664(May):45–49, 2017. ISSN 00396028. doi: 10.1016/j.susc.2017.05.013. URL <http://dx.doi.org/10.1016/j.susc.2017.05.013>.
- [13] D. Desjonquieres, M.-C., Spanjaard. *Concepts in Surface Physics*. Springer-Verlag Berlin Heidelberg, Berlin, 2 edition, 1993.
- [14] R. Smoluchowski. Anisotropy of the electronic work function of metals. *Physical Review*, 60(9):661–674, 1941. ISSN 0031899X. doi: 10.1103/PhysRev.60.661.
- [15] Anubhav Jain, Shyue Ping Ong, Geoffroy Hautier, Wei Chen, William Davidson Richards, Stephen Dacek, Shreyas Cholia, Dan Gunter, David Skinner, Gerbrand Ceder, and Kristin A. Persson. Commentary: The materials project: A materials genome approach to accelerating materials innovation. *APL Materials*, 1(1):011002 1, 2013. ISSN 2166532X. doi: 10.1063/1.4812323.
- [16] Chen Zheng, Chi Chen, Yiming Chen, and Shyue Ping Ong. Random Forest Models for Accurate Identification of Coordination Environments from X-Ray Absorption Near-Edge Structure. *Patterns*, 1(2):100013, 2020. ISSN 26663899. doi: 10.1016/j.patter.2020.100013. URL <https://doi.org/10.1016/j.patter.2020.100013>.
- [17] Chi Chen, Weike Ye, Yunxing Zuo, Chen Zheng, and Shyue Ping Ong. Graph Networks as a Universal Machine Learning Framework for Molecules and Crystals. *Chemistry of Materials*, 31(9):3564–3572, 2019. ISSN 15205002. doi: 10.1021/acs.chemmater.9b01294.
- [18] Weike Ye, Chi Chen, Zhenbin Wang, Iek-Heng Chu, and Shyue Ping Ong. Deep neural networks for accurate predictions of crystal stability. *Nature Communications*, 9(1):3800, dec 2018. ISSN 2041-1723. doi: 10.1038/s41467-018-06322-x. URL <http://www.nature.com/articles/s41467-018-06322-x>.
- [19] L Vitos, A V Ruban, H L Skriver, and J Kolla. The surface energy of metals. *Surface Science*, 411:186–202, 1998.
- [20] Sam De Waele, Kurt Lejaeghere, Michael Sluydts, and Stefaan Cottenier. Error estimates for density-functional theory predictions of surface energy and work function. *Physical Review B*, 94:1–13, 2016. doi: 10.1103/PhysRevB.94.235418.
- [21] Aini Palizhati, Wen Zhong, Kevin Tran, Seoin Back, and Zachary W. Ulissi. Toward Predicting Intermetallics Surface Properties with High-Throughput DFT and Convolutional Neural Networks. *Journal of Chemical Information and Modeling*, 59(11):4742–4749,

2019. ISSN 15205142. doi: 10.1021/acs.jcim.9b00550.

- [22] L. Vitos, A. V. Ruban, H. L. Skriver, and J. Kollár. The energetics of steps on transition metal surfaces. *Philosophical Magazine B: Physics of Condensed Matter; Statistical Mechanics, Electronic, Optical and Magnetic Properties*, 78(5-6):487–495, 1998. ISSN 13642812. doi: 10.1080/13642819808206750.
- [23] Jian-Min Zhang, Hong-Yan Li, and Ke-Wei Xu. Missing row reconstruction (110), (211) and (311) surfaces for FCC transition metals. *Surface and Interface Analysis*, 39(5): 660–664, 2007. ISSN 01422421. doi: 10.1002/sia.
- [24] Ž. Crljen, D. Šokčević, R. Brako, and P. Lazić. DFT calculations of (111) surfaces of Au, Cu, and Pt: stability and reconstruction. *Vacuum*, 71(1-2):101–106, 2003. ISSN 0042207X. doi: 10.1016/S0042-207X(02)00721-2.
- [25] D. Sturm, M. Heilmaier, J. H. Schneibel, P. Jéhanno, B. Skrotzki, and H. Saage. The influence of silicon on the strength and fracture toughness of molybdenum. *Materials Science and Engineering A*, 463(1-2):107–114, 2007. ISSN 09215093. doi: 10.1016/j.msea.2006.07.153.
- [26] Elisa Sani, Luca Mercatelli, Daniela Fontani, Jean Louis Sans, and Diletta Sciti. Hafnium and tantalum carbides for high temperature solar receivers. *Journal of Renewable and Sustainable Energy*, 3(6), 2011. ISSN 19417012. doi: 10.1063/1.3662099.
- [27] Haiqiang Bai, Lisheng Zhong, Junzhe Wei, Zhen Lin Lv, and Yunhua Xu. Morphological evolution of NbC particles at the interface of niobium–iron diffusion couple. *Materials Science and Technology (United Kingdom)*, 0(September):1–7, 2020. ISSN 17432847. doi: 10.1080/02670836.2020.1821985. URL <https://doi.org/10.1080/02670836.2020.1821985>.
- [28] David E. Grove, Ujjwal Gupta, and A. W. Castleman. Effect of carbon concentration on changing the morphology of titanium carbide nanoparticles from cubic to cuboctahedron. *ACS Nano*, 4(1):49–54, 2010. ISSN 19360851. doi: 10.1021/nn9010413.
- [29] Shenbao Jin, Ping Shen, Dongshuai Zhou, and Qichuan Jiang. A common regularity of stoichiometry-induced morphology evolution of transition metal carbides, nitrides, and diborides during self-propagating high-temperature synthesis. *Crystal Growth and Design*, 12(6):2814–2824, 2012. ISSN 15287483. doi: 10.1021/cg201604z.
- [30] David E. Grove, Ujjwal Gupta, and A. W. Castleman. Effect of hydrocarbons on the morphology of synthesized niobium carbide nanoparticles. *Langmuir*, 26(21):16517–16521, 2010. ISSN 07437463. doi: 10.1021/la101738c.
- [31] Jinfeng Nie, Yuying Wu, Pengting Li, Hui Li, and Liu Xiangfa. Morphological evolution of TiC from octahedron to cube induced by elemental nickel. *CrystEngComm*, 14(November): 2213–2221, 2012. doi: 10.1039/c1ce06205k.

- [32] Payam Kaghazchi. Carbon-induced Ru nanorod formation. *RSC Advances*, 4(4):1646, 2014. ISSN 2046-2069. doi: 10.1039/c3ra45985c. URL <http://xlink.rsc.org/?DOI=c3ra45985c>.
- [33] Tao Wang, Xinxin Tian, Yong Yang, Yong Wang Li, Jianguo Wang, Matthias Beller, and Haijun Jiao. Coverage-Dependent N₂ Adsorption and Its Modification of Iron Surfaces Structures. *Journal of Physical Chemistry C*, 120(5):2846–2854, 2016. ISSN 19327455. doi: 10.1021/acs.jpcc.5b11953.
- [34] Tao Wang, Shengguang Wang, Qiquan Luo, Yong Wang Li, Jianguo Wang, Matthias Beller, and Haijun Jiao. Hydrogen adsorption structures and energetics on iron surfaces at high coverage. *Journal of Physical Chemistry C*, 118(8):4181–4188, 2014. ISSN 19327447. doi: 10.1021/jp410635z.
- [35] Tao Wang, Xinxin Tian, Yong Yang, Yong-Wang Li, Jianguo Wang, Matthias Beller, and Haijun Jiao. Structures of seven molybdenum surfaces and their coverage dependent hydrogen adsorption. *Phys. Chem. Chem. Phys.*, 18(8):6005–6012, 2016. ISSN 1463-9076. doi: 10.1039/C5CP07349A. URL <http://xlink.rsc.org/?DOI=C5CP07349A>.
- [36] Richard Tran, Zihan Xu, Balachandran Radhakrishnan, Donald Winston, Wenhao Sun, Kristin Aslaug Persson, and Shyue Ping Ong. Data Descriptor: Surface energies of elemental crystals. *Scientific Data*, 3(160080):1–13, 2016. ISSN 0929-1903. doi: 10.1038/cgt.2016.38.
- [37] D. J. Eaglesham, A. E. White, L. C. Feldman, N. Moriya, and D. C. Jacobson. Equilibrium shape of Si. *Physical Review Letters*, 70(11):1643–1646, 1993. ISSN 00319007. doi: 10.1103/PhysRevLett.70.1643.
- [38] Marc F. V. Hidalgo, Yuh-Chieh Lin, Antonin Grenier, Dongdong Xiao, Jatinkumar Rana, Huolin Xin, Richard Tran, Mateusz J Zuba, Jennifer Donohue, Frederick O. Omenya, Iek-Heng Chu, Zhenbin Wang, XiangGuo Li, Natasha Chernova, Karena W. Chapman, Guangwen Zhou, Louis F.J. Piper, Shyue Ping Ong, and M. Stanley Whittingham. Rational Synthesis and Electrochemical Performance of LiVOPO₄ Polymorphs. *Journal of Materials Chemistry A*, 7(14):8423–8432, 2019. ISSN 2050-7488. doi: 10.1039/C8TA12531G. URL <http://pubs.rsc.org/en/Content/ArticleLanding/2019/TA/C8TA12531G>.
- [39] N. J. Petch. The cleavage strength of polycrystals. *J. Iron Steel Inst.*, 174(19):25–8, 1953.
- [40] E. O. Hall. The deformation and ageing of mild steel: II Characteristics of the Lüders deformation. *Proceedings of the Physical Society. Section B*, 64(9):742–747, 1951. ISSN 03701301. doi: 10.1088/0370-1301/64/9/302.
- [41] Hui Zheng, Richard Tran, Xiang Guo Li, Balachandran Radhakrishnan, and Shyue Ping Ong. Role of Zr in strengthening MoSi₂ from density functional theory calculations. *Acta Materialia*, 145:470–476, 2018. ISSN 13596454. doi: 10.1016/j.actamat.2017.12.017. URL <https://doi.org/10.1016/j.actamat.2017.12.017>.

- [42] Litong Yang, Yong Jiang, Yuan Wu, G. Robert Odette, Zhangjian Zhou, and Zheng Lu. The ferrite/oxide interface and helium management in nano-structured ferritic alloys from the first principles. *Acta Materialia*, 103:474–482, 2016. ISSN 13596454. doi: 10.1016/j.actamat.2015.10.031. URL <http://dx.doi.org/10.1016/j.actamat.2015.10.031>.
- [43] G Liu, G J Zhang, F Jiang, X D Ding, Y J Sun, J Sun, and E Ma. Nanostructured high-strength molybdenum alloys with unprecedented tensile ductility. *Nature materials*, 12(4):344–50, 2013. ISSN 1476-1122. doi: 10.1038/nmat3544.
- [44] Rainer Schweinfest, Anthony T Paxton, and Michael W Finnis. Bismuth embrittlement of copper is an atomic size effect. *Nature*, 432(7020):1008–11, dec 2004. ISSN 1476-4687. doi: 10.1038/nature03198. URL <http://www.ncbi.nlm.nih.gov/pubmed/15616557>.
- [45] A Y Lozovoi, A T Paxton, and M W Finnis. Structural and chemical embrittlement of grain boundaries by impurities: A general theory and first-principles calculations for copper. *Phys. Rev. B*, 74(15):155416, oct 2006. doi: 10.1103/PhysRevB.74.155416. URL <https://link.aps.org/doi/10.1103/PhysRevB.74.155416>.
- [46] Georg Schusteritsch, Thomas D. Kühne, Zheng Xiao Guo, and Efthimios Kaxiras. The effect of Ag, Pb and Bi impurities on grain boundary sliding and intergranular decohesion in Copper. *Philosophical Magazine*, 96(27):2868–2886, 2016. ISSN 14786443. doi: 10.1080/14786435.2016.1217360. URL <http://dx.doi.org/10.1080/14786435.2016.1217360>.
- [47] Joongoo Kang, Greg C. Glatzmaier, and Su Huai Wei. Origin of the bismuth-induced decohesion of nickel and copper grain boundaries. *Physical Review Letters*, 111(5):055502, jul 2013. ISSN 00319007. doi: 10.1103/PhysRevLett.111.055502. URL <http://link.aps.org/doi/10.1103/PhysRevLett.111.055502>.
- [48] Daniel Scheiber, Vsevolod I Razumovskiy, Peter Puschnig, Reinhard Pippan, and Lorenz Romaner. Ab initio description of segregation and cohesion of grain boundaries in W-25at.% Re alloys. *Acta Materialia*, 88:180–189, 2015. ISSN 1359-6454. doi: <https://doi.org/10.1016/j.actamat.2014.12.053><http://www.sciencedirect.com/science/article/pii/S1359645414009793>.
- [49] Jian-Hong Liao, Hui-Yun Bor, Chuen-Guang Chao, and Tzeng-Feng Liu. Influence of Rhenium on the Mechanical Behavior and Fracture Mechanism of a Fine-Grain Superalloy at Elevated Temperatures. *Materials Transactions*, 52(2):201–209, 2011. ISSN 1345-9678. doi: 10.2320/matertrans.M2010299.
- [50] Zhi-Wu Li, Xiang-Shan Kong, Chang-Song Liu, and Qian-Feng Fang. Segregation of alloying atoms at a tilt symmetric grain boundary in tungsten and their strengthening and embrittling effects. *Chinese Physics B*, 23(10):106107, oct 2014. ISSN 1674-1056. doi: 10.1088/1674-1056/23/10/106107.

- [51] Rita I. Babicheva, Sergey V. Dmitriev, Ying Zhang, Shaw Wei Kok, Narasimalu Srikanth, Bo Liu, and Kun Zhou. Effect of grain boundary segregations of Fe, Co, Cu, Ti, Mg and Pb on small plastic deformation of nanocrystalline Al. *Computational Materials Science*, 98:410–416, 2015. ISSN 09270256. doi: 10.1016/j.commatsci.2014.11.038. URL <http://linkinghub.elsevier.com/retrieve/pii/S0927025614008180>.
- [52] Liam Huber, Jörg Rottler, and Matthias Miltzner. Atomistic simulations of the interaction of alloying elements with grain boundaries in Mg. *Acta Materialia*, 80: 194–204, nov 2014. ISSN 13596454. doi: 10.1016/j.actamat.2014.07.047. URL <http://www.sciencedirect.com/science/article/pii/S1359645414005655><https://linkinghub.elsevier.com/retrieve/pii/S1359645414005655>.
- [53] Pavel Lejček, Mojmír Šob, and Václav Paidar. Interfacial segregation and grain boundary embrittlement: An overview and critical assessment of experimental data and calculated results. *Progress in Materials Science*, 87:83–139, 2017. ISSN 00796425. doi: 10.1016/j.pmatsci.2016.11.001. URL <http://linkinghub.elsevier.com/retrieve/pii/S0079642516300755>.
- [54] Michael A Gibson and Christopher A Schuh. Segregation-induced changes in grain boundary cohesion and embrittlement in binary alloys. *Acta Materialia*, 95:145–155, 2015. ISSN 13596454. doi: 10.1016/j.actamat.2015.05.004. URL <http://dx.doi.org/10.1016/j.actamat.2015.05.004><http://linkinghub.elsevier.com/retrieve/pii/S135964541500316X>.
- [55] Michael a. Gibson and Christopher a. Schuh. A survey of ab-initio calculations shows that segregation-induced grain boundary embrittlement is predicted by bond-breaking arguments. *Scripta Materialia*, 113:55–58, 2016. ISSN 13596462. doi: 10.1016/j.scriptamat.2015.09.041.
- [56] Andries Rinse Miedema. Surface segregation in alloys of transition-metals. *Zeitschrift Fur Metallkunde*, 7(69):455–461, 1978.
- [57] Donald McLean. *Grain Boundaries in Metals*. Oxford University Press, New York, NY, USA, 1957.
- [58] M.P. Seah. Adsorption-induced interface decohesion. *Acta Metallurgica*, 28(7):955–962, 1980. ISSN 00016160. doi: 10.1016/0001-6160(80)90112-1.
- [59] E.D. Hondros, M.P. Seah, S Hofmann, and C. Lejček. No Title. In R.W. Cahn and P. Haasen, editors, *Physical Metallurgy*, pages 1201–1289. Elsevier B.V., North Holland, Amsterdam, 1996.
- [60] Pavel Lejček, Mojmír Šob, Václav Paidar, and Vaclav Vitek. Why calculated energies of grain boundary segregation are unreliable when segregant solubility is low. *Scripta Materialia*, 68(8):547–550, apr 2013. ISSN 13596462. doi: 10.1016/j.scriptamat.2012.11.019. URL <http://linkinghub.elsevier.com/retrieve/pii/S1359646212007397>.

- [61] AV Ruban, HL Skriver, and JK Nørskov. Surface segregation energies in transition-metal alloys. *Physical Review B*, 59(24):15990–16000, jun 1999. ISSN 0163-1829. doi: 10.1103/PhysRevB.59.15990. URL <http://prb.aps.org/abstract/PRB/v59/i24/p15990>{_}1{%}5Cn<http://link.aps.org/doi/10.1103/PhysRevB.59.15990>.
- [62] Daniel Scheiber, Reinhard Pippan, Peter Puschnig, Andrei Ruban, and Lorenz Rotter. Ab-initio search for cohesion-enhancing solute elements at grain boundaries in molybdenum and tungsten. *International Journal of Refractory Metals and Hard Materials*, 60:75–81, 2016. ISSN 22133917. doi: 10.1016/j.ijrmhm.2016.07.003. URL <http://dx.doi.org/10.1016/j.ijrmhm.2016.07.003>.
- [63] Youhui Zhang, Peng Qu, Yu Ji, Weihao Zhang, Guangrong Gao, Guanrui Wang, Sen Song, Guoqi Li, Wenguang Chen, Weimin Zheng, Feng Chen, Jing Pei, Rong Zhao, Mingguo Zhao, and Luping Shi. A system hierarchy for brain-inspired computing. *Nature*, 586 (October):378–384, 2020. doi: 10.1038/s41586-020-2782-y.
- [64] M. Prezioso, F. Merrikh-Bayat, B. D. Hoskins, G. C. Adam, K. K. Likharev, and D. B. Strukov. Training and operation of an integrated neuromorphic network based on metal-oxide memristors. *Nature*, 521(7550):61–64, 2015. ISSN 14764687. doi: 10.1038/nature14441.
- [65] Shinhyun Choi, Patrick Sheridan, and Wei D. Lu. Data clustering using memristor networks. *Scientific Reports*, 5:1–10, 2015. ISSN 20452322. doi: 10.1038/srep10492.
- [66] J. H. De Boer and E. J.W. Verwey. Semi-conductors with partially and with completely filled 3d-lattice bands. *Proceedings of the Physical Society*, 49(4S):59–71, 1937. ISSN 09595309. doi: 10.1088/0959-5309/49/4S/307.
- [67] Nevill Mott. On Metal-Insulator Transitions. *Journal of Solid State Chemistry*, 88(April): 5–7, 1990.
- [68] Naixie Zhou and Jian Luo. Developing grain boundary diagrams for multicomponent alloys. *Acta Materialia*, 91:202–216, 2015. ISSN 13596454. doi: 10.1016/j.actamat.2015.03.013. URL <http://www.sciencedirect.com/science/article/pii/S1359645415001809>.
- [69] Yoav Kalcheim, Alberto Camjayi, Javier del Valle, Pavel Salev, Marcelo Rozenberg, and Ivan K. Schuller. Non-thermal resistive switching in Mott insulator nanowires. *Nature Communications*, 11(1):1–9, 2020. ISSN 20411723. doi: 10.1038/s41467-020-16752-1. URL <http://dx.doi.org/10.1038/s41467-020-16752-1>.
- [70] Pablo Stoliar, Laurent Cario, Etiene Janod, Benoit Corraze, Catherine Guillot-Deudon, Sabrina Salmon-Bourmand, Vincent Guiot, Julien Tranchant, and Marcelo Rozenberg. Universal electric-field-driven resistive transition in narrow-gap Mott insulators. *Advanced Materials*, 25(23):3222–3226, 2013. ISSN 09359648. doi: 10.1002/adma.201301113.

- [71] D. B. McWhan, A. Menth, J. P. Remeika, W. F. Brinkman, and T. M. Rice. Metal-insulator transitions in pure and doped V₂O₃. *Physical Review B*, 7(5):1920–1931, 1973. ISSN 01631829. doi: 10.1103/PhysRevB.7.1920.
- [72] D. B. McWhan, T. M. Rice, and J. P. Remeika. Mott transition in Cr-doped V₂O₃. *Physical Review Letters*, 23(24):1384–1387, 1969.
- [73] V. Simic-Milosevic, N. Nilius, H. P. Rust, and H. J. Freund. Local band gap modulations in non-stoichiometric V₂O₃ films probed by scanning tunneling spectroscopy. *Physical Review B - Condensed Matter and Materials Physics*, 77(12):1–5, 2008. ISSN 10980121. doi: 10.1103/PhysRevB.77.125112.
- [74] Y. Ueda, K. Kosuge, and S. Kachi. Phase diagram and some physical properties of V₂O_{3+x} ($0 \leq x \leq 0.080$). *Journal of Solid State Chemistry*, 31(2):171–188, 1980. ISSN 00224596. doi: 10.1016/0022-4596(80)90019-5.
- [75] Seokjae Won, Sang Yeon Lee, Jungyeon Hwang, Jucheol Park, and Hyungtak Seo. Electric field-triggered metal-insulator transition resistive switching of bilayered multiphasic VO_x. *Electronic Materials Letters*, 14(1):14–22, 2018. ISSN 20936788. doi: 10.1007/s13391-017-7134-1.
- [76] Jaewoo Jeong, Nagaphani Aetukuri, Tanja Graf, Thomas D Schladt, Mahesh G Samant, and Stuart S P Parkin. Suppression of Metal-Insulator Transition in VO₂ by Electric Field-induced Oxygen Vacancy Formation. *Science*, 339(March):1402–1406, 2013.
- [77] Pilsun Yoo and Peilin Liao. First principles study on hydrogen doping induced metal-to-insulator transition in rare earth nickelates RNiO₃ (R = Pr, Nd, Sm, Eu, Gd, Tb, Dy, Yb). *Physical Chemistry Chemical Physics*, 22(13):6888–6895, 2020. ISSN 1463-9076. doi: 10.1039/C9CP06522A. URL <http://dx.doi.org/10.1039/C9CP06522A>.
- [78] Jp Perdew, K Burke, and M Ernzerhof. Generalized Gradient Approximation Made Simple. *Physical review letters*, 77(18):3865–3868, oct 1996. ISSN 1079-7114.
- [79] P. Hohenberg and W. Kohn. Inhomogeneous electron gas. *Physical Review*, 136:B864, 1964. ISSN 01631829. doi: 10.1103/PhysRevB.7.1912.
- [80] J. Hubbard and Brian Hilton Flowers. Electron correlations in narrow energy bands. *Proceedings of the Royal Society of London. A. Mathematical and Physical Sciences*, 276 (1365):238–257, 1963.
- [81] Chao Sun, Liuming Yan, Baohua Yue, Huiting Liu, and Yanfeng Gao. The modulation of metal-insulator transition temperature of vanadium dioxide: A density functional theory study. *Journal of Materials Chemistry C*, 2(43):9283–9293, 2014. ISSN 20507526. doi: 10.1039/c4tc00778f. URL <http://dx.doi.org/10.1039/C4TC00778F>.
- [82] Frank Lechermann, Noam Bernstein, I. I. Mazin, and Roser Valentí. Uncovering the

Mechanism of the Impurity-Selective Mott Transition in Paramagnetic V₂O₃. *Physical Review Letters*, 121(10):106401, 2018. ISSN 10797114. doi: 10.1103/PhysRevLett.121.106401. URL <https://doi.org/10.1103/PhysRevLett.121.106401>.

- [83] D. B. McWhan and J. P. Remeika. Metal-Insulator Transition in (V_{1-x}C_x)₂O₃. *Physical Review B*, 2(9):3734–3750, 1970. ISSN 0556-2805. doi: 10.1103/PhysRevB.2.3734. URL <https://link.aps.org/doi/10.1103/PhysRevB.2.3734>.
- [84] Pilsun Yoo and Peilin Liao. Metal-to-insulator transition in SmNiO₃ induced by chemical doping: a first principles study. *Molecular Systems Design & Engineering*, 3(1):264–274, 2018. doi: 10.1039/C8ME00002F. URL <http://dx.doi.org/10.1039/C8ME00002F>.
- [85] Michele Kotiuga and Karin M. Rabe. High-density electron doping of SmNiO₃ from first principles. *Physical Review Materials*, 3(11):1–12, 2019. ISSN 24759953. doi: 10.1103/PhysRevMaterials.3.115002.
- [86] Blanka Magyari-Köpe, Seong Geon Park, Hyung Dong Lee, and Yoshio Nishi. First principles calculations of oxygen vacancy-ordering effects in resistance change memory materials incorporating binary transition metal oxides. *Journal of Materials Science*, 47(21):7498–7514, 2012. ISSN 00222461. doi: 10.1007/s10853-012-6638-1.
- [87] W. B. Zhang, N. Yu, W. Y. Yu, and B. Y. Tang. Stability and magnetism of vacancy in NiO: A GGA+U study. *European Physical Journal B*, 64(2):153–158, 2008. ISSN 14346028. doi: 10.1140/epjb/e2008-00303-x.
- [88] Yuanyuan Cui, Bin Liu, Lanli Chen, Hongjie Lup, and Yanfeng Gao. Formation energies of intrinsic point defects in monoclinic VO₂ studied by first-principles calculations. *AIP Advances*, 6(October):105301 1–9, 2016. doi: 10.1063/1.4964495.
- [89] Lanli Chen, Yuanyuan Cui, Siqi Shi, Bin Liu, Hongjie Luo, and Yanfeng Gao. First-principles study of the effect of oxygen vacancy and strain on the phase transition temperature of VO₂. *RSC Advances*, 6(90):86872–86879, 2016. ISSN 20462069. doi: 10.1039/c6ra19121e.
- [90] Udo Schwingenschlögl and Volker Eyert. The vanadium Magnéli phases V_nO_{2n-1}. *Annalen der Physik (Leipzig)*, 13(9):475–510, 2004. ISSN 00033804. doi: 10.1002/andp.200410099.
- [91] Yuzheng Guo and John Robertson. Analysis of metal insulator transitions in VO₂ and V₂O₃ for RRAMs. *Microelectronic Engineering*, 109:278–281, 2013. ISSN 0167-9317. doi: 10.1016/j.mee.2013.03.015. URL <http://dx.doi.org/10.1016/j.mee.2013.03.015>.
- [92] Darshana Wickramaratne, Noam Bernstein, and I. I. Mazin. Role of defects in the metal-insulator transition in VO₂ and V₂O₃. *Physical Review B*, 99(21):1–9, 2019. ISSN 24699969. doi: 10.1103/PhysRevB.99.214103.

- [93] Juan Gabriel Ramirez, Thomas Saerbeck, Siming Wang, J Trastoy, M Malnou, J Lesueur, Jean-paul Crocombette, Javier E Villegas, and Ivan K Schuller. Effect of disorder on the metal-insulator transition of vanadium oxides : Local versus global effects. *Physical Review B*, 205123(91):1–5, 2015. doi: 10.1103/PhysRevB.91.205123.
- [94] B. Hammer and J. K. Norskov. Why gold is the noblest of all the metals. *Nature*, 376(6537):238–240, 1995. ISSN 0028-0836. doi: 10.1038/376238a0.
- [95] Jeff Greeley, Jens K. Norskov, and Manos Mavrikakis. ELECTRONIC STRUCTURE AND CATALYSIS ONMETAL SURFACES. *Annual Review of Physical Chemistry*, 53: 197–223, 2002. ISSN 0732-0582. doi: 10.1146/annurev.immunol.19.1.197.
- [96] B. Hammer and J.K. Norskov. Theoretical Surface Science and Catalysis — Calculations and Concepts. *Advances in Catalysis*, 45:71–129, 2000. ISSN 03600564. doi: [http://dx.doi.org/10.1016/S0360-0564\(02\)45013-4](http://dx.doi.org/10.1016/S0360-0564(02)45013-4).
- [97] Jens K Nørskov, Thomas Bligaard, J Rossmeisl, and C H Christensen. Towards the computational design of solid catalysts. *Nature chemistry*, 1(1):37–46, 2009. ISSN 1755-4349. doi: 10.1038/nchem.121.
- [98] Vojislav Stamenkovic, Bongjin Simon Mun, Karl J J Mayrhofer, Philip N. Ross, Nenad M. Markovic, Jan Rossmeisl, Jeff Greeley, and Jens K. Nørskov. Changing the activity of electrocatalysts for oxygen reduction by tuning the surface electronic structure. *Angewandte Chemie - International Edition*, 45(18):2897–2901, 2006. ISSN 14337851. doi: 10.1002/anie.200504386.
- [99] T. Bligaard, J. K. Norskov, S. Dahl, J. Matthiesen, C. H. Christensen, and J. Sehested. The Bronsted-Evans-Polanyi relation and the volcano curve in heterogeneous catalysis. *Journal of Catalysis*, 224(1):206–217, 2004. ISSN 00219517. doi: 10.1016/j.jcat.2004.02.034.
- [100] A Logadottir, T.H Rod, J.K Nørskov, B Hammer, S Dahl, and C.J.H Jacobsen. The Brønsted–Evans–Polanyi Relation and the Volcano Plot for Ammonia Synthesis over Transition Metal Catalysts. *Journal of Catalysis*, 197(2):229–231, 2001. ISSN 00219517. doi: 10.1006/jcat.2000.3087.
- [101] Qian Lin Tang and Qing Hong Luo. Adsorption of CO₂ at ZnO: A surface structure effect from DFT+ U Calculations. *Journal of Physical Chemistry C*, 117(44):22954–22966, 2013. ISSN 19327447. doi: 10.1021/jp407970a.
- [102] Qian-Lin Tang, Wen-Tian Zou, Run-Kun Huang, Qi Wang, and Xiao-Xuan Duan. Effect of the components' interface on the synthesis of methanol over Cu/ZnO from CO₂/H₂: a microkinetic analysis based on DFT + U calculations. *Phys. Chem. Chem. Phys.*, 17(11):7317–7333, 2015. ISSN 1463-9076. doi: 10.1039/C4CP05518G.
- [103] Mélanie Auffan, Jérôme Rose, Jean-Yves Bottero, Gregory V Lowry, Jean-Pierre Jolivet,

and Mark R Wiesner. Towards a definition of inorganic nanoparticles from an environmental, health and safety perspective. *Nature nanotechnology*, 4(10):634–41, 2009. ISSN 1748-3395. doi: 10.1038/nnano.2009.242.

- [104] George Volonakis, Leonidas Tsetseris, and Stergios Logothetidis. Electronic and structural properties of TiB₂: Bulk, surface, and nanoscale effects. *Materials Science and Engineering B: Solid-State Materials for Advanced Technology*, 176(6):484–489, 2011. ISSN 09215107. doi: 10.1016/j.mseb.2010.03.063.
- [105] Michael A. Boles, Daishun Ling, Taeghwan Hyeon, and Dmitri V. Talapin. The surface science of nanocrystals. *Nature Materials*, 15(2):141–153, 2016. ISSN 1476-1122. doi: 10.1038/nmat4526.
- [106] Mauro Coelho Dos Santos, Olivera Kesler, and Arava Leela Mohana Reddy. Nanomaterials for energy conversion and storage. *Journal of Nanomaterials*, 2012:3127–3171, 2012. ISSN 16874110. doi: 10.1155/2012/159249.
- [107] P. Sharma, S. Ganti, and N. Bhate. Effect of surfaces on the size-dependent elastic state of nano-inhomogeneities. *Applied Physics Letters*, 82(4):535–537, 2003. ISSN 00036951. doi: 10.1063/1.1539929.
- [108] Shinyoung Kang, Yifei Mo, Shyue Ping Ong, and Gerbrand Ceder. Nanoscale stabilization of sodium oxides: Implications for Na-O₂ batteries. *Nano Letters*, 14(2):1016–1020, 2014. ISSN 15306984. doi: 10.1021/nl404557w.
- [109] Alexandra Navrotsky. Energetics of nanoparticle oxides: interplay between surface energy and polymorphism. *Geochemical transactions*, 4(6):34, 2003. ISSN 1467-4866. doi: 10.1186/1467-4866-4-34.
- [110] Wenhao Sun, Saivenkataraman Jayaraman, Wei Chen, Kristin A Persson, and Gerbrand Ceder. Nucleation of metastable aragonite CaCO₃ in seawater. *Proceedings of the National Academy of Sciences*, 112(11):3199–3204, 2015. doi: 10.1073/pnas.1423898112.
- [111] A S Barnard and L A Curtiss. Prediction of TiO₂ nanoparticle phase and shape transitions controlled by surface chemistry. *Nano Letters*, 5(7):1261–1266, 2005. doi: 10.1021/nl050355m.
- [112] Robert W. Balluffi, Samuel M. Allen, and W. Craig Carter. *Kinetics of Materials*. John Wiley & Sons, Hoboken, New Jersey, 2005.
- [113] W.R. Miller and W.A. Tyson. Surface Free Energies of Solid Metals. Estimation From Liquid Surface Tension Measurements. *Surface Science*, 62(1):267–276, 1977.
- [114] John J Gilman. Direct Measurements of the Surface Energies of Crystals. *Journal of Applied Physics*, 31:2208–2218, 1960. doi: 10.1063/1.1735524.

- [115] J. J. Métois and P. Müller. Absolute surface energy determination. *Surface Science*, 548(1-3):13–21, 2004. ISSN 00396028. doi: 10.1016/j.susc.2003.11.027.
- [116] C. Bombis, A. Emundts, M. Nowicki, and H. P. Bonzel. Absolute surface free energies of Pb. *Surface Science*, 511(1-3):83–96, 2002. ISSN 00396028. doi: 10.1016/S0039-6028(02)01554-6.
- [117] Wei-Bing Zhang, Chuan Chen, and Shun-Ying Zhang. Equilibrium Crystal Shape of Ni from First Principles. *The Journal of Physical Chemistry C*, 117(41):21274–21280, oct 2013. ISSN 1932-7447. doi: 10.1021/jp404569m.
- [118] A K Niessen, F R de Boer, R Boom, W C M Mattens, and A R Miedema. *Cohesion in metals*. Elsevier Scientific Pub. Co., New York, NY, 1998.
- [119] K C Mills and Y C Su. Review of surface tension data for metallic elements and alloys: Part 1 – Pure metals. *International Materials Reviews*, 51(6):329–351, dec 2006. ISSN 0950-6608. doi: 10.1179/174328006X102510.
- [120] B. J. Keene. Review of data for the surface tension of pure metals. *International Materials Reviews*, 38(4):157–192, 1993. ISSN 09506608. doi: 10.1179/095066093790326285.
- [121] M. J. Harrison, D. P. Woodruff, J. Robinson, D. Sander, W. Pan, and J. Kirschner. Adsorbate-induced surface reconstruction and surface-stress changes in Cu (100) O: Experiment and theory. *Physical Review B - Condensed Matter and Materials Physics*, 74(16):1–7, 2006. ISSN 10980121. doi: 10.1103/PhysRevB.74.165402.
- [122] H. P. Bonzel, D. K. Yu, and M. Scheffler. The three-dimensional equilibrium crystal shape of Pb: Recent results of theory and experiment. *Applied Physics A: Materials Science and Processing*, 87(3):391–397, 2007. ISSN 09478396. doi: 10.1007/s00339-007-3951-7.
- [123] K. F. Wojciechowski. Surface energy of metals: Theory and experiment. *Surface Science*, 437(3):285–288, 1999. ISSN 00396028. doi: 10.1016/S0039-6028(99)00741-4.
- [124] Nina Kosova, Evgeniya Devyatkina, Arseny Slobodyuk, and Vasily Kaichev. Surface chemistry study of LiCoO₂ coated with alumina. *Solid State Ionics*, 179(27-32):1745–1749, 2008. ISSN 01672738. doi: 10.1016/j.ssi.2008.02.013.
- [125] M Methfessel. Trends of the Surface Relaxations, Surface Energies, and Workf Functions of the 4d Transition Metals. *Physical Review B*, 46(8):4816–4829, 1992.
- [126] I. Galanakis, N. Papanikolaou, and P. H. Dederichs. Applicability of the Broken-Bond Rule to the Surface Energy of the fcc Metals. *Surface Science*, 511(1-3):1–12, 2002. doi: 10.1016/S0039-6028(02)01547-9.
- [127] L. Vitos, J. Kollar, and H.L. Skriver. Full charge-density scheme with a kinetic-energy correction: Application to ground- state properties of the 4d metals. *Physical Review B*, 55

(20):13521–13527, 1997. doi: 10.1103/PhysRevB.55.13521.

- [128] Dengke Yu and Matthias Scheffler. First-principles study of low-index surfaces of lead. *Physical Review B - Condensed Matter and Materials Physics*, 70(May):1–8, 2004. ISSN 01631829. doi: 10.1103/PhysRevB.70.155417.
- [129] R. E. Schlier and H. E. Farnsworth. Structure and Adsorption Characteristics of Clean Surfaces of Germanium and Silicon. *The Journal of Chemical Physics*, 30(4):917, 1959. ISSN 00219606. doi: doi:10.1063/1.1730126.
- [130] Walter A. Harrison. Surface reconstruction on semiconductors. *Surface Science*, 55(1):1–19, 1976. ISSN 00396028. doi: 10.1016/0039-6028(76)90372-1.
- [131] A. Stekolnikov, J. Furthmüller, and F. Bechstedt. Absolute surface energies of group-IV semiconductors: Dependence on orientation and reconstruction. *Physical Review B*, 65(11):1–10, 2002. ISSN 0163-1829. doi: 10.1103/PhysRevB.65.115318.
- [132] Wenhao Sun and Gerbrand Ceder. Efficient creation and convergence of surface slabs. *Surface Science*, 617:53–59, 2013. ISSN 00396028. doi: 10.1016/j.susc.2013.05.016.
- [133] Jian Min Zhang, Min Yan Zhang, and Ke Wei Xu. Missing row reconstruction on three low index surfaces of ten FCC metals. *Crystal Research and Technology*, 44(3):275–280, 2009. ISSN 02321300. doi: 10.1002/crat.200800402.
- [134] Shyue Ping Ong, Shreyas Cholia, Anubhav Jain, Miriam Brafman, Dan Gunter, Gerbrand Ceder, and Kristin A. Persson. The Materials Application Programming Interface (API): A simple, flexible and efficient API for materials data based on REpresentational State Transfer (REST) principles. *Computational Materials Science*, 97:209–215, 2015. ISSN 09270256. doi: 10.1016/j.commatsci.2014.10.037.
- [135] Shyue Ping Ong, William Davidson Richards, Anubhav Jain, Geoffroy Hautier, Michael Kocher, Shreyas Cholia, Dan Gunter, Vincent L. Chevrier, Kristin A. Persson, and Gerbrand Ceder. Python Materials Genomics (pymatgen): A robust, open-source python library for materials analysis. *Computational Materials Science*, 68:314–319, 2013. ISSN 09270256. doi: 10.1016/j.commatsci.2012.10.028. URL <http://linkinghub.elsevier.com/retrieve/pii/S0927025612006295>.
- [136] G Kresse and J Furthmüller. Efficient iterative schemes for ab initio total-energy calculations using a plane-wave basis set. *Physical review. B, Condensed matter*, 54(16):11169–11186, oct 1996. ISSN 0163-1829.
- [137] J. Kresse, G., Furthmuller. Software VASP, Vienna. *Physical Review B*, 54(11):169, 1996.
- [138] Mohamed Hacene, Ani Anciaux-Sedrakian, Xavier Rozanska, Diego Klahr, Thomas Guignon, and Paul Fleurat-Lessard. Accelerating VASP electronic structure calculations using graphic processing units. *Journal of Computational Chemistry*, 33(32):2581–2589,

2012. ISSN 01928651. doi: 10.1002/jcc.23096.

- [139] M Hutchinson and Michael Widom. VASP on a GPU : Application to exact-exchange calculations of the stability of elemental boron. *Computer Physics Communications*, 7 (183):1422–1426, 2011.
- [140] Peter E. Blöchl. Projector augmented-wave method, 1994. ISSN 0163-1829.
- [141] M. Methfessel and A. T. Paxton. High-precision sampling for Brillouin-zone integration in metals. *Physical Review B*, 40(6):3616–3621, 1989. ISSN 01631829. doi: 10.1103/PhysRevB.40.3616.
- [142] S Johnson and J Joannopoulos. Block-iterative frequency-domain methods for Maxwell’s equations in a planewave basis. *Optics Express*, 8(3):173–190, 2001. ISSN 10944087. doi: 10.1364/OE.8.000173.
- [143] T L Einstein. Equilibrium Shape of Crystals. In *Handbook of Crystal Growth*, chapter 5, pages 215–264. Elsevier B.V., second edi edition, 2015. ISBN 9780444563699. doi: 10.1016/B978-0-444-56369-9.00005-1.
- [144] Salvador Miracle-Sole. Wulff shape of equilibrium crystals, 2013.
- [145] Anubhav Jain, Shyue Ping Ong, Wei Chen, Bharat Medasani, Xiaohui Qu, Michael Kocher, Miriam Brafman, Guido Petretto, Gian-Marco Rignanese, Geoffroy Hautier, Daniel Gunter, and Kristin A. Persson. FireWorks: a dynamic workflow system designed for high-throughput applications. *Concurrency and Computation: Practice and Experience*, 27(17):5037–5059, dec 2015. ISSN 15320626.
- [146] Kurt Lejaeghere, V. Van Speybroeck, G. Van Oost, and S. Cottenier. Error Estimates for Solid-State Density-Functional Theory Predictions: An Overview by Means of the Ground-State Elemental Crystals. *Critical Reviews in Solid State and Materials Sciences*, 39(1):1–24, 2014. ISSN 1040-8436. doi: 10.1080/10408436.2013.772503.
- [147] R. J. Jaccodine. Surface Energy of Germanium and Silicon. *Journal of The Electrochemical Society*, 110(6):524, 1963. ISSN 00134651. doi: 10.1149/1.2425806.
- [148] A J Osteraas, Douglas A Olsen, Richard W Moravec, and A Jean Osteraas. The Critical Surface Tension Values of Group VIA Elements. *The Journal of Physical Chemistry*, 71 (13):4464–4466, 1967.
- [149] G. Guisbiers, S. Arscott, M. Gaudet, A. Belfiore, and R. Snyders. Selenium surface energy determination from size-dependent considerations. In *Nanoelectronics Conference*, pages 105–109, Singapore, 2013. IEEE. ISBN 9781467348423.
- [150] N Eustathopoulos, M.G. Nicholas, and B. Drevet. *Pergamon materials series: wettability at high teperatures*. PERGAMON-ELSEVIER SCIENCE LTD, Kidlington, Oxford, 1999.

- [151] John P Perdew, J. A. Chevary, S. H. Vosko, Koblar A Jackson, Mark R Pederson, D J Singh, and Carlos Fiolhais. Atoms, molecules, solids, and surfaces: Applications of the generalized gradient approximation for exchange and correlation. *Physical Review B*, 46(11):6671–6687, 1992.
- [152] Newton Ooi, Asit Raikar, and James B Adams. Density functional study of graphite bulk and surface properties. *Carbon*, 44:231–242, 2006. doi: 10.1016/j.carbon.2005.07.036.
- [153] Gabor A. Samorjai and Yimin Li. *Introduction to surface chemistry and catalysts*. John Wiley & Sons, 2010.
- [154] G. Binnig, H. Rohrer, Ch Gerber, and E. Weibel. 7 x 7 Reconstruction on Si(111) Resolved in Real Space. *Physical Review Letters*, 50(2):120–123, 1983. ISSN 00319007. doi: 10.1103/PhysRevLett.50.120.
- [155] Kd Brommer, M Needels, and B Larson. Ab Initio Theory of the Si(111)-(7X7) Surface Reconstruction. *Physical review letters*, 68(9):1355–1359, 1992. ISSN 0031-9007. doi: 10.1103/PhysRevLett.68.1355.
- [156] J. L F Da Silva, Catherine Stampfl, and Matthias Scheffler. Converged properties of clean metal surfaces by all-electron first-principles calculations. *Surface Science*, 600(3): 703–715, 2006. ISSN 00396028. doi: 10.1016/j.susc.2005.12.008.
- [157] Angelos Michaelides and Matthias Scheffler. An introduction to the theory of metal surfaces. . . . of *Surface and Interface Science*, pages 1–40, 2010.
- [158] Simon J Binnie. *Ab initio surface energetics : Beyond chemical accuracy*. PhD thesis, University College London, 2011.
- [159] J Goniakowski, J. M. Holender, L. N. Kantorovich, and M.J. Gillan. Influence of gradient corrections on the bulk and surface properties of TiO₂ and SnO₂. *Physical Review B - Condensed Matter*, 53(3):957–960, 1996.
- [160] J.K. Mackenzie, A.J.W. Moore, and J.F. Nicholas. Bonds broken at atomically flat crystal surfaces—I. *Journal of Physics and Chemistry of Solids*, 23(3):185–196, 1962. ISSN 00223697. doi: 10.1016/0022-3697(62)90001-X.
- [161] J. K. Mackenzie and J. F. Nicholas. Bonds Broken At Atomically Flat Crystal Surfaces-II. *Journal of Physics and Chemistry of Solids*, 23(3):197–205, 1962.
- [162] K Doll, M. N. Harrison, and V. R. Saunders. A density functional study of lithium bulk and surfaces This. *Journal of physics. Condensed matter*, 11:5007–5019, 1999.
- [163] K Kokko, P T Salo, R Laihia, and K Mansikka. First-principles calculations for work function and surface energy of thin lithium films. *Surface Science*, 348(100):168–174, 1996.

- [164] Su-Hyun Yoo, Ji-Hwan Lee, Young-Kwang Jung, and Aloysius Soon. Exploring stereographic surface energy maps of cubic metals via an effective pair-potential approach. *Physical Review B*, 93:1–8, 2016. doi: 10.1103/PhysRevB.93.035434.
- [165] M Ropo, K Kokko, and L Vitos. Assessing the Perdew-Burke-Ernzerhof exchange-correlation density functional revised for metallic bulk and surface systems. *Physical Review B*, 77(195445):1–6, 2008. doi: 10.1103/PhysRevB.77.195445.
- [166] J. Che, C. Chan, W-E. Jian, and T. Leung. Surface atomic structures, surface energies, and equilibrium crystal shape of molybdenum. *Physical Review B*, 57(3):1875–1880, jan 1998. ISSN 0163-1829. doi: 10.1103/PhysRevB.57.1875.
- [167] Georg Heimel, Lorenz Romaner, Jean Luc Bredas, and Egbert Zojer. Interface energetics and level alignment at covalent metal-molecule junctions: pi-conjugated thiols on gold. *Physical Review Letters*, 96(19):2–5, 2006. ISSN 00319007. doi: 10.1103/PhysRevLett.96.196806.
- [168] Hao Lu, Guomin Hua, and Dongyang Li. Dependence of the mechanical behavior of alloys on their electron work function - An alternative parameter for materials design. *Applied Physics Letters*, 103(26):2619021–2619024, 2013. ISSN 00036951. doi: 10.1063/1.4852675.
- [169] Hao Lu, Ziran Liu, Xianguo Yan, Dongyang Li, Leo Parent, and Harry Tian. Electron work function – a promising guiding parameter for material design. *Nature Publishing Group*, pages 1–11, 2016. ISSN 2045-2322. doi: 10.1038/srep24366.
- [170] Guomin Hua and Dongyang Li. Electron work function: a novel probe for toughness. *Phys. Chem. Chem. Phys.*, 18(6):4753–4759, 2016. ISSN 1463-9076. doi: 10.1039/C5CP04873G.
- [171] Hiroyuki Kawano. Effective work functions for ionic and electronic emissions from mono- and polycrystalline surfaces. *Progress in Surface Science*, 83:1–165, 2008. doi: 10.1016/j.progsurf.2007.11.001.
- [172] Tuo Li, Benjamin L. Rickman, and W. Andreas Schroeder. Density functional theory analysis of hexagonal close-packed elemental metal photocathodes. *Physical Review Special Topics - Accelerators and Beams*, 18(7):1–11, 2015. ISSN 10984402. doi: 10.1103/PhysRevSTAB.18.073401.
- [173] H B Michaelson. Relation Between an Atomic Electronegativity Scale and the Work Function. *IBM Journal of Research and Development*, 22(1):72–80, 1978. ISSN 0018-8646. doi: 10.1147/rd.221.0072.
- [174] A. R. Miedema, F. R. De Boer, and P. F. De Chatel. Empirical description of the role of electronegativity in alloy formation. *Journal of Physics F: Metal Physics*, 3(8):1558–1576, 1973. ISSN 03054608. doi: 10.1088/0305-4608/3/8/012.

- [175] J. Sokolov and F. Jona. Trends in metal surface relaxation. *Solid State Communications*, 49(4):307–312, 1984.
- [176] Jian Wang and Shao Qing Wang. Surface energy and work function of fcc and bcc crystals: Density functional study. *Surface Science*, 630(March):216–224, 2014. ISSN 00396028. doi: 10.1016/j.susc.2014.08.017.
- [177] De Peng Ji, Quanxi Zhu, and Shao Qing Wang. Detailed first-principles studies on surface energy and work function of hexagonal metals. *Surface Science*, 651:137–146, 2016. ISSN 00396028. doi: 10.1016/j.susc.2016.04.007.
- [178] Ivor Brodie. Uncertainty, topography, and work function. *Physical Review B*, 51(19): 13660–13668, 1995. ISSN 01631829. doi: 10.1103/PhysRevB.51.13660.
- [179] K F Wojciechowski and M Borna. Work function of transition metals calculated from the Brodie’s expression. *Vacuum*, 48(3):257–259, 1997.
- [180] F.R. Fazylov. Macroscopic theory of the electron work function in solids. *Philosophical Magazine*, 94(17):1956–1966, 2014. ISSN 1478-6435. doi: 10.1080/14786435.2014.903007.
- [181] Herbert B. Michaelson. The work function of the elements and its periodicity. *Journal of Applied Physics*, 48(11):4729–4733, 1977. ISSN 00218979. doi: 10.1063/1.323539.
- [182] M G Helander, M T Greiner, Z B Wang, and Z H Lu. Pitfalls in measuring work function using photoelectron spectroscopy. *Applied Sur*, 256:2602–2605, 2010. doi: 10.1016/j.apsusc.2009.11.002.
- [183] Gregory N. Derry, Megan E. Kern, and Eli H. Worth. Recommended values of clean metal surface work functions. *Journal of Vacuum Science & Technology A: Vacuum, Surfaces, and Films*, 33(6):060801, 2015. ISSN 0734-2101. doi: 10.1116/1.4934685.
- [184] Nicholas E. Singh-Miller and Nicola Marzari. Surface energies, work functions, and surface relaxations of low-index metallic surfaces from first principles. *Physical Review B - Condensed Matter and Materials Physics*, 80(23), 2009. ISSN 10980121. doi: 10.1103/PhysRevB.80.235407.
- [185] H. Skriver and N. Rosengaard. Surface energy and work function of elemental metals. *Physical Review B*, 46(11):7157–7168, sep 1992. ISSN 0163-1829. doi: 10.1103/PhysRevB.46.7157.
- [186] Tomasz Durakiewicz, Al Arko, John J. Joyce, Dave P. Moore, and Stanislaw Halas. Electronic work-function calculations of polycrystalline metal surfaces revisited. *Physical Review B - Condensed Matter and Materials Physics*, 64(4):1–8, 2001. ISSN 1550235X. doi: 10.1103/PhysRevB.64.045101.

- [187] M. Aldén, B. Johansson, and H. L. Skriver. Surface shift of the occupied and unoccupied 4f levels of the rare-earth metals. *Physical Review B*, 51(8):5386–5396, 1995. ISSN 01631829. doi: 10.1103/PhysRevB.51.5386.
- [188] T A Delchar. *Modern Techniques of Surface Science*. Cambridge University Press, Cambridge, 3rd edition, 1986. ISBN 9781107023109.
- [189] F. C. Frank and J. S. Kasper. Complex alloy structures regarded as sphere packings. I. Definitions and basic principles. *Acta Crystallographica*, 11:184–190, 1958. doi: 10.1107/S0365110X58000487.
- [190] Joseph H. Montoya and Kristin A. Persson. A high-throughput framework for determining adsorption energies on solid surfaces. *npj Computational Materials*, 3(1):14, 2017. ISSN 2057-3960. doi: 10.1038/s41524-017-0017-z. URL <http://www.nature.com/articles/s41524-017-0017-z>.
- [191] Anubhav Jain, Shyue Ping Ong, Wei Chen, Bharat Medasani, Xiaohui Qu, Michael Kocher, Miriam Brafman, Guido Petretto, Gian Marco Rignanese, Geoffroy Hautier, Daniel Gunter, and Kristin A. Persson. FireWorks: A dynamic workflow system designed for high-throughput applications. *Concurrency Computation*, 27(17):5037–5059, dec 2015. ISSN 15320634. doi: 10.1002/cpe.3505.
- [192] Kiran Mathew, Joseph H Montoya, Alireza Faghaninia, Shyam Dwarakanath, Muratahan Aykol, Hanmei Tang, Iek-heng Chu, Tess Smidt, Brandon Bocklund, Matthew Horton, John Dagdelen, Brandon Wood, Zi-kui Liu, Jeffrey Neaton, Shyue Ping, Kristin Persson, and Anubhav Jain. Atomate : A high-level interface to generate , execute , and analyze computational materials science workflows. *Computational Materials Science*, 139:140–152, 2017. ISSN 0927-0256. doi: 10.1016/j.commatsci.2017.07.030.
- [193] Donald Winston, Joseph H. Montoya, and Kristin A. Persson. Interactive leaderboard for requesting and tracking expensive calculations of optional properties across a database of materials. *11th Gateway Computing Environments Conference*, page doi:10.6084/m9.figshare.4491623.v2, 2016. doi: 10.6084/m9.figshare.4491623.v2. URL https://figshare.com/articles/Interactive_Leaderboard_for_Requesting_and_Tracking_Expensive_Calculations_of_Optional_Properties_across_a_Database_of_Materials/4491623.
- [194] Crystalium. <http://crystalium.materialsvirtuallab.org/>, 2016.
- [195] The materials project. <https://materialsproject.org/>, 2015.
- [196] William M. Haynes, David R. Lide, and Thomas J. Bruno. *CRC handbook of chemistry and physics*. CRC Press, Boca Raton, Fl, 97th edition, 2017.
- [197] O. K. Kultashev Rozkhov and E. Ye. *Rare Earth Metals and Alloys*. Nauka, Moscow, 1971.

- [198] R M Eastmen and C H B Mee. Work function measurements on (100), (110) and (111) surfaces of aluminium. *Journal of Physics F: Metal Physics*, 3(March):1738–1745, 1973.
- [199] J.K. Grepstad, P.O Gartland, and B.J. Slagsvold. Anisotropic work function of clean and smooth low-index faces of aluminium. *Surface Science*, 57(July):348–362, 1976.
- [200] Reza Rahemi and Dongyang Li. Variation in electron work function with temperature and its effect on the Young's modulus of metals. *Scripta Materialia*, 99:41–44, 2015. ISSN 13596462. doi: 10.1016/j.scriptamat.2014.11.022.
- [201] A. Kiejna, K. F. Wojciechowski, and J. Zebrowski. The temperature dependence of metal work functions. *Journal of Physics F: Metal Physics*, 9(7):1361, 1979. ISSN 0305-4608. doi: 10.1088/0305-4608/9/7/016.
- [202] K. M. Ho and K. P. Bohnen. Stability of the missing-row reconstruction on fcc (110) transition-metal surfaces. *Physical Review Letters*, 59(16):1833–1836, 1987. ISSN 00319007. doi: 10.1103/PhysRevLett.59.1833.
- [203] Nicola Gaston, Dirk Andrae, Beate Paulus, Ulrich Wedig, and Martin Jansen. Understanding the hcp anisotropy in Cd and Zn: the role of electron correlation in determining the potential energy surface. *Phys. Chem. Chem. Phys.*, 12(3):681–687, 2010. ISSN 1463-9076. doi: 10.1039/B915967C. URL <http://xlink.rsc.org/?DOI=B915967C>.
- [204] C. J. Fall, N. Binggeli, and A. Baldereschi. Anomaly in the anisotropy of the aluminum work function. *Physical Review B*, 58(12):R7544–R7547, 1998. ISSN 0163-1829. doi: 10.1103/PhysRevB.58.R7544.
- [205] N. D. Lang and W. Kohn. Theory of metal surfaces: Work function. *Physical Review B*, 3(4):1215–1223, feb 1971. ISSN 01631829. doi: 10.1103/PhysRevB.3.1215.
- [206] R. A. Andrievskii, N. S. Strel'nikova, N. I. Poltoratskii, E. D. Kharkhardin, and V. S. Smirnov. Melting point in systems ZrC-HfC, TaC-ZrC, TaC-HfC. *Soviet Powder Metallurgy and Metal Ceramics*, 6(1):65–67, 1967. ISSN 00385735. doi: 10.1007/BF00773385.
- [207] Haihua Chen, Hao Liang, Lingxiao Liu, Huishan Li, Kui Liu, and Fang Peng. Hardness measurements for high-pressure prepared TaB and nano-TaC ceramics. *Results in Physics*, 7:3859–3862, 2017. ISSN 22113797. doi: 10.1016/j.rinp.2017.10.006. URL <https://doi.org/10.1016/j.rinp.2017.10.006>.
- [208] M. Desmaison-Brut, N. Alexandre, and J. Desmaison. Comparison of the oxidation behaviour of two dense hot isostatically pressed tantalum carbide (TaC and Ta₂C) materials. *Journal of the European Ceramic Society*, 17(11):1325–1334, 1997. ISSN 09552219. doi: 10.1016/s0955-2219(96)00235-x.
- [209] Chase J. Smith, Morgan A. Ross, Nicholas De Leon, Christopher R. Weinberger, and Gregory B. Thompson. Ultra-high temperature deformation in TaC and HfC. *Journal*

of the European Ceramic Society, 38(16):5319–5332, 2018. ISSN 1873619X. doi: 10.1016/j.jeurceramsoc.2018.07.017.

- [210] Jingguang G. Chen. Carbide and nitride overlayers on early transition metal surfaces: Preparation, characterization, and reactivities. *Chemical Reviews*, 96(4):1477–1498, 1996. ISSN 00092665. doi: 10.1021/cr950232u.
- [211] Mingshui Yao, Qiaohong Li, Guolin Hou, Chen Lu, Benli Cheng, Kechen Wu, Gang Xu, Fangli Yuan, Fei Ding, and Yunfa Chen. Dopant-Controlled Morphology Evolution of WO₃ Polyhedra Synthesized by RF Thermal Plasma and Their Sensing Properties. *ACS Applied Materials & Interfaces*, 7(4):2856–2866, 2015. ISSN 1944-8244. doi: 10.1021/am5081277. URL <http://pubs.acs.org/doi/10.1021/am5081277>.
- [212] Michael T. Tang, Zachary W. Ulissi, and Karen Chan. Theoretical Investigations of Transition Metal Surface Energies under Lattice Strain and CO Environment. *Journal of Physical Chemistry C*, 122(26):14481–14487, 2018. ISSN 19327455. doi: 10.1021/acs.jpcc.8b02094.
- [213] Raghunath Kanakala, Roberto Escudero, Gabriel Rojas-George, Mohan Ramisetty, and Olivia A. Graeve. Mechanisms of combustion synthesis and magnetic response of high-surface-area hexaboride compounds. *ACS Applied Materials and Interfaces*, 3(4):1093–1100, 2011. ISSN 19448244. doi: 10.1021/am1012276.
- [214] Raghunath Kanakala, Gabriel Rojas-George, and Olivia A. Graeve. Unique preparation of hexaboride nanocubes: A first example of boride formation by combustion synthesis. *Journal of the American Ceramic Society*, 93(10):3136–3141, 2010. ISSN 00027820. doi: 10.1111/j.1551-2916.2010.03853.x.
- [215] James P. Kelly and Olivia A. Graeve. Statistical experimental design approach for the solvothermal synthesis of nanostructured tantalum carbide powders. *Journal of the American Ceramic Society*, 94(6):1706–1715, 2011. ISSN 00027820. doi: 10.1111/j.1551-2916.2010.04304.x.
- [216] James P. Kelly, Raghunath Kanakala, and Olivia A. Graeve. A solvothermal approach for the preparation of nanostructured carbide and boride ultra-high-temperature ceramics. *Journal of the American Ceramic Society*, 93(10):3035–3038, 2010. ISSN 00027820. doi: 10.1111/j.1551-2916.2010.04007.x.
- [217] P W Tasker. The stability of ionic crystal surfaces. *Journal of Physics C: Solid State Physics*, 12(22):4977–4984, 2001. ISSN 0022-3719. doi: 10.1088/0022-3719/12/22/036.
- [218] Stefan Maintz, Volker L. Deringer, Andrei L. Tchougréeff, and Richard Dronskowski. LOBSTER: A tool to extract chemical bonding from plane-wave based DFT. *Journal of Computational Chemistry*, 37(11):1030–1035, 2016. ISSN 1096987X. doi: 10.1002/jcc.24300.

- [219] Wenhao Sun, Christopher J Bartel, Elisabetta Arca, Sage R Bauers, Bethany Matthews, Bernardo Orvañanos, Bor-Rong Chen, Michael F Toney, Laura T Schelhas, William Tumas, Janet Tate, Andriy Zakutayev, Stephan Lany, Aaron M Holder, and Gerbrand Ceder. A map of the inorganic ternary metal nitrides. *Nature Materials*, 18(7):732–739, 2019. ISSN 1476-4660. doi: 10.1038/s41563-019-0396-2.
- [220] Allen L. Bowman. The variation of lattice parameter with carbon content of tantalum carbide. *Journal of Physical Chemistry*, 65(9):1596–1598, 1961. ISSN 00223654. doi: 10.1021/j100905a028.
- [221] James P. Kelly and Olivia A. Graeve. Mechanisms of pore formation in high-temperature carbides: Case study of TaC prepared by spark plasma sintering. *Acta Materialia*, 84: 472–483, 2015. ISSN 13596454. doi: 10.1016/j.actamat.2014.11.005.
- [222] W. K. Burton, N. Cabrera, and F. C. Frank. The Growth of Crystals and the Equilibrium Structure of their Surfaces. *Philosophical Transactions of the Royal Society A: Mathematical, Physical and Engineering Sciences*, 243(866):299–358, 1951. ISSN 1364-503X. doi: 10.1098/rsta.1951.0006.
- [223] S. Zaima, Y. Shibata, H. Adachi, C. Oshima, S. Otani, M. Aono, and Y. Ishizawa. Atomic chemical composition and reactivity of the TiC(111) surface. *Surface Science*, 157(2-3): 380–392, 1985. ISSN 00396028. doi: 10.1016/0039-6028(85)90680-6.
- [224] J. Shields. *Applications of Mo Metal and Its Alloys*. 2013. ISBN 9781907470301.
- [225] R Causey, C Kunz, and D Cowgill. Deuterium retention and release from molybdenum exposed to a Penning discharge. *Journal of Nuclear Materials*, 337-339:600–603, 2005. ISSN 00223115. doi: 10.1016/j.jnucmat.2004.10.005.
- [226] J. Schlichting. Molybdenum disilicide as a component of modern high- temperature composites. *INIS*, 10(23), 1978.
- [227] N S Rasor, J D McClelland, Atomics International, and Canoga Park. Thermal Properties of Graphite, Molybdenum, and Tantalum to their Destruction Temperatures. *J. Phys. Chem. Solids*, 15:17–26, 1960.
- [228] Hsueh Chuan Hsu, Shih Ching Wu, Shih Kuang Hsu, Tien Yu Chang, and Wen Fu Ho. Effect of ball milling on properties of porous Ti-7.5Mo alloy for biomedical applications. *Journal of Alloys and Compounds*, 582:793–801, 2014. ISSN 09258388. doi: 10.1016/j.jallcom.2013.08.147.
- [229] Ming Xia, Ting Lei, Ninglei Lv, and Nianfeng Li. Synthesis and electrocatalytic hydrogen evolution performance of Ni–Mo–Cu alloy coating electrode. *International Journal of Hydrogen Energy*, 39(10):4794–4802, 2014. ISSN 03603199. doi: 10.1016/j.ijhydene.2014.01.091.

- [230] Tadao Watanabe and Sadahiro Tsurekawa. Toughening of brittle materials by grain boundary engineering. *Materials Science and Engineering A*, 387-389(1-2 SPEC. ISS.): 447–455, 2004. ISSN 09215093. doi: 10.1016/j.msea.2004.01.140.
- [231] James R. Rice and Jian Sheng Wang. Embrittlement of interfaces by solute segregation. *Materials Science and Engineering A*, 107(C):23–40, 1989. ISSN 09215093. doi: 10.1016/0921-5093(89)90372-9.
- [232] Gerd Duscher, Matthew F Chisholm, Uwe Alber, and Manfred Rühle. Bismuth-induced embrittlement of copper grain boundaries. *Nature materials*, 3(9):621–6, sep 2004. ISSN 1476-1122. doi: 10.1038/nmat1191.
- [233] Xiaomeng Shi and Jian Luo. Grain boundary wetting and prewetting in Ni-doped Mo. *Applied Physics Letters*, 94(25):11–13, 2009. ISSN 00036951. doi: 10.1063/1.3155443.
- [234] Ks Hwang and Hs Huang. Identification of the Segregation Layer and its Effects on the Activated Sintering and Ductility of Ni-Doped Molybdenum. *Acta materialia*, 51(13): 3915–3926, 2003. ISSN 13596454. doi: 10.1016/S1359-6454(03)00216-7.
- [235] M. K. Miller, E. a. Kenik, M. S. Mousa, K. F. Russell, and a. J. Bryhan. Improvement in the ductility of molybdenum alloys due to grain boundary segregation. *Scripta Materialia*, 46(2002):299–303, 2002. ISSN 13596462. doi: 10.1016/S1359-6462(01)01242-8.
- [236] A Charai, I Kutcherinenko, J Pbnisson, V Pontikis, L Priester, K Wolski, and T Vystavel. Electron microscopy and Auger spectroscopy study of the wetting of the grain boundaries in the systems Mo-Pb , Mo-Sn , Mo-Ni and Ni-Pb. *Journal de Physique IV*, 12:277–87, 2002.
- [237] Rebecca Janisch and Christian Elsässer. Segregated light elements at grain boundaries in niobium and molybdenum. *Physical Review B*, 67(22):224101, jun 2003. ISSN 0163-1829. doi: 10.1103/PhysRevB.67.224101.
- [238] A.H. Contrell. Strengthening of grain boundaries by segregated interstitials in iron. *Materials Science and Technology*, 6(2):121–123, 1990.
- [239] Lejcek Pavel. *Grain boundary segregation in metals*. 2008. ISBN 9783642125041. doi: 10.1007/978-3-642-12505-8.
- [240] Patrick R. Cantwell, Ming Tang, Shen J. Dillon, Jian Luo, Gregory S. Rohrer, and Martin P. Harmer. Grain boundary complexions. *Acta Materialia*, 62(152):1–48, jan 2014. ISSN 13596454. doi: 10.1016/j.actamat.2013.07.037.
- [241] Hao Jin, Ilya Elfimov, and Matthias Militzer. Study of the interaction of solutes with ??5 (013) tilt grain boundaries in iron using density-functional theory. *Journal of Applied Physics*, 115(013), 2014. ISSN 00218979. doi: 10.1063/1.4867400.

- [242] V I Razumovskiy, A Y Lozovoi, and I M Razumovskii. ScienceDirect First-principles-aided design of a new Ni-base superalloy : Influence of transition metal alloying elements on grain boundary and bulk cohesion. *Acta Materialia*, 82:369–377, 2015. ISSN 1359-6454. doi: 10.1016/j.actamat.2014.08.047.
- [243] Wenguan Liu, Han Han, Cuilan Ren, Huiqin Yin, Yang Zou, Ping Huai, and Hongjie Xu. Effects of rare-earth on the cohesion of Ni Σ 5 (012) grain boundary from first-principles calculations. *Computational Materials Science*, 96:374–378, 2015. ISSN 09270256. doi: 10.1016/j.commatsci.2014.09.035.
- [244] A. Miedema. Surface segregation in alloys of transition-metals. *Zeitschrift Fur Metallkunde*, 7(69):455–461, 1978.
- [245] Donald McLean. *Grain Boundaries in Metals*. Oxford University Press, 1957.
- [246] a Brokman and R W Balluffi. Coincidence lattice model for the structure and energy of grain boundaries. *Acta Metallurgica*, 29(10):1703–1719, 1981. ISSN 00016160. doi: 10.1016/0001-6160(81)90005-5.
- [247] J Friedel. Electronic structure of primary solid solutions in metals. *Adv. Phys.*, 50 (February):539–595, 2001. ISSN 0001-8732. doi: 10.1080/00018735400101233.
- [248] Linus Pauling. The Nature of the Chemical Bond. IV. The Energy of Single Bonds and the Relative Electronegativity of Atoms. *Journal of the American Chemical Society*, 54(9):3570–3582, 1932. ISSN 0002-7863. doi: 10.1021/ja01348a011. URL <http://pubs.acs.org/doi/abs/10.1021/ja01348a011>.
- [249] J.M Pénisson and T Vystavel. Wetting of molybdenum grain boundaries by nickel: effect of the boundary structure and energy. *Acta Materialia*, 48(13):3303–3310, 2000. ISSN 13596454. doi: 10.1016/S1359-6454(00)00157-9.
- [250] A-B-C Phase Diagram, ASM Alloy Phase Diagrams Database, 2006. URL <http://www1.asminternational.org/AsmEnterprise/APD>.
- [251] Wayne D. Kaplan, Dominique Chatain, Paul Wynblatt, and W. Craig Carter. A review of wetting versus adsorption, complexions, and related phenomena: The rosetta stone of wetting. *Journal of Materials Science*, 48(17):5681–5717, 2013. ISSN 00222461. doi: 10.1007/s10853-013-7462-y.
- [252] M. P. Harmer. The Phase Behavior of Interfaces. *Science*, 332(6026):182–183, 2011. ISSN 0036-8075. doi: 10.1126/science.1204204.
- [253] Jian Luo. Developing Interfacial Phase Diagrams for Applications in Activated Sintering and Beyond: Current Status and Future Directions. *Journal of the American Ceramic Society*, 95(8):2358–2371, 2012. doi: 10.1111/j.1551-2916.2011.05059.x.

- [254] Xiaomeng Shi and Jian Luo. Developing grain boundary diagrams as a materials science tool: A case study of nickel-doped molybdenum. *Physical Review B - Condensed Matter and Materials Physics*, 84(1):1–14, 2011. ISSN 10980121. doi: 10.1103/PhysRevB.84.014105.
- [255] Jae Il Jung, Naixie Zhou, and Jian Luo. Effects of sintering aids on the densification of Mo-Si-B alloys. *Journal of Materials Science*, 47(24):8308–8319, 2012. ISSN 00222461. doi: 10.1007/s10853-012-6815-2.
- [256] J. Luo, V. K. Gupta, D. H. Yoon, and H. M. Meyer. Segregation-induced grain boundary premelting in nickel-doped tungsten. *Applied Physics Letters*, 87(23):1–3, 2005. ISSN 00036951. doi: 10.1063/1.2138796.
- [257] Vivek K. Gupta, Dang Hyok Yoon, Harry M. Meyer, and Jian Luo. Thin intergranular films and solid-state activated sintering in nickel-doped tungsten. *Acta Materialia*, 55(9):3131–3142, 2007. ISSN 13596454. doi: 10.1016/j.actamat.2007.01.017.
- [258] K. S. Hwang and H. S. Huang. Liquid phase sintering of molybdenum with Ni and Cu additions. *Materials Chemistry and Physics*, 67(1-3):92–100, 2001. ISSN 02540584. doi: 10.1016/S0254-0584(00)00425-9.
- [259] K. S. Hwang and H. S. Huang. Ductility improvement of Ni-added molybdenum compacts through the addition of Cu and Fe powders. *International Journal of Refractory Metals and Hard Materials*, 22(4-5):185–191, 2004. ISSN 02634368. doi: 10.1016/j.ijrmhm.2004.06.003.
- [260] Javier del Valle, Juan Gabriel Ramírez, Marcelo J Rozenberg, and Ivan K Schuller. Challenges in materials and devices for resistive-switching-based neuromorphic computing. *Journal of Applied Physics*, 124(21):211101, dec 2018. ISSN 0021-8979. doi: 10.1063/1.5047800. URL <http://aip.scitation.org/doi/10.1063/1.5047800>.
- [261] G. A. Thomas, D. H. Rapkine, S. A. Carter, and A. J. Millis. Observation of gap and kinetic energy in a correlated insulator. *Physical Review Letters*, 73(11):1529–1532, 1994.
- [262] A. Zimmers, L. Aigouy, M. Mortier, A. Sharoni, Siming Wang, K. G. West, J. G. Ramirez, and Ivan K. Schuller. Role of thermal heating on the voltage induced insulator-metal transition in VO₂. *Physical Review Letters*, 110(5):1–5, 2013. ISSN 00319007. doi: 10.1103/PhysRevLett.110.056601.
- [263] T. Hennen, D. Bedau, J. A.J. Rupp, C. Funck, S. Menzel, M. Grobis, R. Waser, and D. J. Wouters. Switching speed analysis and controlled oscillatory behavior of a Cr-doped V₂O₃ threshold switching device for memory selector and neuromorphic computing application. *2019 IEEE 11th International Memory Workshop, IMW 2019*, pages 1–4, 2019. doi: 10.1109/IMW.2019.8739556.
- [264] Wei Bao, C. Broholm, S. A. Carter, T. F. Rosenbaum, G. Aeppli, S. F. Trevino, P. Metcalf,

J. M. Honig, and J. Spalek. Incommensurate spin density wave in metallic V₂-yO₃. *Physical Review Letters*, 71(5):766–769, 1993. ISSN 00319007. doi: 10.1103/PhysRevLett.71.766.

- [265] Zhiyong Zhu and Udo Schwingenschlögl. Comprehensive picture of VO₂ from band theory. *Physical Review B - Condensed Matter and Materials Physics*, 86(7):2–5, 2012. ISSN 10980121. doi: 10.1103/PhysRevB.86.075149.
- [266] Aron J. Cohen, Paula Mori-Sánchez, and Weitao Yang. Insights into current limitations of density functional theory. *Science*, 321(5890):792–794, 2008. ISSN 00368075. doi: 10.1126/science.1158722.
- [267] N J Szymanski, Z T Y Liu, T Alderson, N J Podraza, P Sarin, and S V Khare. Electronic and optical properties of vanadium oxides from first principles. *Computational Materials Science*, 146:310–318, 2018. ISSN 0927-0256. doi: 10.1016/j.commatsci.2018.01.048. URL <https://doi.org/10.1016/j.commatsci.2018.01.048>.
- [268] Yuzheng Guo, Stewart J. Clark, and John Robertson. Calculation of metallic and insulating phases of V₂O₃ by hybrid density functionals. *Journal of Chemical Physics*, 140(5):3–10, 2014. ISSN 00219606. doi: 10.1063/1.4863325.
- [269] Ricardo Grau-Crespo, Hao Wang, and Udo Schwingenschlögl. Why the Heyd-Scuseria-Ernzerhof hybrid functional description of VO₂ phases is not correct. *Physical Review B*, 86(8):081101, 2012. ISSN 1098-0121. doi: 10.1103/PhysRevB.86.081101. URL <https://link.aps.org/doi/10.1103/PhysRevB.86.081101>.
- [270] Berenike Stahl and Thomas Bredow. Critical Assessment of the DFT + U Approach for the Prediction of Vanadium Dioxide Properties. *Journal of Computational Chemistry*, 41(3):1–8, 2019. doi: 10.1002/jcc.26096.
- [271] L. F. Mattheiss. Band properties of metallic corundum-phase V₂O₃. *Journal of Physics: Condensed Matter*, 6(32):6477–6484, 1994. ISSN 09538984. doi: 10.1088/0953-8984/6/32/009.
- [272] R. M. Moon. Antiferromagnetism in V₂O₃. *Physical Review Letters*, 25(8):527–529, 1970. ISSN 00319007. doi: 10.1103/PhysRevLett.25.527.
- [273] Daniel Grieger and Michele Fabrizio. Low-temperature magnetic ordering and structural distortions in vanadium sesquioxide V₂O₃. *Physical Review B - Condensed Matter and Materials Physics*, 92(7):1–14, 2015. ISSN 1550235X. doi: 10.1103/PhysRevB.92.075121.
- [274] Nils E.R. Zimmermann, Matthew K. Horton, Anubhav Jain, and Maciej Haranczyk. Assessing local structure motifs using order parameters for motif recognition, interstitial identification, and diffusion path characterization. *Frontiers in Materials*, 4(November):1–13, 2017. ISSN 22968016. doi: 10.3389/fmats.2017.00034.

- [275] Danny Broberg, Bharat Medasani, Nils E.R. Zimmermann, Guodong Yu, Andrew Canning, Maciej Haranczyk, Mark Asta, and Geoffroy Hautier. PyCDT: A Python toolkit for modeling point defects in semiconductors and insulators. *Computer Physics Communications*, 226:165–179, 2018. ISSN 00104655. doi: 10.1016/j.cpc.2018.01.004. URL <https://doi.org/10.1016/j.cpc.2018.01.004>.
- [276] Christoph Freysoldt, Jörg Neugebauer, and Chris G. Van De Walle. Fully Ab initio finite-size corrections for charged-defect supercell calculations. *Physical Review Letters*, 102(1):1–4, 2009. ISSN 00319007. doi: 10.1103/PhysRevLett.102.016402.
- [277] Makondelele Netsianda, Phuti E. Ngoepe, C. Richard A. Catlow, and Scott M. Woodley. The displacive phase transition of vanadium dioxide and the effect of doping with tungsten. *Chemistry of Materials*, 20(5):1764–1772, 2008. ISSN 08974756. doi: 10.1021/cm701861z.
- [278] F. Pintchovski, W. S. Glaunsinger, and A. Navrotsky. Experimental study of the electronic and lattice contributions to the VO₂ transition. *Journal of Physics and Chemistry of Solids*, 39(9):941–949, 1978. ISSN 00223697. doi: 10.1016/0022-3697(78)90108-7.
- [279] P. D. Dernier and M. Marezio. Crystal structure of the low-temperature antiferromagnetic phase of V₂O₃. *Physical Review B*, 2(9):3771–3776, 1970. ISSN 01631829. doi: 10.1103/PhysRevB.2.3771.
- [280] M. W. Chase. *NIST-JANAF thermochemical tables*. American Institute of Physics, Woodbury, New York, 4th edition, 1998.
- [281] Graeme Henkelman, Andri Arnaldsson, and Hannes Jónsson. A fast and robust algorithm for Bader decomposition of charge density. *Computational Materials Science*, 36(3):354–360, 2006. ISSN 09270256. doi: 10.1016/j.commatsci.2005.04.010.
- [282] Masatoshi Imada, Atsushi Fujimori, and Yoshinori Tokura. Metal-insulator transitions. *Reviews of Modern Physics*, 70(4):1039–1263, 1998. ISSN 13623036. doi: 10.1080/09500839008206369.
- [283] Shriram Ramanathan. Quantum materials for brain sciences and artificial intelligence. *MRS Bulletin*, 43(7):534–540, 2018. ISSN 0883-7694. doi: DOI:10.1557/mrs.2018.147. URL <https://www.cambridge.org/core/article/quantum-materials-for-brain-sciences-and-artificial-intelligence/00F098866AD5FCC4476C43A4326BC306>.
- [284] Kaushik Roy, Akhilesh Jaiswal, and Priyadarshini Panda. Towards spike-based machine intelligence with neuromorphic computing. *Nature*, 575(7784):607–617, 2019. ISSN 1476-4687. doi: 10.1038/s41586-019-1677-2. URL <https://doi.org/10.1038/s41586-019-1677-2>.
- [285] Hai-Tian Zhang, Priyadarshini Panda, Jerome Lin, Yoav Kalcheim, Kai Wang, John W

Freeland, Dillon D Fong, Shashank Priya, Ivan K Schuller, Subramanian K R S Sankaranarayanan, Kaushik Roy, and Shriram Ramanathan. Organismic materials for beyond von Neumann machines. *Applied Physics Reviews*, 7(1):11309, jan 2020. doi: 10.1063/1.5113574. URL <https://doi.org/10.1063/1.5113574>.

- [286] XiaoLiang Hong, Desmond JiaJun Loy, Putu Andhita Dananjaya, Funan Tan, CheeMang Ng, and WenSiang Lew. Oxide-based RRAM materials for neuromorphic computing. *Journal of Materials Science*, 53(12):8720–8746, 2018. ISSN 1573-4803. doi: 10.1007/s10853-018-2134-6. URL <https://doi.org/10.1007/s10853-018-2134-6>.
- [287] Pavel Salev, Javier del Valle, Yoav Kalcheim, and Ivan K Schuller. Giant nonvolatile resistive switching in a Mott oxide and ferroelectric hybrid. *Proceedings of the National Academy of Sciences*, 116(18):8798 LP – 8802, apr 2019. doi: 10.1073/pnas.1822138116. URL <http://www.pnas.org/content/116/18/8798.abstract>.
- [288] Sung-II Kim, Yeongjun Lee, Min-Ho Park, Gyeong-Tak Go, Young-Hoon Kim, Wentao Xu, Hyeyon-Dong Lee, Hobeom Kim, Dae-Gyo Seo, Wanhee Lee, and Tae-Woo Lee. Dimensionality Dependent Plasticity in Halide Perovskite Artificial Synapses for Neuromorphic Computing. *Advanced Electronic Materials*, 5(9):1900008, sep 2019. ISSN 2199-160X. doi: 10.1002aelm.201900008. URL <https://doi.org/10.1002aelm.201900008>.
- [289] Jian Shi, Sieu D Ha, You Zhou, Frank Schoofs, and Shriram Ramanathan. A correlated nickelate synaptic transistor. *Nature Communications*, 4(1):2676, 2013. ISSN 2041-1723. doi: 10.1038/ncomms3676. URL <https://doi.org/10.1038/ncomms3676>.
- [290] Hai-Tian Zhang, Tae Joon Park, Ivan A. Zaluzhnyy, Qi Wang, Shakti Nagnath Wadekar, Sukriti Manna, Robert Andrawis, Peter O. Sprau, Yifei Sun, Zhen Zhang, Chengzi Huang, Hua Zhou, Zhan Zhang, Badri Narayanan, Gopalakrishnan Srinivasan, Nelson Hua, Evgeny Nazaretski, Xiaojing Huang, Hanfei Yan, Mingyuan Ge, Yong S. Chu, Mathew J. Cherukara, Martin V. Holt, Muthu Krishnamurthy, Oleg G. Shpyrko, Subramanian K.R.S. Sankaranarayanan, Alex Frano, Kaushik Roy, and Shriram Ramanathan. Perovskite Neural Trees. *Nat. Commun.*, 11(1):2245, 2020. doi: 10.1038/s41467-020-16105-y.
- [291] U Staub, G I Meijer, F Fauth, R Allenspach, J G Bednorz, J Karpinski, S M Kazakov, L Paolasini, and F D’Acapito. Direct Observation of Charge Order in an Epitaxial $NdNiO_3$ Film. *Physical Review Letters*, 88(12):126402, mar 2002. doi: 10.1103/PhysRevLett.88.126402. URL <https://link.aps.org/doi/10.1103/PhysRevLett.88.126402>.
- [292] A M Glazer. The classification of tilted octahedra in perovskites. *Acta Crystallographica Section B*, 28(11):3384–3392, nov 1972. doi: 10.1107/S0567740872007976. URL <https://doi.org/10.1107/S0567740872007976>.
- [293] S Catalano, M Gibert, J Fowlie, J Íñiguez, J-M Triscone, and J Kreisel. Rare-earth nickelatesRNiO₃: thin films and heterostructures. *Reports on Progress in Physics*, 81(4):46501, 2018. ISSN 0034-4885. doi: 10.1088/1361-6633/aaa37a. URL <http://dx.doi.org/10.1088/1361-6633/aaa37a>.

[org/10.1088/1361-6633/aaa37a](http://dx.doi.org/10.1088/1361-6633/aaa37a).

- [294] María Luisa Medarde. Structural, magnetic and electronic properties of perovskites (R = rare earth). *Journal of Physics: Condensed Matter*, 9(8):1679–1707, 1997. ISSN 0953-8984. doi: 10.1088/0953-8984/9/8/003. URL <http://dx.doi.org/10.1088/0953-8984/9/8/003>.
- [295] Jian Shi, You Zhou, and Shriram Ramanathan. Colossal resistance switching and band gap modulation in a perovskite nickelate by electron doping. *Nature Communications*, 5(1):4860, 2014. ISSN 2041-1723. doi: 10.1038/ncomms5860.
- [296] You Zhou, Xiaofei Guan, Hua Zhou, Koushik Ramadoss, Suhare Adam, Huajun Liu, Sungsik Lee, Jian Shi, Masaru Tsuchiya, Dillon D Fong, and Shriram Ramanathan. Strongly correlated perovskite fuel cells. *Nature*, 534(7606):231–234, 2016. ISSN 1476-4687. doi: 10.1038/nature17653.
- [297] Koushik Ramadoss, Nirajan Mandal, Xia Dai, Zhong Wan, You Zhou, Leonid Rokhinson, Yong P Chen, Jiangpin Hu, and Shriram Ramanathan. Sign reversal of magnetoresistance in a perovskite nickelate by electron doping. *Physical Review B*, 94(23):235124, dec 2016. doi: 10.1103/PhysRevB.94.235124.
- [298] Yifei Sun, Michele Kotiuga, Dawgen Lim, Badri Narayanan, Mathew Cherukara, Zhen Zhang, Yongqi Dong, Ronghui Kou, Cheng-Jun Sun, Qiyang Lu, Iradwikanari Waluyo, Adrian Hunt, Hidekazu Tanaka, Azusa N Hattori, Sampath Gamage, Yohannes Abate, Vilas G Pol, Hua Zhou, Subramanian K R S Sankaranarayanan, Bilge Yildiz, Karin M Rabe, and Shriram Ramanathan. Strongly correlated perovskite lithium ion shuttles. *Proceedings of the National Academy of Sciences*, 115(39):9672 LP – 9677, sep 2018. doi: 10.1073/pnas.1805029115. URL <http://www.pnas.org/content/115/39/9672.abstract>.
- [299] Jikun Chen, Wei Mao, Binghui Ge, Jiaou Wang, Xinyou Ke, Vei Wang, Yiping Wang, Max Döbeli, Wentong Geng, Hiroyuki Matsuzaki, Jian Shi, and Yong Jiang. Revealing the role of lattice distortions in the hydrogen-induced metal-insulator transition of SmNiO₃. *Nature Communications*, 10(1):694, 2019. ISSN 2041-1723. doi: 10.1038/s41467-019-08613-3. URL <https://doi.org/10.1038/s41467-019-08613-3>.
- [300] Zhaoliang Liao, Nicolas Gauquelin, Robert J Green, Knut Müller-Caspary, Ivan Lobato, Lin Li, Sandra Van Aert, Johan Verbeeck, Mark Huijben, Mathieu N Grisolia, Victor Rouco, Ralph El Hage, Javier E Villegas, Alain Mercy, Manuel Bibes, Philippe Ghosez, George A Sawatzky, Guus Rijnders, and Gertjan Koster. Metal–insulator-transition engineering by modulation tilt-control in perovskite nickelates for room temperature optical switching. *Proceedings of the National Academy of Sciences*, 115(38):9515 LP – 9520, sep 2018. doi: 10.1073/pnas.1807457115. URL <http://www.pnas.org/content/115/38/9515.abstract>.
- [301] Changan Wang, Ching-Hao Chang, Angus Huang, Pei-Chun Wang, Ping-Chun Wu, Lin

Yang, Chi Xu, Parul Pandey, Min Zeng, Roman Böttger, Horng-Tay Jeng, Yu-Jia Zeng, Manfred Helm, Ying-Hao Chu, R Ganesh, and Shengqiang Zhou. Tunable disorder and localization in the rare-earth nickelates. *Physical Review Materials*, 3(5):53801, may 2019. doi: 10.1103/PhysRevMaterials.3.053801. URL <https://link.aps.org/doi/10.1103/PhysRevMaterials.3.053801>.

- [302] M Brahlek, A K Choquette, C R Smith, R Engel-Herbert, and S J May. Structural refinement of Pbnm-type perovskite films from analysis of half-order diffraction peaks. *Journal of Applied Physics*, 121(4):45303, jan 2017. ISSN 0021-8979. doi: 10.1063/1.4974362. URL <https://doi.org/10.1063/1.4974362>.
- [303] Jennifer Fowlie, Céline Lichtensteiger, Marta Gibert, Hugo Meley, Philip Willmott, and Jean-Marc Triscone. Thickness-Dependent Perovskite Octahedral Distortions at Heterointerfaces. *Nano Letters*, 19(6):4188–4194, jun 2019. ISSN 1530-6984. doi: 10.1021/acs.nanolett.9b01772. URL <https://doi.org/10.1021/acs.nanolett.9b01772>.
- [304] M Hepting. *Ordering Phenomena in Rare-Earth Nickelate Heterostructures*. Springer Theses. Springer International Publishing, Cham, 2017. ISBN 9783319605319. doi: 10.1007/978-3-319-60531-9. URL <https://books.google.com/books?id=3DUqDwAAQBAJ>.
- [305] Vladimir I. Anisimov, Jan Zaanen, and Ole K. Andersen. Band theory and Mott insulators: Hubbard U instead of Stoner I. *Physical Review B*, 44(3):943–954, 1991. ISSN 01631829. doi: 10.1103/PhysRevB.44.943.
- [306] A Mansour N. and C Melendres A. X-Ray Absorption Spectra and the Local Structure of Nickel in Some Oxycompounds and Fluorides. *J. Phys. IV France*, 7(C2):C2–1171–C2–1172, apr 1997. URL <https://doi.org/10.1051/jp4:19972178>.
- [307] Russell J Woolley, Benoit N Illy, Mary P Ryan, and Stephen J Skinner. *In situ* determination of the nickel oxidation state in $\text{La}_2\text{NiO}_{4+\delta}$ and $\text{La}_4\text{Ni}_3\text{O}_{10-\delta}$ using X-ray absorption near-edge structure. *Journal of Materials Chemistry*, 21(46):18592–18596, 2011. ISSN 0959-9428. doi: 10.1039/C1JM14320D. URL <http://dx.doi.org/10.1039/C1JM14320D>.
- [308] Weiwei Gu, Hongxin Wang, and Kun Wang. Nickel L-edge and K-edge X-ray absorption spectroscopy of non-innocent $\text{Ni}[\text{S}_2\text{C}_2(\text{CF}_3)_2]_2^n$ series ($n = -2, -1, 0$): direct probe of nickel fractional oxidation state changes. *Journal of the Chemical Society. Dalton Transactions*, 43(17):6406–6413, 2014. ISSN 14779226. doi: 10.1039/c4dt00308j.
- [309] G Kresse and J Furthmüller. Efficient iterative schemes for ab initio total-energy calculations using a plane-wave basis set. *Physical Review B*, 54(16):11169–11186, oct 1996. doi: 10.1103/PhysRevB.54.11169. URL <https://link.aps.org/doi/10.1103/PhysRevB.54.11169>.
- [310] G Kresse and D Joubert. From ultrasoft pseudopotentials to the projector augmented-wave method. *Physical Review B*, 59(3):1758–1775, jan 1999. doi: 10.1103/PhysRevB.59.1758. URL <https://link.aps.org/doi/10.1103/PhysRevB.59.1758>.

- [311] John J Rehr, Joshua J Kas, Fernando D Vila, Micah P Prange, and Kevin Jorissen. Parameter-free calculations of X-ray spectra with FEFF9. *Physical Chemistry Chemical Physics*, 12(21):5503–5513, 2010. ISSN 1463-9076. doi: 10.1039/B926434E. URL <http://dx.doi.org/10.1039/B926434E>.
- [312] Xuyong Feng, Po Hsiu Chien, Zhuoying Zhu, Iek Heng Chu, Pengbo Wang, Marcello Immediato-Scuotto, Hesam Arabzadeh, Shyue Ping Ong, and Yan Yan Hu. Studies of functional defects for fast Na-ion conduction in $\text{Na}_{3-y}\text{PS}_{4-x}\text{Cl}_x$ with a combined experimental and computational approach. *Advanced Functional Materials*, 29(9):1–9, 2019. ISSN 16163028. doi: 10.1002/adfm.201807951.
- [313] Julien Varignon, Mathieu N Grisolia, Jorge Íñiguez, Agnès Barthélémy, and Manuel Bibes. Complete phase diagram of rare-earth nickelates from first-principles. *npj Quantum Materials*, 2(1):21, 2017. ISSN 2397-4648. doi: 10.1038/s41535-017-0024-9.
- [314] J A Alonso, J L García-Muñoz, M T Fernández-Díaz, M A G Aranda, M J Martínez-Lope, and M T Casais. Charge disproportionation in RNiO_3 Perovskites: Simultaneous metal-insulator and structural transition in YNiO_3 . *Physical Review Letters*, 82(19):3871–3874, may 1999. doi: 10.1103/PhysRevLett.82.3871. URL <https://link.aps.org/doi/10.1103/PhysRevLett.82.3871>.
- [315] R J Green, M W Haverkort, and G A Sawatzky. Bond disproportionation and dynamical charge fluctuations in the perovskite rare-earth nickelates. *Physical Review B*, 94(19):195127, nov 2016. doi: 10.1103/PhysRevB.94.195127.
- [316] Nicole A Benedek and Craig J Fennie. Why Are There So Few Perovskite Ferroelectrics? *The Journal of Physical Chemistry C*, 117(26):13339–13349, jul 2013. ISSN 1932-7447. doi: 10.1021/jp402046t.
- [317] K Ramadoss, F Zuo, Y Sun, Z Zhang, J Lin, U Bhaskar, S Shin, M A Alam, S Guha, D Weinstein, and S Ramanathan. Proton-Doped Strongly Correlated Perovskite Nickelate Memory Devices. *IEEE Electron Device Letters*, 39(10):1500–1503, 2018. ISSN 1558-0563 VO - 39. doi: 10.1109/LED.2018.2865776.
- [318] Hai-Tian Zhang, Zhen Zhang, Hua Zhou, Hidekazu Tanaka, Dillon D Fong, and Shriram Ramanathan. Beyond electrostatic modification: design and discovery of functional oxide phases via ionic-electronic doping. *Advances in Physics: X*, 4(1):1523686, jan 2019. ISSN null. doi: 10.1080/23746149.2018.1523686. URL <https://doi.org/10.1080/23746149.2018.1523686>.
- [319] Hui Zheng, Xiang Guo Li, Richard Tran, Chi Chen, Matthew Horton, Donald Winston, Kristin Aslaug Persson, and Shyue Ping Ong. Grain boundary properties of elemental metals. *Acta Materialia*, 186:40–49, 2020. ISSN 13596454. doi: 10.1016/j.actamat.2019.12.030. URL <https://doi.org/10.1016/j.actamat.2019.12.030>.
- [320] Emilie Ringe, Richard P. Van Duyne, and Laurence D. Marks. Kinetic and thermodynamic

modified Wulff constructions for twinned nanoparticles. *Journal of Physical Chemistry C*, 117(31):15859–15870, 2013. ISSN 19327447. doi: 10.1021/jp401566m.

- [321] R. Kirchheim. Physics and chemistry of interfacial segregation. In D. Wolf and S. Yip, editors, *Material Interfaces, Atomic Level Structure and Properties*, pages 481–496. Chapman & Hall, London, 1992.
- [322] A.T. Dinsdale. SGTE Data for Pure Elements. *CALPHAD*, 4(15):317–425, 1991.
- [323] B Predel. Phase equilibria, crystallographic and thermodynamic data of binary alloys · li-mg – nd-zr. In O Madelung, editor, *Mo-Os (Molybdenum-Osmium) BT - Li-Mg – Nd-Zr*, pages 1–2. Springer Berlin Heidelberg, Berlin, Heidelberg, 1997. ISBN 978-3-540-68538-8. doi: 10.1007/10522884{_}2077.
- [324] Leo Brewer, R H Lamoreaux, R Ferro, and R Marazza. The Mo-Pt system (Molybdenum-Platinum). *Bulletin of Alloy Phase Diagrams*, 1(2):89–92, 1980. ISSN 0197-0216. doi: 10.1007/BF02881200. URL <http://dx.doi.org/10.1007/BF02881200>.
- [325] H Okamoto. Mo-Re (Molybdenum-Rhenium). *Journal of Phase Equilibria and Diffusion*, 31(6):580–581, 2010. ISSN 1863-7345. doi: 10.1007/s11669-010-9787-4. URL <http://dx.doi.org/10.1007/s11669-010-9787-4>.
- [326] Lei Wang, Thomas Maxisch, and Gerbrand Ceder. Oxidation energies of transition metal oxides within the GGA+U framework. *Physical Review B*, 73(19):195107, may 2006. ISSN 1098-0121. doi: 10.1103/PhysRevB.73.195107. URL <https://link.aps.org/doi/10.1103/PhysRevB.73.195107>.
- [327] Hiroyuki Abe, Masami Terauchi, Michiyoshi Tanaka, and Shik Shin. Electron energy-loss spectroscopy strudy of the metal-insulator transition in V₂O₃. *Japanese Journal of Applied Physics*, 37(2):584–588, 1998. ISSN 0449-1947. doi: 10.1051/jphyscol:1976433.
- [328] P.J. Brown, A. G. Fox, E. N. Maslen, M. A. O’Keefe, and B. T. M. Willis. *International Tables for Crystallography (Vol. C)*. 2006. doi: doi:10.1107/97809553602060000600.
- [329] C T Chantler. Theoretical Form Factor, Attenuation, and Scattering Tabulation for Z=1–92 from E=1–10 eV to E=0.4–1.0 MeV. *Journal of Physical and Chemical Reference Data*, 24(1):71–643, jan 1995. ISSN 0047-2689. doi: 10.1063/1.555974. URL <https://doi.org/10.1063/1.555974>.
- [330] Julien Varignon, Mathieu N. Grisolia, Jorge Íñiguez, Agnès Barthélémy, and Manuel Bibes. Complete phase diagram of rare-earth nickelates from first-principles. *npj Quantum Materials*, 2(1):1–8, 2017. ISSN 23974648. doi: 10.1038/s41535-017-0024-9. URL <http://dx.doi.org/10.1038/s41535-017-0024-9>.